Excitations in Superfluids of Atoms and Polaritons

Florian Pinsker

St. Edmund's College, University of Cambridge

This dissertation is submitted for the degree of Doctor of Philosophy

June, 2014

Contents

Well, I'm beginning to see the light..., The Velvet Underground

Declaration

This dissertation describes work undertaken at the Department of Applied Mathematics and Theoretical Physics at the University of Cambridge. Some of its content has already been submitted to peer reviewed journals or published. Except where stated otherwise, this dissertation is the result of my own work and as such contains nothing which is the outcome of work done in collaboration. This dissertation has not been submitted, in whole or in part, for any degree or diploma other than that of Doctor of Philosophy at the University of Cambridge. The dissertation does not exceed the word limit for the Degree Committee.

Florian Pinsker
Summer 2014

Acknowledgements

I have been fortunate to get a scholarship for doing my PhD study at DAMTP starting in 2010 partly funded by EPSRC and by a KAUST grant. After the first year of courses on different mathematical subjects within a doctoral training site at DAMTP I was able to directly start my PhD research. I had the opportunity to work the following three years on further developing the theory of superfluids with Natasha Berloff as supervisor. Pursuing my research on Bose-Einstein condensation has been a persistent pleasure and in particular collaborating with Natasha Berloff, Hugo Flayac, Alex Dreismann, Peter Cristofolini, Hamid Ohadi, Jesus Sierra, Jakob Yngvason and Jeremy J. Baumberg. The inspiration I have gained from working with those researchers has essentially impacted my understanding of the subject under consideration here and as such a great deal of this thesis has to be credited to them. During my time as a PhD student I was visiting the recently founded KAUST University in the holy land of Saudi Arabia. For this possibility I am grateful and for the funding of my research trip by KAUST. The openness, friendliness and interest I have encountered there was leading to new research projects and a throughout wonderful visit. I am in particular deeply honored to have become part of a permanent exhibition in a tea room in Jeddah.

Prologue

Our ability to identify entities of our experience with abstract mathematical structures has been key for the development of ourselves and our modern societies. A physicist models his/her observations mathematically and by doing so s/he admits that the rules of his/her logical picture are mathematical axioms, which are consistent with experience or experiment and universal in the sense that other human beings might share their meaning. For example when analysing the motion of a planet around a star in the way Newton suggested it, we are guided to think of a four dimensional continuous space in such a way that each object within this space has the property of a position at a given point in time and can be associated with a planet, a star or any other object. This allows us to relate the planet and the star via their positions in this abstract space. Furthermore, invoking the concept/axiom of force between objects enables us to make statements about this relation over periods of times. Thus our mathematical consideration of reality allows us to extrapolate a statement about reality. If it fits with experience our mathematical consideration accurately describes the logical form of reality. Indeed we observe planets to be moving around stars and changing their position according to the gravitational force acting upon them and in many cases we are able to predict future behaviors. In general a physical theory might be regarded as settled once it has shown its reliability and appropriateness in describing aspects of reality and dated if a more general and/or accurate framework has been developed. The truth of a physical statement or picture of the world [1] is only determined by its relation to nature and not by its number of citations [2], the status of the person proposing it or that one just believes in it. The possibility to extrapolate within a physical theory led to the observation of a variety of new physical phenomena such as the Aharonov-Bohm effect in quantum mechanics, where electron beams are affected by an applied magnetic field far from them and so without any counterpart within classical mechanics or entanglement of particles. More generally speaking, extrapolation within physical theories led to the implementations and observations of novel physical states in the laboratory not seen before on our planet.

Over hundreds of years accessing reality by the means of partial differential equations (PDEs) has been proven to be remarkably successful. Newton's classical mechanics, the second law of thermodynamics or the Maxwell equations are ingenious examples in physics with tremendous applications in all technical disciplines and implications on the state of our society. With the rise of wave mechanics in the beginning of the 20th century new kinds of PDEs emerged such as Schrödinger's equation (SE), which gives an accurate picture of e.g. the hydrogen atom and the dynamics of quantum mechanical single-particle processes. Some systems of many particles, however, are very hard to be computed by the means of Schrödinger's many-body quantum mechanics. Instead

it is often more practical (and indeed more accurate when particle numbers vary) to invoke the general framework of quantum field theory. For fixed particle numbers both frameworks are identical and it turns out that under certain physical circumstances effective equations of state functions for particular many-body systems are similar to Schrödinger's equation describing the state of a single-particle. In contrast to SE these effective equations in many-body systems now include mathematical adaptions such as nonlinearities accounting for interactions with other particles or growth and decay terms that vary the mass of the probability amplitude.

In the course of this thesis we are considering Schrödinger-type equations arising as effective theories in the context of the quantum many-body problem. These are ensembles of particles such as atoms or excitations in semiconductors for which quantum effects are to a certain degree non-negligible, thus traces of the quantum world remain within the effective state equation describing them. In general these non relativistic PDEs have first order in time and second order spatial derivatives, while some adaptions include first order spatial derivatives or fractional derivatives. Solutions to these differential equations describe certain kinds of waves within ensembles of particles. Although mathematically similar in structure they can be identified with ensembles of entities/particles that physically have very different constituents. It turns out that the microscopic structure of an ensemble often plays a secondary role for the form of the wave - a phenomenon encountered in many classes of complex systems and referred to as universality [3]. Quantum particles such as atoms and electrons behave themselves as waves, each obeying some wavelength. So in the study of waves in many-body systems the concept of coherence has been widely used describing their temporal and spatial interference. Important examples of coherent waves in physics are lasers or Bose-Einstein condensates (BEC) of atoms and molecules.

Atomic BEC were first realized in experiment unambiguously in dilute and weakly interacting Bose gases [4, 5, 6]. The concept of BEC carries at its heart the idea of coherence as it is indeed a macroscopically occupied quantum state of a single particle mode, i.e., each particle within the condensate is described by the same spatially extended wave function and so the ensemble of particles forms a giant matter wave out of the constituents of the ensemble. By the indistinguishability of its components the individual meaning of a single particle vanishes in the collective form of the condensate. Bosons can share the same quantum state and in principle can form such a collective. In contrast, fermions are prevented to occupy the same quantum state due to Pauli's exclusion principle. Some of the species of molecules used in experiments to form BEC, however, indeed are fermions - by forming quasiparticles due to interactions between them, some fermions can arrange as new entities that behave as bosons and as such can condense into the same single-particle quantum mode and thus induce a giant matter wave in the many-body system. In a proper regime the giant matter wave function satisfies a nonlinear Schrödinger-type equation (NLSE). In the context of Bose-Einstein condensate theory this wave equation was derived first by E.P. Gross and L.P. Pitaevskii in order to describe quantum vortices in liquid Helium [7, 8] and now is referred to as Gross-Pitaevskii equation (GPE). Solutions to the NLSE or GPE include such phenomena as solitons, quantum vortices or quantum vortex rings. These elementary and

topologically stable excitations are spatially localized entities that evolve without changing their form over time. Excitations within the condensate wave function are caused by an access of energy of the BEC and in conservative systems they persist in time due to the missing mechanism to release the energy.

The attempt of generating a single occupied mode in a many-body system might be regarded as being a further logical step in the long tradition of the quest of to purify elements, which led to such developments as extracting aluminum into its elemental state in the beginning of the 19th century [9]. Atomic BEC, besides often consisting of a single kind of atoms, is a purication regarding the states these atoms obey, and as such is very articial and not encountered on earth apart from laboratories starting in 1995 [4, 5, 6].

Investigations on BEC have been key in understanding quantum matter at low temperature with its distinctive properties [10, 11]. BEC is a macroscopic quantum phenomenon often involving a great and seemingly unbounded number of interacting coherent quantum particles [11]. A major route of research on BEC has been on applying the concept of macroscopically occupied many-body states [12, 13] to a great variety of different materials such as solid-state light-matter systems, atoms and molecules of different species, photons or classical waves [14, 15, 16, 17]. Although different in nature, once condensation is established these many-body systems often obey similar coherent matter properties. Important examples are superfluidity, i.e., frictionless flow [18] below a critical velocity [19] or the unique response to motion via elementary excitations such as quantum vortex rings, quantum vortices and dark or bright solitons [20, 21, 22, 23, 24, 25, 26]. On the other hand do various BECs show specific properties depending on the nature of their carrying physical system, such as variable inter-particle interactions due to Feshbach resonances within certain external magnetic fields [27] or local particle sources and sinks in non-equilibrium systems.

An outstanding example are exciton-polaritons, quasiparticles which in some parameter regime show Bose-Einstein statistics and for which recently condensation has been established experimentally [16]. Excitons are coupled electron-hole pairs of oppositely charged spin-half particles in a semiconductor held together by an effective Coulomb force between them [28] as the energy to form a pair is lower than a free electron and a free hole. They interact with light fields [29] and can form quasiparticles themselves, so called exciton-polaritons (polaritons), in the strong coupling regime when confined to a micro-cavity [30]. As they possess integer spin they can condense in dilute systems, despite the fact that some of the elementary constituents are fermions. In particular, as exciton-polaritons are 10^9 times lighter than rubidium atoms [16], condensation could be observed at the Kelvin range in CdTe/CdMgTe micro-cavities or more recently even at room temperatures in flexible polymer-filled micro-cavities [31], which clearly sets them apart from atomic Bose-Einstein condensates observed below 200 nano Kelvin [4, 5, 6]. As a consequence for exciton-polariton quasiparticle systems much less technological effort is required to cool the system below condensation threshold in order to achieve BEC [16, 31]. The requirement for high vacua and the necessity of very good insulation are major obstacles for technological applications of atomic BEC, which stands in stark contrast to the requirements for exciton-polariton condensation and clearly favors the

latter for technological devices feasible outside the laboratory.

Another key property of exciton-polaritons is that they are quasiparticles which can be generated at will by pumping the system with a laser beam (see e.g. [32]). Once created they obey a finite lifetime of about 1-100ps [28, 33]. This finite lifetime is a consequence of the leakage of photons through the cavity mirrors covering the semiconductor [28] and non-radiative dissipative processes [15]. In this sense these BEC are non-equilibrium systems, which besides being feasible at room temperatures allow very high control over the experimentally generated condensate wave function [32]. Taking this into account it is clear that exciton-polariton condensates are excellent candidates for a variety of technical devices as the plethora of recent proposals shows [34, 35, 36, 37, 38, 39, 40, 41] of which some already have been implemented in experiments [42, 43, 44]. Here one very remarkable example of an application for exciton-polariton condensation is that for room-temperature polariton lasers based on GaN micro-cavities [45, 46]. These lasers emit coherent and monochromatic light without population inversion - a major distinction to conventional lasers [46, 15].

From a theoretical viewpoint a successful mean-field model for exciton-polariton condensates is a complex Ginzburg Landau-type equation, which induces the time evolution of the order parameter (condensate wave function) of the system [47, 48, 26, 32] and which in some scenarios is coupled to a reservoir of non-condensed polaritons [49, 32]. Several recent papers show that these systems of PDE's provide good results in modeling exciton-polariton condensates [49, 32], but often a more thorough analysis indicates the necessity to improve our current models by including more physics, such as the disorder due to the sample imperfections [50].

Now, the purpose of this thesis is to introduce the reader to the theories of equilibrium and non-equilibrium BEC described in terms of NLSEs and to present new results within those frameworks in the context of condensed matter physics. It is clear however that the results can be relevant for investigations in analogous systems within different fields due to universality and might have a possible impact for applications and on related areas as well. My thesis is devided in chapters as follows.

1. In the first chapter I introduce the concept of Bose-Einstein condensation as a macroscopically occupied state due to Einstein. In the following I present the Gross-Pitaevskii theory, the basics framework of Bose-Einstein condensation, for atoms as it is derived from a second quantisation scheme and correspondingly mathematically rigorous theorems that show the interconnection with the many-body Schrödinger equation. I discuss state-of-the-art theoretical concepts within the theory of equilibrium condensates such as elementary excitations and the dispersion law due to Bogoluibov. Subsequently I explain the meaning of exciton-polaritons in semi conductor micro cavities in terms of a second quantization model and their condensation. These quasiparticles when condensed are a prime example for non equilibrium BEC. An analog to the atomic Gross-Pitaevskii theory is presented including growth and decay processes, which is widely used for the description of exciton-polariton condensates. Finally, I discuss spinor condensates both for the equilibrium and non equilibrium case.

2. I first present a novel rigorous energy theorem within the 2d Gross-Pitaevskii theory of tightly trapped atoms under rapid rotation based on a collaborative effort with Jakob Yngvason. The main tools for the mathematical proof are:
   - finding a proper wave function minimizing the convex energy functionals
   - splitting up the GP energy functional additively into two parts called reduced GP functional and a Ginzburg-Landau-type energy functional due to the latter formal analogy to the theory of Type-I semiconductors
   - establishing statements on the wave function via the direct use of the Gross-Pitaevskii equation, i.e. the equation describing the minimizer. This allows us to relate the minimizer of the GP equation to the corresponding Thomas Fermi (TF) density.
   - employing a lower bound for the Ginzburg-Landau-type functional developed in [112] by appropriate rescaling of the functional.

   Secondly I present a so far unpublished proof for a novel lower bound to the kinetic energy of the reduced Gross-Pitaevskii energy functional. It uses results from the previous proof relating the reduced GP density to the TF density. Furthermore I apply partial integration in order to express the lower bound to the kinetic energy solely in terms of the TF density, which is an explicitly given function, hence yielding the asymptotic lower bound.

3. In chapter III I present results made in an collaborative effort together with Natasha Berloff and Victor Pèrez-Garcìa for a quantum machine enabling the generation of solitons and quantum vortex rings in highly elongated harmonically trapped atomic Bose-Einstein condensates. This proposal is based on the possibility of locally changing interactions within atomic condensates via applying a magnetic field utilizing the phenomenon of Feshbach resonances. In addition we present numerical results as well as novel mathematical expressions for soliton trains within two component/spinor condensates. Another particular outcome of this investigation is numerically generated evidence for skyrmions/core vortices within two component BEC.

4. In chapter IV I present a study of superfluid flow of an atomic condensate passing small impurities and arrays thereof, which has been contrived in joint work with Natasha Berloff. In the beginning of this chapter the BEC model is introduced including an impurity in relative motion. Then an asymptotic analysis is developed in the stationary frame yielding the critical velocities for the first generation of vortices in BEC when streaming around the small impurity. Subsequently we present numerical results supporting the analytical considerations. Finally we extend the setup of a single impurity in the superfluid's stream to arrays of impurities. This generalization gives rise to new phenomena such as different phases of structurally different excitation generation within such lattices depending in particular on the lattice constant and the superfluid velocity.

5. This chapter is devoted to present results for an effective soliton train generator within exciton-polariton condensates developed collaboratively with Hugo Flayac. The main idea is that pumping on a potential step induced via an external electric field will induce excitations within the condensate due to the induced flow caused by the difference in potential energy and the incoming stream of pumped particles. As increased pumping also increases the density of the condensate and, therefore, the local speed of sound, less solitons are generated within the stream. We show the very high control over the number of generated solitons via this effect over time with varying parameters. The excitations are generated as the nonlinearity of the superfluid's state equation cannot compensate the local access of energy at the step and the phase of the wave function starts winding up. Electric control over soliton generation via varying step function is also demonstrated. Finally we show that via TM-TE splitting we can generate half -soliton trains in both components which separate due to the repulsive interactions between the solitons. We believe this proposal has the potential to be at the heart of polariton semiconductor devices.

6. In the final chapter of this thesis I present the results of a collaboration with experimenters Alexander Dreismann, Peter Cristofolini, Ryan Balili, Gabriel Christmann, Zaharias Hatzopoulos, Pavlos G. Savvidis, and Jeremy J. Baumberg and the theoretician Natasha Berloff on ring like exciton-polariton condensates. In an appropriate parameter regime symmetry breaking within the condensate occurs. This patter formation has been shown to be feasible within experiments and the complex GP (cGP) model and the interconnection between both are extensively discussed. In particular the cGP model predicts the same radius dependence of the pattern structure (number of lobes) as the experimentally generated condensate does, thereby demonstrating the strong interconnection between theory and experiment. Furthermore dynamical considerations are made by disturbing the lobes pattern with a laser beam, which is shown to be in good agreement with the model.

1 Bose-Einstein condensation theory

1.1 Fundamental concepts

1.1.1 Particle statistics

An anomaly at low energy levels

The dawn of research on Bose-Einstein condensation was set with S.N. Bose's discovery of a new method for counting occupation numbers of possible states of photons in phase space, which he developed to derive Planck's law for the spectral distribution in a cavity at thermal equilibrium without the need of any reference to classical theory [51, 52]. Subsequently Einstein applied this remarkable way of counting occupation numbers to a case of *massive* particles. More specifically he considered the atomic ideal gas [12] made of entities now classified as *bosons*, i.e. particles having *integer* spin. By considering all possible distributions for these particles in phase space with respect to their defining properties of indistinguishability and the possibility to occupy the same state more than once, one gets a formula for the mean number of atoms with an energy $E_s = cs^{2/3}$ of a phase space cell s,

$$n_s = \frac{1}{e^{A+\frac{E_s}{\kappa T}} - 1}, \tag{1.1.1}$$

where A, κ, c are constants and T is the temperature of the system. Here the constraint of fixed particle number $n = \sum_s n_s = const$ has to be satisfied as well as the mean energy has some fixed value due to the condition of thermal equilibrium of the many-atom system.

For the possible number of particles within a fixed volume V and at a temperature T he found that particles have to occupy or "condense" into the lowest energy state to conserve the total particle number a phenomenon now referred to as Bose-Einstein condensation. We write

$$n = n_0(T) + n_c(T), \tag{1.1.2}$$

and denote the number of atoms in the ground state (GS) by n_0. The second term on the r.h.s. in (1.1.2) must satisfy $n_c = (cT)^{2/3} \to 0$ as $T \to 0$ [12]. Underlying this observation was that he presumed all particles can in principle share a common ground state - a key aspect of bosons. The complementary class of particles that make up our visible world, fermions, would fill up every free energy cell depending on their energy just once due to Pauli's exclusion principle. This introduces a different particle statistic in phase space and thus a different formula for distributions of particles along energy levels.

Comparison of boson, fermion and Maxwell-Boltzmann statistics

We consider an ensemble of N noninteracting particles of energies ε_i with $i \in \{1, 2, 3, \ldots\}$, introduce the chemical potential μ of the reservoir with which the system is in thermal equilibrium and write $\beta = 1/(k_B T)$ with k_B denoting Boltzmann's constant. For bosons in a state i being indistinguishable and able to occupy same energies the mean occupation number for particles of energy ε_i follows from the grand canonical partition function of statistical mechanics. It is given by [10, 11]

$$\langle n_i \rangle_{\text{bosons}} = \frac{1}{e^{\beta(\varepsilon_i - \mu)} - 1}, \tag{1.1.3}$$

where the chemical potential is fixed by $\sum_i \langle n_i \rangle_{\text{bosons}}(\mu, \beta) = N$. Similarly for fermions that are indistinguishable but cannot share the same energy state one obtains

$$\langle n_i \rangle_{\text{fermions}} = \frac{1}{e^{\beta(\varepsilon_i - \mu)} + 1} \tag{1.1.4}$$

and classically (Maxwell-Boltzmann) for distinguishable particles that can occupy the same energy spot ε_i we have

$$\langle n_i \rangle_{\text{classical}} = \frac{1}{e^{\beta(\varepsilon_i - \mu)}}. \tag{1.1.5}$$

In Fig. 1.1 we show a comparison of the graphs for the different particle distributions. In all three cases μ is fixed by the normalization condition due to the fixed number of particles in closed systems. In particular we see that energy levels for fermions can only be singly occupied while as $\varepsilon_i \to \mu$ that for bosons diverges. If the chemical potential μ were bigger than the lowest energy eigenvalue ε_0, the mean occupation number would become negative for the ground state. Hence, by reductio ad absurdum this case can be considered unphysical. Once the atoms in excited states are less than the total number of particles N occupation of the lowest energy state has to be the consequence [53] and as the temperature decreases lower energy levels are increasingly occupied.

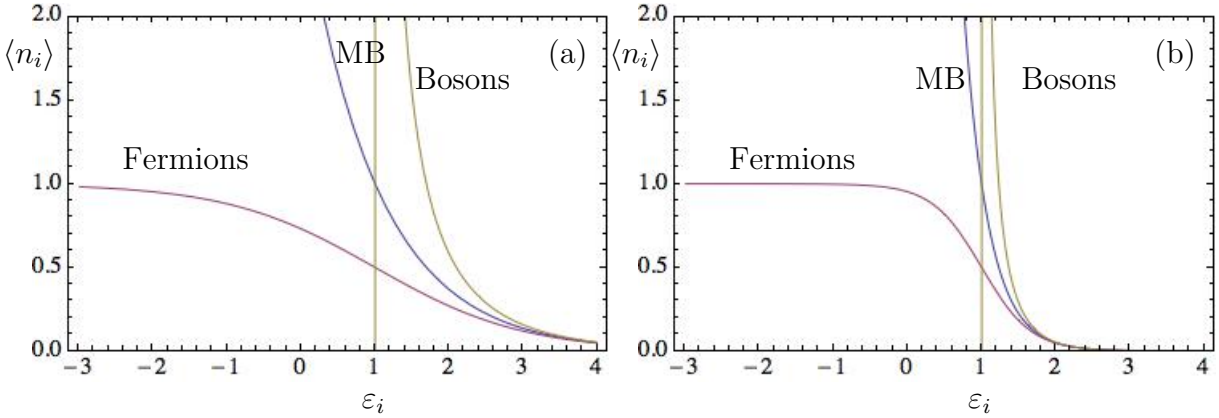

Figure 1.1: Occupation numbers vs energy. Parameters are $\beta = 1$ in picture (a) $\beta = 3$ in picture (b) while $\mu = 1$ in both. As $\varepsilon_i \to \mu$ with $\varepsilon_i > \mu$ the boson distribution diverges.

To distinguish the macroscopically occupied state from the other states one separates it out of the total particle number and defines

$$N = \sum_{i=0}^{\infty} \langle n_i \rangle_{\text{bosons}} = N_0 + N_T, \tag{1.1.6}$$

where we introduced

$$N_0 = \frac{1}{e^{\beta(\varepsilon_0 - \mu)} - 1} \tag{1.1.7}$$

and N_T denotes the remainder, i.e. the thermal component of excited bosons [57] [62]. From (1.1.7) it follows straightforwardly

$$\varepsilon_0 - \mu = k_B T \ln\left(1 + \frac{1}{N_0}\right) \simeq \frac{k_B T}{N_0} \tag{1.1.8}$$

relating the key parameters to the ground state.

1.1.2 Macroscopic occupation of the lowest energy level

Critical temperature in 3 spatial dimensions (3d)

Expression (1.1.8) shows that for Bose gases the lowest energy level ε_0 becomes increasingly occupied, once the chemical potential $\mu \to \mu_c = \varepsilon_0$. This is enhanced when the gas is cooled down below a certain temperature - inevitably a fraction of bosons will occupy the lowest energy level [12, 54, 11]. Now, for an ideal 3d Bose gas of particles with mass m confined to a box of volume V the critical temperature is easily obtained by replacing the sum in (1.1.6) with an integral and by supposing that the thermal particles at the critical temperature satisfy

$$N_T(T_c, \mu = \varepsilon_0) = N, \tag{1.1.9}$$

by which we presume that $N_0 \to 0$ at the transition temperature T_c and that the excited states ε_i are well populated close to the ε_0 energy level [53]. One assumes $\mu = \varepsilon_0$, since then the number of particles in excited states close to the GS is maximized, which we set equal to N. Thus it follows [11, 53] that

$$k_B T_c = \frac{2\pi\hbar^2}{m} \left(\frac{n}{2.612}\right)^{2/3} \tag{1.1.10}$$

with $n = N/V$ and $\hbar$ denoting Plank's constant devided by 2π. Below that the number of particles in the GS with energy ε_0 is [11]

$$N_0(T) = N\left(1 - \left(\frac{T}{T_c}\right)^{3/2}\right). \tag{1.1.11}$$

Applying the same setup of particles in a box leading to a critical temperature for 1d or 2d would fail, since for that case T_c would have to be zero [53]. However, trapping

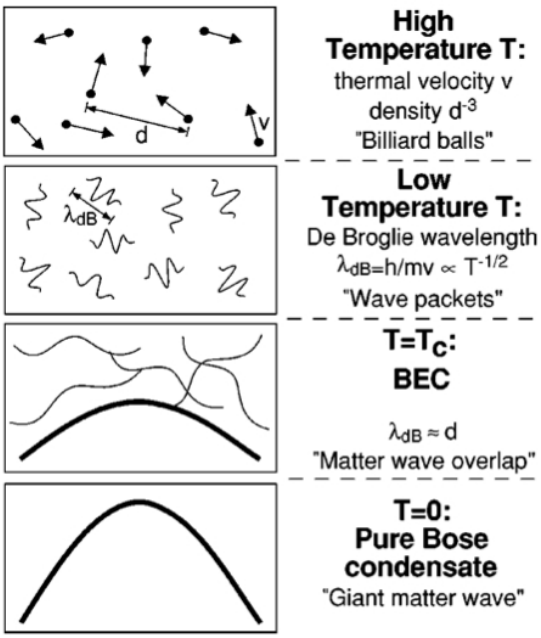

Figure 1.2: BEC at different stages/temperatures of the cooling process [54].

of bosons in a harmonic trap allows a finite critical temperature to occur for 1d and 2d systems as well as discussed in more detail later. To get a rough idea of the particle numbers within different samples of BEC we note that they can vary significantly from $N \simeq 10^3 - 10^{10}$ in dilute systems [10, 4, 5, 6] to $N \simeq 10^{23}$ in chemical samples up to $N \geq 10^{45}$ in hypothetical boson stars [55]. Among the bosons for which BEC has been unambiguously demonstrated are ^{87}Rb, ^{85}Rb, ^{23}Na, ^{7}Li [10] and ^{6}Li [56] or quasiparticles in semiconductor micro cavities such as polaritons [16] or photons [14] or classical waves [17].

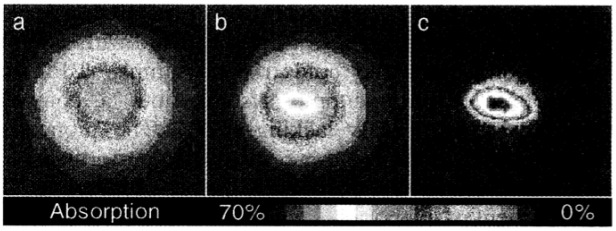

Figure 1.3: (a) shows the velocity distribution above the condensation threshold, (b) just below the condensation threshold and (c) showing an even cooler BEC [5].

Formation of a giant matter wave

The thermal de Broglie wavelength, i.e. the mean wavelength of a particle for a free ideal gas in equilibrium with no internal degrees of freedom at some temperature, say T, is given by [28]

$$\lambda_{\text{deBroglie}} = \frac{2\pi\hbar}{\sqrt{2\pi m k_B T}}, \tag{1.1.12}$$

with m being the mass of the particle. It increases as the temperature $T \to 0$ in principle to infinity. As the wave functions of each boson of the gas start to overlap, however, interactions between particles lead to synchronization of waves and the creation of the giant matter wave, so the ideal gas approximation becomes inaccurate and a microscopic theory including interactions becomes relevant. Usually the giant matter waves formed are confined to a finite area in space, due to magnetic trapping for atomic BEC or the finite sized semiconductor micro cavities in which polariton condensates exist, thereby imposing a constraint on the maximal wavelength. Fig. 1.2 illustrates the stages of the formation of a giant matter wave as the condensate cools down below the critical temperature. As the wave function extends spatially its momentum p distribution of all particles narrows due to de-Broglies postulate $\lambda = h/p$ for matter waves. In Fig. 1.3 experimental data for the transition to BEC is shown in terms of a narrowing of the momentum distribution. The momentum of the measured particles is tightly located at very low temperatures as expected for the formation of BEC and proofing both spatial coherence of the particle waves and macroscopic occupation of a single particle mode [5], both properties now regarded as key requirements for BEC [10].

1.1.3 BEC within the formalisms of quantum mechanics

After reviewing the basics for BEC we introduce the reader in this section to the theoretical formalism of many-body quantum field theory to describe in those terms the phenomenon of macroscopically occupied states and to enable us to discuss interacting systems. A key concept is the field operator of the quantum many-body system. Knowing its form exactly corresponds to having the most complete knowledge about the many-body system.

Annihilation and creation operators

We consider N identical separable quantum particles each described by a wave function $\psi_i \in \mathcal{H}_1$ with $i \in \{1, \ldots, N\}$. N-particle states are vectors in a Hilbert space

$$\mathcal{H}_N = \underbrace{\mathcal{H}_1 \otimes \mathcal{H}_1 \otimes \ldots \otimes \mathcal{H}_1}_{n \text{ times}}, \tag{1.1.13}$$

which is spanned by states $|\psi_1, \psi_2, \ldots, \psi_N\rangle$ with $\psi_i \in \mathcal{H}_1$ where $i \in \{1, 2, \ldots, N\}$. To include the possibility of particle creation and annihilation the Fock space is introduced as

$$\mathcal{F}(\mathcal{H}_1) = \mathbb{C} \oplus \bigoplus_{N \geq 1} \mathcal{H}_N(\mathbb{R}^{3n}, d\vec{x}_1, \ldots, d\vec{x}_N), \tag{1.1.14}$$

where the so called Fock vacuum is given by $\Omega = (1, 0, 0, \ldots)$. Generally, vectors of $\mathcal{F}(\mathcal{H}_1)$ are sequences

$$\Psi = \{\psi_i\}_{i\geq 0} \tag{1.1.15}$$

with $\psi_i \in \mathcal{H}_i$ and must satisfy

$$\|\Psi\|^2 = \sum_{n\in\mathbb{N}_0} \|\psi_n\|^2 < \infty. \tag{1.1.16}$$

The inner product of states in $\mathcal{F}(\mathcal{H}_1)$ is defined as

$$\langle \Psi, \Phi \rangle = \sum_{i\in\mathbb{N}_0} \langle \psi_i, \phi_i \rangle, \tag{1.1.17}$$

so the Fock space has the structure of a Hilbert space. In this work we consider $|\psi_1, \ldots, \psi_N\rangle \in \mathcal{H}_N = L^2(\vec{x}_1, \ldots, \vec{x}_N)$, i.e., many-body states dependent on positions $\vec{x}_1, \ldots \in \mathbb{R}^d$ and in chapter 8 include the spin degree of freedom $|\psi_1, \ldots, \psi_N\rangle \in \mathcal{H}_N = L^2(\vec{x}_1, s_1, \ldots, \vec{x}_N, s_N)$. The Hilbert space $\mathcal{H}_N$ can be divided into a symmetric part $\mathcal{H}_N^s$ and an asymmetric part $\mathcal{H}_N^a$ with respect to permutations of the single particle states. Correspondingly the Fock space $\mathcal{F}(\mathcal{H}_1)$ can be divided into $\mathcal{F}(\mathcal{H}_1^s)$ and $\mathcal{F}(\mathcal{H}_1^a)$. As we consider bosons throughout this work, we restrict our consideration to the symmetric part $\mathcal{H}_N^s$. We write for multiple occupied single-particle states

$$|n_1, \ldots, n'_N\rangle = |\psi_1, \ldots, \psi_1, \psi_2, \psi_2, \ldots, \psi_{N'}\rangle. \tag{1.1.18}$$

In this terminology one defines the creation operator for an additional boson as [57],

$$\psi_i \hat{a}_i^\dagger |n_0, n_1, \ldots, n_i, \ldots\rangle = \sqrt{n_i + 1}\,|n_0, n_1, \ldots, n_i + 1, \ldots\rangle \tag{1.1.19}$$

mapping from $\mathcal{H}^N \to \mathcal{H}^{N+1}$ and the annihilation operator as

$$\psi_i \hat{a}_i |n_0, n_1, \ldots, n_i, \ldots\rangle = \sqrt{n_i}\,|n_0, n_1, \ldots, n_i - 1, \ldots\rangle \tag{1.1.20}$$

mapping $\mathcal{H}^N \to \mathcal{H}^{N-1}$. Here n_i are the eigenvalues of $\hat{n}_i = |\psi_i|^2 \hat{a}_i^\dagger \hat{a}_i$ that give the numbers of bosons in state i. We write synonymously $\psi_i \hat{a}_i^\dagger = \hat{a}_i^\dagger(\psi_i)$. An important feature is that on a symmetric Fock space the commutation relations of the creation and annihilation operators satisfy canonical commutation relations (CCR) [11],

$$[\hat{a}_i, \hat{a}_j^\dagger] = \delta_{ij}, \qquad [\hat{a}_i, \hat{a}_j] = 0 = [\hat{a}_i^\dagger, \hat{a}_j^\dagger]. \tag{1.1.21}$$

On the other hand Fermions do satisfy canonical anti-commutation relations. Employing those terms we introduce the field operator as a superposition of states of different particle numbers [10, 11]

$$\hat{\Psi}_N^\dagger = \sum_i^N \psi_i \hat{a}_i^\dagger. \tag{1.1.22}$$

These field operators act on the Fock vacuum by

$$\hat{\Psi}_N^\dagger |\Omega\rangle = |\psi_1, \ldots, \psi_N\rangle \tag{1.1.23}$$

The creation operators within the field operators represent a linear combination of single particle states corresponding to an ONB in $\mathcal{H}_N^s \subseteq \mathcal{F}(\mathcal{H}_1^s)$, i.e.

$$\hat{a}_i^\dagger|\Omega\rangle = (0, 0, \ldots, 0, \underbrace{1}_{i\text{'s position}}, 0, \ldots), \tag{1.1.24}$$

so that

$$\hat{\Psi}_N^\dagger|\Omega\rangle = (\psi_1, 0, 0\ldots) + (0, \psi_2, 0\ldots) = |\psi_1, \ldots, \psi_N\rangle. \tag{1.1.25}$$

In this sense $\psi_i\hat{a}_i^\dagger$ ($\psi_i\hat{a}_i$) describe the creation (annihilation) operators of the single particle mode ψ_i at position i in a Fock space vector. It is clear that strictly speaking an infinite sequence in Fock space is not equal to a vector in Hilbert space, but from a physicists view the content of information about the physical system is equivalent and we simply write $(\ldots, \psi_N) = |\ldots, \psi_N\rangle$.

In its most general form the field operators $\hat{\Psi}_N^\dagger$ acting on the vacuum $|\Omega\rangle$ gives the N particle state. For fixed particle numbers it is sometimes more convenient to consider the wave function (Schrödinger field) $\psi(\vec{x}_1, \ldots, \vec{x}_N)$ for an N-particle state instead of a field operator acting on Fock space. This is possible as in the case of fixed particle numbers both frameworks are equivalent and the distinction is only due to the different notations. Here the Schrödinger field gives the probability amplitude $|\psi|^2$ of an ensemble being at some point in $\mathbb{R}^{3N}$ phase space and $\psi \in \mathcal{H}_N$. In the course of this thesis the reader will encounter both notions used when appropriate.

Macroscopic occupation of a single mode

Multiple occupation of a single particle state, say M particles are in a state f and the remainder in states ψ_i, means that our field operator can be written as

$$\hat{\Psi}_N^\dagger = \sum_{i=0}^{N-M-1} \psi_i\hat{a}_i^\dagger + \sum_{j=N-M}^{N} f\hat{a}_j^\dagger. \tag{1.1.26}$$

Acting on the Fock vacuum we have

$$\hat{\Psi}_N^\dagger|\Omega\rangle = |\psi_1, \ldots, \psi_{N-M-1}, f, \ldots, f\rangle \tag{1.1.27}$$

So essentially the Hilbert space $\bigotimes^M \mathcal{H}_1$ of multiple occupied states is equivalent to a single particle Hilbert space $\mathcal{H}_1$, since each entry of the M dimensional vector is the same.

In terms of the above quantum field operators one defines the one-body density matrix

$$n^{(1)}(\vec{r}, \vec{r}_*) = \langle\hat{\Psi}_N^\dagger(\vec{r})\hat{\Psi}_N(\vec{r}_*)\rangle. \tag{1.1.28}$$

This definition implies the special case $n(\vec{r}) = \langle\hat{\Psi}_N^\dagger(\vec{r})\hat{\Psi}_N(\vec{r})\rangle$, which is referred to as the diagonal density of the system [11] or the one-particle density. Furthermore the corresponding eigenvalue equation of the one-body density matrix is

$$\int d\vec{r}_* n^{(1)}(\vec{r}, \vec{r}_*)\psi_i(\vec{r}_*) = n_i\psi_i(\vec{r}) \tag{1.1.29}$$

and its solutions $\psi_i(\vec{r}')$ are called the single particle modes of the condensate and provide an ONB in the corresponding Hilbert space [11]. Consequently in its diagonalized form the one-body density matrix can be written as

$$n^{(1)}(\vec{r},\vec{r}_*) = \sum_i n_i \psi_i(\vec{r}_*)\psi_i(\vec{r}), \tag{1.1.30}$$

where n_i denote the occupation numbers of the single particle modes $\psi_i(\vec{r}')$. These occupation numbers correspond to field operators given by

$$\hat{\Psi}_N^\dagger = \sum_{i=0}^{n_0-1} \psi_0 \hat{a}_i^\dagger + \sum_{j=1,N'} \sum_{i=n_0}^{n_{j+1}-1} \psi_j \hat{a}_i^\dagger. \tag{1.1.31}$$

We assume $\hat{a}_i^\dagger(\psi_i)$ to provide an ONB in $\mathcal{H}_N^s \subseteq \mathcal{F}(\mathcal{H}_1^s)$. The quantum field operator (1.1.31) acts on the Fock vacuum by

$$\hat{\Psi}_N^\dagger|\Omega\rangle = |\psi_0,\ldots,\psi_0,\psi_1,\ldots\rangle = |n_0,n_1,\ldots,n_{N'}\rangle \tag{1.1.32}$$

with $N' \leq N$. So different modes j are occupied with multiplicity n_j.

Complete Bose-Einstein condensation

Now in terms of (1.1.30) complete (100%) Bose-Einstein condensation is achieved in a many-body system, iff

$$n^{(1)}(\vec{r},\vec{r}_*) = n_0 \psi_0(\vec{r}_*)\psi_0(\vec{r}), \tag{1.1.33}$$

i.e. $n_0 = N$ or likewise in the Fock space vector notation

$$\hat{\Psi}_N^\dagger|\Omega\rangle = |\psi_0,\psi_0,\ldots,\psi_0\rangle = |N\rangle. \tag{1.1.34}$$

Here $\psi_0(\vec{r}')$ is referred to as condensate wave function [11, 58], which inherits the complete information about the many-body system. It shows the huge reduction of mathematical complexity of the multidimensional system of e.g. $N \sim 5\times 10^5$ particles in dilute gaseous BEC [5], which effectively can be regarded a one-dimensional system described by a single wave function ψ_0 in $\mathcal{H}_1$. Generally, if there is a $c > 0$, so

$$\frac{n_0}{N} \geq c \tag{1.1.35}$$

for all large N one has BEC [13], i.e. even when other states are occupied too.

According to C.N. Yang [59, 60, 10] an additional necessary criterion for BEC is the need to have off-diagonal long-range order (ODLRO), where the one-body density matrix does not vanish at large distances, i.e. when

$$\lim_{|\vec{r}|\to\infty} n^{(1)}(\vec{r},0) = \lim_{N\to\infty} \frac{n_0}{V} > 0. \tag{1.1.36}$$

For example for the simple condensate wave function $\psi_0 = c$ with c being a constant one has ODLRO [59], which corresponds to the picture of an spatially highly extended condensate wave function.

Once we have macroscopic occupation of a single mode ψ_0, i.e. when $n_0 \gg 1$ one can write for the occupation number operator

$$\langle\psi|\hat{a}^\dagger(\psi_0)\hat{a}(\psi_0)|\psi\rangle = n_0\langle\psi|\psi\rangle = \langle\psi|\hat{a}(\psi_0)\hat{a}^\dagger(\psi_0) - 1|\psi\rangle \simeq \langle\psi|\hat{a}(\psi_0)\hat{a}^\dagger(\psi_0)|\psi\rangle. \quad (1.1.37)$$

Here the non-commutativity has been neglected as an approximation in the final step, which is fairly reasonable for $N \geq 10^3$ particles in the 0 mode. So for a macroscopic population of a single particle mode one can introduce the Bogoliubov approximation [11] and we write for the creation operator of a BEC mode $\hat{a}^\dagger(\psi_0) = \sqrt{n_0}\psi_0 = \hat{a}(\psi_0)$ corresponding to neglecting the CCR satisfied by the creation and annihilation operators. By such an approximation fluctuations of quantum numbers of the different modes are assumed to be irrelevant for the description of the condensate.

1.2 Equilibrium condensates

Bose-Einstein condensates in equilibrium have a fixed number of particles. Such systems include condensed rubidium atoms (^{87}Rb) trapped in an electric field [4], where the gain and drain of particles both are zero. When confined to a finite volume most bosons interact with each other and alter their state functions. For separable bosons there exist a great variety of interaction processes and potentials describing their nature [61, 11, 53]. Once particles have interacted and moved far away from each other, however, often the details of the interaction can be neglected - a simplification widely used in scattering theory, where only relations between incoming states and outcoming states are made. In dilute quantum many-body systems at low temperature particles are in slow motion and only occasionally interact with each other. So for short ranged interactions between particles details of the interactions indeed can be neglected to understand the whole system to a satisfying degree. Indeed in cold atomic vapors the mean particle separation is of order 10^2nm while the length scales of atom-atom interactions is one order of magnitude smaller [53]. Simplified interaction potentials, i.e., without considering all details of the scattering process, are a first step towards understanding the complete interacting many-body system. A key concept when these details are less important is that of the two-particle scattering length [63, 61, 62], which we introduce in the beginning of this section.

1.2.1 Tuneable scattering length a

The concept of scattering length a

We consider two slowly and freely moving quantum particles, which scatter due to a short ranged scattering potential, say v. Furthermore they scatter elastically, i.e. have unchanged internal degrees after the collision. As a simple model we take the two-body Schrödinger equation, which imposes the time evolution of the wave function [61],

$$i\hbar\partial_t\psi(\vec{r}_1,\vec{r}_2,t) = \hat{H}\psi(\vec{r}_1,\vec{r}_2,t), \tag{1.2.1}$$

where $\psi(\vec{r}_1,\vec{r}_2,t)$ is the two-body wave function. We assume $\vec{r}_i \in \mathbb{R}^3$ with $i \in \{1,2\}$. The Hamiltonian for two colliding particles is

$$\hat{H} = \frac{\vec{p}^2}{2M} + V(\vec{r}), \tag{1.2.2}$$

where we introduce the relative coordinate $\vec{r} = \vec{r}_1 - \vec{r}_2$ and $\vec{p} = \vec{p}_1 - \vec{p}_2$, and the reduced mass $M = m_1m_2/(m_1+m_2)$. Long time after the collision of the particles one will get time independent states. These correspond to wave functions of the form $\psi(\vec{r},t) = e^{-itE_n/\hbar}\psi(\vec{r})$, so (1.2.1) becomes

$$\hat{H}\psi(\vec{r}) = E_n\psi(\vec{r}), \tag{1.2.3}$$

where E_n is the corresponding nth eigenvalue of an eigenfunction ψ. Freely moving particles which move along z-direction are of the form $\psi(z) = e^{ik_zz}$ with $\vec{r} = (x,z)$.

The scattered particle is asymptotically for large distances described by a wave function including a term with some information of the scattering process [61, 53]

$$\psi \simeq e^{ik_z z} + f(\theta)\frac{e^{i\vec{k}\vec{r}}}{r}, \tag{1.2.4}$$

where $f(\theta)$ is the so called scattering amplitude for which one assumes spherically symmetric interactions between atoms, hence only dependence on the scattering angle θ. The scattering amplitude for spherically symmetric potentials, implying axial symmetry with respect to the direction of the incident particle, can be expanded as [53]

$$f(r,\theta) = \sum_{l=0}^{\infty} A_l R_{kl}(r) P_l(\cos(\theta)) \simeq \frac{1}{i2k}\sum_{l=0}^{\infty}(2l+1)(e^{i2\delta_l}-1)P_l(\cos(\theta)) = f(\theta) \tag{1.2.5}$$

with $l \in \{0,1,2,\ldots\}$ corresponding to the $s, p, d, \ldots$ partial waves of the scattering amplitude. The approximation in the second step is due to an asymptotic approximation of the radial profile, see [53] for details. Here P_l are Legendre polynomials and we have introduced the phase shifts δ_l. As a measure of the strength of a scattering process one introduces the scattering cross section, which under the made assumptions depends only on the magnitude of $\vec{k}$ [53],

$$\sigma(k) = 2\pi \int \left|f(\theta)\right|^2 \sin(\theta) d\theta. \tag{1.2.6}$$

For (isotropic) s-wave scattering, i.e., at low energies, the cross section for indistinguishable particles is simply given by [53, 61, 63]

$$\sigma(k) = 8\pi|f|^2 = \frac{8\pi}{k^2}\sin^2\delta_0 \tag{1.2.7}$$

and in the small k limit on gets

$$\lim_{k\to 0}\sigma(k) = 8\pi a^2. \tag{1.2.8}$$

Here we define the scattering length as

$$a = -\lim_{k\to 0}\frac{\tan\delta_0(k)}{k}. \tag{1.2.9}$$

In this sense the scattering length a does give the complete information of the elastic s-wave scattering process, which clearly is an approximation of the interaction process due to the original potential $V(r)$. On the other hand it can be shown that slowly moving particles, which scatter, have in the first Born approximation a scattering length given by [53]

$$a = \frac{M}{2\pi\hbar^2}\int d\vec{r} V(r), \tag{1.2.10}$$

where $V(r)$ denotes the spherical symmetric interaction potential between the scatterers. In general a different potential implies a different scattering length, however, apparently equivalence classes of different potentials with same scattering length are possible. For two particles with the same mass this implies an effective potential [53]

$$\int d\vec{r} V_{\text{eff}}(r) = \frac{4\pi\hbar^2 a}{m} = V_0, \tag{1.2.11}$$

that could w.l.o.g. be of the form $V_{\text{eff}}(r) = V_0\delta(r)$, which indeed is a good approximation for short ranged interaction processes [11]. For the scalar scattering length one can distinguish two cases, that for positive scatterers, $a > 0$, which corresponds to predominantly repulsive interactions V and negative scattering lengths corresponding to predominantly attractive interactions. For a meaningful treatment of the scattering length in many-body systems it is important to assume a condition for diluteness as then the exact scattering potentials become less relevant for the many-body processes. An appropriate conditions for repulsive scattering potentials is that the mean inter-particle distance has to be much larger than the scattering length a [62]. With attractive scatterers many-body systems might collapse, if there is no process forcing the particles to separate. The main contributor to the effective scattering length in atomic BEC is the repulsive hard core and the van der Waals interaction, which is due to the electric dipole-dipole interactions between atoms [53]. Typical scattering lengths are 10^2 times the atomic length scale [53].

Feshbach resonances

Scattering processes and their effective interactions can in certain cases be significantly altered by external parameters, e.g. due to magnetically induced Feshbach resonances [53]. In such systems the scattering length becomes a function of an external magnetic field [64, 65, 11, 53]

$$a(B) = a_\infty \left(1 - \frac{\Delta B}{B - B_{\text{res}}}\right). \tag{1.2.12}$$

Here B denotes the magnetic field strength, ΔB is the width of the resonance and B_{res} its position and a_∞ denotes the scattering length far away from the resonance. Feshbach resonances allow the spatial and temporal control over self-interactions, which as we will see later will turn out to be employable to generate flows within atomic Bose-Einstein condensates. Furthermore, the sign of effective atom-atom interactions can be changed [53], so it allows us to externally switch from condensates with attractive interactions to a condensate with repulsive interactions and vice versa.

1.2.2 State equations for atomic BEC

Time dependent Gross-Pitaevskii equation

In the general framework of second quantization the time evolution of the time dependent quantum field operators $\hat{\Psi}_N^\dagger(\vec{r},t)$ is governed by the Heisenberg equation [11]

$$i\hbar\partial_t\hat{\Psi}_N(\vec{r},t) = \left[\hat{\Psi}_N(\vec{r},t), \hat{H}(\vec{r},t)\right] \tag{1.2.13}$$

with the Hamiltonian given by

$$\hat{H} = \int\left(\frac{\hbar^2}{2m}\nabla\hat{\Psi}_N^\dagger\nabla\hat{\Psi}_N\right) + \frac{1}{2}\int\hat{\Psi}_N^\dagger(\vec{r})\hat{\Psi}_N^\dagger(\vec{r}_*)V(\vec{r}_*-\vec{r})\hat{\Psi}_N(\vec{r})\hat{\Psi}_N(\vec{r}_*)d\vec{r}_*d\vec{r}. \tag{1.2.14}$$

To simplify the interaction potential in (1.2.14) one assumes effective highly local interactions between particles within the condensate, so the interaction potential is approximated by

$$V(\vec{r}-\vec{r}_*) = g\delta(\vec{r}-\vec{r}_*), \tag{1.2.15}$$

with interaction strength $g = \frac{4\pi\hbar^2 a}{m}$ and a the scattering length associated with the condensed particle scattering as derived in the previous section. Using (4.3.1), (1.2.14) and (1.2.13) we get

$$\begin{aligned} i\hbar\partial_t\hat{\Psi}_N(\vec{r},t) &= \left[\hat{\Psi}_N(\vec{r},t), \hat{H}(\vec{r},t)\right] = \\ &= \left(-\frac{\hbar^2\vec{\nabla}^2}{2m} + V_{ext}(\vec{r},t) + \int d\vec{r}_*\hat{\Psi}_N(\vec{r}_*)V(\vec{r}_*-\vec{r})\hat{\Psi}_N(\vec{r})\right)\hat{\Psi}_N = \\ &= \left(-\frac{\hbar^2\vec{\nabla}^2}{2m} + V_{ext}(\vec{r},t) + g|\hat{\Psi}_N|^2\right)\hat{\Psi}_N. \end{aligned} \tag{1.2.16}$$

By assuming the field operator to be a c-number $\hat{\Psi}_N = \sqrt{n_0}\psi_0$ and setting $\psi_0 = \frac{1}{\sqrt{n_0}}\psi$ the time evolution simplifies to the so called Gross-Pitaevskii equation [8, 7]

$$i\hbar\partial_t\psi(\vec{r},t) = \left(-\frac{\hbar^2\vec{\nabla}^2}{2m} + V_{ext}(\vec{r},t) + g|\psi|^2\right)\psi(\vec{r},t). \tag{1.2.17}$$

Here m is the mass of a single particle and $g|\psi|^2$ represents the self-interactions of the particles with a magnitude g within our condensate. The order parameter (condensate wave function) is a complex function $\psi(\vec{r},t) : \mathbb{R}^{3+1} \to \mathbb{C}$ and inherits the density distribution of the condensed particles within the condensate by the expression $|\psi|^2$, similarly in meaning to usual single particle quantum mechanics. We note that the correspondence to the many-body density matrix will be discussed further in a following section. A crucial difference to Schrödinger's single-body quantum theory is the factor for the energy density due to self-interactions, which is

$$U = \frac{4\pi\hbar^2 a}{m}|\psi|^2. \tag{1.2.18}$$

It gives rise to nonlinear phenomena unique to BEC. Mathematically one can classify (1.2.17) as NLSE for a classical field [66]. The energy of the BEC is analogously obtained as in quantum mechanics by finding the minimizer for the energy functional associated with (1.2.17),

$$\mathcal{E}^{\mathrm{GP}}[\psi] = \int \left(\frac{\hbar^2}{2m} \left| \vec{\nabla}\psi \right|^2 + V_{ext}(\vec{r},t)|\psi|^2 + \frac{g}{2}|\psi|^4 \right) d\vec{r}. \tag{1.2.19}$$

As we consider here a system of fixed particle number, the minimizing function has to satisfy the mass constraint $\|\psi\|_{L^2(\mathbb{R}^3)} = 1$ in rescaled units. In contrast to linear quantum mechanics an energy shift is induced via (1.2.18). The PDE (1.2.17) is the Euler-Lagrange equation for (1.2.19), when including a Lagrange multiplier to respect the conservation of mass.

Galilean invariance of the GPE

For any solution to (1.2.17) a new solution can be obtained by replacing $\vec{r} \to \vec{r} + \vec{v}t$ and by multiplying the wave function with a factor $e^{-i\frac{m}{\hbar}\vec{v}(\vec{r}+\vec{v}t/2)}$, i.e.

$$\psi(\vec{r},t) \to \psi(\vec{r}+\vec{v}t,t)e^{-i\frac{m}{\hbar}\vec{v}(\vec{r}+\vec{v}t/2)}. \tag{1.2.20}$$

This transformation property is analogous to a Galilean boost in linear quantum mechanics and it corresponds to switching the consideration to another relatively moving frame of reference as will be discussed later in more detail. Indeed the additional nonlinear term (1.2.18) does not interfere this interpretation.

Time independent GPE

The equation for stationary states can be obtained by restricting the condensate wave function to be of the form

$$\psi(\vec{r},t) = \phi(\vec{r}) \exp(-i\mu t/\hbar), \tag{1.2.21}$$

with a constant μ associated as chemical potential. By inserting a stationary state into the time dependent GPE (1.2.17), which implies assuming the external potential to be time independent as well, $V_{ext}(\vec{r},t) = V_{ext}(\vec{r})$, one gets the stationary GPE

$$\mu\phi(\vec{r}) = \left(-\frac{\hbar^2\vec{\nabla}^2}{2m} + V_{ext}(\vec{r}) + g|\phi|^2 \right) \phi(\vec{r}). \tag{1.2.22}$$

Generally the chemical potential μ is fixed by the normalization condition $\|\phi\|_{L^2(\mathbb{R}^3)} = 1$. This thermodynamical quantity measures the cost of a particle to be added to a thermally isolated system and the value of μ satisfies the thermodynamical relation $\mu = \partial\mathcal{E}^{\mathrm{GP}}/\partial N$ [11] and as such depends on the total particle number N. In order to obtain the stationary GPE (1.2.17) via the energy functional (1.2.19) one employs the technique of Lagrangian multipliers where one sets

$$\mathcal{E}'^{\mathrm{GP}}[\phi] = \mathcal{E}^{\mathrm{GP}}[\phi] - \mu N. \tag{1.2.23}$$

The global minimum is obtained for a vanishing variational derivative

$$\frac{\delta \mathcal{E}'^{\mathrm{GP}}[\phi]}{\delta \phi^*} = 0, \tag{1.2.24}$$

and yields (1.2.22) [67]. Finally we note that for the uniform BEC $\phi = \sqrt{n_0} = const.$ (1.2.22) simplifies to

$$\mu = g n_0. \tag{1.2.25}$$

Small variations thereof which include the slowly varying potential are referred to as Thomas-Fermi approximation borrowing the term from the density functional theory of electrons due to formal similarity.

1.2.3 Superfluid velocity and streamlines

When we apply a Galilean transformation to the condensate wave function in order to boost into the frame moving with velocity $-\vec{v}_0$ and coordinates $\vec{r}_* = \vec{r} + \vec{v}_0 \cdot t$ and $t' = t$, we get another order parameter

$$\psi'(\vec{r}_*, t) = \psi(\vec{r}_* - \vec{v}_0 \cdot t, t) e^{\left(i \frac{m}{\hbar}\left(\vec{v}_0 \vec{r}_* - \frac{\vec{v}_0^2 t}{2}\right)\right)}. \tag{1.2.26}$$

For the simple homogeneous ground state, i.e. when we set $\psi = \sqrt{n_0} = const.$ then by (1.2.26) we have

$$\psi'(\vec{r}_*, t) = \sqrt{n_0} \exp\left(i \frac{m}{\hbar}\left(\vec{v}_0 \vec{r}_* - \frac{\vec{v}_0^2 t}{2}\right)\right) = \sqrt{n_0} \exp\left(i \phi_0\right). \tag{1.2.27}$$

In the last step we have defined a new function ϕ_0 that is unique up to a multiple of 2π due to different sheets of the complex exponential. Consequently one obtains the following relation for the velocity of the condensate

$$\vec{v}_0 = \frac{\hbar}{m} \vec{\nabla} \phi_0(\vec{r}) \tag{1.2.28}$$

Now the superfluid velocity $\vec{v}$ is identified by generalizing the relation with the velocity of uniform flow $\vec{v}_0$ (1.2.28) by writing

$$\vec{v}(\vec{r}, t) = \frac{\hbar}{m} \vec{\nabla} \theta(\vec{r}, t), \tag{1.2.29}$$

with $\theta : \mathbb{R}^{3+1} \to \mathbb{R}$ denoting the phase of an inhomogeneous BEC. According to the Helmholtz decomposition a general vector field can be decomposed in a sum of an irrotational and a divergence free vector field, i.e., a vector valued function, say $\vec{f}$, on a bounded domain $\Omega \subset \mathbb{R}^3$ can be written as $\vec{f} = -\nabla k + \vec{\nabla} \times \vec{A}$ for appropriately chosen functions $\vec{A}$ and k [68]. By the definition (1.2.29) the superfluid velocity only obeys the first part of that sum, which will turn out to have crucial restrictions on its properties.

Also note that by using (1.2.29) and (1.2.17) one can write the superfluid velocity in terms of the condensate wave function

$$\vec{v}(\vec{r},t) = -\frac{i\hbar}{2m|\psi|^2}\left(\psi^*(\vec{r},t)\vec{\nabla}\psi(\vec{r},t) - \psi(\vec{r},t)\vec{\nabla}\psi^*(\vec{r},t)\right). \tag{1.2.30}$$

As we are going to see in a later section the definitions (1.2.29) and (1.2.30) connect with a conservation law, the continuity equation for the NLSE.

Furthermore we remark that an alternative interpretation of quantum mechanics, Bohmian mechanics, derives its law of motion for position-trajectories in phase space from the corresponding velocity field. It is given by the so called guiding equation

$$\partial_t X_t(\vec{x}) = \vec{v}(t, X_t(\vec{x})) \quad \text{with initial condition} \quad X(0,\vec{x}) = \vec{x} \in \mathbb{R}^3. \tag{1.2.31}$$

Here $X_t(\vec{x})$ denotes a possible trajectory of a quantum particle and the velocity field $\vec{v}$ is dependent on the wave function ψ of the linear SE in the same way as in (1.2.29) and (1.2.30). The nonlinearity introduced in (1.2.17), however, would modify the trajectories to linear quantum mechanics and so would represent streamlines of the possible mean particle positions.

1.2.4 State equations for condensates in motion

Linear motion

Let us write the time dependent GPE (1.2.17) as

$$i\hbar\partial_t\psi(\vec{r},t) = O[\psi]\cdot\psi(\vec{r},t) \tag{1.2.32}$$

and introduce the nonlinear operator

$$O[\psi] = \left(-\frac{\hbar^2\vec{\nabla}^2}{2m} + V_{ext}(\vec{r},t) + g|\psi|^2\right). \tag{1.2.33}$$

We say the condensate is at rest in a frame K, has energy E_0 specified by (1.2.19) and momentum defined as

$$\frac{\vec{p}}{\hbar} = \int n\vec{\nabla}\phi d\vec{r} = \frac{m}{\hbar}\int n\vec{v}d\vec{r}. \tag{1.2.34}$$

When put in motion with velocity $\vec{v}_0$ in the static frame the energy and momentum of the moving fluid are simply obtained via a Galilean transformation of the observables and given by [11, 67]

$$\vec{p}' = \vec{p} - M\vec{v}_0 \tag{1.2.35}$$

$$E' = \frac{|\vec{p}'|^2}{2M} = E_0 - \vec{p}\cdot\vec{v}_0 + \frac{M}{2}|\vec{v}_0|^2. \tag{1.2.36}$$

$M = m$, as we are working with rescaled units in N, denotes the total mass of the fluid. On the other hand we can transform the condensate state equation (1.2.32) to the moving frame by simply using (1.2.26) and obtain

$$i\hbar\left(\partial_t + \frac{m}{\hbar}\vec{v}_0\cdot\vec{\nabla}'\right)\psi(\vec{r}',t) = O'[\psi']\psi(\vec{r}',t), \tag{1.2.37}$$

with

$$O'[\psi'] = \left(-\frac{\hbar^2 \vec{\nabla}'^2}{2m} + V_{ext}(\vec{r}', t) + g|\psi|^2 \right). \tag{1.2.38}$$

Let us define the momentum operator $\hat{p} = -i\hbar\vec{\nabla}$, so we can transform (3.8.13) into

$$(i\partial_t + \frac{1}{2}mv_0^2)\psi(\vec{r}', t) = \frac{1}{2m}(\hat{p}' - m\vec{v}_0)^2\psi(\vec{r}', t) \tag{1.2.39}$$

for a gauge field $\mathcal{A}^\mu = m(-\frac{1}{2}v_0^2, \vec{v}_0)$ of coupling strength m. In this sense a velocity might introduce comparable effects as an electromagnetic field would, when introduced to the system of quantum mechanical equations and vice versa a gauge field of this form will induce linear motion to the system. We note that the form (3.8.13) of the GP equation corresponds to the transformation $O'(\vec{r}', \hat{p}') = O(\vec{r}', \hat{p}') + \vec{v}_0 \cdot \hat{p}'$.

General rotation

We have seen in the derivation of the GP equation (1.2.17) that an external potential can depend on time, i.e. $V_{ext}(\vec{r}, t)$ with $(\vec{r}, t) \in \mathbb{R}^{3+1}$. An important special case of a time-dependent potential is that of a rotating trap. For this case one can remove time dependence from the potential via transforming to a non inertial coordinate frame $\tilde{r} = \tilde{r}(\vec{r}, t)$ with $\tilde{t} = t$ via

$$\tilde{r}_i = \sum_j T_{ij} r_j \tag{1.2.40}$$

for a time-dependent, real and unitary matrix T_{ij} [67] that can be derived from

$$\partial_t \tilde{r} = -\Omega \cdot (\vec{n} \times \tilde{r}). \tag{1.2.41}$$

Ω denotes the rotation frequency, $\vec{n}$ the unit vector along the axis of rotation [67]. The transformation to the rotating frame implies $\Delta = \tilde{\Delta}$ and

$$\partial_t = \tilde{\partial}_t + \partial_t \tilde{r} \cdot \partial_{\tilde{r}} = \partial_{\tilde{t}} - \Omega(\vec{n} \times \tilde{r})\partial_{\tilde{r}}. \tag{1.2.42}$$

Dropping the $\tilde{r}$ and instead writing $\vec{r}$ the GP equation in the rotating frame becomes

$$i\hbar\partial_t\psi(\vec{r}, t) = \left(-\frac{\hbar^2\vec{\nabla}^2}{2m} + V_{ext}(\vec{r}) + g|\psi|^2 + i\Omega(\vec{n} \times \vec{r}) \cdot \nabla \right) \psi(\vec{r}, t). \tag{1.2.43}$$

This form of the GP equation can analogously be obtained by the transformation $H'(\vec{r}', \vec{p}') = H(\vec{r}', \vec{p}') - \vec{\Omega} \cdot \vec{L}(\vec{r}', \vec{p}')$ with $\vec{L} = (\vec{r}' \times \vec{p}')$ [61, 69]. Consequently the energy functional (1.2.19) becomes

$$\mathcal{E}^{\mathrm{GP}}[\psi] = \int \left(\frac{\hbar^2}{2m} \left| \vec{\nabla}\psi \right|^2 + V_{ext}(\vec{r})|\psi|^2 + \frac{g}{2}|\psi|^4 - \psi^*\Omega(\vec{n} \times \vec{r}) \cdot \nabla\psi \right) d\vec{r} \tag{1.2.44}$$

and all variables are defined in the rotating frame [69]. By defining the vector potential

$$\vec{A} = \frac{m}{\hbar}\Omega(\vec{n} \times \vec{r}) \tag{1.2.45}$$

and the effective potential that includes the centrifugal potential

$$V_{eff}(\vec{r}) = V_{ext}(\vec{r}) - \frac{\Omega^2 r_\perp^2}{2\gamma} \tag{1.2.46}$$

with $r_\perp$ denoting the distance to the rotation axis one can rewrite (1.2.44) as

$$\mathcal{E}^{\mathrm{GP}}[\psi] = \int \left(\frac{\hbar^2}{2m} \left| \left(\vec{\nabla} - i\vec{A} \right) \psi \right|^2 + V_{eff}(\vec{r})|\psi|^2 + \frac{g}{2}|\psi|^4 \right) d\vec{r}. \tag{1.2.47}$$

There is an inevitable loss of conservation laws for the rotating case, but one retains $U(1)$ symmetry corresponding to the conservation of mass [67]. Corresponding to (1.2.47) the Gross-Pitaevskii equation in the rotating frame is

$$i\hbar\partial_t \psi(\vec{r},t) = \left(-\frac{\hbar^2}{2m} \left(\vec{\nabla}^2 - i\vec{A} \right) + V_{eff}(\vec{r}) + g|\psi|^2 \right) \psi(\vec{r},t). \tag{1.2.48}$$

Rotation around an axis $\hat{n}$ induces a particle flow away from the axis of rotation. So in order to allow stationary states one has to introduce an appropriate trap $V_{ext}(\vec{r})$ confining the condensate by opposing the centrifugal force due to rotation. This turns out to be a key prerequisite for the results presented in chapter 4. We conclude that the effect of motion on the state equation of the condensate is via additional complex-valued terms within the nonlinear Hamiltonian, which to some extent resembles effects encountered in the study of non equilibrium condensates discussed later.

1.2.5 Critical velocity and Quantum Hydrodynamics

Landau's criterion

In a moving superfluid within a capillary excitations, i.e., deviations from the ground state, may occur. An excitation with momentum $\vec{p}$ present in the fluid has an energy $\varepsilon(\vec{p})$ and the total energy of the fluid at rest carrying such an excitation is given by $E_0 + \varepsilon(\vec{p})$. Let us consider a capillary frame K' where the fluid moves with $\vec{v}_0$, or likewise K' moves with $-\vec{v}_0$ relative to the fluid. In K' the energy including an excitation and the momentum are given by

$$E' = E_0 + \varepsilon(\vec{p}) + \vec{p}\cdot\vec{v}_0 + \frac{M}{2}|v_0|^2 \tag{1.2.49}$$

$$\vec{p}_* = \vec{p} + M\vec{v}_0. \tag{1.2.50}$$

The elementary excitation spectrum in the frame of the capillary K' has the form [15]

$$\varepsilon'(\vec{p}) = \varepsilon(\vec{p}) + \vec{p}\cdot\vec{v}_0. \tag{1.2.51}$$

Consequently elementary excitations in K' are energetically favorable, iff

$$\varepsilon'(\vec{p}) < 0, \tag{1.2.52}$$

so that it is thermodynamically favorable to create excitations [15] and superfluidity vanishes. By the means of this condition one defines the critical velocity

$$v_c = \min_{\vec{p},\forall\vec{p}} \frac{\varepsilon'(\vec{p})}{|\vec{p}|}, \tag{1.2.53}$$

as a threshold below which no excitations are energetically feasible. The quantity $\frac{\varepsilon'(\vec{p})}{|\vec{p}|}$ is non zero as we will see later, hence establishing a regime of superfluidity. It is important to note that the self-interactions are essential for the appearance of a superfluid velocity $v_c > 0$, as the excitation spectrum $\varepsilon'(\vec{p})$ essentially depends on self-interactions. Similarly to (1.2.53) one defines

$$\Omega_c = \min_{\vec{l},\forall\vec{l}} \frac{\varepsilon(\vec{l})}{|\vec{l}|}, \tag{1.2.54}$$

with $\varepsilon(\vec{l})$ being the energy of elementary excitations in the frame of the capillary as function of the angular momentum of the elementary excitation $\vec{l}$. For large $\vec{l}$ inducing rapid variations of the density profile (1.2.54) is expected to fail and the necessity for a microscopic theory arises.

Quantum Hydrodynamics

We now turn to an equivalent treatment of the condensate wave function, which was introduced in a similar context by Madelung [70, 71] as an analog to the linear Schrödinger equation. The motivation for writing down an alternative set of equations was to provide an intuitively more easily accessible framework for quantum mechanics at that time. This set of equations obey a similar form as classical hydrodynamical equations. So this system is usually referred to as quantum hydrodynamical system (QHD) and it can be easily extended to nonlinear Schrödinger-type equations such as the GPE. To do this one writes the condensate wave function in polar coordinates $\psi = \sqrt{n} \cdot e^{i\phi}$ with $\phi, \sqrt{n} : (\vec{r}, t) \in \mathbb{R}^{3+1} \to \mathbb{R}$ and defines the superfluid velocity as (1.2.29). By inserting this ansatz in (1.2.17) and separating imaginary from real parts a continuity equation

$$\dot{n} + \vec{\nabla} \cdot \vec{j} = 0 \tag{1.2.55}$$

and a Hamilton-Jacobi-type equation

$$m\dot{v} + \vec{\nabla}\left(V_{ext}(\vec{r}) + \alpha_1 n - \frac{\hbar^2}{2m\sqrt{n}}\vec{\nabla}^2\sqrt{n} + \frac{mv^2}{2}\right) = 0 \tag{1.2.56}$$

is obtained. Here we have introduced the matter flux

$$\vec{j} = \frac{\hbar}{m}\left(\psi\vec{\nabla}\psi^* - \psi^*\vec{\nabla}\psi\right) = \frac{\hbar}{m}|\psi|^2\vec{\nabla}\phi. \tag{1.2.57}$$

It is connected to the superfluid velocity (1.2.29) via

$$\vec{j} = |\psi|^2\vec{v}. \tag{1.2.58}$$

Through the hydrodynamical relation (1.2.58) one can alternatively identify the superfluid velocity, which complements the method of generalization previously leading to its definition (1.2.29). Furthermore it is worth mentioning that the continuity equation has a unique solution with respect to the Cauchy problem [72]. Generally it represents the conservation of mass for the equilibrium condensate. This holds true as well when a vector potential is included into the GPE (1.2.17) as for the rotating condensate (1.2.48). For this case, however, the superfluid velocity has to be extended to

$$\vec{v} = \frac{\hbar}{m}(\vec{\nabla}\phi - \vec{A}) \tag{1.2.59}$$

to retain (1.2.55) [67]. Now, the so called quantum pressure term in the Hamilton-Jacobi-type equation (1.2.56),

$$\frac{\hbar^2}{2m\sqrt{n}}\vec{\nabla}^2\sqrt{n}, \tag{1.2.60}$$

distinguishes QHD from classical hydrodynamics (derived from Newtonian mechanics). This can be seen by neglecting quantum pressure (via $\hbar \to 0$), which yields an Euler-type equation for a potential flow and zero viscosity fluid,

$$m\dot{v} + \vec{\nabla}\left(V_{ext}(\vec{r}) + \alpha_1 n + \frac{mv^2}{2}\right) = 0 \tag{1.2.61}$$

for functions satisfying sufficient regularity conditions [74].

It is worth noticing that the nonlinear QHD system is not equivalent to NLSE in the sense that solutions to the nonlinear QHD do not necessarily provide solutions to the corresponding NLSE. To gain equivalence the change in phase around any closed contour has to satisfy

$$\oint_L \nabla\phi \cdot dl = 2\pi n \tag{1.2.62}$$

with n being an integer [75]. This condition corresponds to the single-valuedness of the condensate wave functions, which is necessary under elementary assumptions [76] and allows such effects as quantum vortices as discussed subsequently.

1.2.6 BEC in lower dimensions

The concept of Bose-Einstein condensation depends significantly on the spatial dimensions (due to the different energy dependence of the density of states) and is feasible in quasi 2d and 1d systems, when taking certain adaptions to the setup into account [77]. It can be shown that for infinitely large uniform Bose Gases in 1d and 2d no Bose-Einstein condensation can occur at non-zero temperatures. This changes for harmonically trapped condensates. Applying a semiclassical approximation the total number of particles of the Bose gas can be written as

$$N = N_0 + \int_0^\infty dE\rho(E)N\left(\frac{E-\mu}{T}\right) \tag{1.2.63}$$

with the density of states given by $\rho(E) \sim E^{d-1}$ due to harmonic confinement and $N(z) = 1/(\exp(z) - 1)$[77]. After a short calculation one obtains for the number of bosons in the ground state for quasi 2 spatial dimensions

$$N_0^{2\mathrm{d}} \simeq N \left(1 - \left(\frac{T}{T_c}\right)^2\right), \tag{1.2.64}$$

with $T_c = \sqrt{\frac{6N}{\pi^2}}\hbar\omega$, while for quasi 1d one gets [77]

$$N_0^{1\mathrm{d}} \simeq N - \left(\frac{T}{\hbar\omega}\right) \ln\left(\frac{T}{\hbar\omega}\right). \tag{1.2.65}$$

Both formulas for the occupation number of the lowest energy state show the feasibility of macroscopic occupation for small enough temperatures. It turns out that the Gross-Pitaevskii equation in appropriate parameter regimes remains an accurate model, however changes to the interaction parameter g have to be made. I refer to [77, 62, 11, 80, 78] for in depth derivations and explicit formulas for the self interaction strength g and motivate the simple argument as follows.

Gross-Pitaevskii equation in quasi 1*d.-* One starts with a cylindrically-symmetric trap geometry $V(\vec{r}) = (m/2)(\omega_z^2 z^2 + \omega_r^2 r^2)$ with the trapping frequencies ω_r and ω_z and assumes tight confinement in r direction $\omega_z \ll \omega_r$ to provide a quasi 1d regime. Under this assumption the radial component of the condensate wave function approaches a static harmonic oscillator state and can be separated out $\psi^{3\mathrm{d}}(z, r) = \phi(r) \cdot \psi(z)$. Inserting in (1.2.19) one obtains

$$\mathcal{E}_{1\mathrm{d}}^{\mathrm{GP}} = \int \left(\frac{\hbar^2}{2m} |\partial_z \psi|^2 + \hbar\omega_r |\psi|^2 + V_{\mathrm{ext}}(z,t)|\psi|^2 + \frac{g}{4\pi l_r^2}|\psi|^4\right) dz, \tag{1.2.66}$$

with $l_r = \sqrt{\hbar/m\omega_r}$, which includes an energy shift $\hbar\omega_r/2$ from each r component of the transverse harmonic oscillator [78]. The minimizer of (1.2.66) satisfies again 1d GP equation with a modified chemical potential $\mu_{1\mathrm{d}} = \mu - \hbar\omega_r$ and can be obtained analogously as in 3d. The GP equation is the Euler-Lagrange equation of (1.2.66) and given by

$$i\hbar\partial_t \psi(z,t) = \left(-\frac{\hbar^2\partial_z^2}{2m} + V_{ext}(z,t) + \frac{g}{4\pi l_r^2}|\psi|^2\right)\psi(z,t). \tag{1.2.67}$$

Depending on the context we will write $g \to \frac{g}{4\pi l_r^2}$ for the sake of simplicity. Finally we note that analogous considerations apply for a 2d description of the condensate wave function. There have been a variety of successful experimental implementations for lower dimensional condensates and we refer to [79, 16, 78] for details.

1.2.7 Excitations in BEC

Solutions to the Gross-Pitaevskii equation (1.2.17) are nonlinear waves, i.e., linear combinations of solutions cannot be solutions as well. This holds even though the initial

many-body problem with which the GPE can be associated is linear. The adaption introduces certain kinds of new solutions with properties only possible by the presence of the nonlinearity. Depending on the sign of the cubic nonlinearity in (1.2.17) the corresponding additional term can balance other terms and thus certain kinds of energetically stable excitations arise such as solitary waves or vortices [80, 67]. However, a consequence is that a threshold of disturbance is necessary in order to generate these nonlinear excitations which we discuss now as follows.

Bogoliubov energy spectrum

Previously we have introduced the notion of a critical velocity (1.2.53) below which no excitations may occur for appropriate dispersion curves of the possible excitations in the fluid. This phase is referred to as superfluidity and depends significantly on the nonlinearity within the GPE. To see this we turn to the Gross-Pitaevskii equation (1.2.17) without external trapping, but including an explicit chemical potential through $\psi \to \psi \exp(i\mu/\hbar t)$ with $\mu = n_0 g$, i.e,

$$i\frac{\partial \psi}{\partial t} = -\frac{\hbar^2}{2m}\Delta\psi + g|\psi|^2\psi - \mu\psi. \tag{1.2.68}$$

For the small amplitude harmonic modes we make the ansatz of the form $\psi = \phi_0 + \delta\psi$, where ϕ_0 represents the unperturbed part solving the GPE and $\delta\psi$ a small perturbation. By inserting this ansatz in (1.2.68) and dropping terms of order $\delta\psi^2$ we get the Bogoliubov equation for the perturbation

$$i\frac{\partial \delta\psi}{\partial t} = -\frac{\hbar^2}{2m}\Delta\delta\psi + g n_0(\delta\psi + \delta\psi^*). \tag{1.2.69}$$

where $n_0 = |\psi_0|^2$. Assuming $\delta\psi = Ae^{i(\vec{k}\vec{r}-\omega t)} + B^* e^{-i(\vec{k}\vec{r}-\omega t)}$ with $A, B \in \mathbb{C}$ one gets the Bogoliubov law

$$\omega(k)^2 = \frac{\hbar^2}{2m} n_0 g k^2 + \left(\frac{\hbar^2}{2m}\right)^2 \frac{k^4}{4}. \tag{1.2.70}$$

In Fig. 1.4 we plot the dispersion relation (1.2.70) of the excitation spectrum. The sound-like part of the dispersion (linear dispersion) corresponds to the speed of sound $v_s^2 = \hbar^2/(2m)n_0 g$ and implies a finite and nonzero critical velocity (1.2.53), which is equal the speed of sound.

Solitons, dark or bright

Solitons are localized waves moving without changing their form and obeying elastic scattering properties [81]. Historically such waves were first observed in a narrow channel of water, however with less strict assumptions on their behavior when scattering [82]. On the other hand in the strict sense, none of those excitations discussed in this thesis will satisfy all the properties to classify them as solitons, but we use the term 'soliton' simply because it is done so in most literature. More recently the study of

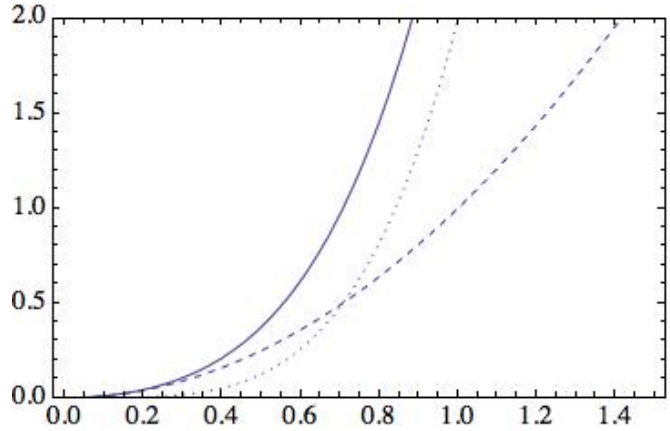

Figure 1.4: The continuous line represents the Bogoliubov dispersion law in rescaled units, $k^2 + 2k^4$, the dotted line the $2k^4$ contribution corresponding to a free particle-like dispersion and the dashed line the sound-like dispersion k^2.

solitons has reached areas from nonlinear fibre optics [83] to Bose-Einstein condensates [84]. These physical systems provide exceptional playgrounds for the study of the properties of nonlinear waves in NLSE systems. For the GPE we distinguish between bright and dark solitons that are excitations in quantum matter consisting of particles waves with effectively repulsive or attractive interactions. Usually solitons are stable in highly elongated geometries, i.e. quasi 1d systems and the (1.2.67) indeed admits solutions, which can be identified as solitons.

Dark solitons,- Consider the case of repulsive interaction $a > 0$ and a chemical potential $\mu = n_0 g$ (as follows from (4.2.26)) in (1.2.67). Then setting $\xi = z - vt$ and supposing $\psi(z,t) = \psi(\xi)$ a solution for a moving dark soliton is given by [11]

$$\psi_{\rm ds}(\xi) = \sqrt{n_0}\left(i\frac{v}{c} + \sqrt{1-\frac{v^2}{c^2}}\tanh\left(\sqrt{1-\frac{v^2}{c^2}}\frac{\xi}{l_0}\right)\right). \tag{1.2.71}$$

To evaluate the energy of a moving dark soliton one calculates the difference between energy without excitation to the energy with excitation to provide convergence of the energy functional (1.2.66) over an infinite domain [11]. The energy of the dark soliton per unit surface is then given by [11]

$$E_{\rm ds}^{\rm GP} = \frac{4}{3}\hbar c n\left(1-\left(\frac{v}{c}\right)^2\right)^{3/2}. \tag{1.2.72}$$

Writing the order parameter (1.2.71) in polar form $\psi_{rmds}(z-vt) = \sqrt{\rho(z)}\cdot\exp(i\phi(z))$ one sees that the phase has a phase jump of

$$\Delta\phi = 2\arccos\left(\frac{v}{c}\right) \tag{1.2.73}$$

as z varies from $-\infty$ to ∞.

Bright solitons,- For attractive self-interactions $a < 0$ the GP equation (1.2.67) admits bright soliton solutions. In the stationary case these are explicitly given by [11]

$$\psi_{\rm bs}(z) = \psi_0(0)\,\mathrm{sech}\left(\frac{z}{\sqrt{2}l_0}\right)e^{-\frac{i\mu t}{\hbar}} \tag{1.2.74}$$

with the healing length $l_0 = \hbar/\sqrt{2m|g|n_0}$, the density at the maximum $n_0 = |\psi_0(0)|^2$ and the chemical potential given by $\mu = gn_0/2$. The generalization for a moving bright soliton is given by

$$\psi_{\rm bs}(z - vt) = \sqrt{n_0}\left(i\frac{v}{c} + \sqrt{1 - \frac{v^2}{c^2}}\,\mathrm{sech}\left(\sqrt{1 - \frac{v^2}{c^2}}\frac{(z - vt)}{l_0}\right)\right), \tag{1.2.75}$$

where v corresponds to the velocity of the bright solitary wave and c denotes the speed of sound. Apparently the form of the wave (1.2.75) does not change for $z - vt = const.$ but it moves along the z-direction. For similar expressions of bright solitons I refer to [85, 81].

Quantized vortices in 2d

Quantum vortices.- First predicted for superconductors, quantized vortices are a basic topological excitation in 2d superfluids [86, 87]. Compared to the non-excited condensate wave function, which in the simplest case is constant and associated with a homogeneously distributed condensate, an adaption thereof by quantized vortices is the superfluids response to an intake of energy, which can be the superfluids response e.g. to rotation [69] or obstacles within the superfluids stream [88]. One defines the mathematically necessary condition of a quantum vortex as follows. The condensate wave function $\psi = |\psi|e^{i\theta} : \mathbb{R}^2 \to \mathbb{C}$ has a quantized vortex with a winding number $n \in \mathbb{N}$ at a single point $\vec{r} \in \mathbb{R}^2$ if the wave function $|\psi| = 0$ and θ increases by an amount of $2\pi n$ along any trivial curve enclosing the singularity at $\vec{r}$. We note that a requirement for the condensate wave function is to be single valued and to be continuously differentiable. Now, the possibility of such a quantum vortex is due to the structure of the condensate wave function imposed by (1.2.17), which leads to a unique definition of the superfluid velocity (1.2.29). As the superfluid velocity is defined as a gradient of a potential field (1.2.29) it is irrotational, i.e.,

$$\vec{\nabla} \times \vec{v} = \vec{\nabla} \times \nabla\theta = 0. \tag{1.2.76}$$

Around nodal points where $\vec{j} = 0$ and $|\psi| = 0$ the condensate wave function becomes indeterminate and so any relation defined upon meaningless, because the phase θ and derivatives thereof are indeterminate.

Generally the principal value of the phase is not unique, since

$$\exp(i\theta) = \exp(i\theta + i2\pi n). \tag{1.2.77}$$

Therefore, using the definition for (1.2.29) and supposing that the path of integration does not pass any singularities we get

$$\int_{\vec{r}_1}^{\vec{r}_2} \vec{v} \cdot d\vec{r} = \int_{\vec{r}_1}^{\vec{r}_2} \vec{\nabla}\theta \cdot d\vec{r} = (\theta(\vec{r}_2) - \theta(\vec{r}_1)) + 2\pi n. \tag{1.2.78}$$

For any path not passing a nodal point the superfluid velocity $\nabla\theta$ is well defined. Clearly the line integral does not depend on the path of integration and closed curves give a zero integral or discrete positive values due to the non-uniqueness in (1.2.77) as can be seen in the formula (1.2.78). Generally the value of a line integral for closed loops depends on the homotopy class,

$$\oint \vec{v} \cdot d\vec{r} = \oint \vec{\nabla}\theta \cdot d\vec{r} = 2\pi n, \tag{1.2.79}$$

i.e. no intersection with a nodal point where $\psi = 0$ is associated with integral zero, and the more nodal points are enclosed by the integration path the higher the winding number n. Thus, the circulation is quantized and the formal definition of a quantum vortex fulfilled. Condition (1.2.79) is referred to as the Onsager-Feynman quantization condition [15]. It is due to this quantization that vortices remain stable as no continuous transition between condensates with vortex and without exists, i.e. vortices are topologically stable excitations for the NLSE.

Mathematical form of quantum vortices.- To determine the adaption of the condensate wave function due to quantum vortices we consider the NLSE in rescaled units ($\vec{r} \to l_0\vec{r}$, $\psi \to \sqrt{n_0}\psi$, so that $\psi \to 1$ at ∞), i.e.

$$0 = -\frac{1}{2}\Delta\psi - (1 - |\psi|^2)\psi \tag{1.2.80}$$

in two spatial dimensions. Let us make an ansatz of the form

$$\psi(x) = U(r)e^{in\theta}. \tag{1.2.81}$$

Then inserting in (1.2.80) the modulus satisfies

$$U'' + \frac{1}{r}U' - \frac{n^2}{r^2}U + (1 - U^2)U = 0 \tag{1.2.82}$$

which is well posed for $U(0) = 0$ and $U(\infty) = 1$ [80]. For $r \to 0$ one obtains by inserting into (1.2.82) the asymptotic solution

$$U_n = a_1 r^{|n|} + a_2 r^{|n|+2} + \dots \tag{1.2.83}$$

and for $r \to \infty$ we obtain

$$U_n = 1 - \frac{b_1}{r} - \frac{b_2}{r^2} - \dots \tag{1.2.84}$$

with $b_1 = 0$ and $b_2 = n^2/2$ [80, 11]. Alternatively one obtains for a singly charged vortex the approximate vortex solution for (1.2.17) in 2d given by [73]

$$U_1(r) = \sqrt{n_0}\frac{r/l_0}{\sqrt{(r/l_0)^2 + 2}} \tag{1.2.85}$$

with n_0 denoting the density as $r \to \infty$.

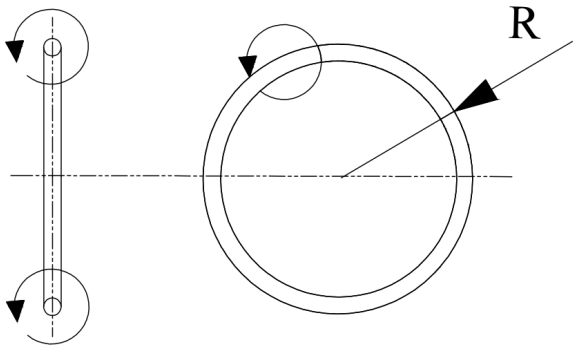

Figure 1.5: Vortex Ring of radius R.

Vortex rings in 3d with radius R

Roughly speaking, the 3d analog to the 2d quantum vortex are quantized vortex rings. These are the stable elementary excitations of the atomic BEC within 3d. Considering the profile of a vortex ring corresponds to considering two oppositely winded vortices as illustrated in Fig. 1.5. The energy of a vortex ring depends in particular on its radius and we refer to [11] for a more detailed analysis of the form of these 3d excitations. However, for big radii compared to the healing length, $R \gg l_0$, one obtains the simple expression for the energy of the vortex ring [11],

$$E(R) = 2\pi^2 R \frac{\hbar^2}{m} n \ln\left(\frac{1.59R}{l_0}\right) \tag{1.2.86}$$

where n denotes the density of the superfluid. Consequently its velocity of a large vortex ring is given by

$$v = \frac{dE(R)}{dp} = \frac{dE/dR}{dp/dR} = \frac{\hbar}{2mR} \ln\left(\frac{1.59R}{l_0}\right). \tag{1.2.87}$$

1.2.8 Energy and mass conservation in GP theory

We now derive fundamental properties of the GP theory of equilibrium condensates and in particular in the beginning show its formal connection to classical mechanics.

Classical Hamilton equations

In classical mechanics a many body state is determined by its pairs of conjugated variables $\{q_j, p_j\}$ with $j = 1, 2, 3, \ldots$. The Hamilton equations of classical mechanics induce trajectories for $\{q_j, p_j\}$ in phase space for the conjugated variables $\Gamma \equiv \mathbb{R}_q^{3N} \times \mathbb{R}_p^{3N}$ over time $t \in \mathbb{R}$ and are given by

$$\partial_t q_j = \frac{\partial H}{\partial p_j} \tag{1.2.88}$$

$$\partial_t p_j = -\frac{\partial H}{\partial q_j}, \tag{1.2.89}$$

where we introduced the Hamilton function $H[q_i, p_j, t]$, which corresponds to the energy as time dependent function of phase space. Defining the complex canonical variable $a_j = \alpha q_j + i\beta p_j$, where $\alpha, \beta \in \mathbb{C}$ we can rewrite the system of Hamilton equations (1.2.88) and (1.2.89) as

$$i\lambda \partial_t a_j = \frac{\partial H}{\partial a_j^*} \tag{1.2.90}$$

with $\lambda = \frac{1}{\alpha\beta^* + \alpha^*\beta}$ [67]. Furthermore, the global $U(1)$ symmetry, i.e. $a_j \to a_j e^{i\theta}$ with $\theta \in \mathbb{R}$ implies that $N = \sum_j |a_j|^2$ is a constant of motion, $\partial_t N = 0$.

We now show that the Gross-Pitaevskii equation derived from a second quantization scheme (1.2.17) can analogously be considered as a complex order parameter satisfying a Hamilton equation. This will conveniently allow us to discuss the conserved quantities within GP theory.

The condensate wave function in a classical field framework and its properties

An important sub-class of Hamiltonian classical field theories is that for which the relation

$$i\psi_t(\vec{r}) = \frac{\delta \mathcal{E}[\psi]}{\delta \psi^*(\vec{r})} \tag{1.2.91}$$

holds, where $\mathcal{E}[\psi]$ is a real-valued energy functional of the field ψ [67]. A particular example of such an energy functional is the Gross-Pitaevskii functional (1.2.19). Putting (1.2.19) into (1.2.91) we obtain the Gross-Pitaevskii equation (1.2.17) describing the state evolution of the condensate wave function.

Energy.- By using (1.2.91) one sees that the energy is conserved over time, i.e.

$$\frac{\partial \mathcal{E}^{\mathrm{GP}}[\psi]}{\partial t} = \int \left(\frac{\partial \mathcal{E}^{\mathrm{GP}}[\psi]}{\partial \psi} \frac{\partial \psi}{\partial t} + \frac{\partial \mathcal{E}^{\mathrm{GP}}[\psi]}{\partial \psi^*} \frac{\partial \psi^*}{\partial t} \right) d\vec{r} = 0. \tag{1.2.92}$$

Mass conservation.- As for the classical field the $U(1)$ symmetry of the functional $\mathcal{E}^{\mathrm{GP}}[\psi]$ is defined as invariance with respect to the transformation $\psi(\vec{r}) \to \psi(\vec{r}) e^{i\theta}$, where $\theta \in \mathbb{R}$. From this follows conservation of mass

$$0 = \frac{\partial \mathcal{E}^{\mathrm{GP}}[\psi]}{\partial \theta} = \int \left(\frac{\partial \mathcal{E}^{\mathrm{GP}}[\psi]}{\partial \psi} i\psi - \frac{\partial \mathcal{E}^{\mathrm{GP}}[\psi]}{\partial \psi^*} i\psi^* \right) d\vec{r} = \\ = \int \left(\psi \dot{\psi}^* + \dot{\psi} \psi^* \right) d\vec{r} = \dot{N} \tag{1.2.93}$$

1.2.9 Rigorous mathematical treatment of BEC

Quantum many-body problem

An alternative and equivalent viewpoint on BEC for fixed particle numbers can be taken by starting from Schrödinger's equation for N-particles, which resembles the

second quantization terminology when considering fixed particle numbers. Instead of considering operators on a Fock space we now work with the concept of N-particle wave functions $\psi_N(\vec{x}_1, \ldots, \vec{x}_N) \in \mathcal{H}(\mathbb{R}^{3N})$. For an ensemble of bosons they satisfy $\psi_N(\vec{x}_1, \ldots, \vec{x}_N) = \psi_N(\vec{x}_{\pi_1}, \ldots, \vec{x}_{\pi_N})$ for any permutation π corresponding to the CCR of the annihilation and creation operators within the Fock space formalism. Many-body sates consisting of fermions would be multiplied by sign(π) under the action of a permutation. The permutation properties of bosons can be taken into account by restricting the many-particle Hilbert space to its symmetric subspace. Usually one assumes the state or wave function $\psi \in L^2(\mathbb{R}^{3N+1})$ (including time) and this is a good choice in particular for spatially extended quantum gases.

Now, the many-body Schrödinger equation imposes the time evolution of the wave function,

$$i\hbar\partial_t\psi(C,t) = \hat{H}\psi(C,t), \tag{1.2.94}$$

with some Hamilton operator of the form [62],

$$\hat{H} = \left(-\frac{\hbar^2}{2m} \sum_{n=1}^{N} \Delta_i + V_{\text{ext}}(C,t) + \sum_{1 \le i < j \le N} v(\vec{x}_i - \vec{x}_j) \right). \tag{1.2.95}$$

Eq. (1.2.94) is a linear partial differential equation, which obeys a unique solution [55]. Due to linearity superpositions of many body quantum states are solutions as well. We write for particle positions $C = (\vec{x}_1 = \vec{x}, \vec{x}_2 \ldots, \vec{x}_N)$, $V_{\text{ext}}(C,t)$ denotes a time dependent external (electric field) trap and $v(\vec{x}_i - \vec{x}_j)$ two-body interactions between particles $\vec{x}_i$ and $\vec{x}_j$. This Hamilton operator e.g. pre-excludes the existence of three body interactions, which for dilute ensembles are quite rare events compared to two body interactions. Hence the model provides a reasonable approximation for this case. The (complex valued) quantum states satisfy Born's rule: - $|\psi(\vec{X},t)|^2$ is the probability density for a particle configuration at $(\vec{X},t) \in \mathbb{R}^{3N+1}$ and the states are normalized $\|\psi\|_{L^2}^2 = 1$. As we will see later non equilibrium systems do not necessarily have a conserved mass, since particles can be created or destroyed, but only in stationary situations where the influx equals the drain of particles. For this special case one has a finite and time independent norm as well, however with a slightly different interpretation as according to Born's rule.

In (1.2.95) we assume an electric field confinement of the Bosons, but the absence of a magnetic field. We do so as this is a usual setting for experimentally realized BEC. In the special case of non-interacting particles one can simply write the many body wave function as a plain product

$$\psi(C,t) = \prod_{i=1}^{N} \psi_i(x_i,t). \tag{1.2.96}$$

In a previous section we have defined BEC as a macroscopic occupation of a single mode. Hence a product of some single particle functions $\psi_i(x_i)$ could be envisaged as a candidate wave function for a BEC state. Indeed for noninteracting systems we can write

$$\psi(C,t) = \prod_{i=1}^{N} \psi_0(x_i,t), \tag{1.2.97}$$

which corresponds to a special case, i.e., without external trap $V = 0$, conceived by Einstein [12] in the paper where he introduced BEC. For interacting particles, however, such a factorization cannot be expected in a strict sense of a simple product of mathematical functions, but as we will see later, in a modified way. An example for the non appropriateness of product states in this formalism is the scenario of particles with delta function point interactions. Here one has infinite energy at the collision points, so excluding those solutions. In the proofs on BEC discussed in [62], they therefore introduce a function which smoothens the wave function, once particles collide, i.e. employ an ansatz $\psi(C) = \phi_0(\vec{x}_1) \cdots \phi_0(\vec{x}_N) \cdot F(\vec{x}_1, \ldots, \vec{x}_N)$, where F vanishes for $\vec{x}_i = \vec{x}_j$ with $i = j$, but is 1 otherwise.

The Schrödinger equation (1.2.94) gives the dynamics of the many body system. On the other hand time independent states correspond to wave functions of the form $\psi = e^{-itE_n/\hbar}\psi$, so it becomes

$$\hat{H}\psi_n(C) = E_n\psi_n(C), \tag{1.2.98}$$

where E_n is the corresponding nth eigenvalue of a solution. Bose-Einstein condensation for atoms is achieved for very cold atoms and therefore for energy levels close to or at the absolute ground state. In a rigorous treatment often condensation in the ground state with energy E_0 is considered as it was envisaged by Einstein initially.

Gross-Pitaevskii Energy functional.- The stationary quantum many-body problem (1.2.98) can be significantly simplified by effective theories in certain parameter regimes [62, 55, 11]. For dilute and weakly interacting Bose gases in the ground state, which can be formalized by the parameter limit referred to as Gross-Pitaevskii limit, where $N \to \infty$ and $g = 4\pi Na$ fixed [62], the Gross-Pitaevskii equation (1.2.17) provides a convenient tool to understand BEC even in a mathematically rigorous sense. Corresponding to the eigenvalue problem (1.2.98) one defines the GP energy functional (1.2.19). The energy of the system is given by

$$\inf \mathcal{E}^{\mathrm{GP}}[\phi] = E^{\mathrm{GP}}, \tag{1.2.99}$$

which is provided by inserting a solution to (1.2.17). Now, it has been shown that in the *GP-limit*, $N \to \infty$ while $N \cdot a =$ fixed, energy and density of the GP theory converge to the corresponding quantities of the quantum many body problem as stated in the following rigorous theorem.

Theorem 1.2.1 (Lieb-Seiringer-Yngvason) *If $N \to \infty$ while $N \cdot a =$ fixed , then*

$$\lim_{N\to\infty} \frac{E_0}{N} = E^{\mathrm{GP}} \tag{1.2.100}$$

and

$$\lim_{N\to\infty} n(\vec{r}) = |\phi|^2 \tag{1.2.101}$$

in the weak L^1-sense.

Bose-Einstein condensation in the Gross-Pitaevskii limit

A key concept for BEC in the second quantization framework is that of the one-particle density matrix (4.4.2). In the many body Schrödinger equation framework the reduced one-particle density matrix for the ground state ψ_0 is defined similarly as

$$\gamma(\vec{x},\vec{x}') = N \cdot \int \psi_0(\vec{x},X)\cdot\psi_0(\vec{x}',X)dX, \tag{1.2.102}$$

with $X=(\vec{x}_2,\ldots,\vec{x}_N)$ and $dX=\prod_{j=2}^{N} d\vec{x}_j$. It implies $\int\gamma(\vec{x},\vec{x})=\mathrm{tr}[\gamma]=N$ and BEC means that the operator has an eigenvalue of order N in the thermodynamical limit [62].

In the GP limit the reduced one-particle density matrix factorises, so that γ/N becomes a simple product $f(\vec{r})\vec{f(r')}$. The function $f(\vec{r})$ is then called the condensate wave function. This is analog to (1.1.33). Further it could be proved that in this limit the condensate wave function is the solution to the Gross-Pitaevkii equation ϕ^{GP} as stated in the following theorem.

Theorem 1.2.2 (Lieb-Seiringer) *For each fixed g*

$$\lim_{N\to\infty}\frac{1}{N}\gamma(\vec{r},\vec{r}') = \phi^{\mathrm{GP}}(\vec{r})\phi^{\mathrm{GP}}(\vec{r}'). \tag{1.2.103}$$

Convergence is in the senses that $\mathrm{Trace}\left|\frac{1}{N}\gamma - P^{\mathrm{GP}}\right| \to 0$ *and* $\int\left(\frac{1}{N}\gamma(\vec{r},\vec{r}')-\phi^{\mathrm{GP}}(\vec{r})\phi^{\mathrm{GP}}(\vec{r}')\right)^2 d\vec{r}d\vec{r}' \to 0$.

We note that this convergence is not pointwise. From a physicists view this theorem indeed proves rigorously that the GP equation can correctly describe the condensate wavefunction. Furthermore one can deduce for the interpretation of the GP density that the one-particle density associated with the many-body wave function gives the same predictions as the GP density. Because the one-particle density is the mean-value of particles at a given point the GP density is.

1.3 Condensates out of equilibrium

Open particle systems allow gain of energy and particles/quasiparticles, which sets them apart from the conserved atomic systems in thermal equilibrium introduced in the previous section. In an open system the notion of BEC is complicated in particular as particle distributions do not satisfy the same simple relation for the occupation numbers of states as the ideal Bose gas in thermal equilibrium does (1.1.3), while weakly interacting and closed systems relate to this distribution to a higher degree. The importance of the distribution of particles on energy levels is that for (noninteracting and conserved) bosons there is a statistical pressure for particles to occupy the lowest mode significantly, when compared to the higher modes and once a critical temperature has been surpassed. On the other hand BEC is by definition a macroscopically occupied single particle mode with very high spatial coherence and often when formed in appropriate physical setups coherent particles could be added to the condensate or removed from it without compromising the concept. Indeed BEC is proven recently to be feasible in non-equilibrium systems of exciton-polaritons within semiconductor micro cavities [16]. Besides this outstanding example there are a variety of other feasible systems constituting non-equilibrium BEC such as bulk nonlinear crystals, atomic clouds embedded in optical fibers and cavities, photonic crystal cavities and superconducting quantum circuits based on Josephson junctions [15]. In this thesis, however, our emphasis is on the non equilibrium exciton-polariton (polariton) condensates. Polaritons are quasiparticles formed within a semiconductor micro cavity and constitute themselves as superpositions between a light field and bound electron-hole pairs, the so called excitons [29]. These quasiparticles can be generated at will by external excitation through a laser field, while on the other hand they have a lifetime from a few up to hundreds of *ps* [33], controlled primarily by the leakage of photons from the microcavity [16, 47, 28, 15], which is small in comparison with the time scale of polariton condensates that persists over minutes [32]. Hence, polariton condensates are a true manifestation of a non-equilibrium condensate that can be analyzed experimentally with relative ease compared to atomic BEC [15, 16], due to the lack of complicated cooling devices, which indeed are necessary for atomic bose gas condensation.

In the beginning of this section I introduce the basic second quantization formalism of polariton condensates. Thereafter I will introduce the phenomenological model for exciton-polariton condensates and its various extensions. Then I discuss elementary properties of the non-equilibrium system.

1.3.1 Exciton-polariton condensates

Foundations of exciton-polaritons

Photons.- Photons can be trapped inside a cavity. We suppose the trapping geometry to restrict each photon mode to a finite interval in z-direction. This spatial confinement of photons is achieved by metallic or planar dielectric mirrors [15]. The dielectric crystalline mirrors consist of alternating layers of two different dielectric constants. The reflectivity

increases with the number of layers [28, 49]. On the top and bottom two such distributed Bragg reflectors (DBR) sandwich the cavity spacer of length l_0 and refraction index n_0. Fig. 1.6 shows an illustration of such a setup. It is important to remarks that although the reflectivity of the DBR's is very high some photons will leak out of the system, which can be used to analyze the physics within experimentally. Due to this confinement the

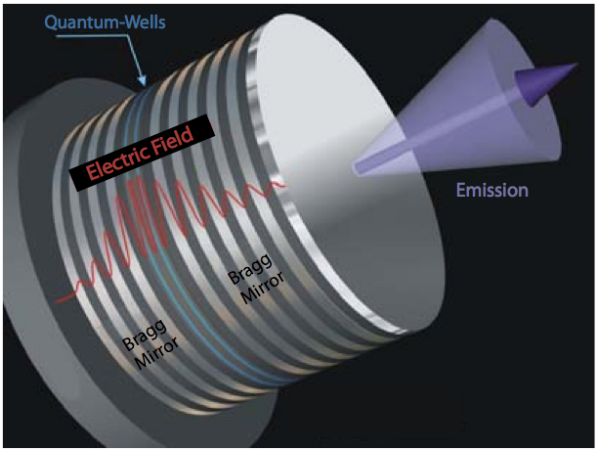

Figure 1.6: Schematic illustration of a micro cavity made of DBR's enclosing a cavity spacer. The illustration hash been taken from [87].

wave function of the photon is of almost finite extend and thus quantized along z-direction, while we assume the photons to propagate freely in the (x, y) plane. We split the wave vector of each photon $\vec{k} \in \mathbb{R}^3$ into the in plane component $\vec{k}_{||} = \vec{k}_x + \vec{k}_y$ and the component along cavity axis that is quantized $\vec{k}_z = \pi M / l_0$ with quantum number M. Consequently the dispersion relation of the photon within the cavity becomes

$$E_\phi(\vec{k}_{||}) = \frac{\hbar c k}{n_0} = \sqrt{E_z^2 + \frac{\hbar^2 c^2 k_{||}^2}{n_0^2}}. \tag{1.3.1}$$

Here c is the speed of light and $E_z = \hbar c |\vec{k}_z| / n_0$ is the minimum energy of a cavity eigenmode [15, 49]. Applying a first order Taylor expansion we get

$$E_\phi(\vec{k}_{||}) \simeq \frac{\hbar c}{n_0} k_z + \frac{1}{2} \frac{\hbar c k_{||}^2}{n_0 k_z}, \tag{1.3.2}$$

which is a good approximation of (1.3.1) for small $k_{||}$. For (1.3.2) the first term can be associated with a rest energy of the cavity photon, while the second term represents the kinetic energy of the photon for in plane motion. Consequently one can associate an effective mass to confined photons in analogy to the kinetic energy of intrinsic massive bodies, i.e. $E = \frac{\hbar^2 k^2}{2m}$, by writing

$$m_\phi = \frac{\hbar k_z}{c}. \tag{1.3.3}$$

We want to point out that this is only an effective mass and not a fundamental property of the cavity photon itself.

Excitons.- We now turn to a quantized quasi particle called exciton within a quantum well. A quantum well consists of a thin semiconductor layer in which the quasiparticles are formed and which is embedded in different semiconductors that provide a barrier for the quasiparticles and its constituents [15]. The geometry is chosen such that we have confinement to the same plane (x, y) as the photon modes are confined to. These quantum wells are placed within the cavity spacer as Fig. 1.6 illustrates.

When in a semiconductor an electron is excited into the conduction band it leaves behind a hole in the valence band. This hole can be regarded to carry a charge $+e$ opposite that of the free electron. An exciton is a quasiparticle consisting of an electron bound to a hole by the Coulomb interaction between them. Forming a composite boson it is effectively a neutral quasiparticle. Such a coupled state of an electron with mass m_e and a hole with effective mass m_h can be written in the center of mass frame as

$$\hat{e}_{\vec{K},n} = \sum_{\vec{k},\vec{k}'} \delta_{\vec{K},\vec{k}+\vec{k}'} f_n \left(\frac{m_h \vec{k} - m_e \vec{k}'}{m_e + m_h} \right) \hat{a}^\dagger_{\vec{k}} \hat{b}^\dagger_{\vec{k}'} \tag{1.3.4}$$

with K being the center of mass momentum and where $a^\dagger_{\vec{k}}$ denotes the creation operator of the electron and $\hat{b}^\dagger_{\vec{k}'}$ the creation operator of the hole, while $f_n(\vec{k})$ is the wave function of the electron-hole pair [28]. It follows that excitons are bosons for large interparticle spacings in terms of its Bohr radius [28]. Furthermore does the exciton form a dipole that indeed interacts with a light field [29] and as such can form new quasiparticles itself.

Exciton-Polaritons.- Let us now introduce the concept of exciton-polariton quasiparticles in semiconductor microcavities as illustrated in Fig. 1.6. To do so we employ a 2d coupled harmonic oscillator model, which takes into account the physics of the polaritons as quasiparticles made of photons and excitons. The basic Hamiltonian describing the interaction between laser and excitons is [15, 28, 87]

$$\begin{aligned} \hat{H}_{pol} = \hat{H}_{cav} + \hat{H}_{exc} + \hat{H}_I = \sum_{\vec{k}_{||}} E_\phi(\vec{k}_{||}) \phi^\dagger_{\vec{k}_{||}} \phi_{\vec{k}_{||}} + \sum_{\vec{k}_{||}} E_\xi(\vec{k}_{||}) \xi^\dagger_{\vec{k}_{||}} \xi_{\vec{k}_{||}} + \\ + \hbar\Omega_R \sum_{\vec{k}_{||}} E_\phi(\vec{k}_{||}) \left(\phi^\dagger_{\vec{k}_{||}} \xi_{\vec{k}_{||}} + \xi^\dagger_{\vec{k}_{||}} \phi_{\vec{k}_{||}} \right). \end{aligned} \tag{1.3.5}$$

Here $\phi^\dagger_{\vec{k}_{||}}$ is the creation and $\phi_{\vec{k}_{||}}$ the annihilation operator of a photon, while $\xi^\dagger_{\vec{k}_{||}}$ and $\xi_{\vec{k}_{||}}$ are the corresponding operators for the exciton. Ω_R is the Rabi frequency, its amount corresponds to the coupling-strength between both fields. For the sake of simplicity we introduce the abbreviation $g_0 = \hbar\Omega_R$. The coupling constant is the amount of light matter interaction and can be determined by [89]

$$g_0 = e\hbar \sqrt{\frac{f_{\text{osc}}/S}{8\varepsilon d m_e}} \int \psi^*_{exc}(\vec{r}) \psi_{cav}(\vec{r}) d\vec{r}. \tag{1.3.6}$$

Here ϕ_{exc} is the quantum-well (QW) exciton wave function and ϕ_{cav} the cavity photon wave function. e denotes the elementary charge, f_{osc}/S the QW-exciton oscillator strength per surface area S, ε the dielectric constant, d the quantum well thickness and m_e the electron mass [90].

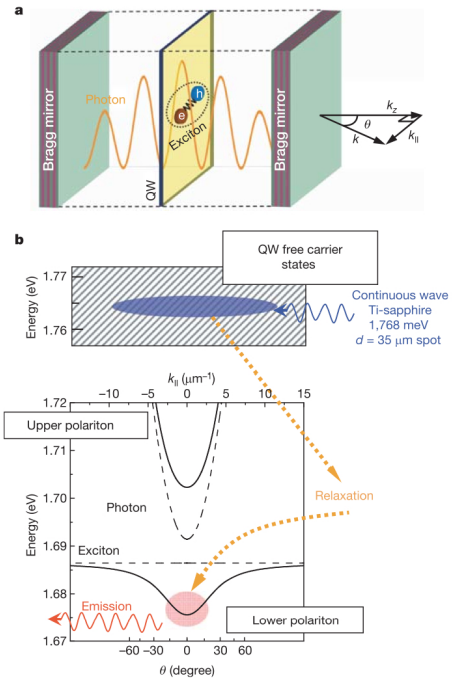

Figure 1.7: Panel (a) shows the concept of the exciton-polariton in a semiconductor micro cavity. Panel (b) shows the schematic illustration of the upper and lower energy dispersion curve of the polariton. In particular comparisons with the photon and exciton curves are given. The figure has been taken from the original work [16].

To write down (1.3.5) we have assumed that excitons and light interact, which however is only true for certain spin states of the excitons (bright states) as we will discuss in more detail in a later section. One diagonalizes (1.3.5) by finding the eigenvalues and eigenvectors of

$$A = \begin{pmatrix} E_\phi(\vec{k}_{||}) & g_0 \\ g_0 & E_\xi(\vec{k}_{||}) \end{pmatrix} \tag{1.3.7}$$

yielding the two eigenvalues

$$E_{L,U}(\vec{k}_{||}) = \frac{1}{2}\left(E_\phi(\vec{k}_{||}) + E_\xi(\vec{k}_{||}) \mp \sqrt{(E_\xi(\vec{k}_{||}) - E_\phi(\vec{k}_{||}))^2 + 4g_0^2} \right) \tag{1.3.8}$$

The energy eigenvalues $E_{L,U}(\vec{k}_{||})$ are referred to as the upper and lower (polariton) branch. An illustration of them is given in Fig. 1.7. These two dispersions correspond

to the basis vectors

$$\psi_L(\vec{k}_{||}) = \begin{pmatrix} h_{2,\vec{k}_{||}} \\ -h_{1,\vec{k}_{||}} \end{pmatrix}, \qquad \psi_U(\vec{k}_{||}) = \begin{pmatrix} h_{1,\vec{k}_{||}} \\ h_{2,\vec{k}_{||}} \end{pmatrix}, \tag{1.3.9}$$

where the so called Hopfield coefficients are given by [28, 90]

$$h_{1,\vec{k}_{||}} = \sqrt{\frac{1}{2}\left(1 - \frac{\delta(\vec{k}_{||})}{\sqrt{\delta(\vec{k}_{||})^2 + 4g_0^2}}\right)} \tag{1.3.10}$$

and

$$h_{2,\vec{k}_{||}} = \sqrt{\frac{1}{2}\left(1 + \frac{\delta(\vec{k}_{||})}{\sqrt{\delta(\vec{k}_{||})^2 + 4g_0^2}}\right)}. \tag{1.3.11}$$

In addition we have introduced the micro cavity's detuning [87, 90]

$$\delta(\vec{k}_{||}) = E_\xi(\vec{k}_{||}) - E_\phi(\vec{k}_{||}). \tag{1.3.12}$$

If $\delta(\vec{k}_{||}) = 0$ the Hopfield coefficients satisfy $|h_{1,\vec{k}_{||}}|^2 = |h_{2,\vec{k}_{||}}|^2 = \frac{1}{2}$ and the polaritons are exactly half exciton and half photon quasiparticles. In any case the real-valued Hopfield coefficients satisfy the normalization condition $h^2_{1,\vec{k}_{||}} + h^2_{2,\vec{k}_{||}} = 1$ and they quantify the excitonic and photonic content of the polariton; $|h_{1,\vec{k}_{||}}|^2$ and $|h_{2,\vec{k}_{||}}|^2$ correspond to the fraction of photon and exciton within a given exciton-polariton. By employing the Hopfield coefficients one obtains the diagonalized Hamiltonian [15, 28]

$$\hat{H}_{pol} = \sum_{\vec{k}_{||}} E_L(\vec{k}_{||}) p^\dagger_{\vec{k}_{||}} p_{\vec{k}_{||}} + \sum_{\vec{k}_{||}} E_U(\vec{k}_{||}) q^\dagger_{\vec{k}_{||}} q_{\vec{k}_{||}}. \tag{1.3.13}$$

Here $p^\dagger_{\vec{k}_{||}}$ are the creation and $p_{\vec{k}_{||}}$ annihilation operators of a lower branch mode, while $q^\dagger_{\vec{k}_{||}}$ and $q_{\vec{k}_{||}}$ are the corresponding quantities for the upper polariton branch. We note that (1.3.13) has a translational symmetry along the cavity plane [15]. The dispersion curve of the lower polariton branch are illustrated in Fig. 1.7 and for low $|\vec{k}_{||}|$ resembles that of the cavity photon (1.3.2) and for higher $|\vec{k}_{||}|$ that of the exciton. The difference between $E_U(0) - E_L(0)$ gives the Rabi splitting, i.e. the coupling strength between exciton and photon, if the detuning is zero at $\vec{k}_{||} = 0$.

Condensation

Polaritons are quasiparticles within a semiconductor micro cavity obeying two different energy dispersions, the lower and the upper polariton branch. The effective mass of the

exciton-polaritons is determined by the curvature of the dispersion relations for each branch and given by

$$m_{U,L} = \hbar^2 \left(\frac{\partial^2 E_{U,L}}{\partial k^2} \right)^{-1} . \tag{1.3.14}$$

Consequently the effective mass of the polaritons when $|\vec{k}_{||}| \sim 0$ is [28]

$$m_L(|\vec{k}_{||}| \sim 0) \simeq \frac{m_\phi}{|h_{2,\vec{k}_{||}}|^2} \sim 10^{-4} m_{exc}, \qquad m_U(|\vec{k}_{||}| \sim 0) \simeq \frac{m_\phi}{|h_{1,\vec{k}_{||}}|^2}, \tag{1.3.15}$$

with $m_{exc} = m_h + m_e$ denoting the effective exciton mass. The relatively light mass of polaritons in comparison to atoms or excitons implies a much higher critical temperature at which the transition to a condensed state happens. That polariton's/exciton's can condense is due to the fact that they have effectively integer spin. But due to the polariton's composite nature an upper bound on the possible polariton density has to be imposed. Indeed polaritons lose their bosonic features at roughly $n_B = 1/a_B^2$, where a_B denotes the Bohr radius of the exciton in the given material. To allow polariton condensation, this condition has to be taken into account [49]. Analogue arguments apply for composite atomic condensates, where atoms considered at their own are fermions, but the composite particles obey bosonic statistics. A comparison of key parameters between atoms, excitons and polaritons is shown in Fig. 1.8; it particular shows quantitativ values for the critical temperature depending on the species. Note that excitons themselves are bosons and thus can in principle condense to a single mode as well.

TABLE I. Parameter comparison of BEC systems.

Systems	Atomic gases	Excitons	Polaritons
Effective mass m^*/m_e	10^3	10^{-1}	10^{-5}
Bohr radius a_B	10^{-1} Å	10^2 Å	10^2 Å
Particle spacing: $n^{-1/d}$	10^3 Å	10^2 Å	1 μm
Critical temperature T_c	1 nK–1 μK	1 mK–1 K	1–>300 K
Thermalization time/Lifetime	1 ms/1 s~10^{-3}	10 ps/1 ns~10^{-2}	(1–10 ps)/(1–10 ps)=0.1–10

Figure 1.8: Comparison of key parameters for various candidates eligible for the BEC transition as taken from [28].

The weak and the strong coupling regime

Regarding the interaction between the excitons and the photons at least two di?erent regimes can be distinguished, that of strong coupling and that of weak coupling, although clearly a continuum exists in-between [47]. Generally speaking weak coupling between two fields accounts for a perturbation of each field by the other without a significant adaption of their properties. This regime is often utilized for semiconductor-based

emitters like VCSELs (vertical cavity surface emitting lasers) or quantum-dot polariton based single-photon sources. Strong coupling implies new quantum mechanical eigenstates for the system and a splitting between the exciton and cavity modes appears [90].

To illustrate the differences between those two regimes we now take into account the finite lifetime of the photon and exciton that make up a polariton. We introduce the cavity photon decay rate γ_{cav} and γ_{exc}, which takes non radiative exciton decay into account [28]. For uncoupled decaying exciton-photon states one writes

$$H_{\vec{k}_{||}} = \begin{pmatrix} E_\phi(\vec{k}_{||}) - i\hbar\gamma_{cav} & g_0 \\ g_0 & E_\xi(\vec{k}_{||}) - i\hbar\gamma_{exc} \end{pmatrix} \tag{1.3.16}$$

with new energy eigenvalues given by

$$E_{L,U}(\vec{k}_{||}) = \frac{1}{2}\left(E_\phi(\vec{k}_{||}) + E_\xi(\vec{k}_{||}) - i\hbar(\gamma_{exc}+\gamma_{cav})\right) \mp \sqrt{g_0^2 + \frac{1}{4}\left(\delta(\vec{k}_{||}) - i\hbar(\gamma_{exc}-\gamma_{cav})\right)}). \tag{1.3.17}$$

The energy dispersion of the upper and lower dispersion branch is modified by the decay represented by γ_{cav} and γ_{exc} and the energy difference between the branches becomes

$$\hbar\Omega' = \sqrt{4g_0^2 - \hbar^2(\gamma_{exc}-\gamma_{cav})^2}. \tag{1.3.18}$$

Now, strong light matter coupling means that (1.3.18) is real-valued, which corresponds to the regime where the coupling dominates dissipative processes [15, 28].

From the decay rates one in particular deduces the lifetime of the polaritons [49, 90], which for the lower branch is [28]

$$\frac{1}{\tau_p^L(k)} = \frac{|h_{1,\vec{k}_{||}}|^2}{\tau_{cav}} + \frac{|h_{2,\vec{k}_{||}}|^2}{\tau_{exc}} \tag{1.3.19}$$

with $\gamma_{cav} = 1/\tau_{cav}$, $\gamma_{exc} = 1/\tau_{exc}$ and for the upper branch

$$\frac{1}{\tau_p^U(k)} = \frac{|h_{1,\vec{k}_{||}}|^2}{\tau_{cav}} + \frac{|h_{2,\vec{k}_{||}}|^2}{\tau_{exc}}. \tag{1.3.20}$$

In state-of-the-art semiconductor micro cavities one has $\gamma_{cav} \simeq 1-100ps$ and $\gamma_{exc} \simeq 1ns$ and thus the main contribution for the finite lifetime is due to the leakage of cavity photons and the induced decay of polaritons [28, 33]. The lifetime significantly depends on the number of DBRs forming the micro cavity.

Measuring the polariton condensate

The emission of leaking photons from the microcavity either stems from the cavity photon or usually in polariton experiments the lower dispersion polaritons depending on

the coupling strength between the exciton and photon modes. In this sense the system shows either regular lasing or polariton condensation. Furthermore it shows a cross over between weak coupling at higher temperatures and high pumping strengths to strong coupling at lower temperatures and pumping [47], while here we turn our focus to the latter case. The decay of polaritons is mainly due to the leakage of photons of energy $E_{L,P} = \hbar\omega$ out of the cavity and has the same in plane wave vector $\vec{k}_{||}$ as the polariton it has been emitted from. The decay rate depends on the quality of the cavity mirrors, which can be increased or decreased in a simple fashion e.g. by adding additional layers to the DBRs [28, 49]. In measurements the in-plane $\vec{k}_{||}$ vector of the leaking cavity photons directly corresponds to the angle of emission out of the microcavity and the energy allowing to measure directly the full exciton-polariton wave vectors [28]. This is illustrated in Fig. 1.6 and Fig. 1.7.

Self-interactions of lower branch polaritons

Until now we have neglected in our discussion interactions between the condensed quasiparticles. Such interactions are present and indeed stem from the exciton quasiparticles, which interact with each other via the exchange of electrons [15, 47]. The effective Coulomb interactions between electron and hole pairs with each other can be simplified by contact two-body interactions between excitons given by [15, 87],

$$\hat{H}_{\xi\xi} = \frac{1}{2}\sum_{\vec{k}_{||},\vec{k}'_{||},} V_{\vec{q}}^{\xi\xi}\xi^{\dagger}_{\vec{k}_{||}+\vec{q}}\xi^{\dagger}_{\vec{k}'_{||}-\vec{q}}\xi_{\vec{k}_{||}}\xi_{\vec{k}'_{||}} \tag{1.3.21}$$

where $\xi_{\vec{k}_{||}}$ ($\xi^{\dagger}_{\vec{k}_{||}}$) are the exciton annihilation (creation) operators. In the polariton basis these are taken into account in the Hamiltonian [15, 87] with an additional term

$$\hat{H}_{PP} = \frac{1}{2}\sum_{\vec{k}_{||},\vec{k}'_{||},\vec{q}} V^{PP}_{\vec{q},\vec{k}_{||},\vec{k}'_{||}} p^{\dagger}_{\vec{k}_{||}+\vec{q}} p^{\dagger}_{\vec{k}'_{||}-\vec{q}} p_{\vec{k}_{||}} p_{\vec{k}'_{||}}, \tag{1.3.22}$$

with

$$V^{PP}_{\vec{q},\vec{k}_{||},\vec{k}'_{||}} = V_{\vec{q}}^{\xi\xi}\xi_L(\vec{k}_{||}+\vec{q})\xi_L(\vec{k}'_{||}-\vec{q})\xi_L(\vec{k}_{||})\xi_L(\vec{k}'_{||}) \tag{1.3.23}$$

and $\xi_L(\vec{k}'_{||})$ ($\xi^{\dagger}_L(\vec{k}'_{||})$) denoting the lower exciton branch annihilation (creation) operators, which follow from the eigen vectors (1.3.9) [87]. So the combined Hamiltonian of (1.3.13) and (1.3.22) is then given by

$$\hat{H}_{pol} = \hat{H}_P + \hat{H}_{PP}. \tag{1.3.24}$$

As in the derivation of the Gross-Pitaevskii equation for atomic condensates (1.2.17) delta function self-interactions between the field operators can be assumed, if the conditions for diluteness and relative shortness of the scattering length are satisfied for the system.

1.3.2 A non-equilibrium complex nonlinear Schrödinger-type model

The Superfluid State equation

A key property of polaritons in polariton condensates is that they interact with each other inducing enriched dynamics of the coherent matter waves they form, such as a nonzero finite speed of sound below which there is a superfluid phase [15]. In contrast does the linear single-body Schrödinger equation obey excitations, the so called Reighleight waves, which occur once only a small modulation of the condensate is induced, while the nonlinear counterpart lacks such excitations [15]. In contrast to the linear equation the nonlinearity can compensate a sufficiently small local gain of energy and therefore prevent the phase of the superfluid to wind up, and so the emergence of excitations such as quantized vortices. Similarly to the atomic case we formulate an alternative description to the second quantization framework [15, 47, 28] for the condensate wave function of the lower polariton branch in terms of a GP-like equation,

$$i\hbar\partial_t\psi(\vec{r},t) = \left(\hat{E}_L + V_{ext}(\vec{r},t) + \alpha|\psi|^2\right)\psi(\vec{r},t), \tag{1.3.25}$$

where the lower branch dispersion $\hat{E}_L$ is often approximated as $-\frac{\hbar^2\nabla^2}{2m^*}$ with m^* denoting the effective mass of the polariton. This approximation corresponds in $\vec{k}_{||}$-space to setting the dispersion relation (1.3.8) for low momentum polaritons (small $\vec{k}_{||}$) to $\hat{E}_L(\vec{k}_{||}) \sim -\vec{k}_{||}^2$. $\psi(\vec{r},t) : \mathbb{R}^{2+1} \to \mathbb{C}$ is the order parameter of the many-body system, i.e. the condensate wave function. Further (1.3.25) includes the self-interactions between polaritons of strength α that stem to the leading order from the electron-electron exchange interactions when two excitons swap their electrons [47]. The magnitude of self-interactions is given through [87, 15]

$$\alpha = \frac{6E_b X_{exc}^2 a_B^2}{S}, \tag{1.3.26}$$

where a_B is the 2d Bohr radius, X_{exc} the excitonic fraction and S is a normalization and E_b is the excitonic binding energy.

Gain and Loss

We present two alternatives of modelling growth and decay. The nonuniqness of the theoretical model comes from the phenomenological nature of the model. So far a unique model has not been completely derived from a second quantization scheme, but only motived by physical arguments. Now, introduced in [48] gain and loss of polaritons can be modeled by extending the condensate dynamics via

$$\partial_t\psi = \left(P(\vec{r}) - \gamma|\psi|^2\right)\psi, \tag{1.3.27}$$

where $P(\vec{r})$ is the pumping distribution and γ the factor for the density dependent decay rate. On the other hand according to [91, 15] the time dynamics of (1.3.25) in an

incoherently pumped mean field polariton condensate are enhanced by

$$\partial_t \psi = \left(\frac{P}{\gamma_R + R|\psi|^2} - \gamma_L \right) \psi, \tag{1.3.28}$$

where the first term on the r.h.s. in (1.3.28) is a saturating nonlinearity, which for small amplitudes becomes (1.3.27) as can be seen by applying a first order Taylor expansion. Here γ_R represents the reservoir decay rate, γ_L the condensate decay rate and R the scattering rate from the reservoir into the condensate. Multiplying (1.3.28) by ψ^* and adding the hermitian conjugate we get for the condensate particle magnitude

$$\partial_t n = 2 \left(\frac{P}{\gamma_R + Rn} - \gamma_L \right) n. \tag{1.3.29}$$

The dynamics imposed by (1.3.29) implies that the higher the magnitude $n(\vec{r})$ is at a given point the lower the gain for the condensate wave function there and vice versa. If the left hand side in (1.3.29) is negative a decrease of particles follows while when it is positive the condensate gains particles/mass at a given point $\vec{r}$. Now, adding (1.3.28) to (1.3.25) we obtain a non equilibrium order parameter equation for the polariton condensate

$$i\hbar \partial_t \psi(\vec{r}, t) = \left(-\frac{\hbar^2 \nabla^2}{2m} + V_{ext}(\vec{r}, t) + \alpha |\psi|^2 \right) \psi(\vec{r}, t) + \\ + i \left(\frac{P}{\gamma_R + R|\psi|^2} - \gamma_L \right) \psi(\vec{r}, t). \tag{1.3.30}$$

We note that the complex terms due to pumping and decay resemble to some extend those induced by motion (3.8.13) and (1.2.48) or an electromagnetic field. Furthermore for stationary condensates the $U(1)$ symmetry is preserved. Generally energy relaxation can be taken into account by introducing additional decay of particles as a function of energy. The most straightforward way to phenomenologically model the process of energy relaxation is via a factor $\partial_t \to (1 + i\mu)\partial_t$ introduced to the nonlinear hamiltonian in (1.3.30) [47].

Dynamical reservoir

In addition to the equation for the condensate field ψ, one can introduce a dynamical reservoir population equation for the wave function in correspondence with the form in (1.3.30). The latter is indeed an approximating of the reservoir when $\frac{\partial n_R}{\partial t} \simeq 0$ applies and can be extended to include time dependence explicitly [91] by

$$\frac{\partial n_R}{\partial t} = P - \gamma_R n_R - R \left| \psi \right|^2 n_R. \tag{1.3.31}$$

P denotes the spatial and time dependent pumping geometry associated with the applied laser beam that corresponds as coherent photon source. γ_R represents the reservoir decay rate and the third term on the r.h.s. represents the loss due to stimulated scattering from the reservoir into the polariton condensate. As $\gamma_L \ll \gamma_R$ the reservoir dynamics is faster than that of the condensate and one can indeed assume $\frac{\partial n_R}{\partial t} \simeq 0$ as only the time averaged mean value of the reservoir is felt by the condensate.

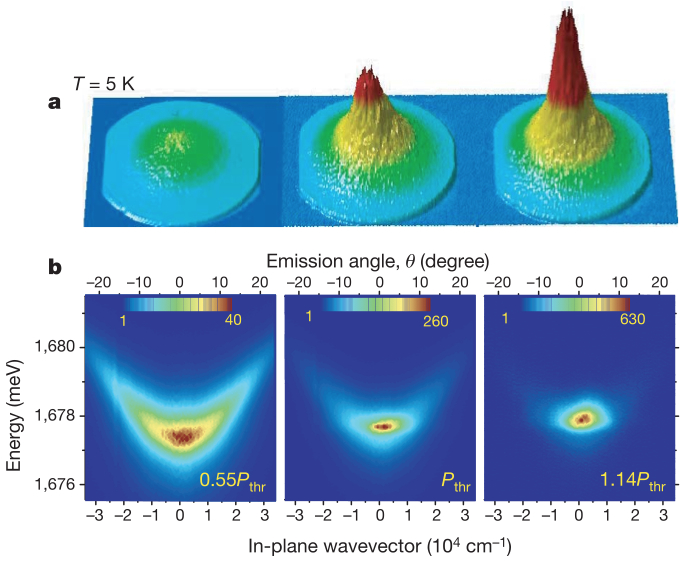

Figure 1.9: Measured far-field emission (momentum distribution) at 5K as condensation within a 2d polariton condensate takes place, showing the typical narrowing at $k_{||} = 0$ for increased power. (a) is $0.55P_{\text{thr}}$, (b) is P_{thr} and (c) is $1.14P_{\text{thr}}$, where the power $P_{\text{thr}} = 1.67kWcm^{-2}$ and corresponds to the condensation threshold. [16]

Incoherent pumping

With the mean field theory presented by (1.3.30) we have introduced a model describing the dynamics induced through an incoherent pumping scheme. This scheme pre supposes a physical situation where a significant density of incoherent polaritons are located in the so called bottleneck region in $k_{||}$-space, that is closely around the inflection point of the lower polariton dispersion. Then further relaxation to the bottom of the lower polariton branch via phonon-polariton scattering is decreasing due the reduced density of states in the final states. However, once the polariton density is above some threshold polariton-polariton scattering provides another energy relaxation process as they scatter into the bottom of the lower branch, while the other polaritons scatters into the excited excitonic region. Due to the statistical pressure by the bosonic nature of polaritons once the density of polaritons at the bottom of the lower branch is above order one, increase of particles is stimulated. When the gain of polaritons there exceeds the losses caused by decay a coherent polariton condensate forms at $|\vec{k}_{||}| \sim 0$ [15]. Fig. 1.9 shows the condensation of polaritons in momentum space around the threshold as measured in experiments. Fig. 1.7 illustrates the form of the lower polariton branch and at which position on the dispersion the condensate forms on the lower energy branch. As mentioned earlier, the momentum vector of the polariton is experimentally determined by the angle and magnitude of outgoing photons.

Bogoliubov excitation spectrum for the lower polariton branch

To quantify the effects of pumping and decay on the elementary excitation spectrum of the modified GPE (1.3.25) for a homogeneous ground state $\psi_L = \sqrt{n_L}\exp(-i\omega t)$ one considers the linearized Bogoliubov equations for the perturbation $\delta\psi_L(\vec{r})$ and its complex conjugate,

$$\begin{aligned} i\partial_t \begin{pmatrix} \delta\psi_L(\vec{r}) \\ \delta\psi_L^*(\vec{r}) \end{pmatrix} = \\ = \begin{pmatrix} \omega_L(\vec{k}_{||}) + 2\alpha n_L - \omega - i\Gamma/2 & \alpha n_L - i\Gamma/2 \\ -\alpha n_L - i\Gamma/2 & -\omega_L(\vec{k}_{||}) - 2\alpha n_L + \omega - i\Gamma/2 \end{pmatrix} \begin{pmatrix} \delta\psi_L(\vec{r}) \\ \delta\psi_L^*(\vec{r}) \end{pmatrix}, \end{aligned} \tag{1.3.32}$$

with $\omega_L(\vec{k}_{||}) = \omega_L^0 - \hbar\vec{\nabla}^2/2m_L$ [15]. ω_L^0 is the frequency of the bottom of the lower polariton branch and g_L the magnitude of polariton self-interactions. In addition we have introduced an effective damping rate [15]

$$\Gamma = \frac{PRn_L}{(\gamma_R + Rn_L)^2}. \tag{1.3.33}$$

Then by considering the small amplitude harmonic modes as in the corresponding section for equilibrium condensates we obtain

$$\omega_{\mathrm{Bog}}(\vec{k}_{||}) = \pm\sqrt{\frac{\hbar^2\vec{k}_{||}^2}{2m_L}\left(\frac{\hbar^2\vec{k}_{||}^2}{2m_L} + \alpha n_L\right) - \frac{\Gamma^2}{4}} - i\frac{\Gamma}{2}. \tag{1.3.34}$$

Here P is the constant pumping [15]. In contrast to equilibrium BEC additional terms due to the gain and loss have been introduced to the dispersion curve in (1.3.34). The non equilibrium dispersion resembles the equilibrium case once the limit to the conservative system $\Gamma \to 0$ is applied.

In the equilibrium case we have seen that there are a variety of elementary excitations, which depend on the dimensionality of the condensate. Analog excitations indeed do exist within polariton condensates [15]. However, it has been shown numerically that due to the pumping and decay terms these excitations do not persist for infinite times but disperse [92].

1.4 Spinor condensates

By definition BEC is a many-body phenomenon of macroscopically occupied states of very high coherence. While we so far have considered single mode condensates, we now turn to condensates of two components. So the operator of the many-body system (1.1.22) becomes

$$\hat{\Psi}_N^\dagger = \sum_{i=0}^{N-M-1} f_1 \hat{a}_i^\dagger + \sum_{j=N-M}^{N} f_2 \hat{a}_j^\dagger. \tag{1.4.1}$$

Applying the Bogoliubov c-number approximation one can simplify the operator to be effectively described by two classical condensate wave functions f_1 and f_2. From a theoretical point of view it is clear that several components of BEC can in principle coexists, but depending on internal parameters communicate their presence to each other. Examples of several components of condensates are systems including different spin states of the condensed atoms that induce a hyperfine splitting between the components [11] or one can envisage different species of atoms to condense into the same trap, which due to their different mass, and scattering length would impose enhanced dynamics on the system of condensates. First we shortly review the two component formalism for atomic condensates and secondly that for polariton condensates which stems from the pseudo spin of the polariton quasiparticles.

1.4.1 Multicomponent atomic condensates

Although a second quantization approach applies for the treatment of multicomponent condensates we will shortcut the arguments leading to an effective mean-field model, but note that similar considerations as for the single component case apply for the derivation. So to capture the two component atomic BEC (occupying the hyperfine states $|F=1, m_F=-1\rangle$ and $|F=2, m_F=1\rangle$) we simply introduce the generalized GP energy functional [11]

$$\mathcal{E}_2^{\mathrm{GP}}[\psi_1,\psi_2] = \int \left(\frac{\gamma}{2} \left| \vec{\nabla}\psi_1 \right|^2 + \frac{\gamma}{2} \left| \vec{\nabla}\psi_2 \right|^2 + V_{\mathrm{ext}}^{(1)}(\vec{r}) n_1 + \right. \\ \left. + (V_{ext}^{(2)}(\vec{r}) + V_{hf}) n_2 + \frac{1}{2} g_1 n_1^2 + \frac{1}{2} g_2 n_2^2 + g_{12} n_1 n_2 \right) d\vec{r}. \tag{1.4.2}$$

In contrast to the convex single component functional (1.2.19), $\mathcal{E}_2^{\mathrm{GP}}[\psi_1,\psi_2]$ is an expression of the wave function of the condensate component ψ_1 and of component ψ_2 and its minimizer, say $\Psi = (\psi_1, \psi_2)$, provides the energy of the BEC system. Further introduced symbols in (1.4.2) are given as follows: g_i denotes the self-interactions of component i, while g_{12} isotropic cross-interactions between components and n_i denotes the magnitude of the component i. Here V_{hf} is the hyperfine splitting between two atomic states due to the relative energy shift between components [11]. $V_{\mathrm{ext}}^{(i)}(\vec{r})$ are the trapping potentials felt by component 1 and 2, respectively. Analogously to the single

component theory the minimizing functions are then obtained by the variational approach $i\hbar\partial\psi_i/\partial_t\psi_i = \delta E/\delta\psi_i^*$ with $i = 1, 2$. Applying the variational approach under the assumption of fixed mass (included by a Lagrangian multiplier) one gets a system of two coupled Gross-Pitaevskii equations, corresponding to Euler-Lagrange equations for the spinor field $\Psi = (\psi_1, \psi_2)$,

$$i\hbar\partial_t\psi_1 = \left(-\frac{\hbar^2}{2m}\vec{\nabla}^2 + V_{\text{ext}}^{(1)} + g_1|\psi_1|^2 + g_{12}|\psi_2|^2\right)\psi_1 \tag{1.4.3}$$

and

$$i\hbar\partial_t\psi_2 = \left(-\frac{\hbar^2}{2m}\vec{\nabla}^2 + V_{\text{ext}}^{(2)} + V_{\text{hf}} + g_2|\psi_2|^2 + g_{12}|\psi_1|^2\right)\psi_2 \tag{1.4.4}$$

with self-interactions explicitly given by $g_1 = 4\pi\hbar^2 a_1/m$ and $g_2 = 4\pi\hbar^2 a_2/m$ and cross-interaction given by $g_{12} = 4\pi\hbar^2 a_{12}/m$. Here we denote the scattering length between particles of state 1 and 2 by a_{12}. Atom numbers are assumed to be conserved in this model, so neglecting the scattering from one component into the other [11]. Remarkably mixtures of dilute ^{87}Rb atom gases in the condensed phase in two different hyperfine states have been realized in experiment and are well described by this model [11]. More recently different species consisting of e.g. a ^{87}Rb atom condensate and a ^{85}Rb atom condensate were realized [93]. Now as the above system of coupled GPE suggests, one can distinguish different regimes depending on the relation of self- and cross-interactions. To induce a separation of phases the condition for the condensate to be immiscible $g_{12} > \sqrt{g_1 g_2}$ has to be satisfied, as the cross talk between components will force them apart [11], which has been shown particularly in [93]. As soon as $g_{12} \leq \sqrt{g_1 g_2}$ condensates become miscible and only fluctuations between components might appear through the relatively small g_{12}. Also in two component systems Feshbach resonaces allow the control over the scattering length and therefore the self-interaction parameter of each component separately [93]. This insight will be utilized in one of the following chapters, where an effective mechanism to generate skyrmions/core vortices will be presented.

1.4.2 Spinor polariton condensates

Similarily to atoms, polaritons obey two component properties due to an intrinsic spin, which becomes relevant once decoherence between the components is induced. It turns out that this spin allows the separation of spin modes e.g. by applying an external magnetic field on the polariton condensate or excitation by oppositely polarized light and thus two component spinor states formally similar to their atomic counterpart become feasible.

Let us introduce first the concept of spin in polaritons and then present a theoretical framework for polariton condensates which takes their spin degree of freedom into account in a circularly polarization basis.

Pseudospin model for polaritons

As the polariton is a quasiparticle the arrangement of the angular momentum of its components is key for the manifestation of the polariton's quasi spin. In standard quantum wells, the electron in the conduction band has a S-symmetry projection of its angular momentum $J_z^e = S_z^e = \pm 1/2$ [15, 87]. A hole with P-symmetry in the valence band has possible angular momenta $J_z^h = S_z^h + M_z^h = \pm 1/2, \pm 3/2$. This includes the case of a hole with spin projection antiparallel to mechanical momentum M_z^h that implies $J_z^h = \pm 1/2$, but otherwise one has angular momentum $J_z^h = \pm 3/2$ [87]. So the total angular momentum of excitions can be $J = \pm 1, \pm 2$. It turns out that only the $J = \pm 1$ states can be excited optically, which is essential to form polaritons in the semiconductor micro cavity [29, 15], i.e. excitons which interact with light have ± 1 spin projections. Due to this interaction one can polarize exciton-polaritons by illuminating the excitons with a polarized light source. Circularily polarized light yields $J = 1, -1$ and linearly polarized light a superposition of $J = +1$ and $J = -1$, with absolute zero spin projection. In Fig. 1.10 we show an analog to the so called Stokes vector on the Poincare sphere representing the polarization state of the polariton stemming from the illumination with the polarized light field. Taken over from the polarization of the light each polarization of the polariton can be associated with a point on this sphere. The north and south poles of the sphere are the circular polarizations (due polarization with circularly polarized light) while the equatorial plane corresponds to linear circulation (stemming from linearly polarized light) [49, 87]. The polariton has spin projection

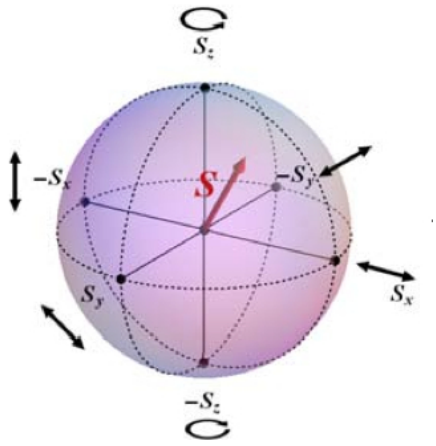

Figure 1.10: Schematic illustration of the pseudo spin representation, where S denotes the stokes vector. The image has been taken from [87].

$J = \pm 1$ that couples to light and separates from the other component $J \pm 2$ in a way that the latter is negligible for the $J = \pm 1$ condensate dynamics. A separation of spin components $J = 1$ and $J = -1$ can be by achieved by excitation through σ_+ and σ_- circulated light [94]. Formally the spin structure of polaritons is analog to that of

electrons and can be represented by the 2x2 pseudo-spin density matrix

$$\rho = \frac{N}{2}\mathbf{I} + \vec{S}\cdot\vec{\sigma}, \tag{1.4.5}$$

where $\mathbf{I}$ is the 2x2 unit matrix, N the total number of particles, $\vec{S} = (S_x, S_y, S_z)$ the pseudo-spin vector and $\vec{\sigma}$ the vector of Pauli matrices [94, 87]. The pseudo-spin's orientation along the z-axis is associated with circular polarized polaritons, while when the pseudo-spin is within the (x, y)-plane one has linear polarized polaritons. For circularly polarized polaritons (1.4.5) reduces to

$$\rho = \frac{N}{2}\mathbf{I} + S_z\cdot\sigma_z. \tag{1.4.6}$$

TM-TE splitting

Polaritons with $\vec{k}_{||} \neq 0$ can be classified as states of dipole momentum orientated along and perpendicular to the wave vector as they in particular obey different energy levels; excitons with dipole moment parallel to the wave vector are called transverse magnetic (TM) and excitons with dipole momentum perpendicular to the wave vector transverse electric (TE). The long-range electron-hole interaction imposes a longitudinal-transverse splitting (LT) of the two types of excitons referred to as TE-TM splitting [94]. This splitting further translates to polaritons with $k_{||} \neq 0$ and accounts for the energy difference between the TM and TE states [49]. In [90] a pseudo spin representation modelling the TE-TM splitting has been introduced and can be described as follows. The propagation of a single free polariton is governed by the effective Hamiltonian extended by an effective magnetic-type field acting upon it [90], i.e.

$$\hat{H}(\vec{k}_{||}) = \frac{\hbar^2\vec{k}_{||}^2}{2m^*} + \mu_B g(\vec{\sigma}\vec{H}_{\text{eff}}). \tag{1.4.7}$$

Here $\vec{\sigma}$ is the Pauli matrix vector, m^* the effective mass of the polariton and we have introduced the effective field

$$\vec{H}_{\text{eff}} = \frac{\hbar}{\mu_B g}\Omega_{\vec{k}_{||}} \tag{1.4.8}$$

where $\Omega_{\vec{k}_{||}}$ has the components

$$\Omega_x = \frac{\Omega}{\vec{k}_{||}^2}(k_x^2 - k_y^2), \qquad \Omega_y = 2\frac{\Omega}{\vec{k}_{||}^2}k_x k_y, \tag{1.4.9}$$

with $\vec{k}_{||} = (k_x, k_y)$, $\Omega = \Delta_{\text{LT}}/\hbar$ and Δ_{LT} is the longitudinal-transverse splitting. Consequently the strength of the energy splitting of the two species of polaritons is by (1.4.7) due to the magnitude of the LT splitting. We refer to [90] for details on the orientation of the effective field in terms of the in-plane wave vector $\vec{k}_{||}$.

The density matrix for the spin without interactions evolves in time by the Liouville-von Neumann equation [87],

$$i\hbar\partial_t\rho = [\hat{H}(\vec{k}_{||}), \rho], \tag{1.4.10}$$

with the Hamiltonian given by (1.4.7). Note that the general form of (1.4.10) can be derived from the Schrödinger equation.

TE-TM splitting in the circularly polarized spinor polariton condensate

Previous considerations on the pseudo-spin dynamics for polaritons apply for many coherent polaritons without interactions as well. When interactions between polaritons play a crucial role, however, the model needs to be extended. In the circularly polarized basis the Hamiltonian respectively Gross-Pitaevskii-type energy functional for the condensate spinor wave function $\Psi = (\psi_+, \psi_-)$ with interactions is becomes [94, 87],

$$E = \int \left(\Psi^* \mathbf{A} \Psi + \frac{\alpha_1}{2} \left(|\psi_+|^4 + |\psi_-|^4 \right) + \alpha_2 |\psi_+|^2 |\psi_-|^2 \right) d\vec{r}. \tag{1.4.11}$$

α_1 denotes the self-interaction strength within each spin component of the spinor and α_2 accounts for the cross-interactions between each spin component. The kinetic energy operator of (1.4.11) is given by

$$\mathbf{A} = \begin{pmatrix} -\frac{\hbar^2 \Delta}{2m^*} & \beta(\partial_y - i\partial_x)^2 \\ \beta(\partial_y + i\partial_x)^2 & -\frac{\hbar^2 \Delta}{2m^*} \end{pmatrix}. \tag{1.4.12}$$

The off-diagonal elements correspond to the TM-TE splitting and impose a splitting of spin components, while it is the simplest form with which they can be associated with the effective magnetic field (1.4.9) [94, 87]. The diagonal terms are the conventional kinetic energy terms of the lower polariton branch. We have used the effective mass m^* of the polariton, which can be written in terms of the effective masses of the TM (m_{TM}) and TE (m_{TE}) energy branches,

$$m^* = \frac{m_{TM} m_{TE}}{m_{TM} + m_{TE}}. \tag{1.4.13}$$

The factor $\beta = \hbar^2/4 \cdot (1/m_{TM} - 1/m_{TE})$ in (1.4.12) denotes the magnitude of the TE-TM splitting between the components. Applying the Lagrangian equations as in the previous section on (1.4.11) yields the state equations for the minimizers ψ_+ and ψ_- of the energy functional (1.4.11). These are given by

$$i\hbar \frac{\partial \psi_+}{\partial_t} = -\frac{\hbar^2}{2m^*} \Delta \psi_+ + \alpha_1 |\psi_+|^2 \psi_+ + \alpha_1 |\psi_-|^2 \psi_+ + \beta(\partial_y - i\partial_x)^2 \psi_- \tag{1.4.14}$$

$$i\hbar \frac{\partial \psi_-}{\partial_t} = -\frac{\hbar^2}{2m^*} \Delta \psi_- + \alpha_1 |\psi_-|^2 \psi_- + \alpha_1 |\psi_+|^2 \psi_- + \beta(\partial_y + i\partial_x)^2 \psi_+. \tag{1.4.15}$$

Besides self-interaction and between components one has the additional TE-TM splitting terms modifying the evolution of the spinor polariton condensate $\Psi = (\psi_+, \psi_-)$. The latter terms induce in particular an exchange between particles of each spin component. We point out that the mass of particles is not conserved for a polariton system, but varies with time, when no stationary state is accessible. We note that another form of splitting between spin components in polariton condensates is due to the intrinsic Zeemann splitting, we refer to [87] for details.

TM-TE splitting model in 1d

In one spatial dimensions the spinor polariton field $\boldsymbol{\psi} = (\psi_+, \psi_-)^T$ due to TM-TE splitting evolves according to the simplified system of cGLE [26]

$$
\begin{aligned}
i\hbar\frac{\partial\psi_+}{\partial t} &= \left[-\frac{\hbar^2\Delta}{2m} + \alpha_1\left(|\psi_+|^2 + n_R\right) + \alpha_2|\psi_-|^2\right]\psi_+ \\
&+ \left[U - \frac{i\hbar}{2}\left(\gamma_d - \gamma_p n_R\right)\right]\psi_+ - \frac{H_x}{2}\psi_- \qquad (1.4.16)\\
i\hbar\frac{\partial\psi_-}{\partial t} &= \left[-\frac{\hbar^2\Delta}{2m} + \alpha_1\left(|\psi_-|^2 + n_R\right) + \alpha_2|\psi_+|^2\right]\psi_- \\
&+ \left[U - \frac{i\hbar}{2}\left(\gamma_d - \gamma_p n_R\right)\right]\psi_- - \frac{H_x}{2}\psi_+ \qquad (1.4.17)\\
& \qquad (1.4.18)
\end{aligned}
$$

Here we have included pumping and decay within the set of equations and a reservoir n_R, which can be dynamical or statical as discussed in a previous section. In contrast to the 2d case (1.4.12) the TM-TE splitting can be assumed to be constant along the 1d geometry; in addition to the case without spin we now have an effective magnetic-type field with amplitude $H_x = 0.01$ meV induced by the energy splitting between TE and TM eigenmodes and that couples both spin components. γ_p denotes a pump rate and γ_d the linear decay of particles. A crucial point is that the polariton-polariton interactions are spin-anisotropic and that the interactions within a spin component are much bigger than between the spin polariton components, i.e. $\alpha_2 = -0.1\alpha_1$, and vary with the number of quantum wells, their separation within the cavity spacer and the detuning between the light and exciton fields [87].

2 Analytical properties of a rapidly rotating Bose-Einstein condensate in a homogeneous trap

Florian Pinsker and Jakob Yngvason, published in a joint work with Michele Correggi and Nicolas Rougerie as part of the paper J. Math. Phys. **53**, 095203 (2012);

We present an asymptotic analysis of the effects of rapid rotation on the ground state properties of a superfluid confined in a two-dimensional trap. The trapping potential is assumed to be radial and homogeneous of degree larger than two in addition to a quadratic term. The energy asymptotics are found between the two critical rotational velocities marking respectively the vortex lattice regime with the creation of a hole of low density within the vortex lattice and the giant vortex phase. These phenomena have previously been established rigorously for a flat trap with fixed boundary but the soft traps considered in the present paper exhibit some significant differences.

2.1 Introduction

Since their first experimental realization in 1995, atomic Bose-Einstein condensates (BECs) have become a subject of tremendous interest, stimulating intense theoretical activity. The BE-condensed alkali vapors that are nowadays produced in many laboratories offer a spectacular level of tunability for several experimental parameters, making them a favorite testing ground for many intriguing quantum phenomena. Among these is *superfluidity*, i.e., the occurrence of frictionless flow, previously observed in liquid helium. Atomic BECs offer a valuable alternative to the latter system, since experiments with dilute gases of ultracold atoms allow to test theories of superfluidity in much more detail.

From a theoretical point of view an appealing aspect of the field is its sound mathematical foundation. The most commonly used model for the description of BECs, the so-called Gross-Pitaevskii (GP) theory, is now supported both by extensive comparisons with experiments [95, 182] and a solid mathematical basis [97]. Indeed, substantial advances on the connection between GP theory and many-body quantum physics have been made in recent years, leading to a rigorous derivation of both the stationary [98, 99, 100] and dynamic aspects [101, 102, 103] of the theory.

One of the most striking features of superfluids is their response to rotation of the confining trap. Typical experiments (see [182] for further references) start by cooling

a Bose gas in a magneto-optical trap below the critical temperature for Bose-Einstein condensation. If the trap is set in rotational motion the gas stays to begin with at rest in the inertial frame, but if the rotation speed exceeds some critical value, vortices are nucleated and remain stable over a long time span. This behavior is in strong contrast with that of a classical fluid, which in the stationary state rotates like a rigid body and thus remains at rest in the rotating frame.

In a rotationally symmetric trap, the main two experimentally tunable parameters are the rotation speed and the strength of interparticle interactions, written as $1/\varepsilon^2$ with $\varepsilon > 0$ in the sequel. The ground state of the system strongly depends on the relation between these two parameters.

In this paper we study the ground state of a rotating Bose gas in the framework of the two-dimensional GP theory[1]. We consider the minimization, under a unit mass constraint, of the GP functional[2]

$$\mathcal{E}^{\mathrm{GP}}_{\mathrm{phys}}[\Psi] = \int_{\mathbb{R}^2} \mathrm{d}\vec{r} \left(\frac{1}{2} \left| \left(\nabla - i\vec{A}_{\mathrm{rot}} \right) \Psi \right|^2 + \left(V(r) - \frac{1}{2}\Omega^2_{\mathrm{rot}} r^2 \right) |\Psi|^2 + \frac{|\Psi|^4}{\varepsilon^2} \right) \tag{2.1.1}$$

$$\vec{A}_{\mathrm{rot}} = \vec{\Omega}_{\mathrm{rot}} \wedge \vec{r} = \Omega_{\mathrm{rot}} r \vec{e}_\theta, \tag{2.1.2}$$

where Ω_{rot} is the rotational velocity, $r = |\mathbf{r}|$ with $\mathbf{r} \in \mathbb{R}^2$ is the distance from the rotation axis, and $\mathbf{e}_\vartheta$ stands for the unit vector in the direction transverse to $\mathbf{r}$. The confinement is provided by a potential of the form

$$V(r) := kr^s + \tfrac{1}{2}\Omega^2_{\mathrm{osc}} r^2 \tag{2.1.3}$$

with $k > 0$. We restrict to the case $2 < s < \infty$ (anharmonic, 'soft' potentials) and shall mainly study the Thomas-Fermi (TF) limit $\varepsilon \to 0$. The case $s = 2$ is special in many respects because the potential $-\Omega^2_{\mathrm{rot}} r^2$ due to the centrifugal force is also a quadratic function of r. As a consequence an upper bound is set to the allowed values of the rotational speed and different physics is expected in the regime where the centrifugal force nearly compensates the trapping force (see [95] and references therein, [104] and [105]).

The parameter regime considered here concerns the rotational velocities where a vortex lattice wavefunction is an appropriate trial function for the minimizer of the GP energy functional. This vortex lattice solution then gives the next to the leading order contribution of the energy functional, which matches the contribution of the lower bound. We introduce now additional functionals in which terms we will in particular express the GP energy functional.

[1] Such a description is justified if the trap almost confines the gas on a plain orthogonal to the axis of rotation or, on the contrary, the trap is very elongated along the axis, in which case the behavior can be expected to be essentially independent of the coordinate in that direction.

[2] The subscript 'phys' stands for physical, i.e., this is the functional in the original physical variables, as opposed to the rescaled functionals introduced in Sect. 1.1 below. Units have been chosen such that $\hbar$ as well as the mass are equal to 1.

2.1.1 Rescaled Functionals

In this paper we focus on the analysis of the minimization of the GP energy functional (2.1.1) under the mass constraint

$$\|\Psi\|_2^2 := \int_{\mathbb{R}^2} \mathrm{d}\vec{r}\ |\Psi|^2 = 1.$$

The trapping is given by the potential (2.1.3) with $\Omega_{\mathrm{osc}} < \Omega_{\mathrm{rot}}$, and $0 < \varepsilon \ll 1$, i.e., we study the TF limit of the model. The power s in (2.1.3) characterizes the homogeneous trap and we assume that $2 < s < \infty$. We also introduce the parameter

$$\Omega_{\mathrm{eff}} := \sqrt{\Omega_{\mathrm{rot}}^2 - \Omega_{\mathrm{osc}}^2}, \tag{2.1.4}$$

so that the effective potential in (2.1.1) can be written in the form

$$V(r) - \tfrac{1}{2}\Omega_{\mathrm{rot}}^2 r^2 = kr^s - \tfrac{1}{2}\Omega_{\mathrm{eff}} r^2. \tag{2.1.5}$$

Since we are interested in exploring the rotation regime $\Omega_{\mathrm{rot}} \to \infty$ but want also to keep track of the effect of the quadratic term in the expression above we shall assume that

$$\Omega_{\mathrm{eff}}^2 = \gamma \Omega_{\mathrm{rot}}^2 \tag{2.1.6}$$

for some given $0 < \gamma \leq 1$.

In this excerpt of the paper [23], we shall consider rotational velocities that satisfy

$$\Omega_{\mathrm{rot}} \gtrsim \varepsilon^{-\frac{s-2}{s+2}}. \tag{2.1.7}$$

Then a natural scaling parameter is given by the position R_{m} of the unique minimum point of the effective potential (2.1.5), which is explicitly given by

$$R_{\mathrm{m}} := \left(\frac{\gamma \Omega_{\mathrm{rot}}^2}{sk}\right)^{\frac{1}{s-2}} = \mathcal{O}\left(\Omega_{\mathrm{rot}}^{\frac{2}{s-2}}\right). \tag{2.1.8}$$

Rescaling

$$\vec{r} = R_{\mathrm{m}}\vec{x}, \qquad \Psi(\vec{r}) = R_{\mathrm{m}}^{-1}\psi(\vec{r}), \qquad \Omega_{\mathrm{rot}} = R_{\mathrm{m}}^{-2}\Omega, \qquad \vec{A}_\Omega = \Omega x \vec{e}_\theta \tag{2.1.9}$$

the GP functional becomes

$$\mathcal{E}^{\mathrm{GP}}[\Psi] = \int_{\mathbb{R}^2} \left(|(\vec{\nabla} + i\Omega x \vec{e}_\theta)\Psi|^2 + \gamma^2\Omega^2 \left(\frac{2}{s}x^s - x^2\right)|\Psi|^2 + \varepsilon^{-2}|\Psi|^4 \right) d\vec{x}. \tag{2.1.10}$$

In the course of this work we will consider a similar GP functional as well, which is associated with (2.1.10),

$$\hat{\mathcal{E}}^{\mathrm{GP}}[\psi] = \int_{\mathbb{R}^2} \left(|\vec{\nabla}\psi|^2 + \gamma^2\Omega^2 \left(\frac{2}{s}x^s - x^2\right)|\psi|^2 + \varepsilon^{-2}|\psi|^4 \right) d\vec{x}. \tag{2.1.11}$$

Both functionals map functions $\psi \in H^1(\mathbb{R}^2)$ with $\|\psi\|_2 = 1$. For simplicity we introduce the notation

$$V(x) \equiv \gamma^2\Omega^2 \left(\frac{2}{s}x^s - x^2\right) \tag{2.1.12}$$

for the potential term in above energy functionals and a simple expansion at the potentials' minimum $x = 1$ yields

$$V(x) \simeq \gamma^2\Omega^2 \left(\left(\frac{2}{s} - 1\right) + (x-1)^2 2\,(s-2)\right). \tag{2.1.13}$$

Now, the unique minimizer of (2.1.11) under the mass constraint denoted by g satisfies the variational equation

$$-\Delta g + V(x)g + \frac{2}{\varepsilon^2}g^3 = \mu g, \tag{2.1.14}$$

where μ is a Lagrangian multiplier given by

$$\hat{E}^{\mathrm{GP}} + \varepsilon^{-2}\|g\|_4^4 = \mu. \tag{2.1.15}$$

Thomas Fermi (TF) energy functional and rough estimates

Besides the GP functional we also consider the TF functional given by

$$\mathcal{E}^{\mathrm{TF}}[\rho = \psi^2] = \int_{\mathbb{R}^2} \left(\gamma^2\Omega^2 \left(\frac{2}{s}x^s - x^2\right)|\psi|^2 + \varepsilon^{-2}|\psi|^4\right) d\vec{x} \tag{2.1.16}$$

on the domain

$$\left\{\rho \in L^2(\mathbb{R}^2) | \rho \geq 0, r^s\rho \in L^1(\mathbb{R}^2)\right\} \tag{2.1.17}$$

with the mass constraint $\|\rho\|_1 = 1$. Its unique minimizer, the TF density, is

$$\begin{aligned}\rho^{\mathrm{TF}}(x) &= \frac{\varepsilon^2}{2}\left(\mu^{\mathrm{TF}} - \gamma^2\Omega^2\left(\frac{2}{s}x^s - x^2\right)\right)_+ \simeq \\ &\simeq \frac{\gamma^2\varepsilon^2\Omega^2}{2}\left(\frac{2}{s}(x_{\mathrm{in}}^s - 1) + (1 - x_{\mathrm{in}}^2) - (x-1)^2 2(s-2)\right) + \mathcal{O}(\omega^2|1-x|^3).\end{aligned} \tag{2.1.18}$$

Multiplying (2.1.18) with ρ^{TF}, integrating and the normalization $\|\rho^{\mathrm{TF}}\|_1 = 1$ yields

$$\mu^{\mathrm{TF}} = E^{\mathrm{TF}} + \frac{1}{\varepsilon^2}\|\rho^{\mathrm{TF}}\|_2^2. \tag{2.1.19}$$

We refer to [106] for the analysis of the support of the TF density. In that work they find that there is an inner radius, which we denote by x_{in} and an outer radius denoted by x_{out} at which the TF density vanishes and between which it is positive. Beyond those

radii the density is zero. By the normalization of the TF density $\|\rho^{\mathrm{TF}}\|_1 = 1$ and a Taylor expansion we have

$$\mu^{\mathrm{TF}}\left(\frac{x_{\mathrm{out}}^2 - x_{\mathrm{in}}^2}{2}\right) - \int_{x_{\mathrm{in}}}^{x_{\mathrm{out}}} dx x V(x) =$$
$$= \left(\mu^{\mathrm{TF}} - \gamma^2\Omega^2\left(\frac{2}{s} - 1\right)\right)\left(\frac{x_{\mathrm{out}}^2 - x_{\mathrm{in}}^2}{2}\right) - \gamma^2\Omega^2\int_{x_{\mathrm{in}}}^{x_{\mathrm{out}}} dx x(x-1)^2 2\,(s-2) =$$
$$= \frac{1}{\pi\varepsilon^2}. \quad (2.1.20)$$

The condition $\rho^{\mathrm{TF}}(x_{\mathrm{in}}) = 0$ and a Taylor expansion yields for the chemical potential

$$\mu^{\mathrm{TF}} = \gamma^2\Omega^2\left(\frac{2}{s}x_{\mathrm{in}}^s - x_{\mathrm{in}}^2\right) =$$
$$= \mu^{\mathrm{TF}}(x_{\mathrm{in}}) \simeq \gamma^2\Omega^2\left(\left(\frac{2}{s} - 1\right) + (x_{\mathrm{in}} - 1)^2 2\,(s-2)\right). \quad (2.1.21)$$

This combined with (2.1.20) yields the width of the support given by

$$l \equiv x_{\mathrm{out}} - x_{\mathrm{in}} \sim (\gamma\omega)^{-\frac{2}{3}} \cdot \left(\frac{1}{\pi 4(s-2)}\right)^{1/3}(1 - o(1)). \quad (2.1.22)$$

Taking the formula for the TF density and the estimate on the width implies

$$\rho^{\mathrm{TF}} \leq C\omega^{2/3}. \quad (2.1.23)$$

Ginzburg-Landau type Functional

A key ingredient of our proof of the energy asymptotics is the energy functional

$$\mathcal{F}_g[u] = \int_{\mathbb{R}^2}\left\{\left|\left(\vec{\nabla} - i\vec{A}\right)u\right|^2 g^2 + \frac{1}{\varepsilon^2}g^4|(1 - |u|^2)|^2\right\} \quad (2.1.24)$$

with $u(\vec{r})$ being a complex function for a given real function g. It will be used to additively decouple the GP energy functional. It also provides the vortex lattice contribution to the energy asymptotics.

2.2 Main result

The main result of this work concerns the energy asymptotics of the rotating BEC. It is stated in particular in terms of the TF energy, which gives the leading order in this parameter regime. The subsequent term is due to the kinetic energy of the vortex lattice.

Theorem 2.2.1 (Energy Asymptotics to E^{GP})
For ε sufficiently small, and if Ω satisfies $\varepsilon^{-1} \ll \Omega \ll \varepsilon^{-4}$

$$E^{\mathrm{GP}} = E^{\mathrm{TF}} + \frac{\Omega|\log(\varepsilon^4\Omega)|}{6}(1 + o(1)). \quad (2.2.1)$$

2.3 Proofs

To proof the above theorem several particular problems need to be solved. First we prove a decomposition of the GP functional (2.1.10), which enables us to estimate two energy functionals seperately.

Proposition 2.3.1 (Energy Decoupling)
For any $\Psi \in \mathcal{D}^{\mathrm{GP}}$ satisfying the normalization condition $\|\Psi\|_2 = 1$ we define the decomposition of the wave function by $\Psi(\vec{r}) \equiv g(r) \cdot u(\vec{r})$, with g denoting the positive minimizer of (2.1.11), and $u(\vec{r})$ beeing complex-valued. Thus, we have the energy decoupling

$$\mathcal{E}^{\mathrm{GP}}[\Psi] = \hat{E}^{\mathrm{GP}} + \mathcal{F}_g[u]. \tag{2.3.1}$$

with

$$\mathcal{F}_g[u] = \int_{\mathbb{R}^2} \left\{ \left| \left(\vec{\nabla} - i\vec{A} \right) u \right|^2 g^2 + \frac{1}{\varepsilon^2} g^4 |(1 - |u|^2)|^2 \right\} \tag{2.3.2}$$

Proof: We write Ψ as $\Psi = \varphi \cdot u$ with φ real-valued and positive and u complex-valued. We use the identity

$$\int |\vec{\nabla}\Psi|^2 = -\int |u|^2 \varphi \Delta\varphi + \int \varphi^2 |\vec{\nabla} u|^2 \tag{2.3.3}$$

to rewrite the kinetic energy term in (2.1.10) as

$$\int \left| \left(\vec{\nabla} - i\vec{A} \right) \Psi \right|^2 = -\int |u|^2 \varphi \Delta\varphi + \int \varphi^2 \left| \left(\vec{\nabla} - i\vec{A} \right) u \right|^2, \tag{2.3.4}$$

which enables us to write the GP functional as

$$\mathcal{E}^{\mathrm{GP}}[\Psi] = \int_{\mathbb{R}^2} \left\{ -|u|^2 \varphi \Delta\varphi + \varphi^2 \left| \left(\vec{\nabla} - i\vec{A} \right) u \right|^2 + V(x)|\Psi|^2 + \varepsilon^{-2}|\Psi|^4 \right\}. \tag{2.3.5}$$

We now choose $\varphi = g$ and insert the corresponding variational equation (2.1.14) in (2.3.5) and afterwards use (2.1.15) and the mass constraint $\|\Psi\|_2 = 1$ to obtain

$$\begin{aligned} \mathcal{E}^{\mathrm{GP}}[\psi] &= \int_{\mathbb{R}^2} \left\{ |\Psi|^2 \left(-\frac{2}{\varepsilon^2} g^2 - V(x) + \mu \right) + g^2 \left| \left(\vec{\nabla} - i\vec{A} \right) u \right|^2 + V(x)|\Psi|^2 + \varepsilon^{-2}|\Psi|^4 \right\} = \\ &= \hat{E}^{\mathrm{GP}} + \int_{\mathbb{R}^2} \left\{ \left| \left(\vec{\nabla} - i\vec{A} \right) u \right|^2 g^2 + \frac{1}{\varepsilon^2} g^4 |(1 - |u|^2)|^2 \right\} \doteqdot \hat{E}^{\mathrm{GP}} + \mathcal{F}_g[u]. \end{aligned} \tag{2.3.6}$$

□

Next we find an upper bound for the minimum of (2.1.11). This together with an approveriate lower bound allows to state precise asymptotics of the condensate GP energy. A trivial lower bound for the $\hat{E}^{\mathrm{GP}}$ is given by E^{TF} and sufficient to proof the main statement [106]. In a subsequent section, however, we will present a refinement of the lower bound.

Proposition 2.3.2 (Upper Bound to $\hat{E}^{\mathrm{GP}}$)
For ε sufficiently small, and if Ω satisfies $\varepsilon^{-1} \ll \Omega \ll \varepsilon^{-4}$

$$\hat{E}^{\mathrm{GP}} \leq E^{\mathrm{TF}} + C\omega^{4/3}|\log \varepsilon|. \tag{2.3.7}$$

Proof: To prove an upper bound to the reduced GP energy we use as trial function a regularization of the TF density defined by

$$\rho(x) = \begin{cases} \rho^{\mathrm{TF}}(x) & x_{\mathrm{in}} + \epsilon \leq x \leq x_{\mathrm{out}} - \epsilon \\ \rho^{\mathrm{TF}}(x_{\mathrm{in}} + \epsilon)\frac{(x-x_{\mathrm{in}})^2}{\epsilon^2} & x_{\mathrm{out}} - \epsilon \leq x \leq x_{\mathrm{out}} \\ \rho^{\mathrm{TF}}(x_{\mathrm{out}} - \epsilon)\frac{(x-x_{\mathrm{out}})^2}{\epsilon^2} & x_{\mathrm{in}} \leq x \leq x_{\mathrm{in}} + \epsilon \\ 0 & \text{otherwise.} \end{cases} \tag{2.3.8}$$

The norm of the trial function satisfies

$$\|\rho\|_1 \geq 1 - C\epsilon\rho^{\mathrm{TF}}(x_{\mathrm{in}} + \epsilon). \tag{2.3.9}$$

Now, a Taylor expansion of the TF density yields

$$\rho^{\mathrm{TF}}(x) = C\gamma^2\left((\varepsilon\Omega)^{2/3} - (\varepsilon\Omega)^2(x-1)^2\right)(1 + o(1)) = \\ = C\gamma^2(\varepsilon\Omega)^{2/3}(1-t^2)(1+o(1)) \tag{2.3.10}$$

with $t = (\varepsilon\Omega)^{2/3}|x-1|$. Hence, we have

$$\left|\vec{\nabla}\rho^{\mathrm{TF}}\right| = C\gamma^2(\varepsilon\Omega)^2|x-1|(1+o(1)) = C\gamma^2(\varepsilon\Omega)^{4/3}|t|(1+o(1)). \tag{2.3.11}$$

This together with (2.1.20) implies

$$|\vec{\nabla}\rho^{\mathrm{TF}}| \leq C(\varepsilon\Omega)^{4/3} \tag{2.3.12}$$

and therwith we have

$$\epsilon\rho^{\mathrm{TF}}(x_{\mathrm{in}} + \epsilon) \leq C\epsilon^2(\varepsilon\Omega)^{4/3}. \tag{2.3.13}$$

So we find for the norm of our trial function

$$\|\rho\|_1 \geq 1 - C\epsilon^2(\varepsilon\Omega)^{4/3}. \tag{2.3.14}$$

Note that in comparison the TF energy is

$$E^{\mathrm{TF}} \sim -\Omega^2 + \frac{(\varepsilon\Omega)^{2/3}}{\varepsilon^2}. \tag{2.3.15}$$

By the definition of the TF functional the potential error term to the potential TF energy is smaller than $\Omega^2\epsilon^2(\varepsilon\Omega)^{4/3}$ and this term satisfies

$$\Omega^2\epsilon^2(\varepsilon\Omega)^{4/3} \ll \frac{(\varepsilon\Omega)^{2/3}}{\varepsilon^2} \tag{2.3.16}$$

as long as $\epsilon \ll (\varepsilon\Omega)^{-4/3}$. Defining $\zeta \equiv \epsilon(\varepsilon\Omega)^{2/3}$ this condition can be written as $\zeta \ll (\varepsilon\Omega)^{-2/3}$. The upper bound to the potential error term succeeds the upper bound to the interaction error term given by $\frac{(\varepsilon\Omega)^{2/3}}{\varepsilon^2}\epsilon^2(\varepsilon\Omega)^{4/3}$, i.e.,

$$\frac{(\varepsilon\Omega)^{2/3}}{\varepsilon^2} \ll \Omega^2, \tag{2.3.17}$$

if $\Omega \gg 1/\varepsilon$, which is an assumption in our proof. Now, defining $1 - t^2 = u$ we get

$$\begin{aligned}\int_{t\in C\cdot[0,1-\epsilon]} \frac{|\vec{\nabla}\rho^{\mathrm{TF}}|^2}{\rho^{\mathrm{TF}}} = C(\varepsilon\Omega)^{4/3} \int_{t\in C\cdot[0,1-\epsilon]} \frac{t^3}{1-t^2}dt \leq \\ \leq C(\varepsilon\Omega)^{4/3} \int_{u\in C\cdot[\epsilon,1]} \frac{1-u}{u}du \leq C(\varepsilon\Omega)^{4/3}|\log\epsilon|. \end{aligned} \tag{2.3.18}$$

We have as condition for the upper bound to the kinetic energy term to be smaller than the lower order term of the TF energy,

$$(\varepsilon\Omega)^{4/3}|\log\epsilon| \ll \frac{(\varepsilon\Omega)^{2/3}}{\varepsilon^2}, \tag{2.3.19}$$

which is true as long as $\Omega \ll \varepsilon^{-4}|\log\tilde{\epsilon}|^{-1}$ for some appropriate adaption of ϵ denoted by $\tilde{\epsilon}$. More important the upper bound to the kinetic energy succeeds the error term

$$\Omega^2\epsilon^2(\varepsilon\Omega)^{4/3} \ll (\varepsilon\Omega)^{4/3}|\log\epsilon| \tag{2.3.20}$$

for an appropriate ϵ. Summarizing above estimates we get

$$\begin{aligned}\hat{E}^{\mathrm{GP}} \leq E^{\mathrm{TF}} + C(\gamma\omega)^{\frac{4}{3}}|\log\epsilon| + \mathcal{O}\left(\Omega^2\epsilon^2(\varepsilon\Omega)^{4/3}\right) + \mathcal{O}\left(\frac{(\varepsilon\Omega)^{2/3}}{\varepsilon^2}\epsilon^2(\varepsilon\Omega)\right) = \\ = E^{\mathrm{TF}} + \mathcal{O}\left((\varepsilon\Omega)^{4/3}|\log\zeta(\varepsilon\Omega)^{-2/3}|\right) + \mathcal{O}\left(\Omega^2\zeta^2\right) + \mathcal{O}\left(\frac{(\varepsilon\Omega)^{2/3}}{\varepsilon^2}\zeta^2\right). \end{aligned} \tag{2.3.21}$$

Minimizing the r.h.s. of (2.3.21) in terms of ζ yields

$$\zeta = \frac{(\varepsilon\Omega)^{2/3}}{\Omega} \ll (\varepsilon\Omega)^{-2/3} \tag{2.3.22}$$

as long as $\Omega \ll \varepsilon^{-4}$. Hence, we have proved all terms beside the TF energy terms are smaller then those of the TF energy for the regime $\varepsilon^{-1} \ll \Omega \ll \varepsilon^{-4}|\log\tilde{\epsilon}|^{-1}$ and the main contribution beyond the TF energy is estimated in (2.3.18).

□

Useful estimates on and properties of g^2

Proposition 2.3.3 (The Minimizer Achieves a Maximum at a Unique Radius.)

The minimizer achieves a maximum at the unique radius denoted by $R^{\rm GP}$.

Proof: We rewrite (2.1.11) by a variable transformation $r^2 \to k$, such that the functional $\hat{\mathcal{E}}^{\rm GP}[g]$ is

$$\pi \int_0^\infty k \left\{ |\vec{\nabla} g|^2 + \frac{1}{\varepsilon^2} g^4 + V'(k) g^2 \right\} dk, \tag{2.3.23}$$

and the normalization condition is

$$\int_0^1 g^2 dk = 1/\pi. \tag{2.3.24}$$

The variational equation (2.1.14) implies that g is not constant on any open interval (otherwise $g \equiv 0$ that contradicts the mass constraint $\|g\|_2^2 = 1$). This is a consequence of the fact that g satisfies a Lipschitz condition.

Suppose $g(x)$ has more than one local maximum. Then it has a minimum at some point $k = k_2$ with $0 < k_2 < \infty$, positioned on the right side of a maximum at $k = k_1$, i.e., $k_1 < k_2$. For $0 < \varepsilon < g^2(k_1) - g^2(k_2)$ we consider the set

$$\mathcal{I}_\varepsilon = \{k < k_2 : g^2(k_1) - \varepsilon \le g^2(k) \le g^2(k_1)\}. \tag{2.3.25}$$

Since g^2 is continuous, the function

$$F(\varepsilon) \equiv \int_{\mathcal{I}_\varepsilon} g^2 dk \tag{2.3.26}$$

is strictly positive and $F(\varepsilon) \to 0$ for $\varepsilon \to 0$. Likewise, for a $\kappa > 0$ we consider

$$\mathcal{J}_\kappa = \{k > k_1 : g^2(k_2) \le g^2(k) \le g^2(k_2) + \kappa\}. \tag{2.3.27}$$

So, the function

$$G(\kappa) \equiv \int_{\mathcal{J}_\kappa} g^2 dk \tag{2.3.28}$$

has the same properties as F. There is at least another maximum at $k = k_3$. For $0 < \delta < g^2(k_3) - g^2(k_2)$ we consider the set

$$\mathcal{K}_\delta = \{k > k_2 : g^2(k_3) - \delta \le g^2(k) \le g^2(k_3)\}. \tag{2.3.29}$$

Again since g^2 is continuous and strictly positive, the function

$$H(\varepsilon) \equiv \int_{\mathcal{K}_\delta} g^2 dk \tag{2.3.30}$$

is strictly positive as well and $F(\varepsilon) \to 0$ for $\varepsilon \to 0$.

Since g^2 is a continuous function there always exist $\overline{\delta}, \overline{\varepsilon}, \overline{\kappa} > 0$ with $g^2(k_2) + \overline{\kappa} < g^2(k_1) - \overline{\varepsilon}$ and $g^2(k_2) + \overline{\kappa} < g^2(k_3) - \overline{\delta}$. This implies that $\mathcal{I}_{\overline{\varepsilon}}$, $\mathcal{J}_{\overline{\kappa}}$ and $\mathcal{K}_{\overline{\delta}}$ are disjoint sets. Since the integrand of F, G and H is positiv and continuous, G is continuous in $\overline{\kappa}$ as well as F is continuous in $\overline{\varepsilon}$ etc., we are able to specify those parameters by the condition

$$F(\overline{\varepsilon}) = G(\overline{\kappa}) = H(\overline{\delta}). \tag{2.3.31}$$

Given any potential V with a unique minimum. Then we have $V(k_1) > V(k_2)$ or $V(k_3) > V(k_2)$. If the first case applies mass can be rearranged from k_1 to k_2, i.e., we consider the function

$$\overline{g}_1^2(k) = \begin{cases} g(k_1)^2 - \overline{\varepsilon} & \text{if } k \in \mathcal{I}_{\overline{\varepsilon}} \\ g(k_2)^2 + \overline{\kappa} & \text{if } k \in \mathcal{J}_{\overline{\kappa}} \\ g(k)^2 & \text{otherwise} \end{cases} \tag{2.3.32}$$

The energy due to the potential term V in (2.3.23) evaluated for (2.3.32) is smaller than it is for g^2. Also the mass constraint of this function equals the normalization condition (2.3.24): What we subtract from g^2 in $\mathcal{I}_{\overline{\varepsilon}}$ equals what we add to g^2 in $\mathcal{J}_{\overline{\kappa}}$, or rather $F(\overline{\varepsilon}) = G(\overline{\kappa})$. Furthermore, the kinetic energy of $\overline{g}^2$ vanishes on the sets $\mathcal{I}_{\overline{\varepsilon}}$ and $\mathcal{J}_{\overline{\kappa}}$, but doesn't differ from g^2 elsewhere. Therefore it is smaller than the kinetic energy of g^2. By the definition of $\overline{g}^2$, mass is rearranged from $\mathcal{I}_{\overline{\varepsilon}}$ to $\mathcal{J}_{\overline{\kappa}}$, where the density is lower, such that

$$\int \overline{g}^4 < \int g^4. \tag{2.3.33}$$

If we consider $V(k_3) > V(k_2)$ we have to put mass from k_3 to k_2 to lower the energy, i.e., we define a function

$$\overline{g}_2^2(k) = \begin{cases} g(k_2)^2 + \overline{\kappa} & \text{if } k \in \mathcal{J}_{\overline{\kappa}} \\ g(k_2)^2 - \overline{\delta} & \text{if } k \in \mathcal{K}_{\overline{\delta}} \\ g(k)^2 & \text{otherwise} \end{cases} \tag{2.3.34}$$

We find that the energy due to the potential term V in (2.3.23) evaluated for (2.3.34) is smaller than it is for g^2. The arguementation in the previous case for the kinetic energy and the interaction term can be applied straightforewardly to this case, which leads us to the following conclution.

The functional evaluated for $\overline{g}_\star^2$ ($\star = 1, 2$) is strictly smaller. This contradicts the assumption that g^2 is the minimizer. Therefore by the construction $\overline{g}_\star^2$ the minimizer g has only one maximum.

□

Proposition 2.3.4 (Difference between the chemical potentials μ and μ^{TF}) *The difference between the chemical potentials can be estimated by*

$$|\mu - \mu^{\mathrm{TF}}| \leq C\Omega |\log \varepsilon|^{1/2} + C\omega^{\frac{4}{3}} |\log \varepsilon|. \tag{2.3.35}$$

Proof: For the sake of brevity we define $A \equiv C\omega^{\frac{4}{3}}|\log\varepsilon|$. By the definition of the TF functional (2.1.16), the TF density (2.1.18), the chemical potential μ^{TF} (2.1.19) and the upper bound for $\hat{E}^{\mathrm{GP}}$ we find the estimate

$$\begin{aligned}\int_{\mathbb{R}^2} d\vec{x}x(g^2-\rho^{\mathrm{TF}})^2 &= \|g\|_4^4 + \|\rho^{\mathrm{TF}}\|_2^2 - 2\int_{\mathbb{R}^2} d\vec{x}g^2\rho^{\mathrm{TF}} \leq \\ &\|g\|_4^4 - (\gamma\varepsilon\Omega)^2\int_{\mathbb{R}^2} d\vec{x}x^2g^2 + \int_{\mathbb{R}^2} d\vec{x}\cdot\frac{2}{s}x^sg^2 + \|\rho^{\mathrm{TF}}\|_2^2 - \varepsilon^2\mu^{\mathrm{TF}} \leq \\ &\leq \varepsilon^2\left(\mathcal{E}^{\mathrm{TF}}[g^2] - E^{\mathrm{TF}}\right) \leq \varepsilon^2\left(\hat{E}^{\mathrm{GP}} - E^{\mathrm{TF}}\right) \equiv \varepsilon^2 A, \quad (2.3.36)\end{aligned}$$

where we used an abberivation in the last step. Using Cauchy-Schwarz inequality, the trivial bound $\|\rho^{\mathrm{TF}}\|_2^2 \leq \|\rho^{\mathrm{TF}}\|_\infty = \rho^{\mathrm{TF}}(1)$ yields

$$\|g\|_4^4 - \|\rho^{\mathrm{TF}}\|_2^2 = 2\int_{\mathbb{R}^2} d\vec{x}\rho^{\mathrm{TF}}(g^2-\rho^{\mathrm{TF}}) + \int_{\mathbb{R}^2} d\vec{x}(g^2-\rho^{\mathrm{TF}})^2 \leq C\varepsilon\left(\rho^{\mathrm{TF}}(1)A\right)^{1/2} + \varepsilon^2 A. \quad (2.3.37)$$

As a consequence we get an estimate for the difference between the chemical potentials μ^{TF} and μ,

$$\varepsilon^2\left|\mu-\mu^{\mathrm{TF}}\right| = \varepsilon^2\left(\hat{E}^{\mathrm{GP}} - E^{\mathrm{TF}}\right) + \|g\|_4^4 - \|\rho^{\mathrm{TF}}\|_2^2 \leq C\varepsilon\left(\rho^{\mathrm{TF}}(1)A\right)^{1/2} + \varepsilon^2 A. \quad (2.3.38)$$

Using $\rho^{\mathrm{TF}}(1) \leq C\omega^{\frac{2}{3}}$ yields the result.

□

Proposition 2.3.5 (Pointwise Estimate for $g(x)^2$ on $\mathcal{A}^{\mathrm{TF}}$)
Suppose $\varepsilon \to 0$ then for

$$\vec{x} \in \mathcal{A}^{\mathrm{TF}} \equiv \{\vec{x} : x \in [x_{\mathrm{in}} + \max[C\Omega^{-1/2}, \varepsilon^{1/3}\omega^{-5/9}], x_{\mathrm{out}} - \max[C\Omega^{-1/2}, \varepsilon^{1/3}\omega^{-5/9}]]\} \quad (2.3.39)$$

we have

$$|g(x)^2 - \rho^{\mathrm{TF}}(x)| \leq \rho^{\mathrm{TF}}(x)o(1). \quad (2.3.40)$$

Proof: At first we rewrite the variational equation (2.1.14) for the minimizer g as

$$-\Delta g = \frac{2}{\varepsilon^2}\left[\tilde{\rho}(x) - g^2\right]g \quad (2.3.41)$$

with the density

$$\tilde{\rho}(x) \equiv \frac{\varepsilon^2}{2}\left(\mu - \Omega^2\left(\frac{2x^s}{s} - x^2\right)\right). \quad (2.3.42)$$

An important fact is that above function differs from the TF density only by its chemical potential.

Now we determine the set where $\tilde{\rho} = \rho^{\mathrm{TF}}(1 \pm o(1))$: One finds by the estimate to the difference between the chemical potentials (2.3.35)

$$\|\tilde{\rho}(x) - \rho^{\mathrm{TF}}\|_\infty \leq C\varepsilon^2\Omega|\log\varepsilon|^{1/2}, \quad (2.3.43)$$

By a simple Taylor approximation of the density we determine the set of $\vec{x}$ such that the difference of the chemical potentials is beyond the first order by $x \in [x_{\text{in}} + C\Omega^{-1/2}, x_{\text{out}} - C\Omega^{-1/2}]$ and denote it as $\mathcal{A}$. Moreover, we split this set into the part defined by the property $x \leq 1$ denoted by $\mathcal{A}_<$ and the complement $\mathcal{A}_>$ with the property $x > 1$.

The following strategy in this proof is to find pointwise estimates to g^2 on $\mathcal{A}$ by providing suitable super- and subsolutions inside a local interval $x \in [x_0 - \kappa, x_0 + \kappa]$ where $\tilde{x}_{\text{in}} + \kappa < x_0 < \tilde{x}_{\text{out}} - \kappa$ with $\kappa \geq 0$ and $\tilde{x}_{\text{in}}$ denoting the inner radius of the set $\mathcal{A}$ and $\tilde{x}_{\text{out}}$ the outer radius. We refer to [107] chapter 9.3 for the justification of the method of sub- and supersolutions.

As candidate for the supersolution on $\mathcal{A}_<$ we consider a function of the form

$$W(x) = \\ = \sqrt{\tilde{\rho}(x_0+\kappa)} \coth\left[\coth^{-1}\left(\sqrt{\frac{\tilde{\rho}(1)}{\tilde{\rho}(x_0+\kappa)}}\right) + \frac{\kappa^2 - |x-x_0|^2}{3\kappa\varepsilon}\sqrt{2\tilde{\rho}(x_0+\kappa)}\right]. \quad (2.3.44)$$

As it was shown in [108] one has

$$-\Delta W \geq \frac{2}{\varepsilon^2}\left(\tilde{\rho}(x_0+\kappa) - W^2\right) W \geq \frac{2}{\varepsilon^2}\left(\tilde{\rho}(x_0) - W^2\right) W, \quad (2.3.45)$$

for any $x \in [x_0 - \kappa, x_0 + \kappa]$, because $\tilde{\rho}(x)$ is an increasing function in x for $x \leq 1$. Note that the proof for the domain $\mathcal{A}_>$ is very similar, with the important distinction that $\tilde{\rho}(x)$ is an decreasing function in x. Thus, the candidate for the subsolution (2.3.44) has to be adapted by $\kappa \to -\kappa$. For the sake of brevity we turn again to the case $\mathcal{A}_<$ and make notes on the other case when it is necessary. At the boundary of the interval the function (2.3.44) coincides with the density $\tilde{\rho}(x)$, i.e, $W(x_0 - \kappa) = W(x_0 + \kappa) = \sqrt{\tilde{\rho}(1)} \geq \sqrt{\tilde{\rho}(R^{\text{GP}}/R = x^{\text{GP}})}$, which is larger than $g(x^{\text{GP}})$. Hence W is a supersolution to g and by the maximum principle we have

$$g(x_0) \leq W(x_0) \leq \sqrt{\tilde{\rho}(x_0+\kappa)} \coth\left[\frac{\kappa}{3\varepsilon}\sqrt{2\tilde{\rho}(x_0+\kappa)}\right], \quad (2.3.46)$$

where we have used the fact that $\coth(x)$ is a nonincreasing function. Above inequality can be written as

$$g(x_0) \leq W(x_0) \leq \sqrt{\tilde{\rho}(x_0)}\left(1 + \frac{|\tilde{\rho}(x_0+\kappa) - \tilde{\rho}(x_0)|}{\tilde{\rho}(x_0)}\right) \coth\left[\frac{\kappa}{3\varepsilon}\sqrt{2\tilde{\rho}(x_0+\kappa)}\right]. \quad (2.3.47)$$

When the argument in $\coth(x)$ tends to infinity one has

$$\coth(x) = \frac{1+e^{-2x}}{1-e^{-2x}} \leq (1 + Ce^{-2x}) \quad (2.3.48)$$

The argument of coth in our formula (2.3.47) tends to infinity if the condition

$$\frac{\kappa}{\varepsilon}\sqrt{\tilde{\rho}(x_0+\kappa)} \gg 1 \quad (2.3.49)$$

is satisfied. Assuming that is the case we have

$$g(x_0) \leq \sqrt{\tilde{\rho}(x_0)} \left(1 + \frac{|\tilde{\rho}(x_0+\kappa) - \tilde{\rho}(x_0)|}{\tilde{\rho}(x_0)}\right)(1+o(1))\,. \tag{2.3.50}$$

To estimate the second term in the first brackets of the r.h.s. of (2.3.50) we use

$$|(\tilde{\rho}(x+\kappa) - \tilde{\rho}(x))| = C\kappa\omega^{4/3} \tag{2.3.51}$$

This together with (2.3.43) implies

$$\frac{|(\tilde{\rho}(x+\kappa) - \tilde{\rho}(x))|}{\tilde{\rho}(x)} \leq C\kappa\frac{\omega^{4/3}}{\tilde{\rho}(x)} \ll 1 \tag{2.3.52}$$

To fulfill both conditions $\tilde{\rho} \gg \left(\varepsilon\omega^{4/3}\right)^{2/3}$. We summarize our finding by stating the result

$$g(x) \leq \sqrt{\tilde{\rho}(x)}\,(1+o(1))\,. \tag{2.3.53}$$

for any $x \in [x_0 - \kappa, x_0 + \kappa]$. To cover the whole set $\mathcal{A}$ we extend the estimate to $\tilde{x}_{\text{in}} \leq x \leq \tilde{x}_{\text{out}}$ with the help of the formula (2.3.52).

As before we fix some x_0 in a interval $\tilde{x}_{\text{in}} + \delta \leq x_0 \leq \tilde{x}_{\text{out}} - \delta$. Since $\tilde{\rho}(x)$ is an increasing function for $x \leq 1$ and g is positive,

$$-\Delta g \geq \frac{2}{\varepsilon^2}\left[\tilde{\rho}(x_0 - \delta) - g^2\right] g. \tag{2.3.54}$$

for any $x \in [x_0 - \delta, x_0 + \delta]$. We find a subsolution by imposing a Dirichlet boundary condition to the same problem on the boundary $\partial\mathcal{B}_1$. In [109] it was proven that there is a unique positive function h satisfying

$$\begin{cases} -\Delta h = 1/\tilde{\varepsilon}^2[1-h^2]h & \text{in } \Omega \\ h = 0 & \text{on } \partial\Omega \end{cases} \tag{2.3.55}$$

as $\tilde{\varepsilon} \to 0$ and it is stated that $h \leq 1$. In particular, if we consider the domain $\Omega = \mathcal{B}_1$, it follows from the uniqueness of the positive solution h, that it is radially symmetric. In [110] it was proven that there is a lower bound to h, namely

$$1 - C\exp\left\{-\frac{\text{dist}(r, \partial\Omega)}{2\tilde{\varepsilon}}\right\} \leq h. \tag{2.3.56}$$

This implies for our problem with $\Omega = \mathcal{B}_1$

$$1 - C\exp\left\{-\frac{1-x^2}{2\tilde{\varepsilon}}\right\} \leq h(x) \leq 1. \tag{2.3.57}$$

If we now define

$$\tilde{h}(x) \equiv \sqrt{\tilde{\rho}(x_0 - \delta)}h\left(\frac{x - x_0}{\delta}\right) \tag{2.3.58}$$

and

$$\tilde{\varepsilon} \equiv \frac{\varepsilon}{\delta\sqrt{2\tilde{\rho}(x_0-\delta)}}, \tag{2.3.59}$$

then for any $\vec{x} \in \mathcal{B}(x_0-\delta, x_0+\delta)$ the function $\tilde{h}$ solves

$$-\Delta\tilde{h} = \frac{2}{\varepsilon^2}\left[\tilde{\rho}(x_0-\delta) - \tilde{h}^2\right]\tilde{h}, \tag{2.3.60}$$

with Dirichlet conditions at the boundary $x = x_0 \pm \delta$. Therefore, $\tilde{h}$ is a subsolution for the problem (2.3.41) and the maximum principle states $g(x) \geq \tilde{h}(x)$: By (2.3.52) with a similar condition as on κ but now for δ we have

$$g(x_0) \geq \tilde{h}(x_0) \geq \sqrt{\tilde{\rho}(x_0)}\left[1 - C\exp\left(-\frac{1}{2\tilde{\varepsilon}}\right)\right](1+o(1)) \tag{2.3.61}$$

for any x_0 such that $\tilde{x}_{\text{in}} + \delta \leq x_0 \leq 1-\delta$ and find the condition

$$\tilde{\varepsilon} \ll 1, \tag{2.3.62}$$

which is the analogon to (2.3.49) in the proof of the upper bound to get

$$g(x_0) \geq \sqrt{\tilde{\rho}(x_0)}\,(1+o(1))\,. \tag{2.3.63}$$

The proof for the case $\mathcal{A}_>$ can be done analogously but with $\delta \to -\delta$. To extend (2.3.63) to the boundaries we use (2.3.52).

□

Proposition 2.3.6 (Exponential Smallness of the Minimizer)
Suppose that $\varepsilon \to 0$ and $\varepsilon^{-1} \ll \Omega$, then on the set

$$\mathcal{T} \equiv \{\vec{x} \in \mathbb{R}^2 : x^2 \leq x_{\text{in}}^2 - \Omega^{-1/2}\varepsilon^{1/2}|\log\varepsilon|\}, \tag{2.3.64}$$

the minimizer g satisfies

$$g^2(x) \leq Cg^2(x^{\text{GP}})\exp\left\{-\frac{x_{\text{in}}^2 - x^2}{\Omega^{-1/2}\varepsilon|\log\varepsilon|}\right\}. \tag{2.3.65}$$

Proof: As starting point we take the inequality $-\Delta(g^2) \leq -2g\Delta g$, and insert the variational equation for g (2.1.14) to obtain

$$-\Delta(g^2) \leq \frac{2}{\varepsilon^2}\left(\frac{\varepsilon^2}{2}\left(\mu - \Omega^2\left(\frac{2x^s}{s} - x^2\right)\right) - g^2\right)g^2. \tag{2.3.66}$$

Now we rewrite this inequality as

$$-\Delta(g^2) \leq \frac{2}{\varepsilon^2}\left(\rho^{\text{TF}}(x) + \varepsilon^2\left(\mu - \mu^{\text{TF}}\right) - g^2\right)g^2 \tag{2.3.67}$$

In the following we consider the set defined by

$$\mathcal{T} \equiv \{\vec{x} \in \mathbb{R}^2_1 : x^2 \leq x_{\rm in}^2 - z^2\}, \tag{2.3.68}$$

and find on this set by the estimate of the difference between the chemical potentials (2.3.35)

$$\rho^{\rm TF}(x) + \varepsilon^2 \left(\mu - \mu^{\rm TF}\right) \leq -C\omega^2 \cdot z^2 + C\varepsilon^2\Omega|\log\varepsilon|^{1/2} \leq -C\omega^2 \cdot z^2 \tag{2.3.69}$$

for $z^2 \gg \Omega^{-1}|\log\varepsilon|^{1/2}$. Combining (2.3.67) and (2.3.69) we find the following differential equation

$$-\Delta(g^2) + \frac{C}{\varepsilon^2}\omega^2 z^2 g^2 \leq 0. \tag{2.3.70}$$

Now we consider the function

$$W(x) = \exp\left\{-\frac{x_{\rm in}^2 - x^2}{f}\right\}, \tag{2.3.71}$$

For $z^2 \gg f$ the function W is small on the boundary $\partial\mathcal{T}$. Exponential smallness requires that

$$\frac{z^2}{f} \equiv \left(\frac{1}{\varepsilon}\right)^{\alpha} \tag{2.3.72}$$

with $\alpha > 0$. For any $x \leq x_{\rm in}$ the function (2.3.71) satisfies

$$-\Delta W + \frac{C}{\varepsilon^2}\omega^2 z^2 \cdot W \geq W\left(-C\left(\frac{4x_{\rm in}^2}{f^2} + \frac{2}{f}\right) + \frac{C}{\varepsilon^2}\omega^2 z^2\right) \geq 0 \tag{2.3.73}$$

for any

$$z \gg \frac{C}{f\Omega} \tag{2.3.74}$$

We choose $z = \Omega^{-1/4}\varepsilon^{1/4}|\log\varepsilon|^{1/2}$. If we multiply W by $g(x)^2$ we obtain a supersolution to the solution of (2.3.70), i.e.,

$$g(x)^2 \leq Cg(x^{\rm GP})^2 W(x), \tag{2.3.75}$$

for any $x^2 \leq x_{\rm in}^2 - z^2$.

□

2.3.1 Estimates on the Ginzburg-Landau Functional for $1/\varepsilon \ll \Omega$

Theorem 2.3.1 (Lower Bound to the GL functional)
For $\varepsilon^{-1} \ll \Omega \ll \varepsilon^{-4}$ as $\varepsilon \to 0$ we have

$$\mathcal{F}_g[u] \geq (1 - o(1))\,\frac{\Omega|\log\left(\varepsilon^2\Omega/\rho\right)|}{2} \tag{2.3.76}$$

with $\rho \sim (\varepsilon\Omega)^{2/3}$.

Proof: To deal with the dependence of (2.3.2) on $g^2(x)$ we decompose the integration domain into small cells: Let $\hat{\mathcal{L}}$ be the lattice

$$\hat{\mathcal{L}} = \left\{ \vec{x}_i = (m\hat{l}, n\hat{l}), m, n \in \mathbb{Z} | \mathcal{Q}_i \subset \mathcal{A}^{\mathrm{TF}} \right\} \tag{2.3.77}$$

where $\mathcal{Q}_i$ denotes the lattice cell centered at $\vec{x}_i \in \hat{\mathcal{L}}$ and the lattice constant satisfies

$$\sqrt{\frac{|\log \varepsilon|}{\Omega}} \ll \hat{l} \ll C\omega^{-1/3}. \tag{2.3.78}$$

By reducing the integration domain to $\mathcal{A}^{\mathrm{TF}}$ and with the help of (2.3.40) we obtain

$$\begin{aligned} \mathcal{F}_g[u] &\geq \int_{\mathcal{A}^{\mathrm{TF}}} d\vec{x} \left\{ \frac{1}{\varepsilon^2} g^4 \left(1 - |u|^2\right)^2 + \left| \left(\vec{\nabla} - i\vec{A}\right) u \right|^2 g^2 \right\} = \\ &= \sum_{\vec{x}_i \in \hat{\mathcal{L}}} \int_{\mathcal{Q}_i} d\vec{x} \rho^{\mathrm{TF}}(x) \left\{ \frac{1}{\varepsilon^2} g^2 \left(1 - |u|^2\right)^2 + \left| \left(\vec{\nabla} - i\vec{A}\right) u \right|^2 \right\} (1 - o(1)) = \\ &= \sum_{\vec{x}_i \in \hat{\mathcal{L}}} \rho^{\mathrm{TF}}(x_i) \mathcal{E}'^{(i)}[u](1 - o(1)). \end{aligned} \tag{2.3.79}$$

In the last step we have defined the functional

$$\mathcal{E}'^{(i)}[u] \equiv \int_{\mathcal{Q}_i} d\vec{x} \left\{ \frac{1}{\varepsilon^2} g^2 \left(1 - |u|^2\right)^2 + \left| \left(\vec{\nabla} - i\vec{A}\right) u \right|^2 \right\}. \tag{2.3.80}$$

As above we can exchange g^2 with ρ^{TF} and a remainder by the pointwise bound (2.3.40),

$$\begin{aligned} \mathcal{E}'^{(i)}[u] \equiv \int_{\mathcal{Q}_i} d\vec{x} \left\{ \frac{1}{\varepsilon^2} \rho^{\mathrm{TF}} \left(1 - |u|^2\right)^2 + \left| \left(\vec{\nabla} - i\vec{A}\right) u \right|^2 \right\} (1 - o(1)) \equiv \\ \equiv \mathcal{E}^{(i)}[u](1 - o(1)). \end{aligned} \tag{2.3.81}$$

Proposition 2.3.7 (Lower Bound inside cells)
If $\varepsilon^{-1} \ll \Omega \ll \varepsilon^{-4}$ as $\varepsilon \to 0$, it is possible to find a $\hat{l}$ satisfying (2.3.78) *such that*

$$\mathcal{E}^{(i)}[u] \geq (1 - o(1)) \frac{\Omega \hat{l}^2 |\log\left(\varepsilon^2 \Omega/\rho\right)|}{2} \tag{2.3.82}$$

with $\rho \sim (\varepsilon\Omega)^{2/3}$.

Proof: As in [111] the strategy is to rescale the cells $\mathcal{Q}_i$ in such a way that we consider the minimization of a GL functional in a different regime. For this purpose we set $\vec{s} \equiv \hat{l}^{-1}(\vec{x} - \vec{x}_i)$,

$$\tilde{u}(\vec{s}) \equiv \overline{u}(\vec{x}_i + \hat{l}\vec{s}) \qquad \vec{B}(\vec{s}) \equiv \hat{l}\vec{A}'(\vec{x}_i + \hat{l}\vec{s}) \tag{2.3.83}$$

In those coordinates (2.3.81) is

$$\mathcal{E}^{(i)}[u] = \tilde{\mathcal{E}}^{(i)}[\tilde{u}] \equiv \int_{\mathcal{Q}_1} d\vec{s} \left\{ \frac{1}{\varepsilon^2} \rho^{\mathrm{TF}}(x_i) \hat{l}^2 \left(1 - |\tilde{u}|^2\right)^2 + \left| \left(\vec{\nabla} - i\vec{B}\right) \tilde{u} \right|^2 \right\}. \tag{2.3.84}$$

with $\mathcal{Q}_1$ being an unitary square centered at the origin. Note that the rescaled vector potential $\vec{B}$ is explicitly given by

$$\vec{B}(\vec{s}) = \frac{\Omega \hat{l} \vec{e}_z \wedge \vec{x}_i}{2} + \frac{\Omega \hat{l}^2 \vec{e}_z \wedge \vec{s}}{2}, \tag{2.3.85}$$

and the corresponding magnetic field is

$$\tilde{h} \equiv \mathrm{curl}\vec{B} = \Omega \hat{l}^2. \tag{2.3.86}$$

Our concern is the minimization of (2.3.84). By gauge invariance one can simplify the functional to

$$\inf_{\tilde{u} \in H^1(\mathcal{Q}_1)} \tilde{\mathcal{E}}^{(i)}[\tilde{u}] \geq \inf_{\tilde{u} \in H^1(\mathcal{Q}_1)} \int_{\mathcal{Q}_1} d\vec{s} \left\{ \frac{1}{\varepsilon^2} \rho^{\mathrm{TF}}(x_i) \hat{l}^2 (1 - |\tilde{u}|^2)^2 + \left| \left(\vec{\nabla} - i\hat{l}^2 \vec{A} \right) \tilde{u} \right|^2 \right\}. \tag{2.3.87}$$

We now introduce a new infinitesimal parameter ϵ defined as

$$\epsilon \equiv \frac{\varepsilon}{\hat{l}\sqrt{\rho^{\mathrm{TF}}(x_i)}} \ll 1. \tag{2.3.88}$$

It follows that

$$\mathcal{E}^{(i)}[u] \geq \inf_{\tilde{u} \in H^1(\mathcal{Q}_1)} \int_{\mathcal{Q}_1} \mathrm{d}\vec{s} \left\{ \left| \left(\nabla - \frac{i\tilde{h}_{\mathrm{ex}} \vec{e}_z \wedge \vec{s}}{2} \right) \tilde{u} \right|^2 + \frac{1}{\epsilon^2} \left(1 - |\tilde{u}|^2 \right)^2 \right\}, \tag{2.3.89}$$

for a magnetic field $\tilde{h}_{\mathrm{ex}}$ satisfying the conditions

$$|\log \epsilon| \ll \tilde{h}_{\mathrm{ex}} \equiv \Omega \hat{l}^2 \ll \frac{1}{\epsilon^2} \equiv \frac{\rho^{\mathrm{TF}} \hat{l}^2}{\varepsilon^2}. \tag{2.3.90}$$

The upper bound on the r.h.s. of (2.3.90) implies the condition

$$\rho^{\mathrm{TF}} \gg \varepsilon^2 \Omega. \tag{2.3.91}$$

Additionally, to ensure that the cell size is much smaller than the width of the annulus the condition

$$\hat{l} \ll g^{-2} \sim \omega^{-2/3} \tag{2.3.92}$$

has to be satisfied. The upper bound of the first condition,i.e.,

$$|\log \epsilon| \ll \Omega l^2 \ll \epsilon^{-2} \equiv \frac{l^2 g^2}{\varepsilon^2} \tag{2.3.93}$$

is satisfied as long as

$$\Omega \ll \varepsilon^{-4} \tag{2.3.94}$$

The lower bound is simultaneously fulfilled as long as $\epsilon \to 0$. The second upper bound (2.3.92) enforces as estimate for the quantity Ωl^2

$$\Omega l^2 \lesssim \frac{\Omega}{\omega^{4/3}} (\varepsilon^4 \Omega)^{\alpha} \tag{2.3.95}$$

for some $\alpha \geq 0$ and with the help of (2.3.94). The lower bound in (2.3.90) can be satisfied simultaneously as long as

$$|\log(\varepsilon^4\Omega)| \ll (\varepsilon^4\Omega)^{\alpha-\frac{1}{3}}, \tag{2.3.96}$$

where we assumed $|\log\epsilon| \sim \log(\varepsilon^4\Omega)|$. This is always fulfilled as long as $0 < \alpha < 1/3$, because

$$|\log x| \ll x^{-\alpha}. \tag{2.3.97}$$

For our proof of the lower bound we need that the condition

$$\hat{l}\sqrt{\rho^{\mathrm{TF}}(x_i)} \ll 1, \tag{2.3.98}$$

holds, but this is satisfied as a consequence of (2.3.92). (Note that we have $1/\sqrt{\rho^{\mathrm{TF}}} \geq C\omega^{-1/3}$). Hence

$$\Omega\hat{l}^2 \geq |\log\varepsilon| \geq |\log\epsilon|, \tag{2.3.99}$$

because $0 \geq \log\epsilon = \log\varepsilon - \log\left(\hat{l}\sqrt{\rho^{\mathrm{TF}}(x_i)}\right)$, which implies $\log\epsilon \geq \log\varepsilon$ and $|\log\epsilon| \leq |\log\varepsilon|$.
The functional on the right hand side of (2.3.89) is precisely the GL functional on $\mathcal{Q}_1$ with external magnetic field $\tilde{h}_{\mathrm{ex}}\vec{e}_z$ and parameter ϵ, i.e.,

$$\tilde{\mathcal{E}}^{\mathrm{GL}}\left[\tilde{u},\vec{A}\right] \equiv \int_{\mathcal{Q}_1} \mathrm{d}\vec{s}\,\left\{\left|\left(\nabla - i\vec{A}\right)\tilde{u}\right|^2 + \left|\mathrm{curl}\vec{A}' - \tilde{h}_{\mathrm{ex}}\vec{e}_z\right|^2 + \epsilon^{-2}\left(1-|\tilde{u}|^2\right)^2\right\}, \tag{2.3.100}$$

evaluated on the configuration

$$\left(\tilde{u}\,,\vec{A}'\right) = \left(u\,,\tilde{h}_{\mathrm{ex}}(\epsilon)\vec{e}_z \wedge \vec{s}/2\right) \tag{2.3.101}$$

and (2.3.90) corresponds to the GL regime where the external magnetic field is between the first and the second critical fields. We can thus apply the lower bound for the GL functional proven in [112], Theorem 1.1 (note that in the definition of the GL functional given in [112] there is overall factor 1/2), to get

$$\begin{aligned}\mathcal{E}^{(i)}[u] \geq (1-o(1))\tilde{h}_{\mathrm{ex}}\log\frac{1}{\epsilon\sqrt{\tilde{h}_{\mathrm{ex}}}} = (1-o(1))\frac{\Omega\hat{l}^2}{2}\log\frac{\rho^{\mathrm{TF}}(x_i)}{\varepsilon^2\Omega} \geq \\ \geq (1-o(1))\,\frac{\Omega\hat{l}^2|\log\left(\varepsilon^2\Omega/\rho\right)|}{2}\end{aligned} \tag{2.3.102}$$

with $\rho \sim (\varepsilon\Omega)^{2/3}$ beeing the order of magnitude of the TF density ρ^{TF}.

□

We note that the normalization of ρ^{TF} over the set where $\rho^{\mathrm{TF}}(x_i) \gg \varepsilon^2\Omega$ holds is $1-o(1)$ if $\Omega \ll \varepsilon^{-4}$.

Collecting the lower bounds inside all cells proven in the proposition above, we have

$$\tilde{\mathcal{E}}^{\mathrm{GP}}[u] \geq (1-o(1))\,\frac{\Omega\hat{l}^2|\log(\varepsilon^2\Omega/\rho)|}{2}\sum_{\vec{x}_i\in\mathcal{L}}\rho^{\mathrm{TF}}(x_i)(1-o(1)). \tag{2.3.103}$$

To replace the Riemann sum by the integral we use the symmetry of the lattice cell and the L^1-normalization of ρ^{TF},

$$\sum_{\vec{x}_i\in\mathcal{L}}\rho^{\mathrm{TF}}(x_i) \geq \frac{1}{\hat{l}^2}\left(\int_{\cup_i\mathcal{Q}^i}\mathrm{d}\vec{x}\,\rho^{\mathrm{TF}}(x) - C\max[\hat{l},\omega\hat{l}]\right) \geq \frac{(1-o(1))}{\hat{l}^2}. \tag{2.3.104}$$

□

Theorem 2.3.2 (Upper Bound to the GL **functional)**
For $\varepsilon^{-1}\ll\Omega\ll\varepsilon^{-4}$ as $\varepsilon\to 0$ we have

$$\mathcal{F}_g[u] \leq (1+o(1))\,\frac{\Omega|\log(\varepsilon^2\Omega/\rho)|}{2}. \tag{2.3.105}$$

with $\rho\sim\omega^{2/3}$.

Proof: We start with the trial function for the rescaled GL functional $\mathcal{F}_g[u]$: Similarily to [111] we decompose the support of our trial function $\mathbb{R}^2$ into cells $\mathcal{Q}^i$ whose centers $\vec{x}_i$ are arranged in a regular lattice denoted by $\mathcal{L}$. The lattice constant l is choosen such that each cells area is

$$|Q^i| = 2\pi\cdot\Omega^{-1}. \tag{2.3.106}$$

and the lattice constant is given by

$$l = (const.)\Omega^{-1/2}. \tag{2.3.107}$$

Hence, as in [111] the total number of cells in the unit disc $\mathcal{B}_1$ is

$$N = \frac{\Omega}{2}\left(1+o(1)\right). \tag{2.3.108}$$

Now, since the area of support for the TF density is $\sim\omega^{\frac{2}{3}}$ the total number of lattice points inside $\mathrm{supp}\left(\rho^{\mathrm{TF}}\right)$ is given by

$$N^{\mathrm{TF}} = N\cdot\omega^{-\frac{2}{3}}. \tag{2.3.109}$$

The position vector $\vec{x}\in\mathbb{R}^2$ can also be considered as a complex number $\zeta = x+iy\in\mathbb{C}$. Hence, we define a phase function by

$$v(\vec{x}) \equiv \prod_{\zeta_i\in\mathcal{L}}\frac{\zeta-\zeta_i}{|\zeta-\zeta_i|}. \tag{2.3.110}$$

To avoid singularities at the lattice points in the trial function we multiply v with a function defined as

$$\xi(\vec{x}) \equiv \begin{cases} 1 & \text{if} \quad |\zeta - \zeta_i| > t \quad \text{for all } i \\ t^{-1}|\zeta - \zeta_i| & \text{if} \quad |\zeta - \zeta_i| \leq t \end{cases} \tag{2.3.111}$$

where t is a variational parameter. Thus, we choose our trial function for the upper bound to (2.3.2) to be

$$h = \xi v. \tag{2.3.112}$$

Proposition 2.3.8 (Vortex Kinetic Energy)
For $\varepsilon \to 0$ and $\Omega \ll \varepsilon^{-4}$ we have

$$\int_{\mathbb{R}^2} g^2 |(\vec{\nabla} - i\vec{A})u|^2 \leq (1 + o(1)) \frac{\Omega |\log (t^2 \Omega)|}{2} \tag{2.3.113}$$

Proof: Since v is a phase and ξ real-valued we obtain

$$\int_{\mathbb{R}^2} g^2 |(\vec{\nabla} - i\vec{A})v\xi|^2 = \sum_i \int_{|\zeta - \zeta_i| \leq t} g^2 |\vec{\nabla}(\xi)v|^2 + \int_{\mathbb{R}^2} g^2 |i\xi\vec{\nabla}(v) - i\vec{A}\xi v|^2 =$$
$$= \sum_i \int_{|\zeta - \zeta_i| \leq t} g^2 |\vec{\nabla}\xi|^2 + \int_{\mathbb{R}^2} g^2 |\xi \vec{E}|^2. \tag{2.3.114}$$

We turn to the first term in (2.3.114). By definition we have $|\vec{\nabla}\xi| = t^{-1}$ inside each vortex disc $\mathcal{B}_t^i$ and the gradient is zero in the complement. Inserting the estimate $g^2(x) \leq \rho^{\mathrm{TF}}(x)(1 + o(1))$ inside $\mathcal{A}^{\mathrm{TF}}$, we obtain for the first term on the r.h.s. in (2.3.114) the estimate

$$\|g\vec{\nabla}\xi\|_2^2 \leq C/t^2 \sum_i \int_{\mathcal{B}_t^i \cap \mathcal{A}^{\mathrm{TF}}} \rho^{\mathrm{TF}}(x) \, (1 + o(1)) + \text{remainder}. \tag{2.3.115}$$

The remainder in (2.3.115) is inside $\mathcal{T}$ exponential small, because g^2 satisfies on this set (2.3.65). The area of the remaining set $\mathbb{R}^2 \backslash \{\mathcal{A}^{\mathrm{TF}} \cup \mathcal{T}\} \equiv \mathcal{W}$ is

$$A_{\mathcal{W}} \leq C\varepsilon^{1/3} \tag{2.3.116}$$

and the number of vortices in $\mathcal{W}$ satisfies

$$N_{\mathcal{W}} \leq CN \cdot \varepsilon^{1/3}. \tag{2.3.117}$$

Hence, we find for the remainder in (2.3.115) by Cauchy-Schwarz inequality and using $g^2 \leq C\omega^{2/3}$

$$\text{remainder} \leq C\omega^{2/3}\Omega^{1/2}\varepsilon^{1/6}. \tag{2.3.118}$$

By the number of vortices in the support of ρ^{TF}, i.e., N^{TF} and $\|\rho^{\mathrm{TF}}\|_{L_1(\mathcal{A}^{\mathrm{TF}})} = 1 - o(1)$ we find argueing as we did for the remainder

$$\frac{C}{t^2} \sum_i \int_{\mathcal{B}_t^i \cap \mathcal{A}^{\mathrm{TF}}} \rho^{\mathrm{TF}}(x) \, (1 + o(1)) \leq C\omega^{1/3}\Omega^{1/2}. \tag{2.3.119}$$

Next, we turn to the second term in (2.3.114). We use the property that g^2 is close to $\rho^{\rm TF}$ in $\mathcal{A}^{\rm TF}$, i.e., $g^2/\rho^{\rm TF} \leq (1+o(1))$ justified by the pointwise bound (2.3.40) to find

$$\begin{aligned}\int_{\mathbb{R}^2\setminus\mathcal{A}^{\rm TF}} d\vec{x} g^2(x)\xi^2(x)|\vec{E}(\vec{x})|^2 + \int_{\mathcal{A}^{\rm TF}} d\vec{x}\frac{g^2}{\rho^{\rm TF}}(x)\cdot\rho^{\rm TF}(x)\xi^2(x)|\vec{E}(\vec{x})|^2 \leq \\ \leq \int_{\mathbb{R}^2\setminus\mathcal{A}^{\rm TF}} d\vec{x} g^2(x)\xi^2(x)|\vec{E}(\vec{x})|^2 + \int_{\mathcal{A}^{\rm TF}} d\vec{x}\rho^{\rm TF}(x)\xi^2(x)|\vec{E}(\vec{x})|^2\cdot(1+o(1)) \leq \\ \leq \int_{\mathbb{R}^2\setminus\mathcal{A}^{\rm TF}} d\vec{x} g^2(x)\xi^2(x)|\vec{E}(\vec{x})|^2 + \\ + \left(1+\mathcal{O}((t^2\Omega)^{1/2})\right)\sum_i \sup_{\vec{r}\in\mathcal{Q}^i}\rho^{\rm TF}(\vec{x})\left(\pi\left|\log\left(t^2\Omega\right)\right| + \mathcal{O}(1)\right)\cdot(1+o(1))\,. \quad (2.3.120)\end{aligned}$$

To get the second term in the last line of above inequality we use a calculation already made in the paper [111]. Recall from [111] the facts

$$|\vec{E}(\vec{x})|^2 \leq |\vec{E}_i(\vec{x})|^2 + const.\left(\frac{\Omega^{1/2}}{|\vec{x}-\vec{x}_i|}+\Omega\right) \quad (2.3.121)$$

and

$$|\vec{E}_i(\vec{x})|^2 \leq \frac{1}{|\vec{x}-\vec{x}_i|^2}. \quad (2.3.122)$$

Hence they find

$$\begin{aligned}\int_{Q^i\setminus\mathcal{B}_t^i} {\rm d}\vec{x}\,|\vec{E}(\vec{x})|^2 - \int_{Q^i\setminus\mathcal{B}_t^i}{\rm d}\vec{x}\,|\vec{E}_i(\vec{x})|^2 \leq \\ \leq {\rm const.}\int_t^{C\,\Omega'^{-1/2}} {\rm d}x\;x\;\left(\Omega^{1/2}x^{-1}+\Omega\right) = O(1) \quad (2.3.123)\end{aligned}$$

while

$$\begin{aligned}\int_{\mathcal{B}_t^i}{\rm d}\vec{x}\,\xi(\vec{x})^2|\vec{E}(\vec{x})|^2 - \int_{\mathcal{B}_t^i}{\rm d}\vec{x}\,\xi(\vec{x})^2|\vec{E}_i(\vec{x})|^2 \leq \\ \leq {\rm const.}\int_0^t {\rm d}x\,x\,(x/t)^2(\Omega^{1/2}x^{-1}+\Omega) = O((t^2\Omega)^{1/2}). \quad (2.3.124)\end{aligned}$$

On the other hand, since $\vec{E}_i(\vec{x}) \leq |\vec{x}-\vec{x}_i|^{-1}$,

$$\int_{Q^i\setminus\mathcal{B}_t^i}{\rm d}\vec{x}\,|\vec{E}_i(\vec{x})|^2 \leq 2\pi\int_t^{C\,\Omega^{-1/2}}{\rm d}x\,x\,x^{-2} = \pi|\log(t^2\Omega)| + O(1) \quad (2.3.125)$$

and

$$\int_{\mathcal{B}_t^i}{\rm d}\vec{x}\,\xi(\vec{x})^2|\vec{E}_i(\vec{x})|^2 \leq 2\pi\int_0^t {\rm d}x\,x\,(x/t)^2x^{-2} = O(1). \quad (2.3.126)$$

We now estimate the Riemann approximation error

$$\mathcal{R} \equiv |Q^0| \sum_i \sum_{\vec{x} \in Q^i} \rho^{\mathrm{TF}}(\vec{x}) - \int_{\mathcal{A}^{\mathrm{TF}}} d\vec{x} \rho^{\mathrm{TF}}(\vec{x}) \leq$$

$$\leq |Q^0| \sum_i \left\{ \sup_{\vec{x} \in Q^i} \rho^{\mathrm{TF}}(\vec{x}) - \inf_{\vec{x} \in Q^i} \rho^{\mathrm{TF}}(\vec{x}) \right\}. \quad (2.3.127)$$

Multiplying the area of a cell times the value of the lattice constant l and $\|d\rho^{\mathrm{TF}}/dx\|_\infty \leq C\omega^{4/3}$ and the number of vortices inside $\mathrm{supp}\left(\rho^{\mathrm{TF}}\right)$ is

$$\mathcal{R} \leq C|\mathcal{Q}_i| \cdot l \cdot \omega^{4/3} \cdot N^{\mathrm{TF}} \ll 1 \quad (2.3.128)$$

as long as $\Omega \ll \varepsilon^{-4}$. Hence,

$$\int_{\mathbb{R}^2} d\vec{x} g^2(x) \xi^2(x) |\vec{E}(\vec{x})|^2 \leq \int_{\mathbb{R}^2 \setminus \mathcal{A}^{\mathrm{TF}}} d\vec{x} \cdot \xi^2(x) g^2(x) |\vec{E}(\vec{x})|^2 +$$

$$+ \left(1 + \mathcal{O}((t^2\Omega)^{1/2})\right) |\mathcal{Q}_0|^{-1} \left(\pi \left|\log\left(t^2\Omega\right)\right| + \mathcal{O}(1)\right) \cdot (1 + o(1)). \quad (2.3.129)$$

It remains to estimate the first term on the r.h.s. of (2.3.129). By the definition of ξ and since $|\vec{E}_i(\vec{x})|^2 \leq \frac{1}{|\vec{x} - \vec{x}_i|^2}$ we have

$$\int_{\mathcal{W}} d\vec{x} \cdot \xi^2(x) g^2(x) |\vec{E}(\vec{x})|^2 \leq \int_{\mathcal{W}} d\vec{x} g^2(x) \frac{\xi^2(x)}{|\vec{x} - \vec{x}_i|^2} + C \int_{\mathcal{W}} d\vec{x} g^2(x) \frac{\Omega^{1/2}}{|\vec{x} - \vec{x}_i|} + C\Omega \cdot o(1) \leq$$

$$\leq \int_{\mathcal{W}} d\vec{x} g^2(x) \frac{\xi^2(x)}{|\vec{x} - \vec{x}_i|^2} + C\Omega \quad (2.3.130)$$

For the first term on the r.h.s. of (2.3.130) we find with $N_{\mathcal{W}} \leq C \max[\Omega^{-1/2}, \varepsilon^{1/3}\omega^{-5/9}]$ (see pointwise estimate and exponential smallness)

$$\int_{\mathcal{W}} d\vec{x} g^2(x) \frac{\xi^2(x)}{|\vec{x} - \vec{x}_i|^2} \ll C\Omega \cdot \left(1 + \mathcal{O}((t^2\Omega)^{1/2})\right) \left(\pi \left|\log\left(t^2\Omega\right)\right| + \mathcal{O}(1)\right) \quad (2.3.131)$$

as long as $\Omega \ll \varepsilon^{-4}$.

□

Proposition 2.3.9 (Vortex Interaction Energy)
For $\varepsilon \to 0$ and $\varepsilon^{-1} \ll \Omega \lesssim \varepsilon^{-4}$ we have

$$\int_{\mathbb{R}^2} d\vec{x} \left\{ \frac{g^4}{\varepsilon^2} (1 - |u|^2)^2 \right\} \leq C\Omega. \quad (2.3.132)$$

Proof: First we consider the contribution to the vortex interaction energy due to $\mathcal{W}$. Since $g^2 \leq C\Omega^{-1/2}\omega^{4/3}$ and with $N_{\mathcal{W}} \leq C\max[\Omega^{-1/2}, \varepsilon^{1/3}\omega^{-5/9}]$ (see pointwise estimate and exponential smallness) we have

$$\begin{aligned}\sum_i \frac{1}{\varepsilon^2}\int_{\mathcal{B}_t^i\cap\mathcal{W}} g^4\left(1-\left(\frac{x}{t}\right)^2\right)^2(1+o(1)) \leq \\ \leq \frac{C\omega^{4/3}}{\varepsilon^2}\sum_i\int_{\mathcal{B}_t^i\cap\mathcal{W}}\left(1-\left(\frac{x}{t}\right)^2\right)^2(1+o(1)) \leq \\ \leq C\omega^{4/3}\varepsilon^{-2}\Omega^{-1/2}\Omega\cdot t^2 + C\omega^{4/3}\varepsilon^{-2}\varepsilon^{1/3}\omega^{-5/9}\Omega\cdot t^2 \leq C\Omega. \quad (2.3.133)\end{aligned}$$

Using $\rho^{\mathrm{TF}} \leq C\omega^{2/3}$ we find for the contribution due to $\mathcal{A}^{\mathrm{TF}}$

$$\begin{aligned}\sum_i \frac{1}{\varepsilon^2}\int_{\mathcal{B}_t^i\cap\mathcal{A}^{\mathrm{TF}}} (\rho^{\mathrm{TF}})^2\left(1-\left(\frac{x}{t}\right)^2\right)^2(1+o(1)) \leq \\ \leq \frac{C\omega^{2/3}}{\varepsilon^2}\sum_i \sup_{\vec{r}\in\mathcal{Q}^i}\rho^{\mathrm{TF}}(x_i)\int_{\mathcal{B}_t^i}\left(1-\left(\frac{x}{t}\right)^2\right)^2(1+o(1)) \leq \\ \leq \frac{Ct^2\omega^{2/3}}{\varepsilon^2}\sum_i \sup_{\vec{x}\in\mathcal{Q}^i}\rho^{\mathrm{TF}}(x_i)(1+o(1)) \leq \frac{Ct^2\Omega\omega^{2/3}}{\varepsilon^2}(1+o(1)). \quad (2.3.134)\end{aligned}$$

Choosing $t^2 = \varepsilon^2/\rho$ with $\rho = \omega^{2/3}$ yields the result.

□

□

2.4 Lower bound for the kinetic energy

This section is devoted to present a novel lower bound to the kinetic energy term of the reduced GP energy functional.

Theorem 2.4.1 (Lower Bound to reduced kinetic energy)
For ε sufficiently small, and if Ω satisfies $\varepsilon^{-1} \ll \Omega \ll \varepsilon^{-4}$

$$\int_{\mathbb{R}^2}|\vec{\nabla}g|^2 \geq (1+o(1))\int_{\mathcal{A}_+^{\mathrm{TF}}}\frac{\left(\vec{\nabla}\rho^{\mathrm{TF}}\right)^2}{\rho^{\mathrm{TF}}}. \quad (2.4.1)$$

with $\mathcal{A}_+^{\mathrm{TF}} = \mathcal{A}^{\mathrm{TF}} \cap \{x : x \leq 1\}$.

Proof: The starting point for our proof is the definition of the spherically symmetric rescaled GP density in terms of the corresponding variational equation

$$\rho^{\mathrm{GP}}(x) \equiv g^2(x) = \frac{\varepsilon^2}{2}\left(\mu - \mu^{\mathrm{TF}} + \frac{2}{\varepsilon^2}\rho^{\mathrm{TF}} + \frac{\Delta g}{g}\right)(x) \quad (2.4.2)$$

and let us by the way recall the explicitly given rescaled TF density

$$\rho^{\mathrm{TF}}(x) = \frac{\varepsilon^2}{2}\left(\mu^{\mathrm{TF}} - \Omega^2\left(\frac{2x^s}{s} - x^2\right)\right). \tag{2.4.3}$$

A crucial point in our argumentation is proposition 4.3.5, i.e.,

$$\rho^{\mathrm{GP}}(x) = \rho^{\mathrm{TF}}\left(1 + o(1)\right)(x) \tag{2.4.4}$$

holds for some specified set $\mathcal{A}^{\mathrm{TF}} \subseteq \mathbb{R}^2$. On the other hand this equation determines the asymptotically small function $o(1)(x)$ in terms of the introduced densities. Clearly, by the radial symmetry of the densities $o(1)$ is radial symmetric too. But be aware that in the following the symbol $o(1)$ denotes different functions as well, but they all share the property of being $o(1)$ for all $x \in \mathcal{A}^{\mathrm{TF}}$ and having their origin in above function $o(1)$ are radially symmetric. Now, in particular (2.4.4) says considering the definition of the GP density (or rather the variational equation) (2.4.2)

$$\frac{\Delta g}{g}(x) = \frac{o(1)}{\varepsilon^2}\rho^{\mathrm{TF}}(x) \qquad \text{for } x \in \mathcal{A}^{\mathrm{TF}} \subseteq \mathbb{R}^2, \tag{2.4.5}$$

which is a useful insight in the following argumentation. For the sake of analogy to previous estimates [111] on the kinetic energy for the TF density we rewrite the kinetic energy of the reduced GP functional due to its minimizer g in terms of its GP density (2.4.2) yielding

$$\int_{\mathbb{R}^2} |\vec{\nabla} g|^2 = \int_{\mathbb{R}^2} \frac{|\vec{\nabla}\rho^{\mathrm{GP}}|^2}{\rho^{\mathrm{GP}}} = \int_{\mathbb{R}^2} \frac{\left(\vec{\nabla}\rho^{\mathrm{TF}} + \frac{\varepsilon^2}{2}\vec{\nabla}\left(\frac{\Delta g}{g}\right)\right)^2}{\rho^{\mathrm{GP}}}. \tag{2.4.6}$$

In difference to the kinetic energy from the TF density (2.4.6) has two additional terms involving the GP minimizer and the divisor is now the GP density. However, we show that the leading order kinetic energy is exactly the kinetic energy due to the TF density. To do so we exploit the (pointwise) positivity of the integrand to reduce the integration domain and by using (2.4.4) on this subdomain we get an estimate to (2.4.6) from below:

$$\begin{aligned}
\int_{\mathbb{R}^2} |\vec{\nabla} g|^2 &\geq \int_{\mathcal{A}_+^{\mathrm{TF}}} \frac{\left(\vec{\nabla}\rho^{\mathrm{TF}} + \frac{\varepsilon^2}{2}\vec{\nabla}\left(\frac{\Delta g}{g}\right)\right)^2}{\rho^{\mathrm{GP}}} \geq \\
&\geq \int_{\mathcal{A}_+^{\mathrm{TF}}} \frac{\left(\vec{\nabla}\rho^{\mathrm{TF}} + \frac{\varepsilon^2}{2}\vec{\nabla}\left(\frac{\Delta g}{g}\right)\right)^2}{\rho^{\mathrm{TF}}}(1 + o(1))(r) \geq \\
&\geq \inf_{\zeta \in \mathcal{A}_+^{\mathrm{TF}}}(1 + o(1))(\zeta) \int_{\mathcal{A}_+^{\mathrm{TF}}} \frac{\left(\vec{\nabla}\rho^{\mathrm{TF}} + \frac{\varepsilon^2}{2}\vec{\nabla}\left(\frac{\Delta g}{g}\right)\right)^2}{\rho^{\mathrm{TF}}}
\end{aligned} \tag{2.4.7}$$

Here the domain $\mathcal{A}_+^{\mathrm{TF}} \subset \mathcal{A}^{\mathrm{TF}} \subseteq \mathbb{R}^2$ is specified later. Furthermore, we suppress the quadratic and therefore positive term due to the minimizer g within the integrand to get

$$\int_{\mathbb{R}^2} |\vec{\nabla} g|^2 \geq (1+o(1)) \int_{\mathcal{A}_+^{\mathrm{TF}}} \frac{(\vec{\nabla}\rho^{\mathrm{TF}})^2 + \vec{\nabla}\rho^{\mathrm{TF}} \cdot \varepsilon^2 \vec{\nabla}\left(\frac{\Delta g}{g}\right)}{\rho^{\mathrm{TF}}}. \tag{2.4.8}$$

Our knowledge about the (to us) not explicitly known term $\vec{\nabla}\left(\frac{\Delta g}{g}\right)$ is quite limited, but having (2.4.5) in our pocket we proceed by using partial integration to disburden this term from the gradient, where in addition we exploit the rotational symmetry of the problem:

$$\begin{aligned} 2\pi \int_{x_i}^{x_o} & \frac{\left(\frac{d}{dx}\rho^{\mathrm{TF}}\right)^2 + \frac{d}{dx}\rho^{\mathrm{TF}} \cdot \varepsilon^2 \frac{d}{dx}\left(\frac{\Delta g}{g}\right)}{\rho^{\mathrm{TF}}} = \\ &= -2\pi \int_{x_i}^{x_o} \frac{d}{dx}\left(\frac{\frac{d}{dx}\rho^{\mathrm{TF}}}{\rho^{\mathrm{TF}}}\right)\rho^{\mathrm{TF}} - 2\pi \int_{x_i}^{x_o} \frac{d}{dx}\left(\frac{\frac{d}{dx}\rho^{\mathrm{TF}}}{\rho^{\mathrm{TF}}}\right)\left(\frac{\Delta g}{g}\right)\varepsilon^2 + \\ &\quad + 2\pi \left(\frac{\frac{d}{dx}\rho^{\mathrm{TF}}}{\rho^{\mathrm{TF}}}\right)\rho^{\mathrm{TF}}\Big|_{x_i}^{x_o} + 2\pi \left(\frac{\frac{d}{dx}\rho^{\mathrm{TF}}}{\rho^{\mathrm{TF}}}\right)\left(\frac{\Delta g}{g}\right)\varepsilon^2\Big|_{x_i}^{x_o} = \star \end{aligned} \tag{2.4.9}$$

Here x_i denotes the inner radius of $\mathcal{A}_+^{\mathrm{TF}}$ and x_o its outer radius . We get using (2.4.5)

$$\star = -2\pi \int_{x_i}^{x_o} \frac{d}{dx}\left(\frac{\frac{d}{dx}\rho^{\mathrm{TF}}}{\rho^{\mathrm{TF}}}\right)\rho^{\mathrm{TF}}(1+o(1)) + 2\pi \left(\frac{\frac{d}{dx}\rho^{\mathrm{TF}}}{\rho^{\mathrm{TF}}}\right)\rho^{\mathrm{TF}}\Big|_{x_i}^{x_o}(1+o(1)). \tag{2.4.10}$$

Now let us discuss the sign's of both terms from above by calculating these functions of ρ^{TF}. The derivative of the TF density is

$$\frac{d}{dx}\rho^{\mathrm{TF}}(x) = \omega^2\left(x - x^{s-1}\right) \tag{2.4.11}$$

being positive on $\mathcal{A}^{\mathrm{TF}}$ as long as $x \leq 1$. Moreover, we have

$$\begin{aligned} \frac{d}{dx}\left(\frac{\frac{d}{dx}\rho^{\mathrm{TF}}}{\rho^{\mathrm{TF}}}\right) &= \\ &= -2\Omega^2 \frac{s\left[\mu^{\mathrm{TF}} s\left((s-1)x^s - x^2\right) + \Omega^2\left\{s^2 x^{s+2} + s(x^4 - 5x^{s+2}) + 2(x^s + x^2)x^s\right\}\right]}{x^2\left(\mu^{\mathrm{TF}} s - 2\Omega^2 x^s + \Omega^2 s x^2\right)^2} \end{aligned} \tag{2.4.12}$$

which is negative making by the way the first term in (2.4.10) positive as long as

$$\frac{1-(s-1)x^{s-2}}{\mu^{\mathrm{TF}} - \Omega^2\left(\frac{2x^s}{s} - x^2\right)} + \frac{2\Omega^2(x - x^{s-1})(x^{s-1} - x)}{\left(\mu^{\mathrm{TF}} - \Omega^2\left(\frac{2x^s}{s} - x^2\right)\right)^2} \leq 0. \tag{2.4.13}$$

Here both divisors are positive on the domain of interest, because both are modulo some C_ε the TF density or the TF density squared. The second term in (2.4.13) is negative as long as $x \leq 1$, but the first one isn't in general for $x \leq 1$. However, aiming to consider the behavior as $\varepsilon \to 0$ we rewrite the condition (2.4.13) using the explicit formula for ρ^{TF}

$$1 - (s-2)x^{s-2} + \frac{\omega^2(x - x^{s-1})(x^{s-1} - x)}{\rho^{\mathrm{TF}}} \leq 0 \tag{2.4.14}$$

or

$$(x - x^{s-1})(x^{s-1} - x) \leq -\left(1 - (s-2)x^{s-2}\right) \frac{\rho^{\mathrm{TF}}}{\omega^2}. \tag{2.4.15}$$

Using the fact $\rho^{\mathrm{TF}} \leq C\omega^{2/3}$ we find the stronger condition

$$(x - x^{s-1})(x^{s-1} - x) \leq -\left(1 - (s-2)x^{s-2}\right) \frac{C}{\omega^{4/3}} \xrightarrow{\omega \to \infty} 0 \tag{2.4.16}$$

Since the l.h.s. is negative for $x \leq 1$ on $\mathcal{A}^{\mathrm{TF}}$ we conclude that both terms in (2.4.10) are positive as long as $x \leq 1$. As a consequence we define $\mathcal{A}^{\mathrm{TF}}_+ = \mathcal{A}^{\mathrm{TF}} \cap \{x : x \leq 1\}$. Let us complete these explicit considerations by a simple ceck: Using a Taylor expansion we get for the TF density

$$\rho^{\mathrm{TF}} \simeq C\gamma^2 \left((\varepsilon\Omega)^{3/2} - (\varepsilon\Omega)^2(x-1)^2\right) \tag{2.4.17}$$

with the derivative being

$$\frac{d}{dx}\rho^{\mathrm{TF}} \sim C_\varepsilon(1-x) \geq 0 \tag{2.4.18}$$

for $x \leq 1$ on $\mathcal{A}^{\mathrm{TF}}$ and in addition one has

$$\frac{d}{dx}\left(\frac{\frac{d}{dx}\rho^{\mathrm{TF}}}{\rho^{\mathrm{TF}}}\right) \cdot \rho^{\mathrm{TF}} \leq 0. \tag{2.4.19}$$

We find using (2.4.10) and the positivity of the involved terms as lower bound for the kinetic energy

$$\int_{\mathbb{R}^2} |\vec{\nabla} g|^2 \geq \inf_{\xi \in \mathcal{A}^{\mathrm{TF}}_+} (1 + o(1))(\xi) \Bigg(-2\pi \int_{x_i}^1 \frac{d}{dx}\left(\frac{\frac{d}{dx}\rho^{\mathrm{TF}}}{\rho^{\mathrm{TF}}}\right)\rho^{\mathrm{TF}} + 2\pi \left(\frac{\frac{d}{dx}\rho^{\mathrm{TF}}}{\rho^{\mathrm{TF}}}\right)\rho^{\mathrm{TF}}\Bigg|_{x_i}^1 \Bigg) \tag{2.4.20}$$

and reverse the partial integration to get

$$\int_{\mathbb{R}^2} |\vec{\nabla} g|^2 \geq (1 + o(1)) \int_{\mathcal{A}^{\mathrm{TF}}_+} \frac{\left(\vec{\nabla}\rho^{\mathrm{TF}}\right)^2}{\rho^{\mathrm{TF}}}. \tag{2.4.21}$$

□

3 A Nonlinear quantum piston for the controlled generation of vortex rings and soliton trains

Florian Pinsker, Natalia G. Berloff and Víctor M. Pérez-García, Physical Review A **87**, 053624 (2013)

We propose a simple way to generate nonlinear excitations in a controllable way by managing interactions in Bose-Einstein condensates. Under the action of a quantum analogue of a classical piston the condensed atoms are pushed through the trap generating vortex rings in a fully three-dimensional condensates or soliton trains in quasi-one dimensional scenarios. The vortex rings form due to transverse instability of the shock wave train enhanced and supported by the energy transfer between waves. We elucidate in which sense the self-interactions within the atom cloud define the properties of generated vortex rings and soliton trains. Based on the quantum piston scheme we study the behavior of two component Bose-Einstein condensates and analyze how the presence of an additional superfluid influences the generation of vortex rings or solitons in the other component and vice versa. Finally, we show the dynamical emergence of skyrmions within two component systems in the immiscible regime.

3.1 Introduction

One of the most remarkable achievements in quantum physics in the last decade was that of Bose-Einstein condensation (BEC) in ultra-cold alkaline atomic gases. These physical systems have a high potential for supporting quantum nonlinear coherent excitations and many types of nonlinear waves have been experimentally observed [114, 115, 116, 117, 118, 119, 120, 121, 122, 123, 124, 125] or theoretically proposed to exist (see e.g. the reviews [126, 127]) in ultra-cold quantum degenerate gases. The list includes dark solitons [113], bright solitons [114], bubbles [128] and gap solitons [115], vector solitons [116], vortices, vortex lattices and giant vortices [21, 22, 23], vortex rings [120, 121, 122], dark ring-shaped waves [123], shock waves [121, 124], collapsing waves [125] and many others. In this way Bose-Einstein condensates (BECs) are, apart from their fundamental role in quantum physics, exceptional physical systems for the manifestation and study of nonlinear phenomena and in particular due to their rather simple theoretical description.

Among the various nonlinear excitations the vortex ring occupies a special place. Vortex rings are essentially three-dimensional topological nontrivial structures appearing in

either classical [129] or quantum [130] fluids. They are able to propagate in cylindrically trapped BECs as stable objects [131], similarly to classical fluids [132]. This is an essential difference to most other solitonic structures that become unstable when passing to a fully three-dimensional setting, e.g. one dimensional bright solitons that are unstable to blow-up [125] or dark solitons, that are unstable to the snake instability [134, 133, 120]. This leaves the vortex ring as the only dynamically nontrivial nonlinear excitation observed in fully three-dimensional BECs.

Vortex rings were first observed in BECs as the outcome of the decay of dark solitons [120] and as a result of the decay of quantum shock waves [121]. More recently they have been observed to appear during complex oscillations in soliton-vortex ring structures [122] and during the merging of BEC condensate fragments [135]. However, generating vortex rings involved complicated nonlinear phenomena and in general a simple mechanism allowing the controlled generation of a prescribed finite number of vortex rings is still missing. The main purpose of this paper is to propose such a mechanism allowing the generation of a few vortex rings in a highly controllable way. The same method can be used to create soliton trains of certain frequencies within a one-dimensional model. We will also extend the concepts to coupled BECs showing how skyrmions can be generated using similar techniques.

The plan of this paper is as follows. First in Section 3.2 we introduce the main physical idea of a nonlinear quantum piston. In Section 3.3 we introduce the mathematical equations and nondimensionalisations used throughout the paper. Next we discuss the nonlinear excitations in the form of dark and bright soliton trains for one dimensional problems for single (Sec. 3.4) and two-component (Sec. 3.5) condensates. The controlled generation of vortex rings and skyrmions is discussed in Section 3.6. Finally we summarize our conclusions in Section 3.7.

3.2 Physical idea

The process of vortex ring generation in classical fluids has received a substantial treatment in the literature. One of the most standard ways to obtain vortex rings in classical fluids involves moving a piston through a tube, resulting in a vortex ring being generated at the tube exit. A standard generation geometry consists of the tube exit mounted flush with a wall with the piston stroke ending at the tube exit [136].

In this paper we will use something conceptually much simpler utilizing the possibilities opened by space-dependent Feschbach resonance management in a BEC. Since the first achievements in scattering length control in BECs [27], the technique of Feschbach resonance management has been improved and used in many different applications. Presently, the level of control of the scattering length allows for its very precise tuning [137] and nothing prevents an extended control of the interactions leading to a space dependent scattering length. A large number of theoretical papers have studied nonlinear phenomena in systems with managed interactions (see e.g. Refs. [126, 138, 139, 140, 146, 149, 150] and references therein).

The physical idea is illustrated in Fig. 3.1. Starting from a single equilibrium BEC

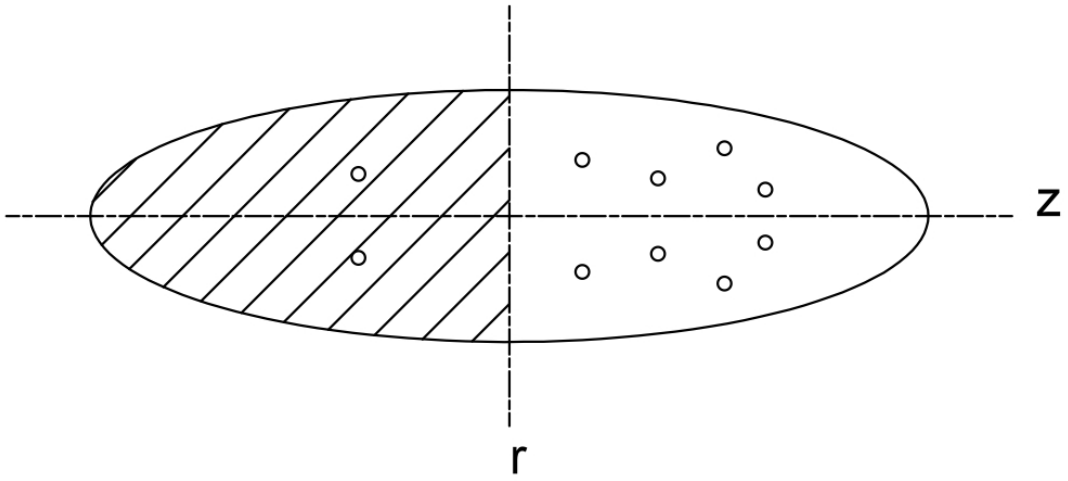

Figure 3.1: Schematic diagram of the quantum piston idea, where the ellipse symbolizes the trapped BEC. The trap is supposed to be radially symmetric and elongated along the z-axis. The area of change in self-interactions is illustrated by the hatched lines. The small circles represent the cross sections of possible vortex rings obtained as a result of the flow induced by the asymmetric interactions playing the role of a quantum piston.

in a trap with a given value of the scattering length $a > 0$, we propose modifying interactions in half of the space (say the left hand side $z < 0$) to a larger value $a_L > a = a_R$ instantaneously. This change would affect the initial configuration by inducing the transverse expansion of the atomic cloud for $z < 0$ generating a flow towards the region with a smaller interaction value at $z > 0$. This process is analogous to the piston-driven flow through an aperture used to generate vortex rings in classical fluids. These effects are achieved simultaneously with a single action on the interactions without restoring to complicated external potentials. We also consider a smooth change of scattering length that would be more realistic in experiments. Modifying interactions to be attractive $a < 0$ on one side would allow the atom cloud with repulsive self-interaction at $z > 0$ to expand towards this region. The nature of nonlinear excitations generated in this way would be different to the repulsive case due to the difference in interatomic relations [11, 151]. Generating a controlled flow within a Bose gas with entirely attractive interactions by imposing a change in interactions would cause similar nonlinear excitations.

Applying the concept of a quantum piston to a two component BEC enables new physics to come into play. One scenario we will consider in this paper is the case in which the interactions are changed only in one of the components that would generate a counterflow between two components thus creating excitations involving the other component, for example generating skyrmions that are stable vortices with the second component filling in the core.

3.3 Mathematical models

We consider a single component BEC modeled in the mean field limit by the nonlinear Gross-Pitaevskii equation [7, 8]

$$i\hbar\frac{\partial\psi}{\partial t} = -\frac{\hbar^2}{2m}\Delta\psi + V_{\text{ext}}^{\text{nat}}(r,z)\psi + g^{\text{nat}}(z)|\psi|^2\psi, \tag{3.3.1}$$

for particles of mass m with self-interactions defined by $g^{\text{nat}}(z) = 4\pi\hbar^2 a_s(z)/m$, where $a_s(z)$ is the s-wave scattering length. The condensate wave function ψ describing a condensate of N bosons located in $\Omega \subset \mathbb{R}^3$ satisfies the mass constraint $\|\psi\|^2_{L_2(\Omega)} = N$. Confinement is due to an external elongated axisymmetric trap $V_{\text{ext}}^{\text{nat}} = (m\omega^2 r^2 + m\omega_z^2 z^2)/2$, where the frequencies satisfy $\omega \gg \omega_z$. We use the rescaled GPE given by

$$i\frac{\partial\psi}{\partial t} = -\Delta\psi + V_{\text{ext}}(r,z)\psi + g(z)|\psi|^2\psi. \tag{3.3.2}$$

Here the spatial coordinates are measured in the healing length of the transverse ground state $a_0 = (\hbar/m\omega\sqrt{2})^{1/2}$ and time t in $\sqrt{2}/\omega$, respectively, while the energies and frequencies are measured in units of $\hbar\omega/\sqrt{2}$ and $\omega/\sqrt{2}$ respectively, and $V_{\text{ext}} = (\lambda^2 r^2 + \lambda_z^2 z^2)/2$. We rescale the wave function such that it is normalized to 1, i.e., $\|\psi\|^2_{L_2(\Omega)} = 1$. Then $g(z) = 4\pi a_s(z)N/a_0$, which is proportional to the local value of the s-wave scattering length $a_s(z)$ and will be taken, starting from $t = 0^+$, to be the step-like function defined

by

$$g(z) = g^L + \frac{g^R - g^L}{1 + e^{-2kz}}, \tag{3.3.3}$$

where the constituents of the local self-interaction are g^R and g^L and the 'smoothness' parameter is taken to be $k > 0$. Finite k accounts for a gradual change in scattering length across $z = 0$. In the limiting case $k \to \infty$ the coupling parameter $g(z)$ becomes a step function

$$g(z) \overset{k\to\infty}{\longrightarrow} \begin{cases} g^R, & z > 0 \\ (g^R + g^L)/2, & z = 0 \\ g^L, & z < 0. \end{cases} \tag{3.3.4}$$

In addition we will study two component Bose-Einstein condensates within a similar quantum piston setting. The wave functions of component A and B will be assumed to be governed by a system of coupled nonlinear Schrödinger-type equations [11, 77].

$$i\hbar\frac{\partial\psi_A}{\partial t} = \left(-\frac{\hbar^2}{2m_A}\Delta + V^{\text{nat}}_{\text{ext},A}(r,z) + g^{\text{nat}}_A|\psi_A|^2 + g^{\text{nat}}_{AB}|\psi_B|^2\right)\psi_A, \tag{3.3.5a}$$

$$i\hbar\frac{\partial\psi_B}{\partial t} = \left(-\frac{\hbar^2}{2m_B}\Delta + V^{\text{nat}}_{\text{ext},B}(r,z) + g^{\text{nat}}_B|\psi_B|^2 + g^{\text{nat}}_{BA}|\psi_A|^2\right)\psi_B. \tag{3.3.5b}$$

Here the mass of a boson from component $i \in \{A, B\}$ is denoted m_i, the symbol g^{nat}_i refers to the corresponding self-interactions and we consider a scaling for which the normalization is $\|\psi_i\|^2_{L_2(\Omega)} = N_i$, where N_i denotes the number of atoms of species i. Depending on the context self-interactions g^{nat}_i can be thought of either as being constant or step functions. Those step-functions are formally defined as in the single component case. The cross-interaction strengths are given by $g^{\text{nat}}_{ij} = 2\pi\hbar^2 a_{ij}/m_{ij}$ with $i \neq j$ and the reduced mass given by $m_{ij} = m_i m_j/(m_i + m_j)$. In this paper we will take $a_{ij} = a_{ji}$ and $m = m_A = m_B$. The harmonic potentials are given by $V_{\text{ext},i} = m_i(\omega r^2 + \omega_z^2 z^2)/2$, where the ω's denote the corresponding trapping frequencies.

The non-dimensionless form is obtained via the transformation $\boldsymbol{x} \to a_0\boldsymbol{x}$, $t \to t\sqrt{2}/\omega$ and $\psi_i \to \psi_i \left(\frac{1}{L_i}\right)^{1/2}/a_0$ with $\frac{1}{L_i} = g_i\hbar^2/(2mg^{\text{nat}}_i)$ where the nondimensionalized self-interaction strength g_i has been introduced. In those terms our coupled system is given by

$$i\frac{\partial\psi_A}{\partial t} = \left(-\Delta + V_{\text{ext},A} + g_A|\psi_A|^2 + g_{AB}|\psi_B|^2\right)\psi_A \tag{3.3.6a}$$

$$i\frac{\partial\psi_B}{\partial t} = \left(-\Delta + V_{\text{ext},B} + g_{AB}|\psi_A|^2 + g_B|\psi_B|^2\right)\psi_B \tag{3.3.6b}$$

with $V_{\text{ext},i} = \lambda_i^2 r^2 + \lambda_{z,i}^2 z^2$ and $g_{ij} = g_j g^{\text{nat}}_{ij}/g^{\text{nat}}_j$. We choose parameters such that the mass constraints $\|\psi_i\|^2_{L_2(\Omega)} = 1$, $\Omega \subset \mathbb{R}^3$.

To follow the time evolution of the fields ψ_i numerically we have used a fourth order finite difference scheme in space together with a fourth order Runge-Kutta discretization in time.

In the next section we consider the generation of nonlinear excitations by changing the interaction strength on one half of the domain for quasi-one dimensional BECs.

3.4 Emergence of soliton trains in quasi-one dimensional single component BECs

The starting point of our investigation of the controlled generation of nonlinear excitations is a strongly cigar shaped Bose-Einstein condensate, i.e., $\omega \gg \omega_z$. Neglecting trapping in z by setting $\omega_z = 0$, the evolution equation (4.2.26) for the wave function becomes [152]

$$i\frac{\partial}{\partial t}\psi_{1D} = -\frac{\partial^2}{\partial z^2}\psi_{1D} + g(z)|\psi_{1D}|^2\psi_{1D} - \mu\psi_{1D}, \tag{3.4.1}$$

where we have introduced a chemical potential via $\psi_{1D} = \psi_{1D}e^{-i\mu t}$, dropped the mass constraint as we consider an infinitely spread BEC here and rescaled time. Initially, i.e., for $t < 0$ the single coherent condensate is uniformly distributed and lies at rest. By $n_0 = \mu/g$ we denote the associated constant equilibrium density distribution and the corresponding self-interaction strength by g. To see the effect of changing self interactions at $t = 0$ instantaneously, i.e., $g \to g(z)$, on the initial state (such that we have step-like self interactions $g(z)$ for all times $t > 0$) we have simulated the dynamical behavior of ψ governed by (3.4.1) for different parameter combinations of $g(z)$ [207].

3.4.1 Results

Starting with a uniformly distributed Bose gas with repulsive self-interactions set to $g = 1$ we observe that for a moderate increase in the interaction strength on the left-hand side the outflow does not produce any solitary trains. When the spatial change in self-interactions is sufficiently large, specifically $g^L/g^R > 2.2$ the transport of atoms from the region of higher interactions on the left to the one of lower interactions on the right is accompanied by the emergence of a dark soliton train.

The wave generated when the interactions are increased on the left half of the cloud ($z < 0$) via $g \to g(z)$ leads to a formation of dispersive shock that propagates on the background density that sets the reference sound speed. As shown by many authors [141, 142, 143, 144, 145] the 1D shock profile can be found by matching the high- and low-intensity boundaries. In such a shock the inner (slow) nonlinear part of the front is a train of dark or gray solitons, while the outer (fast) part is a low-intensity region with oscillations that are effectively sound-like [141, 142, 143, 144, 145]. As the fast outer part propagates further into the less interactive region, the inner part adopts more and more pulses in the solitary train, which is clearly seen on Fig. 3.2. We note that besides the characteristic density depletion the phase of these arrays of solitons show the characteristic phase jumps at each soliton by π. Subsequently the flow of the condensate manifests itself as a regular array of density depletions moving at a constant speed while keeping the shape over time. Results in this regime also agree well with simulations of

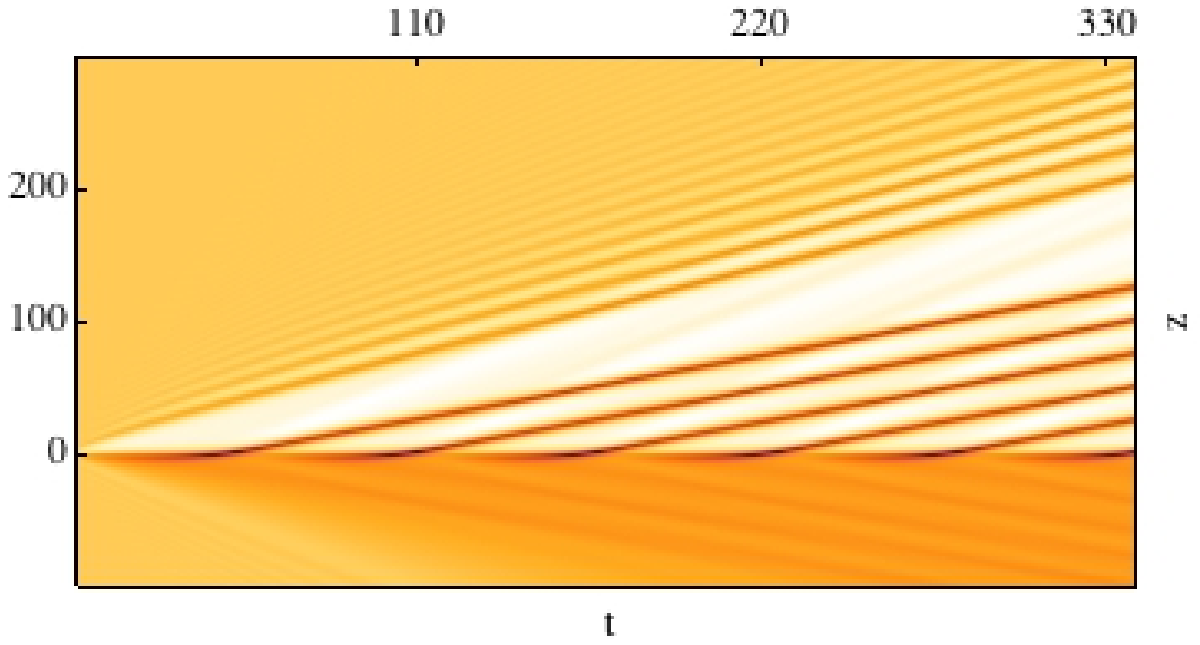

Figure 3.2: Pseudo-color density plot $\rho(z) = |\psi_{1D}(z,t)|^2$ of a uniformly distributed Bose gas with constant interaction $g = 1 = g^R$ at $t = 0$ evolving in time as a change of $g^L/g^R = 3.4$ has been implemented for $t > 0$. The change in interactions is sharp at $z = 0$, i.e., $k \to \infty$ in (3.3.3). Here luminosity is proportional to density. The dimensionless units are used as specified in the main text .

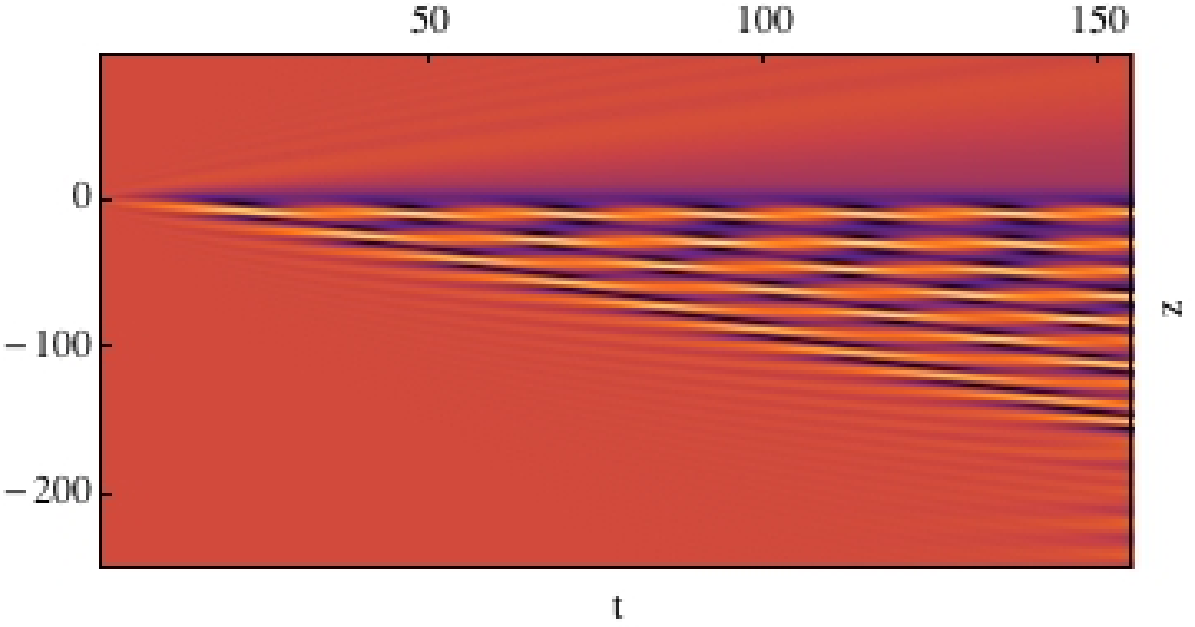

Figure 3.3: Pseudo-color density plot $\rho(z) = |\psi_{1D}(z,t)|^2$ of a uniformly distributed Bose gas with constant interaction $g = 1 = g^R$ at $t = 0$ evolving in time as a change of $g^L/g^R = -1$ has been implemented for $t > 0$. The change in interactions is sharp at $z = 0$, i.e., $k \to \infty$ in (3.3.3). Here luminosity is proportional to density. The dimensionless units are used as specified in the main text.

the nonpolinomial Schrödinger equation in trapped systems reported in Ref. [146]. In addition we note that in a different context soliton patterns arise due to a mechanism where two spatially distinct condensates collide within a harmonic trap [147] and thereby generate nonlinear excitations. The two condensates in this case have different global phases, so joining the two condensate together is analogous to phase imprinting in a single condensate [148]. In our case we have a condensate with the same global phase where vortices and solitary trains are formed *dynamically*.

In Fig. 3.3 we show the evolution for a BEC between $t = 0$ and $t = 160$ in the case where we have changed self-interactions to negative (attractive) values at the l.h.s. In this particular example parameters have been chosen to be $g = 1 = g^R$ and $g^L = -1$. The emerging structure can be identified as a bright soliton train appearing in a similar process of formation of individual solitons in a localized reservoir. [149, 150]. Furthermore it can be seen in Fig. 3.3 that bright solitons remain approximately at the same position. Similarly to the formation of a dark soliton train as an initial shock wave propagates a bright soliton train is generated. In contrast to the dark soliton train which mainly is due to the reallocation of mass in a directed manner, the bright soliton train forms due to the perturbation at the breaking point such that due to its attractiveness the condensate collapses locally to form bright solitons.

Starting with a system of attractively interacting atoms the introduction of even small

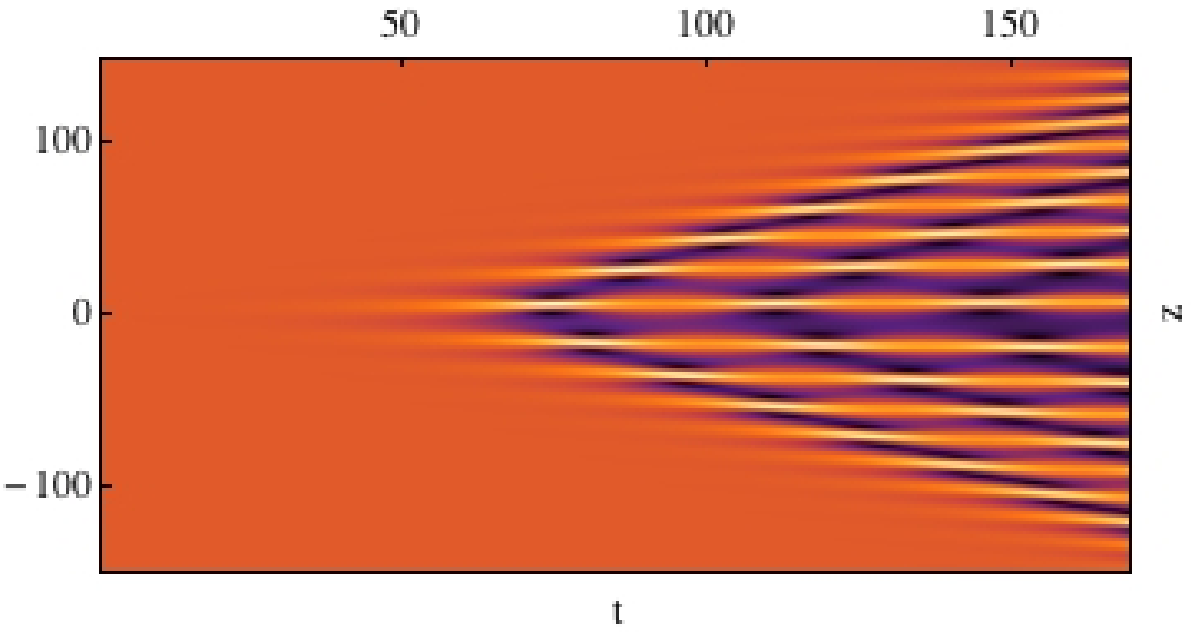

Figure 3.4: Pseudo-color density plot $\rho(z) = |\psi_{1\mathrm{D}}(z,t)|^2$ of a uniformly distributed Bose gas with constant attractive interaction $g = -1 = g^R$ at $t = 0$ evolving in time as a change of $g^L/g^R = 0.99$ has been implemented for $t > 0$. The change in interactions is sharp at $z = 0$, i.e., $k \to \infty$ in (3.3.3). Here luminosity is proportional to density. The dimensionless units are used as specified in the main text.

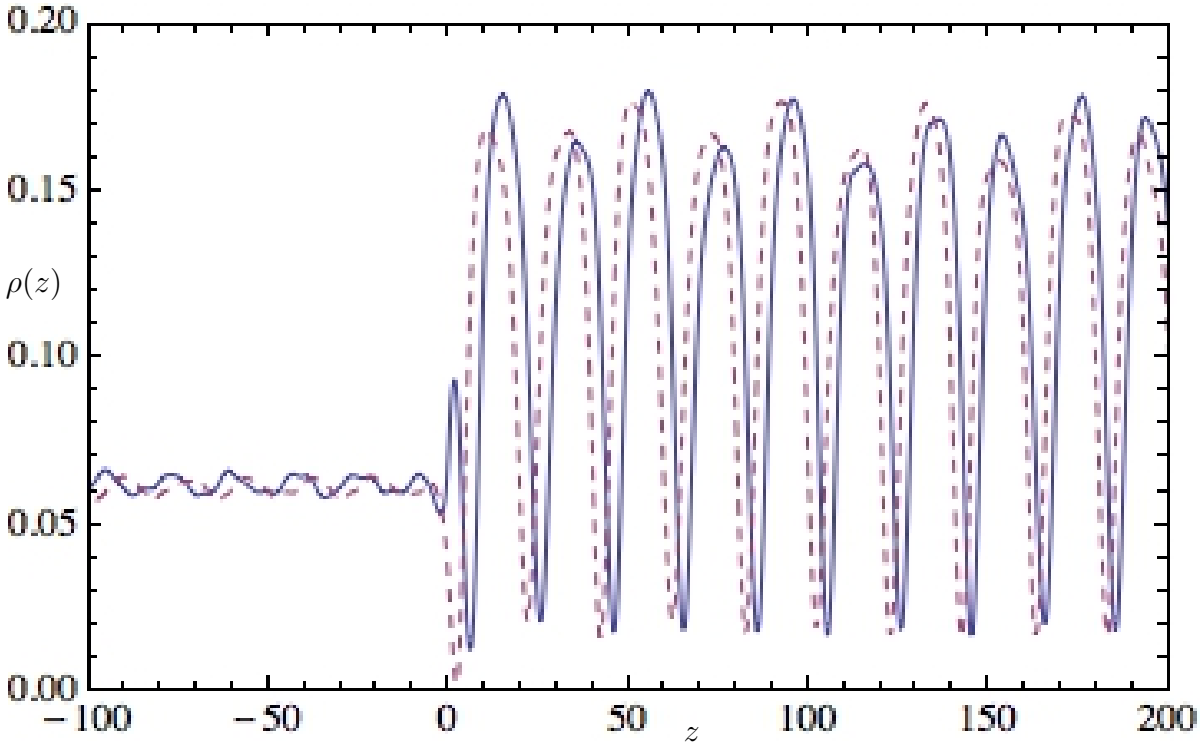

Figure 3.5: Density plot $\rho(z) = |\psi_{1D}(z,t)|^2$ of numerically computed density profiles at $t = 510$ for $g^L/g^R = 4$ and $g^R = 1$ and $k \to \infty$ (solid line) and $k = 1.5$ (dashed line). The dimensionless units are used as specified in the main text

change in interactions leads to the generation of a bright soliton train as Fig. 3.4 illustrates for the case of $g = -1 = g^R$ and $g^L/g^R = 0.99$. Unlike the cases involving repulsive interactions this bright soliton train slowly expands in both directions. However, as $g^L/g^R \to 0$ bright solitons can only be observed for $z > 0$.

3.4.2 Smooth vs. abrupt change in self-interactions

In real experiments one would expect a more gradual change of the interaction strength across $z = 0$. Thus to describe more realistic situations a finite (though maybe small) k has to be considered within Eq. (3.3.3).

In several series of simulations for attractive as well as repulsive condensates we have observed the same qualitative dynamics as for the step-function case, the structure of the solitary wave train and the threshold for its appearance has been very similar even for small k, i.e., a very smooth step. In Fig. 3.5 we present an example where $k = 1.5$ showing the very small deviation in emerging soliton trains due to sharp and gradual changes in self-interactions. Hence, for simplicity we will turn our attention on the limit $k \to \infty$ in what follows.

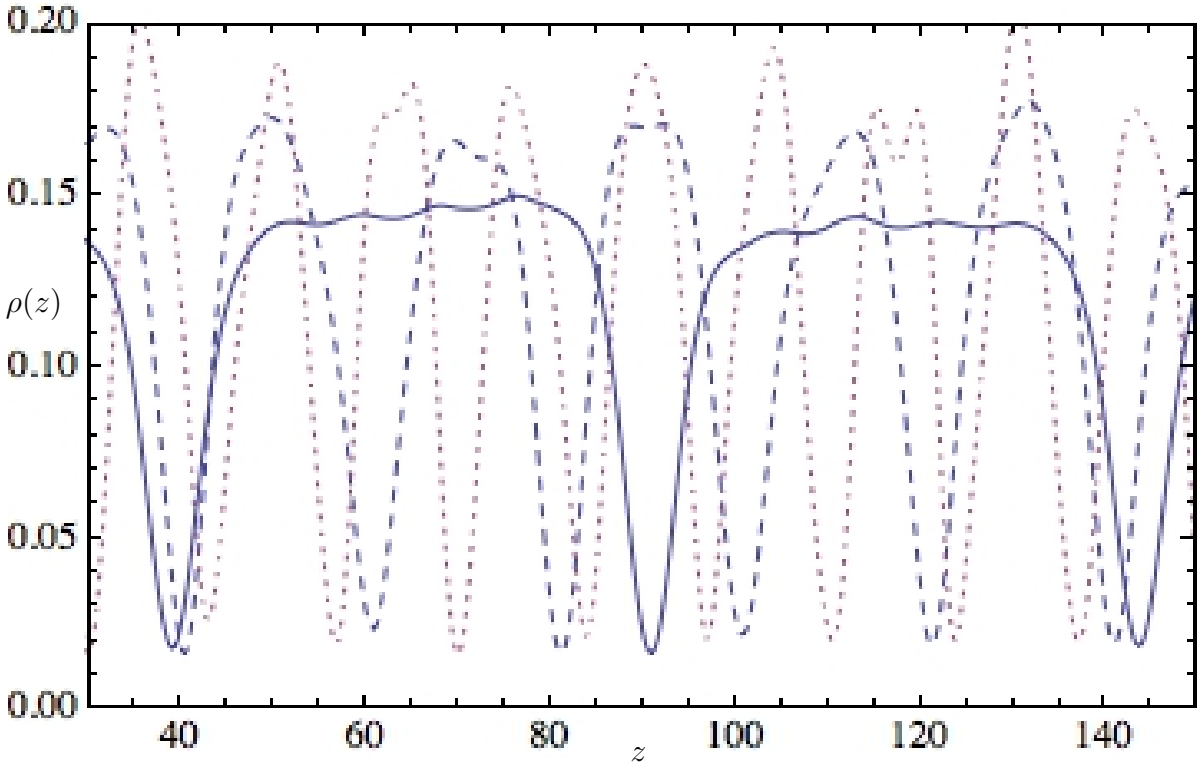

Figure 3.6: Density plots $\rho(z) = |\psi_{1D}(z,t)|^2$ of numerically computed density profiles with step function interactions ($k \to \infty$) at time $t = 500$ of an initially uniformly distributed Bose gas with $g = 1 = g^R$ for different self interaction strenghts ratios $g^L/g^R = 2.5$ (solid line), $g^L/g^R = 4$ (dashed line) and $g^L/g^R = 6$ (dotted line). The dimensionless units are used as specified in the main text

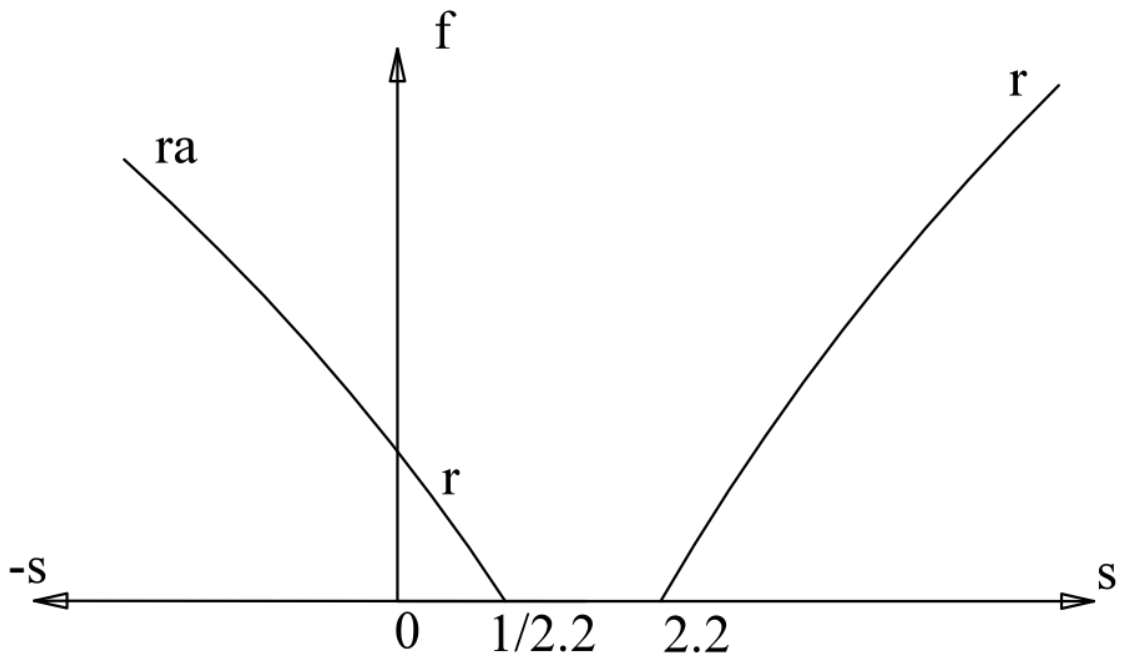

Figure 3.7: A schematic diagram of the relationship between the frequencies f of the soliton trains and the change in interactions $s = g^L/g^R$.The dimensionless units are used as specified in the main text

3.4.3 Properties of soliton trains

For repulsive interactions one would expect that an increase in the change of interactions, g^L/g^R, produces larger flow, so leads to an increase in the spatial frequency, i.e., the number of solitons within some fixed space interval. An example of this behavior is shown in Fig. 3.6 where an initial distribution specified by $g = 1 = g^R$ changes its profile when the interactions are set to $g^L/g^R = 2.5$, $g^L/g^R = 4$ and $g^L/g^R = 6$. The final profiles for $t = 500$ are shown. Fig. 3.6 shows that larger asymmetries in the interaction lead to higher spatial frequencies. In addition we observe that for large asymmetries in interactions the wavefunction profiles resemble the square of a sinus function while for smaller asymmetries the profiles of the density depletions resemble an array of squares of hyperbolic tangents near their minima, i.e., there is a qualitative difference in the form of the density profile depending on the imposed change in interactions. We have also studied the velocities of generated dark soliton trains and found them to be almost independent on the change in interaction strength.

The numerically obtained relationship between the frequencies of soliton trains and the change in interactions $g^L/g^R \in [-2, 8]$ is given in Fig. 3.7 for $g = 1$. Here r denotes entirely repulsive BEC and ra a condensate where we switched to attractive values on one side. For entirely attractive interactions one finds that changing self-interactions to different values leads to bright soliton trains with in general different frequencies on both sides.

3.4.4 Analytical approximations to the soliton train profiles

Eq. (3.4.1) with spatially dependent interactions does not admit in general exact analytical solutions. While we will be constructing solutions of the full equation in Appendix 3.8 (for step-function like self-interactions in the static case), for now we will restrict our attention to the construction of phenomenological solutions fitting the dynamics for uniform g that can be expected to approximate the solutions far from $z = 0$ (the point where the nonlinearity has the transition from g^L to g^R). First we consider the repulsive and then the attractive case. The differential equation (3.4.1) for constant g is integrable [154] and the solution representing a single dark soliton [155] for $g > 0$ can be written as

$$\psi_{g>0}(z,t) = \sqrt{n_0}\left[i\frac{v}{c} + \sqrt{1-\left(\frac{v}{c}\right)^2}\cdot\tanh\left(\sqrt{1-\left(\frac{v}{c}\right)^2}\cdot\sqrt{\frac{n_0 g}{2}}\cdot(z-vt)\right)\right]. \quad (3.4.2)$$

Here v is the velocity of the soliton, $c = \sqrt{2n_0 g}$ is the Bogoliubov speed of sound, n_0 denotes the equilibrium one particle density distribution and one sets $\mu = n_0 g$. In order to get a periodic solution describing a dark soliton train we interchange the hyperbolic tangens in (3.4.2) with a Jacobi elliptic function by letting $\tanh \to \mathrm{sn}$,

$$\psi_{\mathrm{dt}}(z,t) = \sqrt{n_0}\left[i\frac{v}{c} + \sqrt{1-\left(\frac{v}{c}\right)^2}\cdot\mathrm{sn}\left(\sqrt{1-\left(\frac{v}{c}\right)^2}\cdot\sqrt{\frac{n_0 g}{2p^2}}\cdot(z-vt)\,\middle|\,p^2\right)\right]. \quad (3.4.3)$$

A straightforward calculation shows that it is approximately solving (3.4.1), if μ is chosen to be $\mu = gn_0\left(\frac{(1+p^2)}{(2p^2)}(1-\frac{v^2}{2n_0g})+\frac{v^2}{2n_0g}\right)$. Indeed, the above approximate solution becomes exact either if $p \to 1$, where $\mathrm{sn}(z|1) = \tanh(z)$, or if $v \to 0$, so it generalizes the single soliton expression (3.4.2). It is known that Jacobi elliptic functions are periodic solutions of the GP equation with repulsive and attractive interactions [156, 157, 158, 159, 160]. The sinus amplitudinis interpolates between a trigonometric and a hyperbolic function and its dependency on each is controlled by the real-valued elliptic modulus $p \in [0, 1]$.

One property of the analytic dark soliton train (3.4.3) is that its density profile fits with the computationally obtained profile, iff the self-interaction strength g of the analytical solution equals the one used for generating the numerical solution. This in turn enables us to deduce the effective interaction strength g between the condensed atoms from the form of the numerically generated dark soliton train, i.e., from the density profile of the atom cloud by means of (3.4.3). For details we refer to the Appendix 3.9.

We have compared the numerical generated soliton trains with the analytical periodic soliton trains due to the condensate wave functions (3.4.3). A typical example is presented in Fig. 3.8 where parameters for the analytical solution where chosen to be as follows. $v = 0.1018$, $p = 0.9978$, $n_0 = 0.1566$ and $g = 1$ while the numerical solution is considered on a space interval where self-interactions have been $g = 1$ for $t \leq 0$ and $g_L = 3$ for $t > 0$.

A single bright soliton solution to (3.4.1) with constant attractive interactions is given by replacing $\tanh(z) \to 1/\cosh(z)$ in (3.4.2) and setting $g \to |g|$. The transition to the bright soliton train is obtained by $\tanh \to \mathrm{cn}$, i.e.,

$$\psi_{\mathrm{bt}}(z,t) = \sqrt{n_0}\left[i\frac{v}{c} + \sqrt{1-\left(\frac{v}{c}\right)^2}\cdot \mathrm{cn}\left(\sqrt{1-\left(\frac{v}{c}\right)^2}\cdot\sqrt{\frac{n_0|g|}{2p^2}}\cdot(z-vt)\,\middle|\,p^2\right)\right]. \quad (3.4.4)$$

Again a straightforward calculation shows that it is approximately solving (3.4.1), if μ is chosen to be $\mu = |g|n_0\left(\frac{(1-2p^2)}{(2p^2)}(1-\frac{v^2}{2n_0g})+\frac{v^2}{2n_0g}\right)$. Note that the chemical potential is negative for $1 > p^2 \gg 0$ and for $v \to 0$ and $\sqrt{p} \to 1$ converges to $\mu = -|g|n_0/2$. Furthermore, this solution becomes exact either if $\sqrt{p} \to 1$, where $\mathrm{cn}(z|1) = \frac{1}{\cosh(z)}$, or if $v \to 0$, thereby generalizing the single bright soliton expression. We note that similar considerations on the density profile like those made above for dark soliton train solutions apply to bright soliton train solutions as well. However, as the bright soliton train in Fig. 3.3 is not freely expanding the limit $v \to 0$ gives the best approximation to our numerics.

The densities corresponding to the dark soliton train solution (3.4.3) and the bright soliton train solution (3.4.4) are related via

$$\frac{|\psi_{\mathrm{dt}}(z,t)|^2 + |\psi_{\mathrm{bt}}(z,t)|^2}{\left(1+\frac{v^2}{c^2}\right)} = n_0. \quad (3.4.5)$$

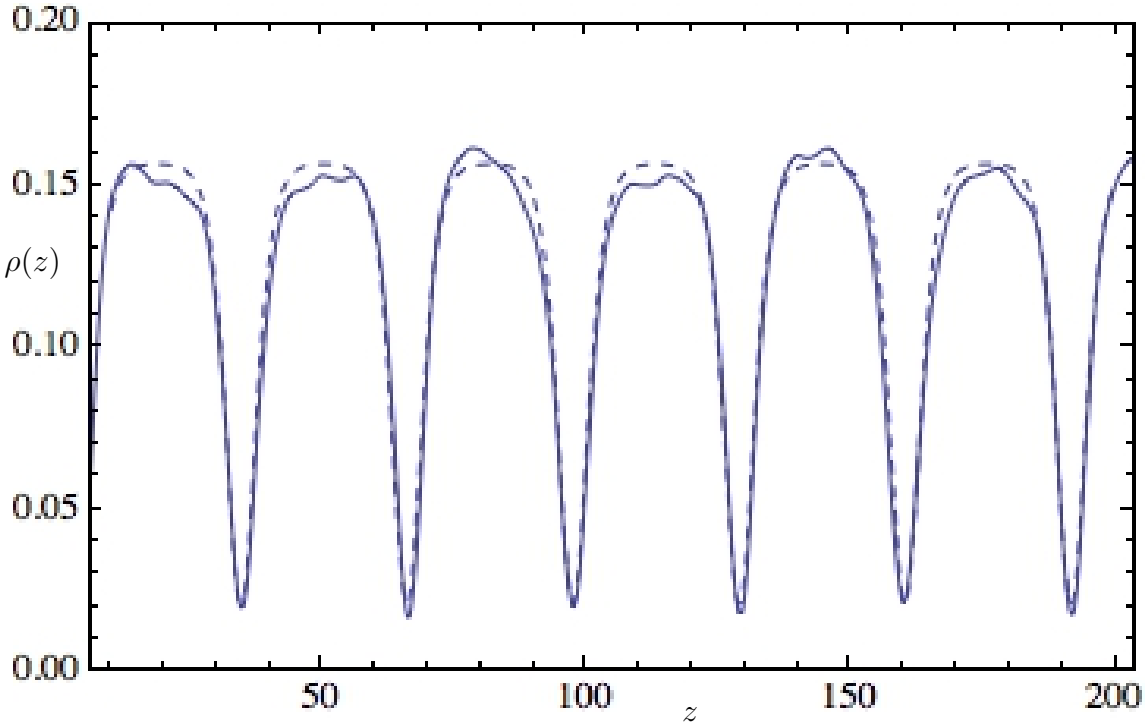

Figure 3.8: Details of analytical (dashed line) and numerically computed (solid line) density profiles $|\psi_{1\mathrm{D}}(z,t)|^2$ of dark soliton trains. At time $t > 0$ the interactions of the condensate on the left are set to $g_L = 3$ on the left-hand side of the domain in the numerical solution. The dimensionless units are used as specified in the main text.

3.5 Emergence of soliton trains in quasi-one dimensional two-component BECs

In the previous sections we have found that the emergence and properties of soliton trains depend on the magnitude of change in self-interaction strength. Next we discuss how the state of a one-dimensional condensate of component A ψ_{1D}^A is affected by the presence of a second component B represented by ψ_{1D}^B. Supposing $\omega \gg \omega_z$, rescaling time and neglecting trapping in z-direction the wave functions are governed by the system

$$i\frac{\partial}{\partial t}\psi_{1D}^A = \left(-\frac{\partial^2}{\partial z^2} + g_A|\psi_{1D}^A|^2 + g_{AB}|\psi_{1D}^B|^2\right)\psi_{1D}^A, \tag{3.5.1}$$

$$i\frac{\partial}{\partial t}\psi_{1D}^B = \left(-\frac{\partial^2}{\partial z^2} + g_B|\psi_{1D}^B|^2 + g_{AB}|\psi_{1D}^A|^2\right)\psi_{1D}^B. \tag{3.5.2}$$

Here the self-interactions g_A, g_B and cross-interactions g_{AB} are either constants or step functions. The dynamical stability of the mixture depends on the criterion $g_A g_B > g_{AB}^2$, therefore, by changing the interaction strength on one part of the cloud it is possible to have a miscible regime on one half and the phase separation regime on the other half of the domain.

First, we assume that initially ($t = 0$) condensates A and B are spatially homogeneous with uniform and repulsive self- and cross-interactions. Then ($t = 0^+$), self-interactions are changed in component A, i.e., formally $g_A \to g_A(z)$ leading to the generation of dark solitons and the appearance of complex dynamics for $t > 0$. An example of the dynamics is shown in Fig. 3.9 (with $g_A^L/g_A^R = 3$ and $g_{AB} = g_A^R = g_B = 1$). In that case, the soliton train in component A is raised by the presence of the second condensate. Dark soliton trains generated in the presence of a second repulsive condensate are not as stable as single component condensates - solitons decay faster. However, we have observed dark soliton trains to appear at slightly lower interaction ratios than in single component condensates, which depends in particular on cross-interaction strength.

Next we consider a two component condensate where one component is attractive and the other component is repulsive. Initially both components are mixed and uniformly distributed. In Fig. 3.10 snapshots of a two component condensate with initial parameters $g_A = 1$, $g_B = -1$ are shown (dotted line). After changing self-interactions of component A to $g_A^L/g_A^R = 2.1$ a dark soliton train is generated. Fig. 3.11 and Fig. 3.12 illustrate the spectrum of the time evolution for each component. The dark soliton train in component A represents the part of the effective potential for the other component B and, therefore, induces excitations in condensate B producing a bright soliton train (dashed line). As it can be seen in Fig. 3.10 the density depletions of one component are at the maxima of the other and vice versa. In particular the frequency of the dark soliton train in A is correlated with that in component B. As we showed above a change of self-interactions in an attractive single component condensate leads to a soliton train expanding in both directions (see Fig. 3.4). Hence, as the dark soliton train in A for $z > 0$ induces a bright soliton train in the other component B, which expands in both directions, this density depletion itself induces a dark soliton train expanding towards

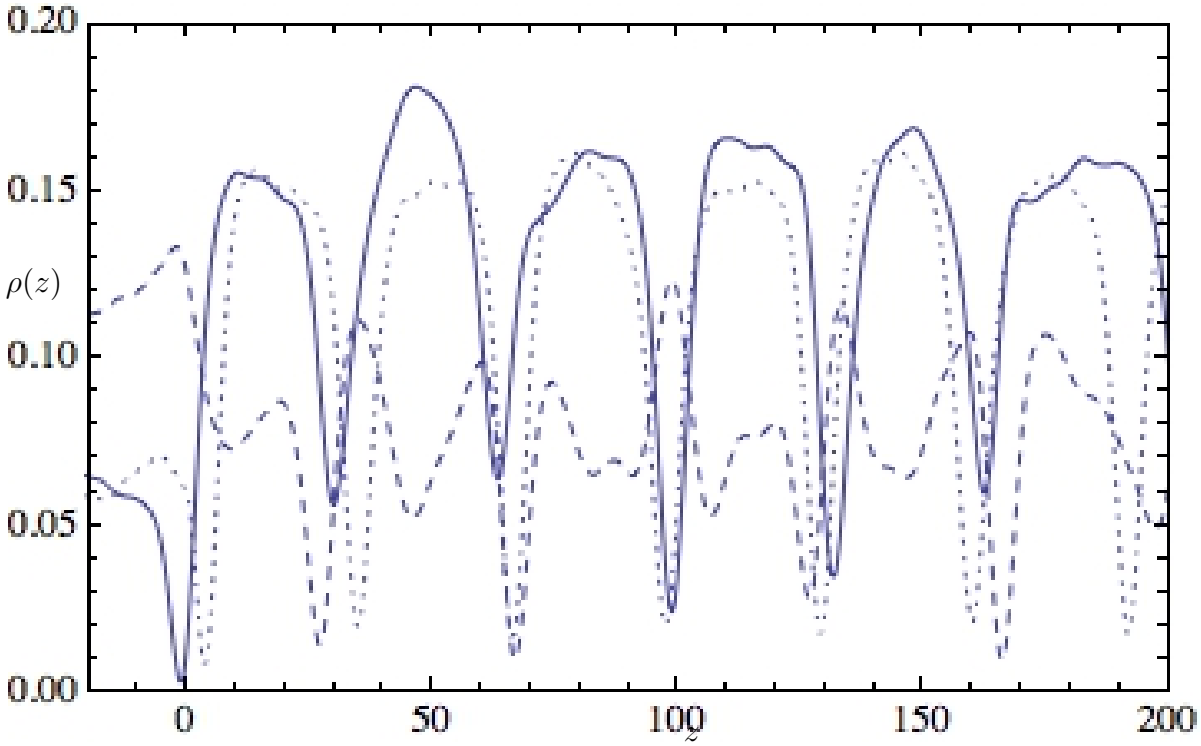

Figure 3.9: Density plot $\rho(z) = |\psi_{1D}(z,t)|^2$ of component A of a coupled BEC (solid line), component B (dashed line) at time $t = 390$ and a single component condensate (dotted line). Initial state has $g_A = g_B = g_{AB} = 1$. At time $t = 0$ the interactions of the condensate A are set to 3 on the left-hand side of the domain. The dimensionless units are used as specified in the main text.

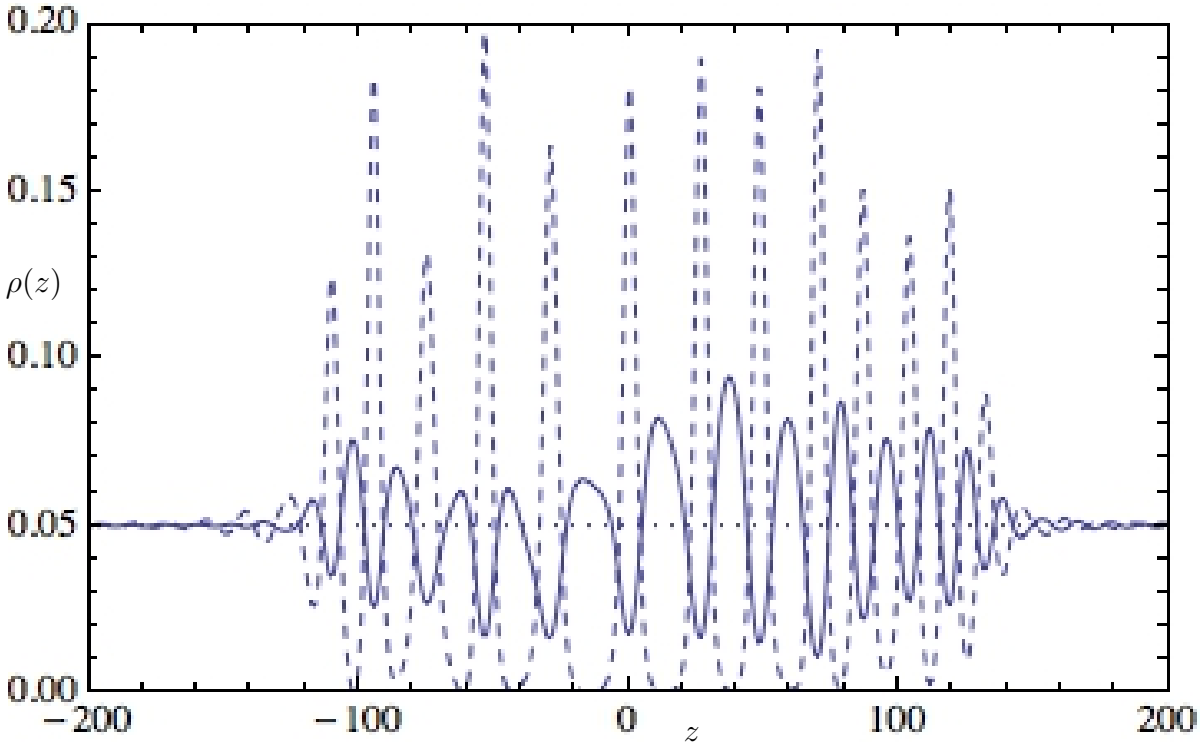

Figure 3.10: Snapshots of density plots $\rho(z) = |\psi_{1\mathrm{d}}(z,t)|^2$ of a two component BEC at $t = 0$ (dotted line) and $t = 300$ - component A (solid line) and B (dashed line). Initial state has $g_A = 1, g_B = -1, g_{AB} = 1$. At time $t = 0$ the interactions of the condensate A are set to 2.1 on the left-hand side of the domain. The dimensionless units are used as specified in the main text.

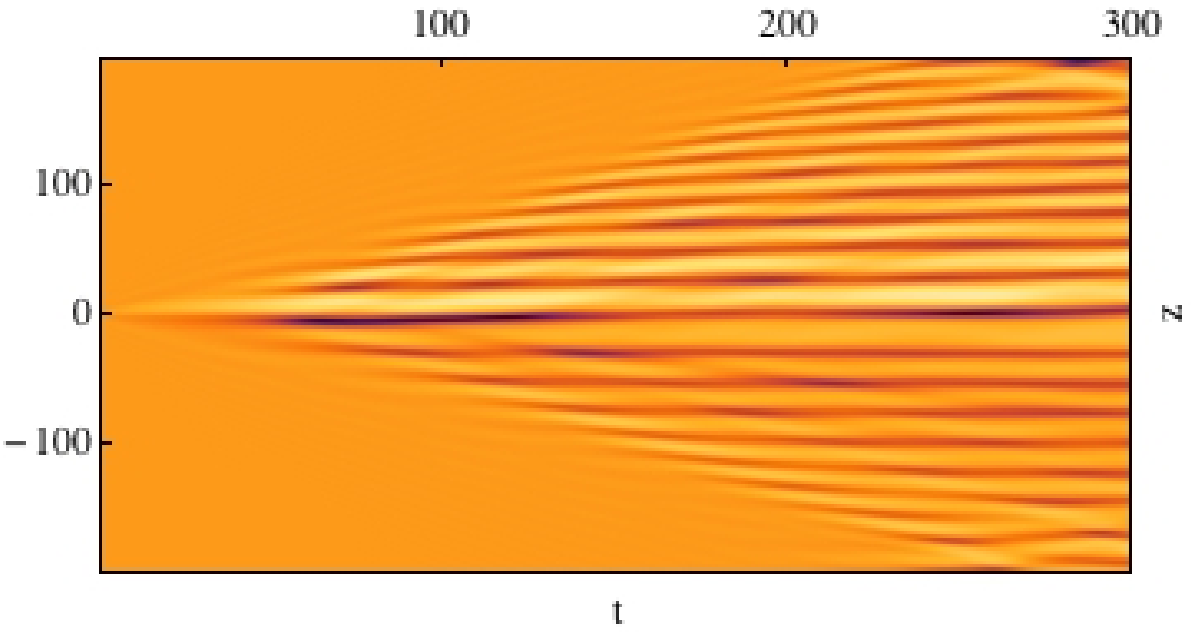

Figure 3.11: Pseudo-color density plot $\rho(z) = |\psi_{1\mathrm{D}}(z,t)|^2$ of component A of a uniformly distributed Bose gas with constant interaction $g_A = g_{AB} = 1 = g^R$ and $g_B = -1$ at $t = 0$ evolving in time as a change of $g^L/g^R = 2.1$ has been implemented in A for $t > 0$. The change in interactions is sharp at $z = 0$, i.e., $k \to \infty$ in (3.3.3). Here luminosity is proportional to density. The dimensionless units are used as specified in the main text.

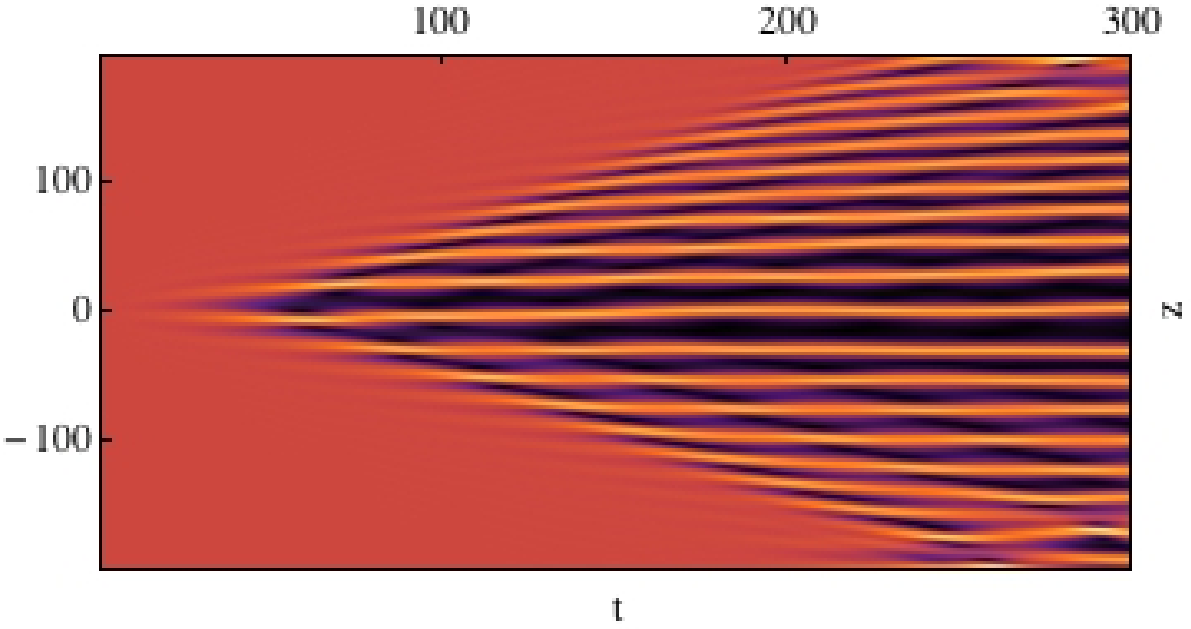

Figure 3.12: Pseudo-color density plot $\rho(z) = |\psi_{1D}(z,t)|^2$ of component B of a uniformly distributed Bose gas with constant interaction $g_B = -1$ and $g_A = g_{AB} = 1 = g^R$ at $t = 0$ evolving in time as a change of $g^L/g^R = 2.1$ has been implemented in A for $t > 0$. The change in interactions is sharp at $z = 0$, i.e., $k \to \infty$ in (3.3.3). Here luminosity is proportional to density. The dimensionless units are used as specified in the main text.

$z < 0$ in component A (Fig. 3.10.) Starting from the same initial distribution and changing interactions in the attractive condensate has a comparable effect, i.e., soliton trains in both components on the whole line are created. In any case only a very small change in self-interactions is sufficient to start this process, which is comparable to the behavior of the attractive single component condensate and due to its instability.

General analytical solutions to two component condensates, where one component is in a state corresponding to a dark soliton train while the other component represents a bright soliton train can be constructed using the previous expressions (3.4.3) and (3.4.4). Thus, a dark soliton train of the form

$$\psi_{\mathrm{A}}(z,t) = \sqrt{n_0}\left[i\frac{v}{c} + \sqrt{1-\left(\frac{v}{c}\right)^2}\cdot \right. \\ \left. \cdot \,\mathrm{sn}\left(\sqrt{1-\left(\frac{v}{c}\right)^2}\cdot\sqrt{\frac{n_0(g_A-g_{AB})}{2p^2}}\cdot(z-vt)\,\middle|\,p^2\right)\right], \quad (3.5.3)$$

can be coupled to a bright soliton train of the form

$$\psi_{\mathrm{B}}(z,t) = \sqrt{n_0}\left[i\frac{v}{c} + \sqrt{1-\left(\frac{v}{c}\right)^2}\cdot \right. \\ \left. \cdot \,\mathrm{cn}\left(\sqrt{1-\left(\frac{v}{c}\right)^2}\cdot\sqrt{\frac{n_0(g_B-g_{BA})}{2p^2}}\cdot(z-vt)\,\middle|\,p^2\right)\right], \quad (3.5.4)$$

where one has to introduce appropriate chemical potentials in (3.5.1) and (3.5.2) and both trains have the same periodicity. We refer to appendix 3.10 for a short outline.

3.6 Controlled generation of vortex rings and soliton trains in $3D$

Let us now remove the constraint of one-dimensional geometries, but we still consider cigar-shaped traps. Due to the phenomenon of snake instability in dimensions higher than one, dark solitons in repulsive condensates decay into more stable excitations such as vortices [162, 163] or vortex rings. Thus we would expect that once dark solitons are generated, they would decay into vortex rings in three-dimensions and the threshold in the self-interaction imbalance for the generation of these excitations would be close to the one obtained in the quasi-one dimensional system discussed earlier.

The scenario of vortex rings nucleation is very similar to that of vortex rings formation after a cavity collapse [133]. When the train of shock waves/dark solitons is formed, some part of the front breaks into vortex rings with an extra energy necessary to drive such transition provided by the part of the train traveling behind [165]. The energy transfer also counteracts the effect of the friction allowing the ring to travel a long distance before breaking apart.

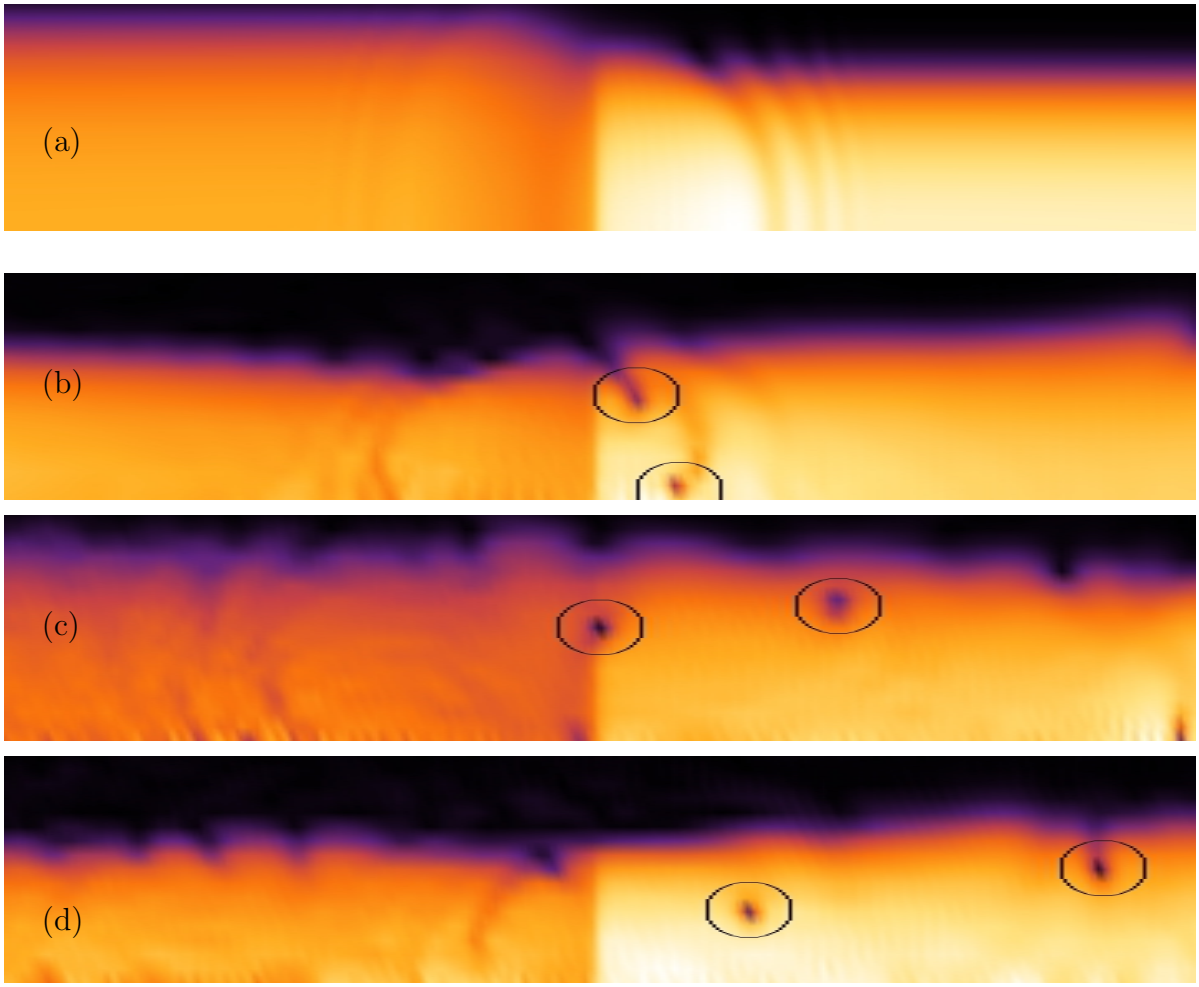

Figure 3.13: (Color online) Same as in Fig. 3.13 but for $g^L/g^R = 2.1$ and times (a) $t = 0.75$, (b) $t = 4.5$, (c) $t = 7.5$, (d) $t = 11.25$. The spatial region shown corresponds to $z \in [-20, 20], r \in [0, 8]$. Black corresponds to low atom densities and yellow to high ones. The dimensionless units are used as specified in the main text.

The presence of the solitary wave train enhances the instability leading to the formation of vortex rings in comparison with the instability of a single grey soliton. The faster the soliton moves the more stable it becomes. To overcome this stability there has to exist the supply of energy which is provided by the waves traveling behind.

3.6.1 Dynamics of single component BEC

We have numerically simulated Eq. (4.2.26) for various parameter combinations [214] and will describe the typical outcome for a specific example corresponding to a large repulsive BEC with $g = 10^5$, with $\lambda_x = \lambda_y = 1, \lambda_z = 0.05$ (i.e. soft longitudinal trapping). Our initial configuration is a ground state BEC corresponding to $g = g^L = g^R$. At time $t = 0$ we suddenly raise interactions strength g_L for $z < 0$ and then observe the subsequent

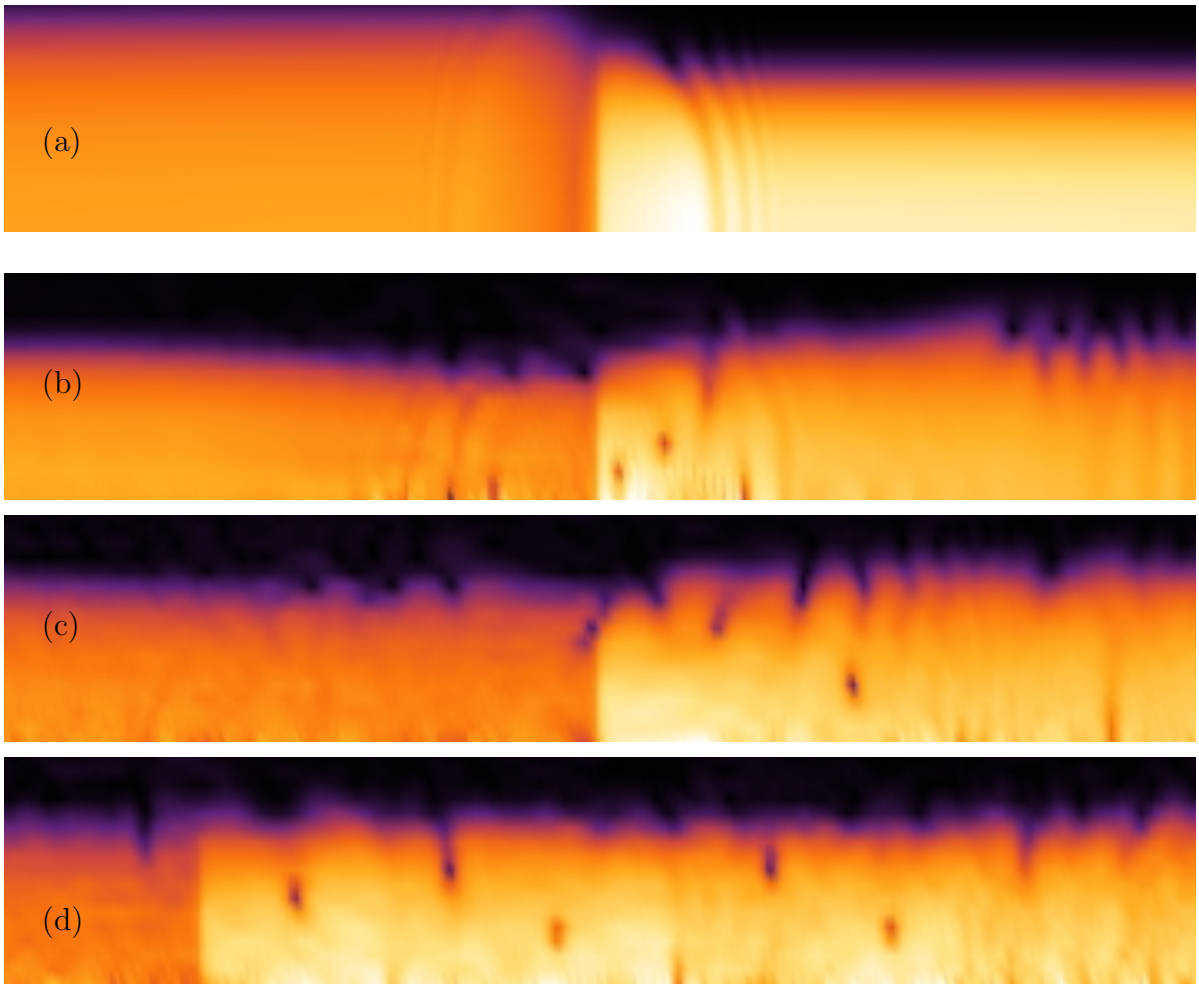

Figure 3.14: (Color online) Pseudocolor plot of atom density $|\psi(r,z,t)|^2$ snapshots for different values of time: (a) $t = 0.75$, (b) $t = 4.5$, (c) $t = 8.625$, (d) $t = 13.875$ and (e) $t = 18.375$. The values of the interactions $g^L/g^R = 2.3$ and the spatial region shown corresponds to $z \in [-30, 30], r \in [0, 8]$ in subplots (a-d) and to $z \in [-10, 50]$ in subplot (e). Black corresponds to low atom densities and yellow to high ones. The dimensionless units are used as specified in the main text.

evolution of the condensate.

Once the non-equilibrium situation is generated there is a flow of atoms from $z < 0$ to $z > 0$ with a flow intensity depending on the ratio g^L/g^R. When a critical value $g^L/g^R \simeq 2$ is surpassed the vortex rings are generated as seen on Fig. 3.13. It shows density plots with density depletions that characterize vortex rings, i.e. zero density around a closed curve in 3d. In addition these density depletions are accompanied by the 2π phase jumps not shown in the pictures. In Fig. 3.13 we present the stages of vortex rings formation for $g^L/g^R = 2.1$. The change in interaction strength leads to a generation of a train of dark solitons, see Fig. 3.13(a), that evolve into vortex rings which enter the condensate around $z = 0$ coming from the low density region, see Fig. 3.13(b), and move slowly through the condensate remaining stable for long times [Fig. 3.13(c,d)]. Another vortex ring with a large radius seems to be present in the lower density regions where it would be experimentally difficult to detect.

Increasing the interactions even further to $g^L/g^R = 2.3$ leads to a richer dynamics as summarized in Fig. 3.14. The short-time dynamics is analogous to the previous cases [Fig. 3.14(a)] but then a complex transient appears where several vortex rings enter the condensate; also rarefaction pulses are clearly identified [see Fig. 3.14(b)]. After that, some of those vortices counter-flow and disappear and a much more regular picture arises with several vortex rings moving to the right in a very clear way. Fig. 3.14(c) shows few vortex rings slowly moving through the condensate for $t = 8.625$ and one being generated around $z = 0$. Fig. 3.14(d) shows a later stage of the evolution where three long-lived vortex rings travel smoothly through the condensate although their relative positions changes due to differences in their speeds (notice the small differences in their radii) and their interaction with sound waves originated after the reflection of the shock wave in the condensate boundary [see Fig. 3.14(e)].

Fig. 3.15 shows that changing interactions to attractive, i.e., a change of $g^L/g^R = -10^{-3}$ for $z < 0$ causes the formation of a shock wave there and the formation of solitonic waves, similar to the formation of bright soliton trains in quasi-one dimensional BECs. Due to the small attractive force between particles and the tight potential in the transverse direction the condensate gently collapses into a quasi-one dimensional setup, thereby carrying stable solitons in its attractive part. Increasing the attractive force to more negative values of scattering length leads to a blowup of the condensate wave function, while lowering implies more stable solitary waves even for BEC without interaction ($g^L = 0$). Lowering scattering lengths on the l.h.s. to positive values leads to vortex ring generation once a threshold is surpassed and to solitary waves as g^L tends to become smaller.

3.6.2 The two component case

We now turn to two component systems of clearly distinct states ψ_A and ψ_B with interactions to be chosen within the phase separation regime, $g_{AB}^2 > g_A g_B$, i.e. cross-interactions between both components are dominating. The harmonic trapping potential for the repulsive two component BEC has been specified by $\lambda_x = \lambda_y = 1, \lambda_z = 0.05$ (i.e. soft longitudinal trapping) for both components. To generate a quantum piston

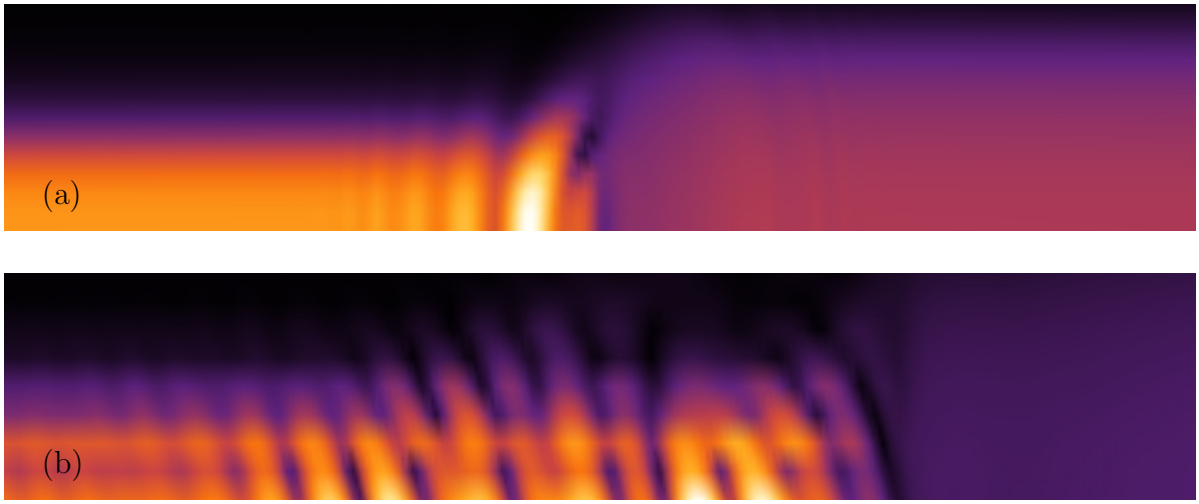

Figure 3.15: (Color online) Pseudocolor plot of atom density $|\psi(r,z,t)|^2$ snapshots for different values of time: (a) $t = 0.75$ and (b) $t = 3.75$. The values of the interactions are $g^L/g^R = -10^{-3}$. Black corresponds to low atom densities and yellow to high ones. The spatial region shown corresponds to $z \in [-20, 20], r \in [0, 6]$ in subplot (a) and to $z \in [-30, 10], r \in [0, 4]$ in subplot (b). The dimensionless units are used as specified in the main text.

induced evolution of the condensate wave functions containing skyrmions we tested various different initial conditions. The initial ground state at $t = 0$ on which we apply the quantum piston scheme consists of one component surrounded by the second component. The initial states are naturally generated by putting both components (each localized regarding a harmonic trap specified by $\lambda_x = \lambda_y = 1, \lambda_z = 0.05$ but one translated along the z-axis to the left and the other to the right) into the single trap without any overlapping of the atom clouds and by evolving the corresponding state in imaginary time until the new common ground state is reached at $t = 0$.

In Fig. 3.16 we show an example of density profiles of a two component BEC in such a ground state at $t = 0$, which is specified by its self-interactions $g_A = 6005$, $g_B = 2650$ and cross-interactions $g_{AB} = 6000$. After a change in self-interactions by a factor $g_A^L/g_A^R = 2.26$ on the l.h.s. in component A has been implemented vortices are generated. In particular we observe the emergence of a vortex ring in component A that is filled with mass of component B, which can be identified as a skyrmion - the corresponding area within the density distributions in Fig. 3.16 is encircled.

3.7 Conclusions

In this paper we have studied several examples of how the spatial and temporal control of the self-interactions in an atomic BEC leads to the formation of nonlinear excitation such as dark/bright solitons/ solitary trains and solitary waves using a nonlinear "quantum piston" concept. In an axisymmetric elongated condensate vortex rings form as the interaction strength on one half of the condensate changes by a factor exceeding 2. This mechanism can be used to controllably generate and study such excitations. Our

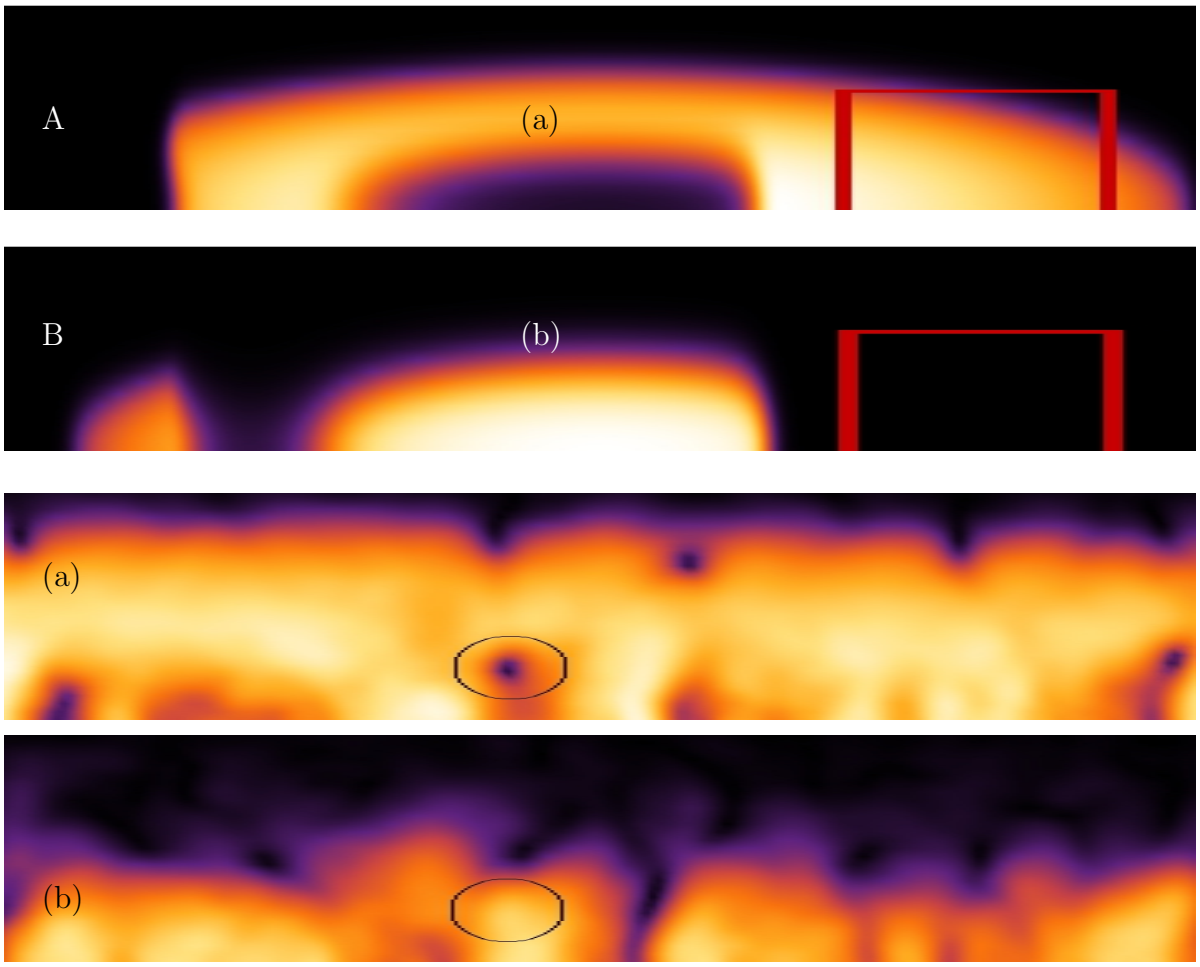

Figure 3.16: (Color online) Pseudocolor plot of atom density $|\psi(r,z,t)|^2$ snapshots of component A and component B in the initial state at $t = 0$. The spatial region shown corresponds to $z \in [-120, 120]$ and $r \in [0, 10]$. Subplots (a),(b) at $t = 35.25$ show details for a region $z \in [30, 60]$, $r \in [0, 7]$. The circle marks the position of a "skyrmion" – vortex in the first component with the density maximum of the second component. The dimensionless units are used as specified in the main text.

proposal, in addition to being conceptually simple and accessible to present experimental techniques improves essentially currently used methods to produce nonlinear excitations. Two component Bose-Einstein condensates could be used to amplify the generation of vortex rings or solitons and give rise to another set of excitations such as skyrmions. The number of vortex rings/skyrmions generated can be controlled by changing the transverse confinement ω/ω_z. For weak transverse confinement a moving solitary wave is subject to snake instability leading to the formation of vortex rings. For a sufficiently tight transverse confinement the solitary wave becomes stable to the snake instability and vortices will not form.

The faster a solitary wave moving the more stable it becomes to the snake instability. In the periodic train the stability is reduced because of the energy transfer between the parts of the train [165]. The vortex generation in the proposed method, therefore, is the result of an intricate interplay between shock wave train generation and the snake instability enhanced by the energy transfer between the parts of the train.

3.8 Stationary solutions to GPE with step-like coupling parameter

We will describe here a procedure to construct time independent solutions of the GPE (3.4.1) with step function coupling parameters. To introduce the method we will consider the second derivative of a 'two branches of the real line' ansatz defined as

$$u(z) = \tanh(g_+(z)) + \tanh(g_-(z)). \tag{3.8.1}$$

Here the basic idea is that one branch (denoted by the subscript $-$) takes into account properties of the solution for $z < 0$ and the other branch (denoted by the subscript $+$) properties relevant in $z > 0$. The arguments of the hyperbolic tangent, g_+ and g_-, are explicitly given by

$$g_+(z) = \lim_{k\to\infty} \frac{\log\left(e^{2kz}+1\right)}{2k} = \begin{cases} |z| & z > 0 \\ 0 & \text{otherwise} \end{cases} \tag{3.8.2}$$

and

$$g_-(z) = \lim_{k\to\infty} \frac{-\log\left(e^{-2kz}+1\right)}{2k} = \begin{cases} 0 & z \geq 0 \\ -|z| & \text{otherwise} \end{cases} \tag{3.8.3}$$

Consequently the derivatives of these functions are

$$g'_+(z) = \lim_{k\to\infty} \frac{1}{1+e^{-2kz}} = \begin{cases} 1 & z > 0 \\ 1/2 & z = 0 \\ 0 & \text{otherwise} \end{cases} \tag{3.8.4}$$

and

$$g'_-(z) = \lim_{k\to\infty} \frac{1}{1+e^{2kz}} = \begin{cases} 1 & z < 0 \\ 1/2 & z = 0 \\ 0 & \text{otherwise} \end{cases} \tag{3.8.5}$$

and the second derivatives satisfy

$$g''_+(z) = \begin{cases} 0 & z \neq 0 \\ \infty & z = 0 \end{cases} \tag{3.8.6}$$

and

$$g''_-(z) = \begin{cases} 0 & z \neq 0 \\ -\infty & z = 0 \end{cases}. \tag{3.8.7}$$

These functions obey the property

$$-g''_+(0) = g''_-(0) = \lim_{k\to\infty}\left(-\frac{k}{2} + k\right) = \infty. \tag{3.8.8}$$

Now consider the second derivative of our ansatz, i.e.,

$$\partial_z^2 u(z) = \operatorname{sech}^2(g_+)g''_+ + \operatorname{sech}^2(g_-)g''_- - \\ - 2\operatorname{sech}^2(g_+)\tanh(g_+)g'^2_+ - 2\operatorname{sech}^2(g_-)\tanh(g_-)g'^2_-, \tag{3.8.9}$$

at $z = 0$, i.e., where by (3.8.8) and the fact that $g_+(0) = g_-(0) = 0$ one gets

$$\operatorname{sech}^2(g_+)g''_+ + \operatorname{sech}^2(g_-)g''_- = (g''_+ + g''_-) = 0. \tag{3.8.10}$$

Hence the second derivative of (3.8.1) satisfies

$$\partial_z^2 u(z=0) = 2\left(\tanh(g_+)^2 - 1\right)\tanh(g_+)g'^2_+ + \\ + 2\left(\tanh(g_-)^2 - 1\right)\tanh(g_-)g'^2_- = 0, \tag{3.8.11}$$

and

$$\partial_z^2 u(z \neq 0) = 2\left(\tanh(g_\pm)^2 - 1\right)\tanh(g_\pm)g'^2_\pm, \tag{3.8.12}$$

where the subindexes + and − correspond to $z > 0$ and $z < 0$ respectively

Let us go a step further and rescale our ansatz in order to get a solution for

$$\partial_z^2 u = \theta(z)|u|^2 u - \mu u \tag{3.8.13}$$

with

$$\theta(z) = \begin{cases} g_1 & \text{if } z < 0 \\ c & \text{if } z = 0 \\ g_2 & \text{if } z > 0. \end{cases} \tag{3.8.14}$$

The rescaled two branches ansatz is given by

$$u \equiv u_+ + u_- \equiv \sqrt{\frac{\mu}{g_2}}\tanh\left[\pm\sqrt{\frac{\mu}{2}}\tilde{g}_+(z)\right] + \\ \sqrt{\frac{\mu}{g_1}}\tanh\left[\pm\sqrt{\frac{\mu}{2}}\tilde{g}_-(z)\right] \tag{3.8.15}$$

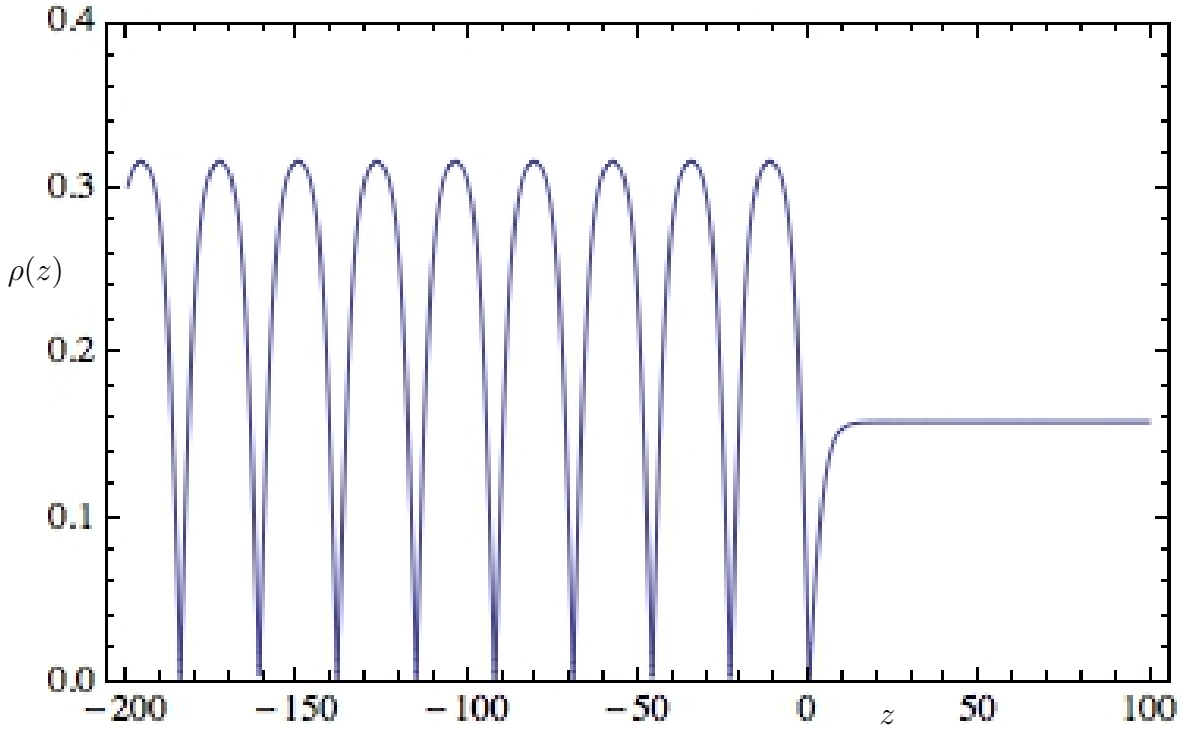

Figure 3.17: Density plot $|\psi_{1\mathrm{d}}(z,t)|^2$ of an example of an exact two branch real line solution to the GPE with constant self-interactions.

with phase functions defined by

$$\tilde{g}_+(z) = \lim_{k\to\infty} \frac{\log\left(e^{2\sqrt{g_1}kz}+1\right)}{2\sqrt{g_1}k} = \begin{cases} |z| & z>0 \\ 0 & \text{otherwise} \end{cases} \tag{3.8.16}$$

and

$$\tilde{g}_-(z) = -\lim_{k\to\infty} \frac{\log\left(e^{-2\sqrt{g_2}kz}+1\right)}{2\sqrt{g_2}k} = \begin{cases} 0 & z\geq 0 \\ -|z| & \text{otherwise} \end{cases} \tag{3.8.17}$$

To verify that (3.8.15) has the desired property we consider its second derivative

$$\begin{aligned} \partial_z^2\left(u_+ + u_-\right) = \frac{\mu}{\sqrt{2g_2}}\mathrm{sech}^2(g_+)g_+'' + \frac{\mu}{\sqrt{2g_1}}\mathrm{sech}^2(g_-)g_-'' - \\ - \mu^{3/2}\left(\frac{1}{\sqrt{g_2}}\mathrm{sech}^2(g_+)\tanh(g_+)g_+'^2 - \right. \\ \left. - \frac{1}{\sqrt{g_1}}\mathrm{sech}^2(g_-)\tanh(g_-)g_-'^2\right) \\ = g_2u_+^3 - \mu u_+ + g_1u_-^3 - \mu u_-. \end{aligned} \tag{3.8.18}$$

Note that u_+ is nonzero, iff $z>0$, as well as u_- is nonzero, iff $z<0$.

Furthermore one can interchange one branch or both by a Jacobi elliptic type function of a similar form as the hyperbolic tangent branches, which is a solution to the same differential equation (3.8.13). In Fig. 3.17 one finds an example of such a solution. On the left hand side one finds the Jacobi elliptic part while on the r.h.s. the density corresponds to a hyperbolic tangent wave function.

3.9 Determining self-interaction strength g of the condensate via the form of the soliton train

The 'free' parameters of the condensate wave function (3.4.3) are $\{n_0, v, p, g\}$ and the form of the analytical dark soliton train solution depends on the parameter p in (3.4.3) - if p is close to 1 the contribution of the hyperbolic tangens is dominating, while for smaller p the solution resembles properties of a squared sinus. Hence, one selects the elliptic modulus p by comparing the form of the numerically generated profile with the form of the analytical expression. The amplitude of the solution and the depth of each soliton are fixed by the requirement that at a maximum of the density graph we have

$$\max \left|\psi_{\mathrm{dt}}\right|^2 = n_0 = c_1, \tag{3.9.1}$$

and at a minimum

$$\min \left|\psi_{\mathrm{dt}}\right|^2 = \left(\frac{v}{\sqrt{2g}}\right)^2 = c_2, \tag{3.9.2}$$

where c_1 and c_2 are fixed numbers. The periodicity is fixed as well, i.e.,

$$\sqrt{1-\left(\frac{v}{c}\right)^2} \cdot \sqrt{\frac{n_0 g}{2p^2}} = c_3, \tag{3.9.3}$$

where c_3 again is a constant. Inserting (3.9.1) and (3.9.2) in (3.9.3) determines g. Hence we can determine the effective interactions between atoms and the velocity of the dark soliton train from the density profile of the condensate at a particular instant in time.

3.10 Dark-bright soliton train solutions for two component BEC

We now show that there exist analytical expressions for a dark soliton train in component A coupled to a bright soliton train in component B. We recognize that

$$\psi_{\mathrm{A}}(z,t) = \sqrt{n_0}\left[i\frac{v}{c} + \sqrt{1-\left(\frac{v}{c}\right)^2}\cdot \right. \\ \left. \cdot \,\mathrm{sn}\left(\sqrt{1-\left(\frac{v}{c}\right)^2}\cdot\sqrt{\frac{n_0(g_A-g_X)}{2p^2}}\cdot(z-vt)\,\middle|\,p^2\right)\right], \tag{3.10.1}$$

satisfies the equation

$$i\partial_t\psi_A = \left(-\partial_z^2 + \left(g_A|\psi_A|^2 - g_X|\psi_A|^2 - \mu\right)\right)\psi_A. \tag{3.10.2}$$

We rewrite some terms

$$\begin{aligned} -g_X|\psi_A|^2 - \mu = -g_X n_0\left(\frac{v^2}{c^2} + \left(1 - \frac{v^2}{c^2}\right)\mathrm{sn}^2\right) - \mu = \\ = g_X n_0\left(\frac{v^2}{c^2} + \left(1 - \frac{v^2}{c^2}\right)\mathrm{cn}^2\right) - \tilde{\mu} \end{aligned} \tag{3.10.3}$$

with $\tilde{\mu} = 2g_X n_0 \frac{v^2}{c^2} + g_X n_0\left(1 - \frac{v^2}{c^2}\right) + \mu$. Hence, by setting $g_X \to g_{AB}$ and defining

$$\begin{aligned} \psi_{\mathrm{B}}(z,t) = \sqrt{n_0}\Bigg[i\frac{v}{c} + \sqrt{1 - \left(\frac{v}{c}\right)^2}\cdot \\ \cdot \mathrm{cn}\left(\sqrt{1 - \left(\frac{v}{c}\right)^2}\cdot\sqrt{\frac{n_0(g_B - g_Y)}{2p^2}}\cdot(z - vt)\,\middle|\,p^2\right)\Bigg], \end{aligned} \tag{3.10.4}$$

with $g_B - g_Y = c = g_A - g_{AB} > 0$ (3.10.1) satisfies

$$i\partial_t\psi_A = \left(-\partial_z^2 + \left(g_A|\psi_A|^2 + g_{AB}|\psi_B|^2 - \tilde{\mu}\right)\right)\psi_A. \tag{3.10.5}$$

On the other hand (3.10.4) satisfies

$$\begin{aligned} i\partial_t\psi_B = \left(-\partial_z^2 + \left((g_B - g_Y)|\psi_B|^2 - \mu'\right)\right)\psi_B = \\ = \left(-\partial_z^2 + \left(g_B|\psi_B|^2 + g_{AB}|\psi_A|^2 - \mu''\right)\right)\psi_B, \end{aligned} \tag{3.10.6}$$

by setting $g_Y \to g_{AB}$ and for an appropriately chosen μ''.

4 Transitions and excitations in a superfluid stream passing small impurities

Florian Pinsker and Natasha G. Berloff, Phys. Rev. A **89**, 053605 (2014).

We analyse asymptotically and numerically the motion around a single impurity and a network of impurities inserted in a two-dimensional superfluid. The criticality for the break down of superfluidity is shown to occur when it becomes energetically favourable to create a doublet – the limiting case between a vortex pair and a rarefaction pulse on the surface of the impurity. Depending on the characteristics of the potential representing the impurity different excitation scenarios are shown to exist for a single impurity as well as for a lattice of impurities. Depending on the lattice characteristics it is shown that several regimes are possible: dissipationless flow, excitations emitted by the lattice boundary, excitations created in the bulk and the formation of large scale structures.

4.1 Introduction

Superfluidity is the property of extraordinary low viscosity in a fluid for which evidence was first found in liquid helium II, i.e., He-4 below the λ-point at 2.17K [166, 167]. Later it was proposed that liquid helium II can be regarded as a degenerated Bose-Einstein gas in the lowest energy mode [18] and the hydrodynamical picture was completed by arguing that the condensed fraction [12] of the superfluid does not take part in the dissipation of momentum [168]; it is due to the non-condensed atoms/molecules or quasi particles that viscosity occurs in superfluids. In 1995 condensation to the lowest energy state was achieved experimentally for weakly interacting dilute Bose-gases [4, 5, 6] and subsequently research on hydrodynamic properties has been presented; superfluidity could be confirmed by moving laser beams of different shapes through the condensate, which showed a drag force only above some critical velocity and dissipationless flow below [169, 170, 19, 171]. Experimental investigations have been accompanied by a great advancement in our theoretical understanding of this matter; a variety of scenarios [8], like superfluid flow around obstacles of different shapes at sonic or supersonic speed [172, 173, 174, 175, 176, 180, 181, 177, 178, 179], solitary waves due to inhomogeneities [25, 26, 88] or the transitions emerging in rotating Bose gases [182, 183, 184, 21, 22] have been considered. In more recent years superfluids made out of quasiparticles such as gaseous coupled fermions (Cooper pairs) [185, 186], spinor condensates [187, 188,

189], exciton-polaritons [190, 191, 16, 192, 193] or classical waves [194, 195, 17] have received much attention [15, 10]. New aspects emerge for investigation and the quest of elucidating defining properties of these novel superfluids goes on [196].

To study the nature of a superfluid, in particular the key property of zero viscosity at zero temperature $T = 0$, a well-established scenario to consider is an obstacle in relative motion to the fluid [169, 170, 19, 172, 173, 174, 175, 176, 180, 181, 177, 178, 179]. It was noted as early as in 1768 by d'Alembert [197] that an incompressible and inviscid potential flow past an obstacle encounters vanishing resistance, i.e., such a fluid is in a state of superfluidity. In this paper, however, we shall consider a *compressible* superfluid with zero viscosity obeying a finite speed of sound, which is to be described by a nonlinear Schrödinger-type equation. Among such superfluids governed by nonlinear Schrödinger-type equations are dilute and weakly interacting Bose-gases [11], condensates of classical waves [17] or exciton-polariton condensates close to equilibrium [193]. Due to the finite speed of sound the fluid obeys a critical velocity $v_{\rm cr}$ above which excitations occur within the condensate; superfluidity starts to dissipate, nodal points in the condensate wave function (with zero absolute value and discontinuities in the phase) might emerge forming quantized vortices [198]. In the presence of an obstacle this criterion needs to be modified as the full depletion of the condensate on the surface means that the local speed of sound is zero, this however does not lead to the excitation formation at low velocities. It has been shown by numerical simulations that this transition takes place when it becomes energetically favourable for a vortex to appear inside the healing layer on the surface of the obstacle [199]. By generating such elementary excitations as vortices or rarefaction pulses (for smaller perturbations) the system limits the superfluid flow velocity by the onset of a drag force on the moving obstacle due to those excitations. Emerging rarefaction pulses in the wake of the obstacle may exchange energy due to sound waves propagating through the condensate or via contact interaction as they encounter other excitations. When acquiring energy rarefaction pulses may transform into vortex pairs (or vortex rings in 3d) or by radiating energy vortex pairs collapse to excitations of lower energy [202].

In this paper we consider a condensate in 2 spatial dimensions (2d) passing finite size obstacles that are about the size of the superfluid's healing length. Initially the obstacles (which are assumed to be repulsive) either induce vortex pairs or rarefaction pulses into the superfluid's stream; weaker impurities imposing just a slight dip of small radius on the superfluid density support the generation of rarefaction pulses while stronger interacting impurities favor the appearance of a vortex pair. Experimentally it has been shown in [203] that vortex pairs are stable excitations in oblate and effectively 2d Bose-Einstein condensates.

Using a species-selective dipole potential the localized impurities were created in experiment [204]. To elucidate what kind of flows can exist in such systems we consider many impurities arranged on specific lattices and demonstrate that various regimes are possible depending on the network configuration. The motion of generated excitations within the lattice is strongly affected by their attraction to the impurities and interactions between excitations.

Our paper is organized as follows. In Section 1 we use asymptotic expansions to

estimate the density, velocity and energy of the condensate moving past a fixed obstacle and determine analytically the speed at which the vortex nucleation takes place as a function of the radius of the obstacle. In Section 2 we analyze how the form of the potential modelling the impurity affects the excitations nucleated. In Section 3 we study various regimes in superfluid flow passing impurity networks. We conclude by summarizing our findings.

4.2 1. Asymptotic expansion for a flow around a disk below the criticality

In this section we extend the analysis done in [177] for the flow around a two-dimensional disk of a radius large compared to the healing length to obtain the corrections due to the finite disk size. The condensate order parameter satisfies the Gross-Pitaevskii equation [11] in the reference frame moving with velocity $\vec{v}$, oriented along the positive x-direction:

$$i\hbar\partial_t\psi = -\frac{\hbar^2}{2M}\Delta\psi + V^{\rm nat}\psi - (E + \frac{1}{2}Mv^2 - g|\psi|^2)\psi. \tag{4.2.1}$$

The expression $E + \frac{1}{2}Mv^2$ is the energy in the moving reference frame at which the impurity is at rest. In this model M is mass of a boson, $g > 0$ is the strength of the repulsive self-interactions within the fluid and dependent on the number of its atoms [11], $V^{\rm nat}$ denotes the potential modeling the impurities, E the single-particle energy in the laboratory frame. A natural scale in our discussion is the healing length, $\xi = \hbar/(2ME)^{1/2}$.

We develop the asymptotics of the order parameter $\psi = \sqrt{\rho}\exp(i\phi)$. We use the nonlinear Schrödinger equation (4.2.1) where, for simplicity, we drop the potential $V^{\rm nat}$ in favor of boundary conditions on the order parameter for which the potential is an impenetrable barrier of radius b, so $\psi(r < b, t) = 0$, where $r^2 = |\vec{x}|^2 = x^2 + y^2$. We write Eq. (4.2.1) in hydrodynamical form using the Madelung transformation

$$\psi = R\mathrm{e}^{iS}, \tag{4.2.2}$$

so that

$$\rho = MR^2, \qquad \phi = (\hbar/M)S, \tag{4.2.3}$$

and rescale the resulting equations using $\vec{x} \to b\vec{x}$, $t \to (\xi bM/\hbar)t$, $v \to (\hbar/\xi M)U$ and $\psi \to \psi_\infty\psi$, where $\psi_\infty = (E/g)^{1/2}$, and using the dimensionless parameter $\varepsilon = \xi/b$. The resulting system of equations becomes

$$\varepsilon^2\nabla^2 R - R(\nabla S)^2 = (R^2 - 1 - U^2)R \tag{4.2.4}$$

$$R\nabla^2 S + 2\nabla R\cdot\nabla S = 0, \tag{4.2.5}$$

subject to the boundary conditions $R = 0$ at $r = 1$, $S \to -Ux$ and $R \to 1$ as $r \to \infty$. We shall assume that both ε and U are small and consider an asymptotic expansion of the solution to Eq. (4.2.4) and (4.2.5).

Boundary layer.- At the boundary layer the quantum pressure contribution plays a crucial role. We introduce $r = 1 + \varepsilon\chi$ and expand R and S as

$$R(\chi,\theta) = \widehat{R}_0(\chi,\theta) + \varepsilon\widehat{R}_1(\chi,\theta) + \varepsilon^2\widehat{R}_2(\chi,\theta) + \dots \tag{4.2.6}$$

$$S(\chi,\theta) = \widehat{S}_0(\chi,\theta) + \varepsilon\widehat{S}_1(\chi,\theta) + \varepsilon^2\widehat{S}_2(\chi,\theta) + \dots \tag{4.2.7}$$

The solutions to $O(\varepsilon^2)$ in $\hat{S}$ and the leading order for R were found in [177] for a spherical object, for the disk these become

$$\widehat{R}_0 = g(\theta)\tanh\left(g(\theta)\chi/\sqrt{2}\right), \quad \widehat{S}_0 = \widehat{S}_0(\theta), \quad \widehat{S}_1 = \widehat{S}_1(\theta) \tag{4.2.8}$$

$$\widehat{S}_2 = -\frac{\partial}{\partial\theta}\left(h(\chi,\theta)\frac{d}{d\theta}\widehat{S}_0\theta\right) + \zeta_2(\theta), \tag{4.2.9}$$

where

$$\begin{aligned} h(\chi,\theta) &= \int_0^{\chi}\frac{d\chi'}{\widehat{R}_0^2(\chi',\theta)}\int_0^{\chi'}\widehat{R}_0^2(\chi'',\theta)d\chi'' \\ &= \frac{1}{2}\chi^2 - \frac{\sqrt{2}\chi}{g(\theta)}\coth\Big(\frac{g(\theta)\chi}{\sqrt{2}}\Big), \end{aligned} \tag{4.2.10}$$

and $\hat{S}_0(\theta), \hat{S}_1(\theta)$ and $\zeta_2(\theta)$ are functions that will be determined by matching to the mainstream and

$$g(\theta) = \sqrt{\left(1 + U^2 - \left(\hat{S}_0'(\theta)\right)^2\right)}. \tag{4.2.11}$$

Mainstream.- To leading order, the mainstream flow is governed by

$$R^2 = 1 + U^2 - (\nabla S)^2 \tag{4.2.12}$$

$$R^2\nabla^2 S + \nabla R^2\nabla S = 0 \tag{4.2.13}$$

that can be combined to a single equation on S

$$(1 + U^2 - 3(\nabla S)^2)\nabla^2 S = 0. \tag{4.2.14}$$

We expand S in powers of ε as in [177]

$$S(r,\theta) = S_0(r,\theta) + \varepsilon S_1(r,\theta) + \varepsilon S_2(r,\theta) + \cdots \tag{4.2.15}$$

where S_0, S_1 etc. are expanded in powers of U as

$$S_0 = US_{11}(r)\cos\theta + U^3(S_{31}(r)\cos\theta + S_{33}(r)\cos 3\theta) + \cdots, \tag{4.2.16}$$

where we assumed that $\theta = 0$ is parallel to $\vec{v}$. The solutions for the mainstream we find up to $O(U^{11})$; the first few are

$$
\begin{aligned}
S_{11} &= -\frac{r^2+1}{r}, \quad S_{31} = \frac{c_1}{r} + \frac{6r^2-1}{6r^5}, \quad S_{33} = \frac{c_2}{r^3} + \frac{1}{2r}, \\
S_{51} &= \frac{c_1}{2r^5} - \frac{2c_1}{r^3} + \frac{c_2}{2r^7} - \frac{c_2}{r^5} + \frac{c_3}{r} - \frac{7}{30r^9}, \\
&+ \frac{19}{12r^7} - \frac{8}{3r^5} + \frac{3}{2r^3} \\
S_{53} &= -\frac{c_1}{2r} + \frac{3c_2}{5r^7} - \frac{3c_2}{r^5} + \frac{c_4}{r^3} - \frac{1}{36r^9} + \frac{11}{30r^7}, \\
&- \frac{2}{r^5} + \frac{1}{2r} \\
S_{55} &= -\frac{3c_2}{2r^3} + \frac{c_5}{r^5} - \frac{3}{4r^3} - \frac{1}{4r}.
\end{aligned} \tag{4.2.17}
$$

To carry out the asymptotic matching, we substitute $r = 1 + \varepsilon\xi$ into the mainstream functions, expand the solution (4.2.16) in powers of ε and match it to the boundary layer solution. To this order it is the same as to request that $S'_{ij}(r) = 0$ at $r = 1$, so on the boundary of the disk. Thus we found the solution S_0 to $O(U^{11})$. The first few terms are (correcting the expression given in [177])

$$
\begin{aligned}
S_0(r,\theta) = -U\frac{(r^2+1)}{r}\cos\theta + U^3\left[\left(\frac{6r^2-1}{6r^5} - \frac{13}{6r}\right)\cos\theta + \left(\frac{1}{2r} - \frac{1}{6r^3}\right)\cos 3\theta\right] \\
+U^5\left[\left(-\frac{7}{30r^9} + \frac{3}{2r^7} - \frac{43}{12r^5} + \frac{35}{6r^3} - \frac{479}{60r}\right)\cos(\theta) + \left(-\frac{1}{36r^9} + \frac{4}{15r^7} - \frac{3}{2r^5} + \frac{43}{30r^3} + \frac{19}{12r}\right)\cos 3\theta \right. \\
\left. + \left(\frac{7}{20r^5} - \frac{1}{2r^3} - \frac{1}{4r}\right)\cos 5\theta\right] + \cdots.
\end{aligned} \tag{4.2.18}
$$

The boundary layer function becomes $\widehat{S}_0 = S_0(1,\theta)$ and the maximum flow velocity is when $\cos\theta = 1$ ($\theta = \pi/2$). The corresponding maximum velocity is

$$
\begin{aligned}
u_{0\max} &= \frac{1}{r}\frac{\partial S_0(r,\theta)}{\partial\theta}\bigg|_{r=1,\theta=\frac{\pi}{2}} = \\
&= 2U + \frac{7}{3}U^3 + \frac{176}{15}U^5 + \frac{1511639}{18900}U^7 + \frac{5084105183}{7938000}U^9 + \frac{311688814107079}{55010340000}U^{11} + \cdots
\end{aligned} \tag{4.2.19}
$$

This coincides with the expression for the velocity (in terms of Mach number) obtained in [205] via a Janzen-Rayleigh expansion applied to the classical problem of the flow of a compressible fluid passing around a solid disk.

The equation (4.2.14) becomes hyperbolic beyond a critical velocity. It first happens at $u_{\max}$ such that

$$
1 + U^2 = 3u_{\max}^2. \tag{4.2.20}
$$

Solving this equation for $u_{\max}$ as shown in Eq. (4.2.19) gives $U = 0.263$, or in dimensionless units $v = 0.37c$. By considering the terms of the mainstream expansion up to $O(U^{40})$ we recover $v = 0.36969(7)c$ in agreement with [205].

To get the analytical expression for the critical velocity for a finite size of the disk we need to consider the $\mathcal{O}(\varepsilon)$ contribution to the mainstream solution that satisfies the equations

$$R_0 R_1 = -\nabla S_0 \cdot \nabla S_1 \tag{4.2.21}$$

$$\left[1 + U^2 - 3(\nabla S_0)^2\right] \nabla^2 S_1 = 6 \nabla S_0 \cdot \nabla S_1 \nabla^2 S_0. \tag{4.2.22}$$

For S_1 we employ the expansion similar to Eq. (4.2.16), solve the ordinary differential equations for S_{ij} to get

$$\begin{aligned} S_1(r,\theta) = \frac{d_1}{r} U \cos\theta &+ U^3 \left[\cos\theta \left(\frac{d_1}{2r^5} - \frac{2d_1}{r^3} + \frac{d_2}{r} \right) \right. \\ &+ \left. \cos 3\theta \left(\frac{d_3}{r^3} - \frac{d_1}{2r} \right) \right] \cdots, \end{aligned} \tag{4.2.23}$$

where the constants of integration d_i are found by matching the boundary-layer solution to (6.5). We substitute $r = 1 + \varepsilon\chi$ in (6.5), expand the solution in powers of ε and match to the dominant linear in χ term in (4.2.9). The corresponding term in $\widehat{S}_2$ is expanded in powers of v and in trigonometric functions. The resulting expression for the mainstream becomes

$$\begin{aligned} \frac{S_1(r,\theta)}{\sqrt{2}} = -U\frac{2}{r}\cos\theta + U^3 &\left[\left(\frac{5}{3r^3} + \frac{1}{r} \right) \cos 3\theta + \left(-\frac{1}{r^5} + \frac{4}{r^3} - \frac{31}{3r} \right) \cos\theta \right] + \\ &+ U^5 \left[\left(-\frac{17}{20r^5} - \frac{3}{r^3} - \frac{5}{2r^3} - \frac{1}{2r} \right) \cos 5\theta \right. \\ &+ \left(-\frac{5}{18r^9} + \frac{53}{15r^7} - \frac{16}{r^5} + \frac{1753}{60r^3} + \frac{1}{r} + \frac{31}{6r} \right) \cos 3\theta \\ &+ \left. \left(-\frac{7}{3r^9} + \frac{37}{3r^7} + \frac{5}{6r^7} - \frac{65}{3r^5} - \frac{31}{6r^5} + \frac{106}{3r^3} - \frac{1161}{20r} \right) \cos\theta \right] + \ldots \end{aligned} \tag{4.2.24}$$

The ε term in the expansion for the maximum value of the velocity on the disk is

$$\begin{aligned} u_{1\,\max} &= \frac{1}{r}\frac{\partial S_1(r,\theta)}{\partial\theta}\Big|_{r=1,\theta=\frac{\pi}{2}} \\ &= \sqrt{2}\left[2U + \frac{46U^3}{3} + \frac{8453U^5}{60} + \frac{5525323U^7}{3780}\right] + \cdots \end{aligned} \tag{4.2.25}$$

It is clear from this expression that the maximum velocity on the surface of the obstacle is growing as the radius of the obstacle decreases for constant velocity of the mainstream. Therefore, the nucleation of the excitations on the surface of the object is not directly relevant to the maximum velocity for the objects of a finite radius as numerical simulations show (see Section 2). As we show in the next section the vortices and other excitations appear when it becomes energetically possible to create a doublet on the surface. The asymptotics for ψ developed in this section allows us to get estimates of the energy of the system.

4.2.1 Critical velocity of nucleation

The effect of the finite size of an obstacle on the critical velocity of vortex nucleation has been studied numerically [199]. It was demonstrated that the nucleation takes place when it becomes energetically favourable to create a vortex on the surface of the obstacle. Here we use this criterion to obtain the critical velocity of nucleation by analytical means.

It is convenient to consider a different rescaling of (4.2.1) in units of $\vec{x} \to \xi\vec{x}$, $t \to (\xi^2 M/\hbar)t$, $v \to (\hbar/\xi M)U$ and $\psi \to (\psi_\infty e^{-iUx})\psi$ such that $\psi \to 1$ as $|\vec{x}| \to \infty$. The Eq. (4.2.1) becomes

$$2i\partial_t\psi = -\Delta\psi + V\psi + (|\psi|^2 - 1)\psi + i2U\partial_x\psi. \tag{4.2.26}$$

V denotes the rescaled potential modeling the fixed impurities inserted into the fluid's flow. The energy of the system (4.2.26) is [206]

$$E = \int |\nabla\psi|^2 + (1 - V - |\psi|^2)^2 d\vec{x}. \tag{4.2.27}$$

The solitary wave solutions such as vortex pairs and rarefaction pulses were analysed numerically in [206] and asymptotically in [202]. The lowest energy of vortical solutions is for the limiting case between a vortex pair and a rarefaction pulse: a doublet – a single nodal point of ψ when two vortices of opposite circulation collide. The doublet is moving through the uniform superfluid with velocity $U \approx 0.45$. Its explicit form can be approximated by adapting the Padé approximations considered in [202]:

$$\begin{aligned} u_d &= 1 + \frac{a_{10}x^2 + a_{01}y^2 - 1}{1 + c_{10}x^2 + c_{01}y^2 + c_{20}x^4 + c_{11}x^2y^2 + c_{02}y^4}, \\ v_d &= \frac{x(b_{00} + b_{10}x^2 + b_{01}y^2)}{1 + c_{10}x^2 + c_{01}y^2 + c_{20}x^4 + c_{11}x^2y^2 + c_{02}y^4}, \end{aligned} \tag{4.2.28}$$

where $u_d(x,y) = \mathrm{Re}(\psi)$ and $v_d(x,y) = \mathrm{Im}(\psi)$ for the doublet. The far field expansions for $|\vec{x}| \to \infty$ were considered in [206]:

$$\begin{aligned} u_d &\approx 1 + m\frac{(2U-m)x^2 - 2U(1-2U^2)y^2}{2(x^2+(1-2U^2)y^2)^2}, \\ v_d &\approx -\frac{mx}{x^2+(1-2U^2)y^2}. \end{aligned} \tag{4.2.29}$$

To match it with (4.2.28) we set

$$\begin{aligned} a_{10} &= \frac{1}{2}c_{20}m(2U-m), \quad a_{01} = -c_{20}m(1-2U^2)U, \\ b_{10} &= -mc_{20}, b_{01} = -mc_{20}(1-2U^2), \\ c_{11} &= 2c_{20}(1-2U^2), \quad c_{02} = c_{20}(1-2U^2)^2 \end{aligned} \tag{4.2.30}$$

and determine $b_{00}, c_{20}, c_{10}, c_{01}$ by expanding the stationary Eq. (4.2.26) with (4.2.28) around zero and setting the constant term, the terms at x^2 and y^2 in the real part of (4.2.26) as well as the term at x in the imaginary part of (4.2.26) to zero. The known value of $m = 3.32$ [206] for $U = 0.45$ complete the determination of unknowns in (4.2.28).

We approximate the wave function of the doublet sitting on the surface of the disk of the radius b by

$$\psi_d = u_d(x, y-b) + iv_d(x, y-b) \tag{4.2.31}$$

and obtain the energy from (4.2.27) where the integration is for $r > b$. The critical velocity of the vortex nucleation from the surface of the moving disk is then associated with the disk velocity at which the asymptotic solution (4.2.2) with S given by Eqs. (4.2.15), (4.2.18) and (6.15) and R given by Eq. (4.2.12) reaches the energy of the doublet sitting on the surface of a stationary disk. Figure 4.1 summarizes our findings and compares the resulting critical velocities with the numerical solutions. We found that the procedure for determining the criticality gives a good approximation for $20 > b/\xi > 2$, for large obstacles the criterion of the velocity exceeding the local speed of sound becomes more accurate, whereas for the obstacle sizes of the order of the healing length the asymptotic expansion of the solution breaks down.

In the next section we show that the shape of the potential modelling the impurity has a profound effect on the type of excitation created.

4.3 2. Nucleation of excitations: vortices and rarefaction pulses

The nonlinear Schrödinger equation (4.2.1) possesses elementary excitations in the form of solitary waves: vortex pairs and rarefaction pulses – finite amplitude sound waves [206]. In 2d rarefaction pulses have lower energy and momentum than vortex pairs, so one may expect that narrow impurities, with radii smaller than healing length, will generate rarefaction pulses rather than vortex pairs [180]. It is also clear from the

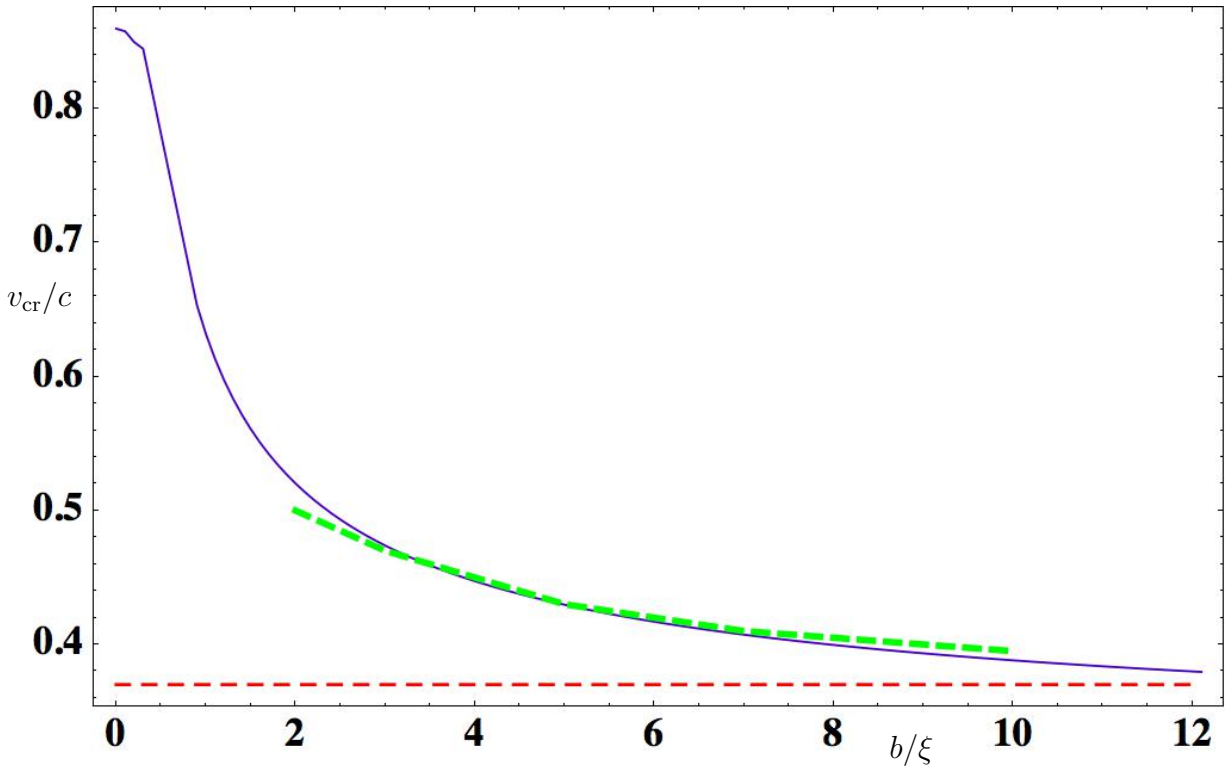

Figure 4.1: Critical velocity of vortex nucleation as a function of obstacle radius b/ξ. Solid line – numerically determined critical velocity. The critical velocity $v_{cr} = 0.36970c$ for an infinite obstacle is given by the thin red dashed line. Thick green dashed line – analytically determined critical velocity as explained in the text.

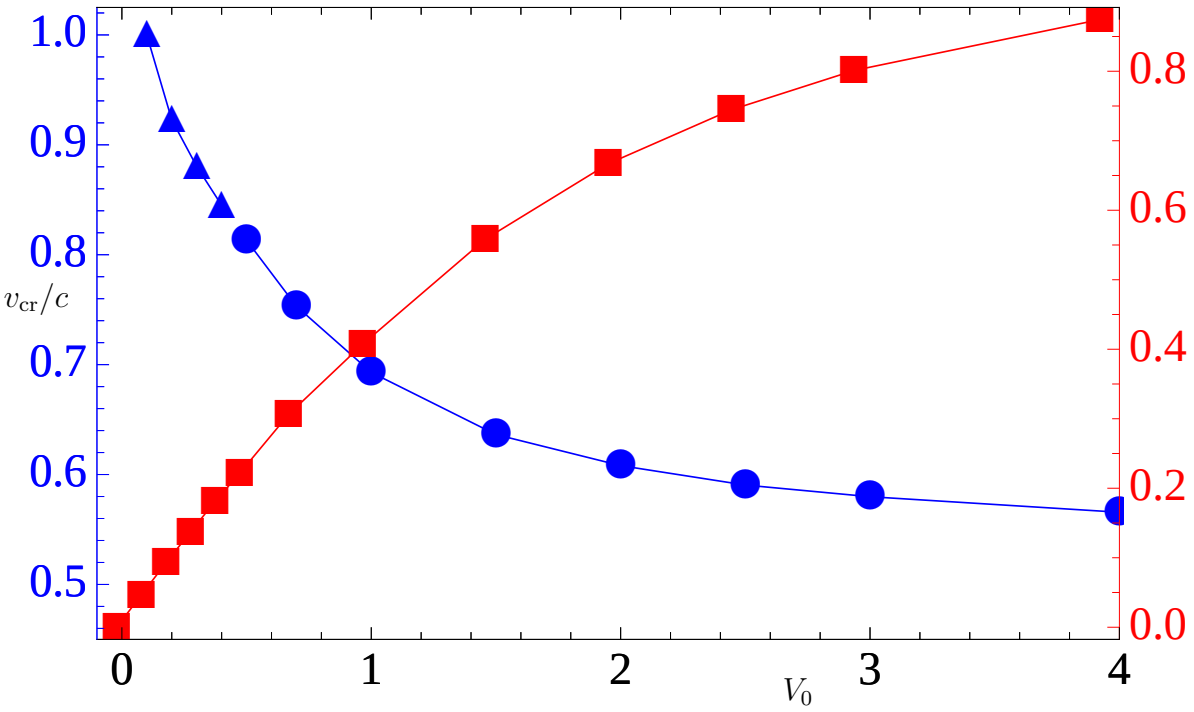

Figure 4.2: Critical velocity at which excitations are generated as function of obstacle height V_0 for fixed $b = \xi$. Dots represent the generation of vortex pairs, while triangles represent rarefaction pulses. Squares represent the depletion of the condensate (uniform density minus the minimum of the density at the centre of the potential) due to the repulsive interactions with the obstacle [207].

topology of the system that if the obstacle does not bring about the zero of the wave function of the condensate through the repulsive interactions the formation of a vortex pair always starts from a finite amplitude sound wave. Therefore, one can envision that depending on the properties of the repulsive interaction induced by the impurity on the condensate different excitations are generated.

We start by modelling the repulsive interactions between the obstacle at positions (x_i, y_i) and the condensate by a potential

$$V = V_0 \left(1 - \tanh\left[(x - x_i)^2 + (y - y_i)^2 - b^2\right]\right). \tag{4.3.1}$$

Here $V_0 > 0$ is the repulsive interaction strength between the impurity and the condensate and b the impurity radius.

Fig. 4.2 shows the dependence of the critical velocity on the height V_0 of the impurity potential. In particular we have numerically found that for a weaker potential (i.e., small V_0) rarefaction pulses are generated rather than vortex pairs. In order to distinguishing the generation of vortex pairs from the generation of the rarefaction pulses we have

throughout this work analyzed the excitations by evaluating if both the real and the imaginary part of the wave function are zero, when passing a radius of two healing lengths measured from the center of the impurity; setting a fixed radius is an unambiguous way to make an identification as for example a rarefaction pulse might gain energy when leaving the obstacle due to sound waves present in the condensate [202] and evolve into a vortex pair. We have observed that the smaller is the strength V_0 the greater is the critical velocity of nucleation; for zero depletion of the condensate the criticality agrees with the asymptotics considered in the previous section.

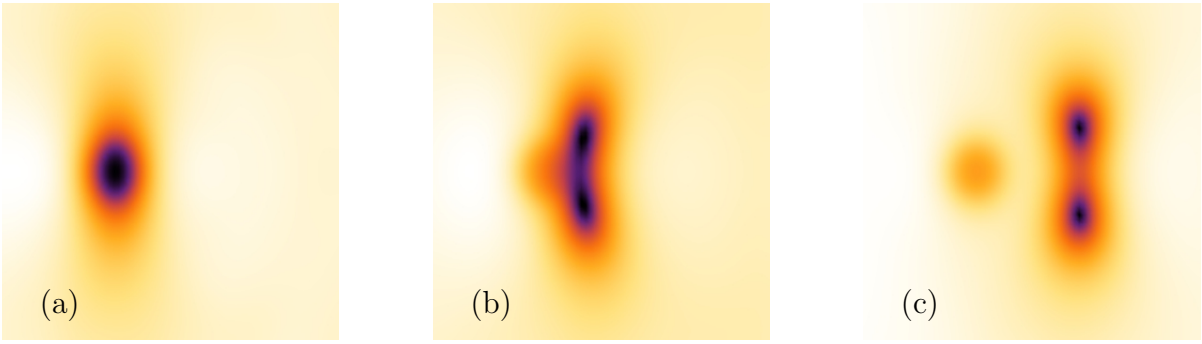

Figure 4.3: Vortex pair generation due to stronger BEC-impurity interaction.- Pseudo-color density plots of superfluid flow around an obstacle specified by $V_0 = 0.7$, $b = 1$ (measured in healing lengths) at $t = 60$; (a), $t = 84$; (b) and $t = 90$; (c) with velocity $v = 0.753c$. The more luminous the picture the higher the density. Each picture shown corresponds to an area of 15×15 [208]. The dimensionless units are used as specified in the main text.

As mentioned above if the obstacle does not completely deplete the condensate density at its centre, then it is topologically impossible to create a vortex pair on non-zero background. Instead a finite amplitude sound wave is created at the condensate density minimum which can evolve into either a vortex pair or a rarefaction pulse as the wave separates from the obstacle and gains energy entering the bulk. The outcome in this case depends on the energetics created by the obstacle: the larger V_0 the more energetic solution emerges. This is illustrated in Figs. 4.3 and 4.4. In Fig. 4.3 we show time snapshots illustrating the emergence of a vortex pair for a stronger barrier. A finite amplitude sound wave formed at the impurity atom (a) evolves into a pair of vortices (b) leaving towards the direction of the stream of the superfluid (c). Fig. 4.4 illustrates the formation of a rarefaction pulse at a weaker obstacle; here after a finite amplitude sound wave is formed at the obstacle it evolves into a rarefaction pulse that is carried away by the stream. In Fig. 4.5 we present the full wave functions of a rarefaction pulse and a vortex pair.

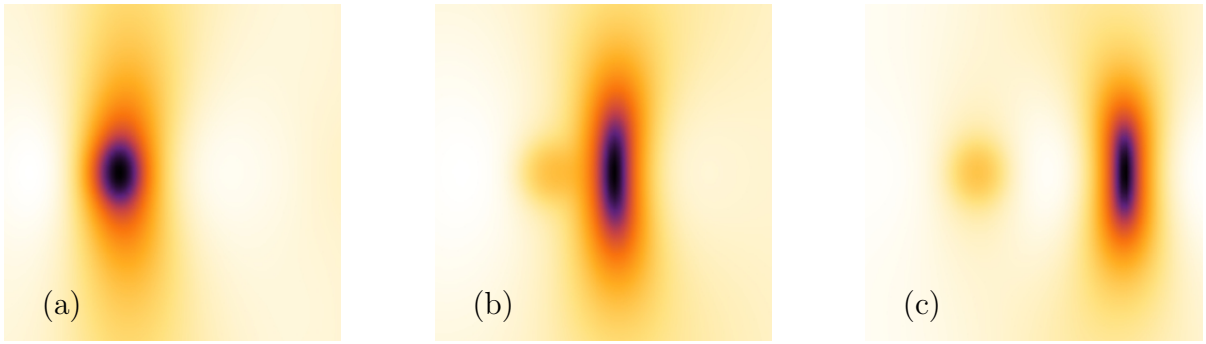

Figure 4.4: *R*arefaction pulse generation due to weaker potential.- Pseudo-color density plots of superfluid flow around an obstacle specified by $V_0 = 0.3$, $b = 1$ at $t = 150$; (a), $t = 175.5$; (b) and $t = 186$; (c) with flow velocity $v = 0.88c$. The more luminous the picture the higher the density. Each picture shown corresponds to an area of 15×15 [208]. The dimensionless units are used as specified in the main text.

Delta-function impurity.- The special case of a single delta-function impurity $V = \delta\left(x - x_i + y - y_i\right)$ can be regarded as a limiting case of the above setup, i.e., a single point obstacle at which the wave function is zero. In this case at the critical velocity slightly below the speed of sound rarefaction pulses are generated, see Fig. 4.6, consistent with considerations in [180]. However, for finite size obstacles in diameter even smaller than the healing length the vortex pairs can be generated as soon as the the depletion of the condensate density is steep enough (even if the wave function is not zero at the obstacle), see Fig. 4.7 where we considered a potential of the form $V = V_0\left(1 - \tanh\left[\alpha((x - x_i)^2 + (y - y_i)^2)\right]\right)$, with $\alpha > 1$.

Our numerical analysis shows that a stronger dip in the condensate makes a vortex pair favorable, while less deep depletions of small radius favor rarefaction pulses. In particular for weak BEC-impurity interactions of bigger radius ($V_0 \ll 1, b \gg 1$) we have found that vortex pairs are generated, see Fig. 4.8. Hence, it depends on the energy put into the system via the potential which excitation can be afforded, i.e., low energy potentials favour energetically cheaper rarefaction pulses while higher energy potentials more expensive vortex pairs.

Supersonic flow.- Finally, for completion, we consider the superfluid at supersonic speed (i.e., for Mach numbers $M = v/c > 1$) passing a narrow and only weakly interacting obstacle, that does not lead to a complete depletion of the condensate density at its position. The case of a strongly interacting (delta function) obstacle has been considered in [181, 212], where oblique dark soliton trains were observed in the wake of the obstacle. Here in Fig. 4.9 we present the emergence of rarefaction pulses in the stream of the condensate accompanied by Cherenkov waves outside the Mach cone. The rarefaction pulse in the wake of the obstacle clearly differs from the solitary waves (or

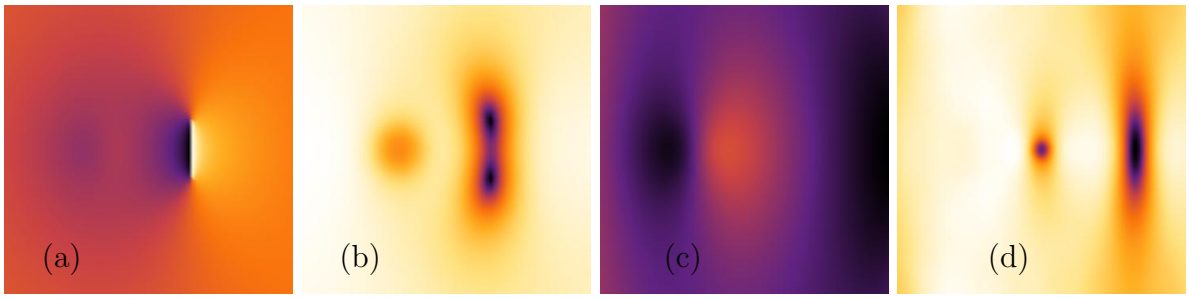

Figure 4.5: *D*ensity and Phase.- Pseudo-color density plots of the phase (a) and density (b) of the flow around an obstacle specified by $V_0 = 0.72$, $b = 1$ at $t = 150$ with flow velocity $v = 0.88c$ forming vortex pairs. It is compared with pseudo-color density plots of the phase (c) and density (d) of the flow around an obstacle inducing rarefaction pulses specified by $V_0 = 0.17$, $b = 1$ at $t = 170$ with flow velocity $v = 0.95c$. The more luminous the picture the higher the density. Each picture shown corresponds to an area of 15×15 [208]. The dimensionless units are used as specified in the main text.

continuous stream of vortex pairs) spotted for heavy (delta function) impurities in [181] in so far as not a full depletion of the condensate has been observed.

4.4 3. Superfluid regimes in the lattice of impurities

In this section we consider N inserted obstacles at positions (x_i, y_i) with $i \in \{1, \ldots, N\}$ that generate an external potential of the form

$$\mathcal{V} = V_0 \sum_{i=1}^{N} \left(1 - \tanh\left[(x - x_i)^2 + (y - y_i)^2 - b^2\right]\right). \tag{4.4.1}$$

The potential function of the whole array $\mathcal{V}$ depends on the spatial order of the inserted impurities, the radius b of the atoms and the strength of BEC-atom interaction V_0. We suppose that there are no interactions between the impurities themselves and that they are stationary, but remark that the additional presence of an atom in the superfluid leads to a change of the potential generated by the other atoms – their states are squeezed [213] within the superfluid. In this work, however, we do not address the issue *how* the size of the impurities materializes, but elucidate that *having a fixed size* affects the superfluid as presented.

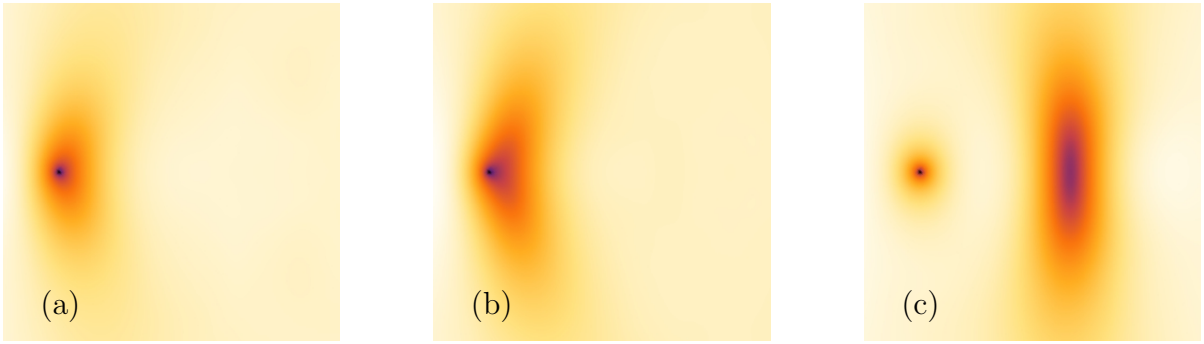

Figure 4.6: *R*arefaction pulse generation due to a delta-function impurity.- Pseudo-color density plots of superfluid flow around a delta impurity at $t = 21.5$ (a), $t = 26.5$ (b), $t = 41.5$ (c), with velocity $v = 0.92c$. Each picture shown corresponds to an area of 12×12 [209]. The more luminous the picture the higher the density. The dimensionless units are used as specified in the main text.

4.4.1 Impurities arranged into regular lattices

Let us consider the superfluid's flow around impurities arranged on a triangular lattice within a finite sized rectangular area. We distinguish different regimes in superfluid flow passing the lattice that besides the characteristics of impurity atoms V_0 and b depend on the velocity v, the distance between nearest neighbors a and the size of the lattice. The various regimes are presented in Fig. 4.10 qualitatively as functions of v and a: Area I corresponds to the superfluid phase, i.e., no excitations emerge in the superfluid's stream. The regime II is characterized by the emergence of vortices from the boundary of the network. III describes very dense packing of impurity atoms, such that for those velocities vortices are created on the boundaries of the entire lattice, while the superfluid is expelled from within the lattice. Region IV is described by excitations within the lattice, which span from excitations smaller then the healing length and ones bigger than a few healing lengths, i.e., emergent macroscopic structures. In region V vortices or rarefaction pulses are generated within the lattice as well as outside the lattice without forming bigger structures as a consequence of the sparsity of the impurity atom distribution.

In Fig. 4.11 we present the superfluid flow towards the right hand side around a sparse triangular lattice in the regions II and V. Above the first critical velocity v_1, excitations are generated at the end of the array and directly move into the wake (b) (region II). Above the second critical velocity v_2 excitations are continuously generated within the lattice and move - carried by the fluids stream - through the impurity network towards the wake of the system (c) (region V). In Fig. 4.12 we show the first v_1 and second v_2 critical velocities as functions of the mean distance between nearest neighbors a at the triangular lattice.

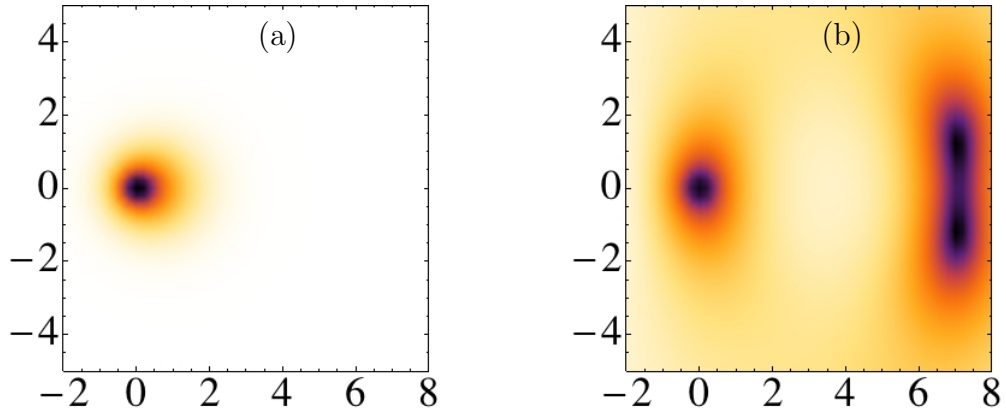

Figure 4.7: *V*ortex pair generation due to a potential of diameter less than a healing length.- Pseudo-color density plots of superfluid flow around a very small obstacle specified by $V_0 = 40$ and $\alpha = 7$ at $t = 0$ (a), $t = 22.8$ (b) with velocity at infinity $v = 0.92c$. Each picture shown corresponds to an area of 10×10 [210]. The more luminous the picture the higher the density. The dimensionless units are used as specified in the main text.

.

Let us take a closer look on the lattice dynamics in region V corresponding to a lattice of intermediate density of impurities. We could identify different processes of three body interactions of vortex dipoles with single vortex among that are the *flyby regime* and the *reconnection regime* [78]. The flyby characterizes the scenario where an incoming vortex pair gets deflected by the third vortex and the reconnection regime describes the situation where vortex 1 of the pair is coupled to the third vortex and the other vortex 2 of the pair is left behind. Moreover the transition from vortex pair to rarefaction pulse and vice versa due to loss or gain of energy through sound waves could be identified. In Fig. 4.13 an example of a vortex pair acquires a velocity component transversal to the motion of the fluid by pinning to the potential spikes is shown (see pictures (a),(b),(c),(d),(e),(f)). Here a vortex pair looses one vortex to an impurity. As the vortex moves away from the obstacle it pulls the trapped vortex back, while acquiring an additional transversal velocity component and heading towards the next impurity. This process can be classified as a *flyby*, when applying a vortex mirror-vortex analogy [215]. In addition we could identify a locally stationary single vortex placed at the centroid of the triangle formed by nearest neighbor impurities. When other vortices enter the scene they almost form a triangle by connecting with the impurity atoms at the corners (*connecting regime*) and due to gain of energy through perturbations subsequently decay into many vortices.

For weaker BEC-impurity interactions we have found an intermediate regime, where

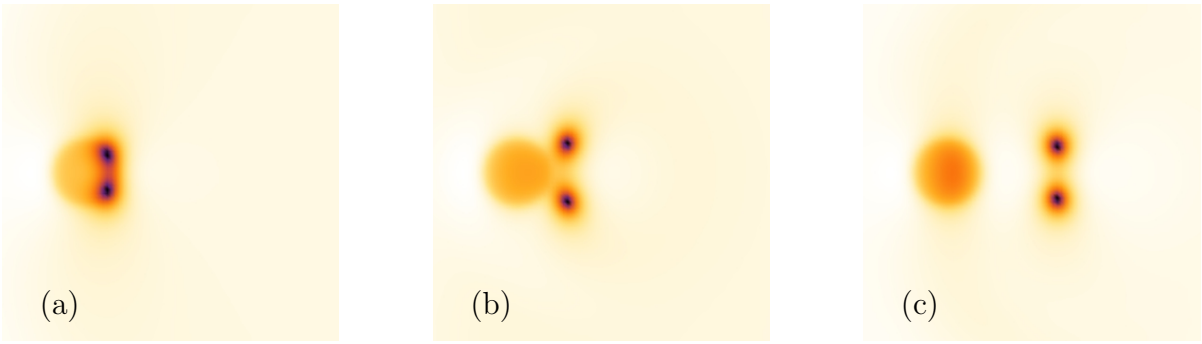

Figure 4.8: *V*ortex pair generation due to a potential of diameter much bigger than healing length and causing only slightly a depletion of the condensate.- Pseudo-color density plots of superfluid flow around a obstacle specified by $V_0 = 0.25$ and $b = 4$ at $t = 57$; (a), $t = 75$; (b), $t = 105$; (c) with velocity at infinity $v = 0.8c$. Each picture shown corresponds to an area of 40×40 [209]. The more luminous the picture the higher the density. The dimensionless units are used as specified in the main text.

.

(for example for parameters $V_0 = 0.1$ and $b = 1$) vortices are generated although single impurities of the same specification would prefer the generation of rarefaction pulses; high energy rarefaction pulses absorb energy due to perturbations present in the lattice and once their energy passes some threshold they transform into an energetically favorable vortex pair [202]. For *very weak* BEC-impurity interactions (V_0 is very small) solely rarefaction pulses are generated in the stream of the condensate within and at the wake of the impurity lattice, which are slightly deflected as they pass weak potential spikes.

The region IV in Fig. 4.10 is characterized by high density arrays of impurities, which yield excitations that span over several neighboring impurities. In Fig. 4.14 we show snakes of excitations moving through the lattice. These excitations are either zeros of wave function and therewith can be identified as vortices or are more comparable with rarefaction pulses not fully depleting the condensate. In particular we have observed that excitations within the lattice might move in opposite direction to the mainstream direction. With more narrow space between impurities further excitations are present within the lattice. As there is not enough space for a fully developed vortex pair or rarefaction pulse between neighboring impurity atoms, excitations in such lattice emerge as finite amplitude sound waves, i.e, spontaneously occurring density depletions between two neighboring atoms, which occasionally persist and move within the lattice generally towards all possible directions.

Finally we have considered very high densities of impurity atoms with V_0 large enough such that the condensate is (almost) expelled from the lattice and the velocity is chosen such that the superfluid phase is surpassed, i.e., III in Fig. 4.10. Here we have found that vortices are generated at the boundaries of the lattice. In the wake some vortices

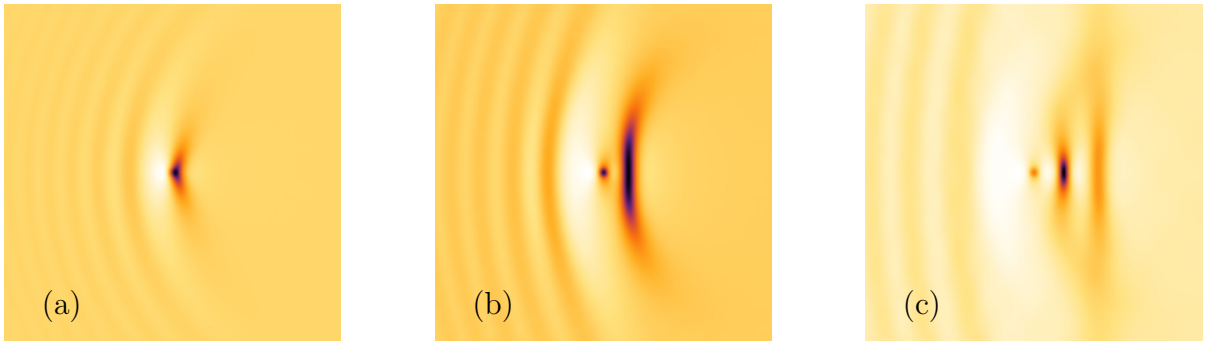

Figure 4.9: *R*arefaction pulse generation due to a small and weakly interacting potential at supersonic speed.- Pseudo-color density plots of superfluid flow around a obstacle specified by $V_0 = 0.2$ and $b = 1$ at $t = 45$; (a), $t = 82.5$; (b) and $t = 180$; (c) with Mach number $v = 1.01c$. The more luminous the picture the higher the density. Each picture shown corresponds to an area of 35×35 [211]. The dimensionless units are used as specified in the main text.

enter the *slipstream region*, such that no significant motion between vortices and lattice is present or movement towards the lattice might occur - an analog situation as encountered for moving obstacles generating turbulent flow in normal fluids. In Fig. 4.15 we indicate the motion of the vortices in the slipstream region for a very slow superfluid with only few vortices present in the wake, i.e., two counter propagating curls of vortices evolving from both edges of the lattice.

4.4.2 Uniformly distributed impurities

We now turn to the regimes of a flow passing randomly distributed impurities occupying a finite area A. These inserted atoms can be regarded as an ideal gas of $N_{\mathcal{A}}$ uniformly distributed noninteracting particles in the plane $\mathbb{R}^2$ at an instant of time. We denote the density of particles (or impurities) given by the total particle number per area by n. To determine the mean distance between particles we recognize that the probability of finding another particle within the distance r from its origin is $P_{[r,r+dr]} = 2\pi rndr$. The probability to find a particle outside the disc, i.e., in $[r, \infty]$, is $P_{[r,\infty]} = 1 - \pi r^2/A$, where A is the total area. Hence the probability distribution function of the distance to the nearest neighbor is

$$P_N(r) = 2\pi rN/A \left(1 - \pi r^2/A\right)^{N-1}, \tag{4.4.2}$$

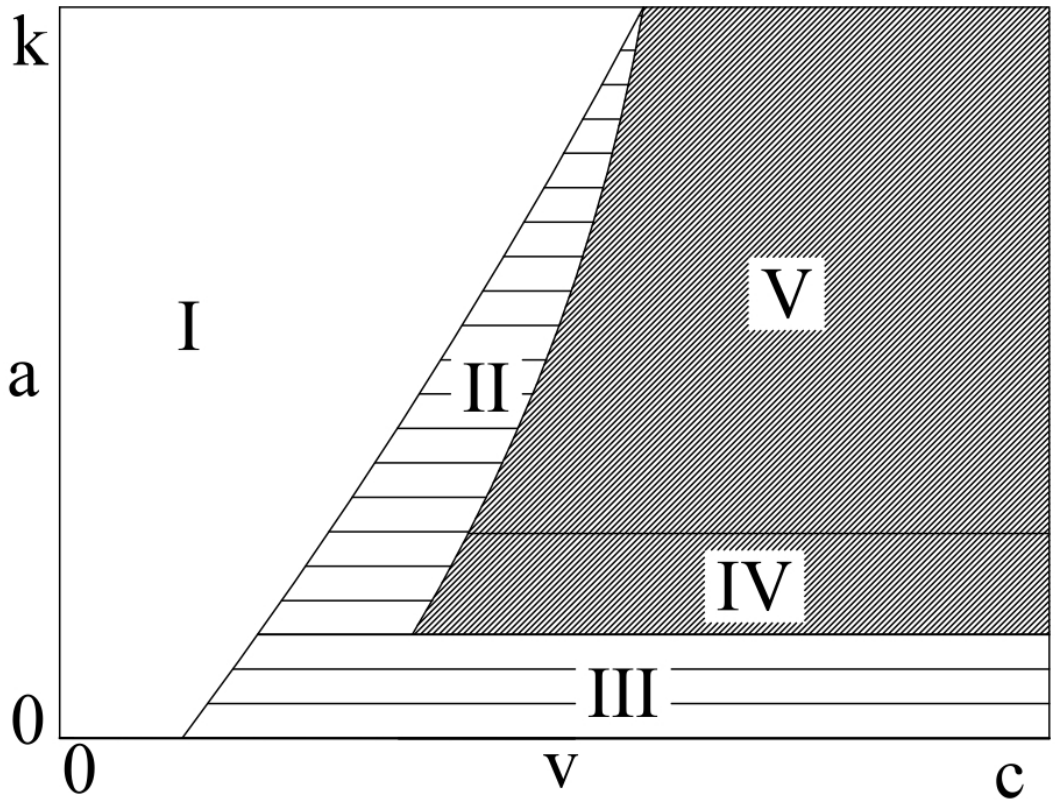

Figure 4.10: Schematics of the distinct regions in superfluid flow around regular lattices on a rectangular area. The boundaries are approximate and are sensitive to the parameters of the impurity network. Here a denotes the distance between nearest neighbors, which ranges from 0 to 12 healing lengths and v the absolute value of the superfluid velocity at infinity ranging up to the speed of sound c.Hatched areas II, III show regions where excitations are outside the lattice and V, IV indicate the regimes where excitations are within the lattice as well.

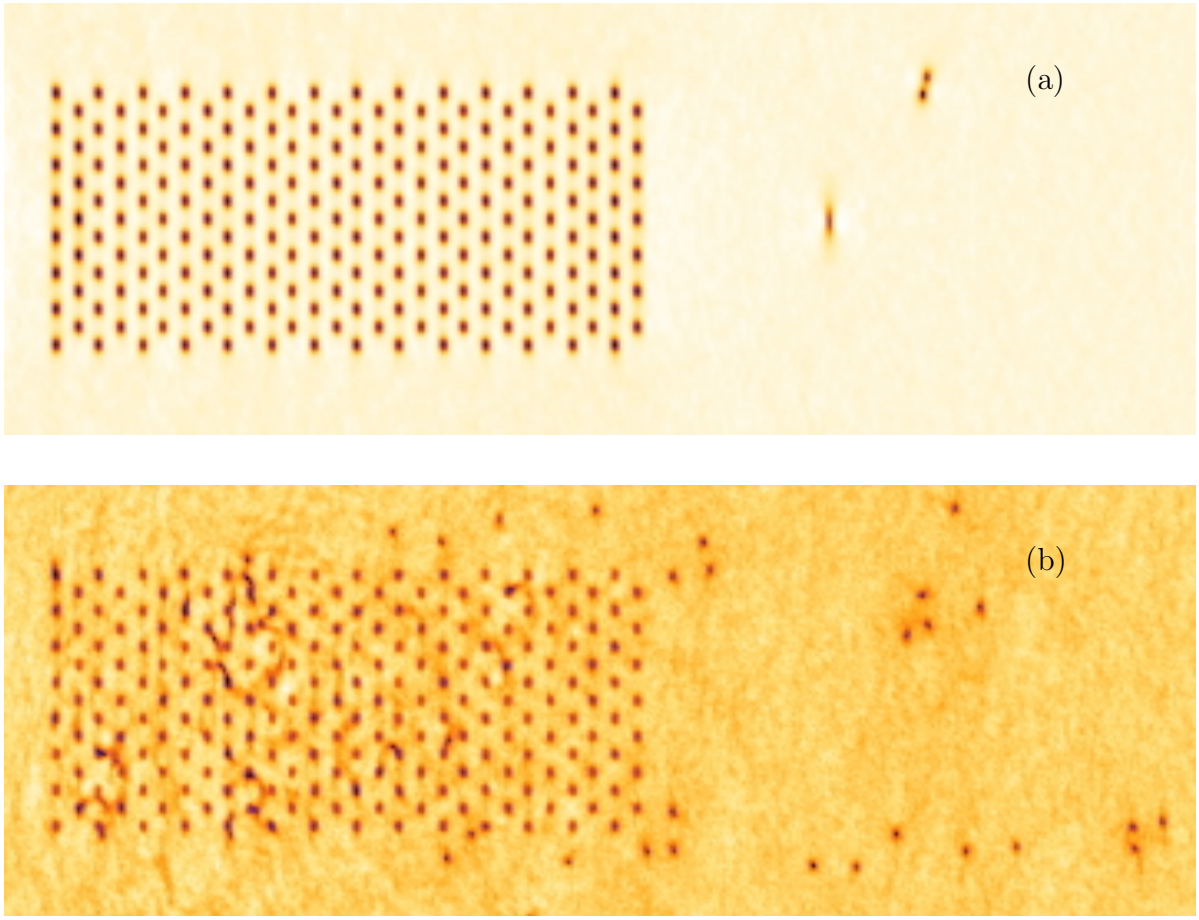

Figure 4.11: Pseudo-color density plots $|\psi|^2(x, y)$ of qualitatively distinguishable phases in superfluid flow passing a hexagonal lattice of impurities. Shown is the condensate density at velocity $v = 0.5c$ (a) and $v = 0.555c$ (b). Other parameters of the system: Array size $A = 240 \times 72$, frame shown 480×120, $a = 5$, $b = 1.5$,$V_0 = 1$, all snapshots at $t = 125$ [214]. The more luminous the picture the higher the density. The dimensionless units are used as specified in the main text.

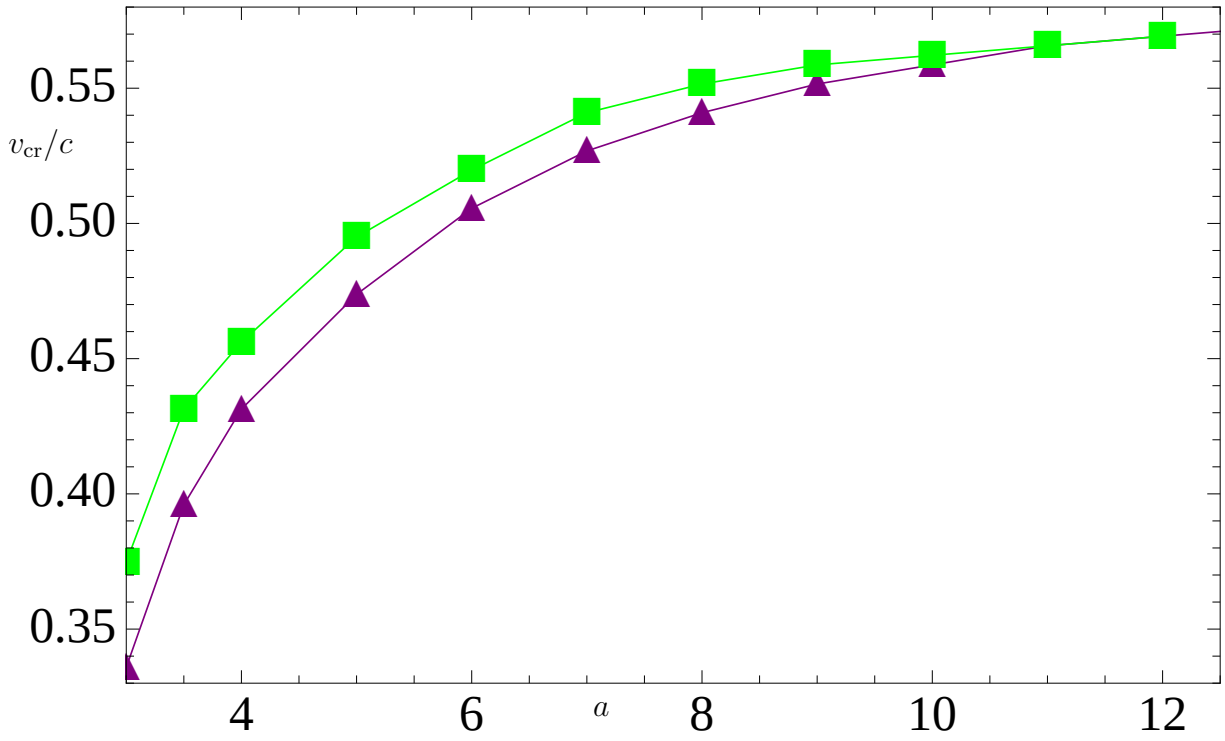

Figure 4.12: Critical velocities as functions of the distance between impurity to its nearest neighbors a. For this comparison the remaining free parameters have been chosen to be $V_0 = 1$, $b = 1.5$ while the area at which the triangular lattice of atoms has been present is 200×120 (measured in healing lengths). Triangles represent data points of the first and squares data points of the second critical velocity. The interpolation between data points is linear. [214].

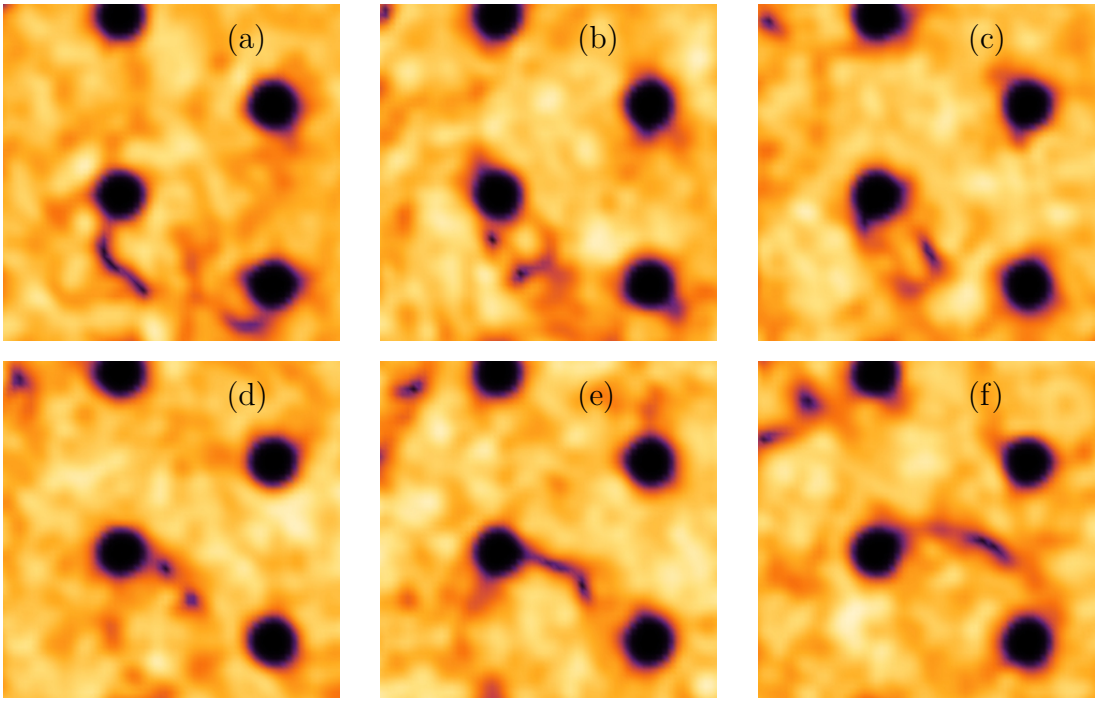

Figure 4.13: Pseudo-color density plots of superfluid flow around a obstacles on arranged on a triangularlattice specified by $V_0 = 10$ and $b = 2$ at $t = 310$; (a), $t = 312.5$; (b), $t = 315$; (c); $t = 317.5$; (d), $t = 320$; (e), $t = 325$; (f) with velocity at infinity $v = 0.67c$. Each picture shown corresponds to an area of 30×30 [216]. The more luminous the picture the higher the density. The dimensionless units are used as specified in the main text.

which for n fixed becomes in the limit $N \to \infty$

$$P(r) = 2\pi r \exp(-\pi r^2 n) n. \tag{4.4.3}$$

Note that (4.4.3) might be regarded as a good approximation to (4.4.2) for large N. Thus, the mean distance $\overline{a}$ is given by considering the expectation value

$$\overline{a} \equiv \mathbb{E}_1[r] = \int_0^\infty r 2\pi \exp(-\frac{\pi r^2}{n}) n dr = \frac{1}{2\sqrt{n}}. \tag{4.4.4}$$

In this sense a random distribution of particles determined by its area and number relates to the mean distance, i.e., $n = N_{\mathcal{A}}/A = \frac{1}{4\overline{a}^2}$. In Fig. 4.16 we present results showing that even for systems of less chosen structure than fixed lattices, qualitatively different phases can be distinguished. That is a phase of dissipationless superfluid flow, the generation of first excitations in the wake of the lattice and generation of excitations within the lattice. In contrast to the hexagonal lattice, however, these transitions are generally not as smooth. Figure 4.16 shows the density of the condensate for the superfluid flow around inserted impurities uniformly distributed on a finite domain [214], [217]. Fig. 4.16 (a) shows a superfluid's flow without dissipation of energy and generation of elementary excitations, (b) corresponds to a flow above criticality carrying excitations in the wake of the superfluid and (c) an even faster flow at which excitations are generated within the array.

4.5 Conclusions

The generation of vorticity by a moving superfluid has generated a lot of experimental and theoretical work. In our paper we re-examine this problem by developing an asymptotic and analytical methods for finding the flow around an obstacle and for determining the critical velocity of vortex nucleation. We numerically study the various excitations generated above the criticality. We determine the regimes when a vortex pair or a finite amplitude sound wave is generated depending on the energetics of the obstacle. We described several novel regimes as a superfluid flows an array of impurities motivated by recent experiments.

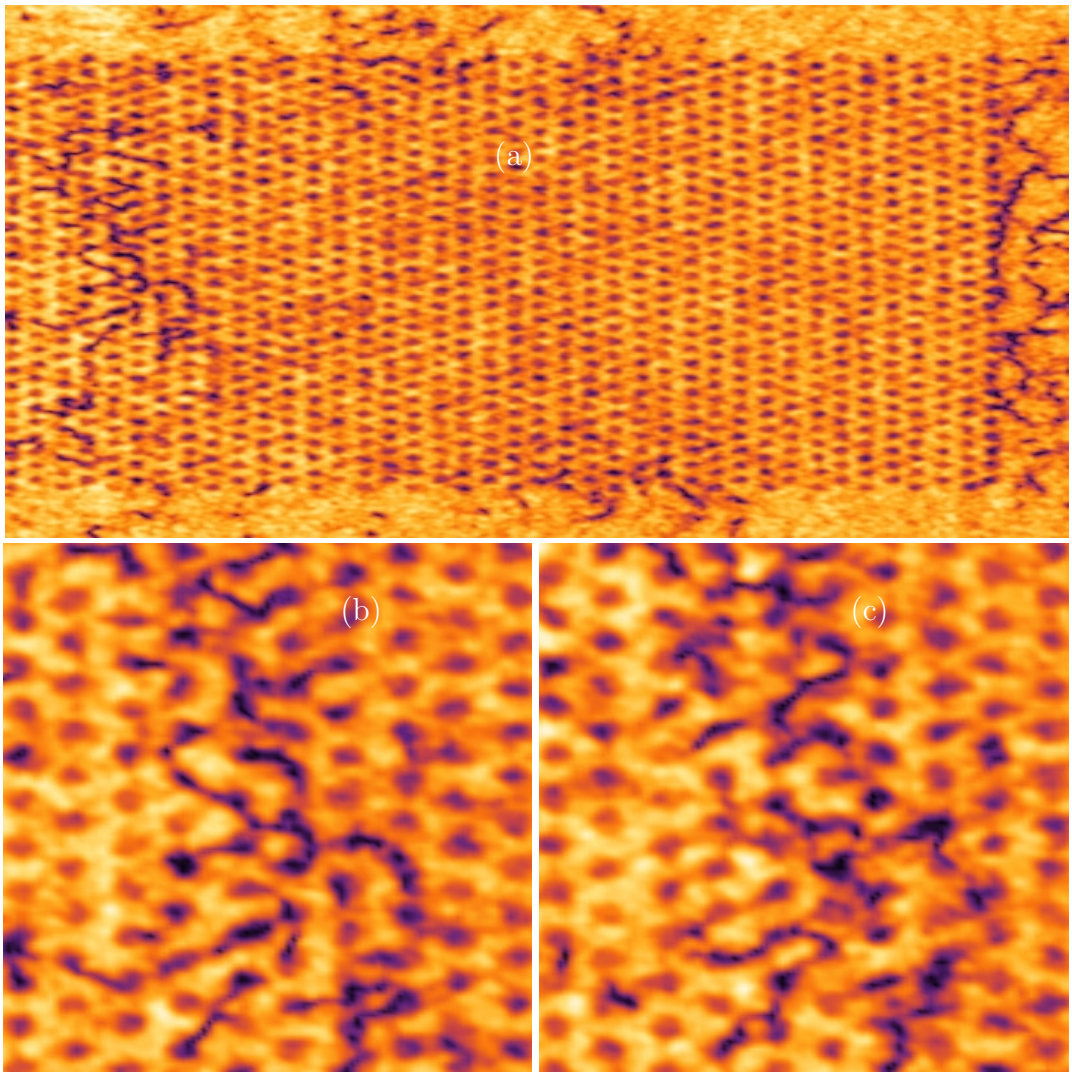

Figure 4.14: Pseudo-color density plots $|\psi|^2(x, y)$ of superfluid flow passing dense hexagonal distributed atoms with velocity $v = 0.5c$. The size of atom array is 290×180, the frame size shown in picture (a) is 220×220 at $t = 522.5$. Picture (b) is a detail of frame size 70×70 at $t = 522.5$ and picture (c) at $t = 525$ (with frame size 70×70). The atom parameters were chosen to be $V_0 = 1$, $a = 3$ and $b = 1.5$. [216]. The more luminous the picture the higher the density. The dimensionless units are used as specified in the main text.

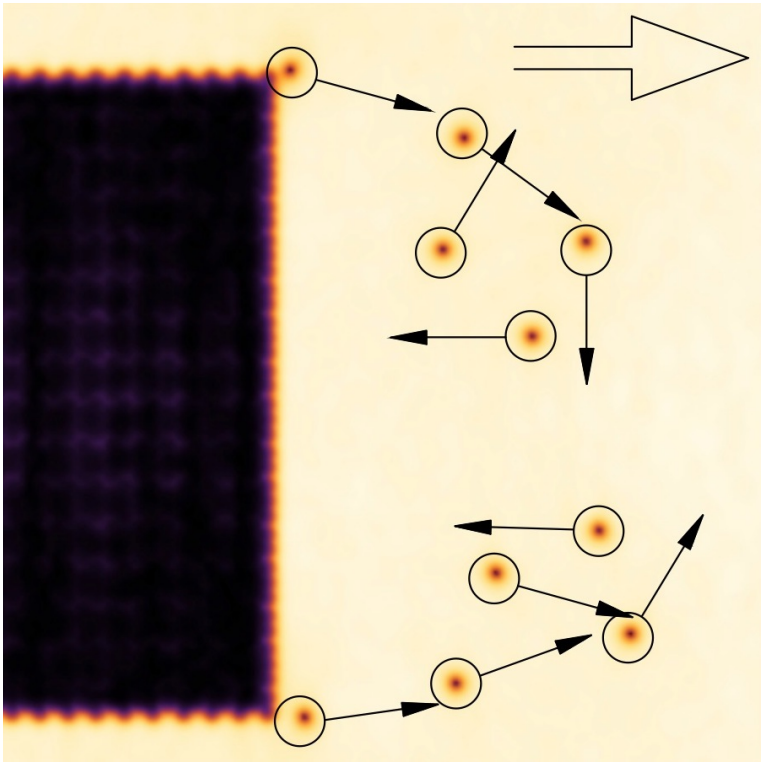

Figure 4.15: Pseudo-color density plots $|\psi|^2(x, y)$ of superfluid flow passing very dense triangular lattice of impurities with velocity $v = 0.2c$. The frame size shown is 150×150 at $t = 539.25$. The impurity parameters were chosen to be $V_0 = 1$, $a = 1.6$ and $b = 1.5$. [216]. The more luminous the picture the higher the density. Arrows point towards the direction of motion of the encircled vortices, and the big arrow indicates the direction of the superfluid mainstream. The dimensionless units are used as specified in the main text.

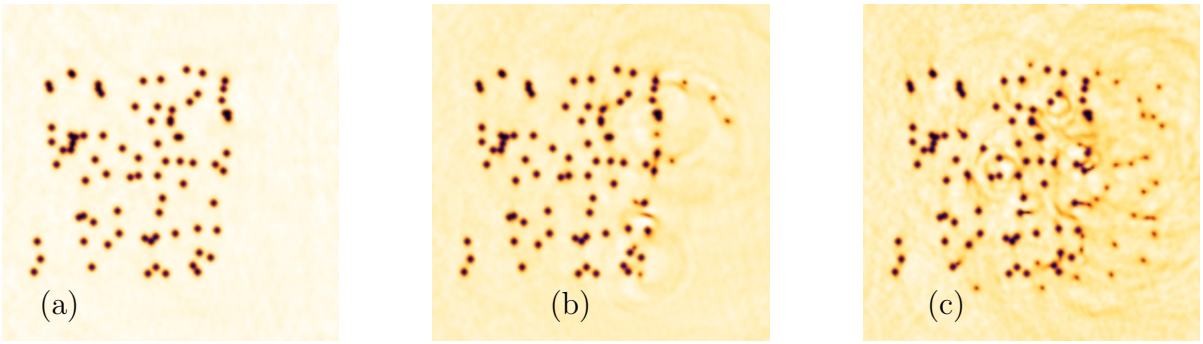

Figure 4.16: Pseudo-color density plots $|\psi|^2(x, y)$ of phases in superfluid flow passing uniformly distributed atoms with different velocities at $t = 165$. The atom number is $N_{\mathcal{A}} = 80$, size of possible atom positions 120×130 (measured in healing length), the frame size shown is 210×210 in same units and the atom parameters were chosen to be $V_0 = 2$ and $b = 2$. Picture (a) shows the flow at $v = 0.2c$, (b) at $v = 0.32c$, (c) at $v = 0.39c$. All pictures show the same (random) distribution of atoms and represent a snapshot at $t = 165$ [218]. The more luminous the picture the higher the density. The dimensionless units are used as specified in the main text.

5 On-demand dark soliton train manipulation in a spinor polariton condensate

Florian Pinsker and Hugo Flayac, Phys. Rev. Lett. **112**, 140405 (2014).

We theoretically demonstrate the generation of dark soliton trains in a one-dimensional exciton-polariton condensate within an experimentally accessible scheme. In particular we show that the frequency of the train can be finely tuned fully optically or electrically to provide a stable and efficient output signal modulation. Taking the polarization degree of freedom into account we elucidate the possibility to form on-demand half-soliton trains.

5.1 Main text

5.1.1 Introduction

The first unambiguous observation of Bose-Einstein condensation in dilute Bose gases at low temperature [4] set off an avalanche of research on this new state of matter. The lowest energy fraction of a degenerated Bose gas occupying low energy modes obeys the property of vanishing viscosity and does not take part in the dissipation of momentum, a phenomenon referred to as superfluidity [18]. This holds true as long as the condensate is only slightly disturbed [169]. As soon as strong dynamical density modulations occur, e.g. when the condensate is abruptly brought out of its equilibrium through an external perturbation, it responds in a unique way by generating robust elementary excitations such as solitons or vortices [113].

More recently the concept of macroscopically populated single particle states [12, 13] was transposed to a variety of mesoscopic systems such as cavity photons [14, 15], magnons [219], indirect excitons [220], exciton-polaritons (polaritons) [16] and even classical waves [17]. In the proper regime all those systems can be described by complex-valued order parameters - the condensate wave functions - with dynamics governed by nonlinear Schrödinger-type equations (NSE) such as the Gross-Pitaevskii (GP) [8, 7] and the complex Ginzburg-Landau equation (cGLE) [48]. Here the nonlinearity associated with self-interactions plays an essential role on the possible states with or without excitations, their dynamics and in particular their stability [221]. Similarly in the slowly varying envelope approximation light waves can be approximated by complex-valued

wave functions governed by NSEs that are formally comparable to those of BECs and thus show analog dynamical behavior such as stationary and moving optical dark or bright solitons in quasi 1D settings [222, 223].

For several decades light waves have been utilized in a wide range of applications such as in nonlinear fibre optic communication [222, 224, 225, 226] while research on new technologies is thriving in particular on elementary circuit components such as optical diodes [227], transistors [228] or realizations of analog devices involving exciton-polariton condensates [229, 230] and conceptually on optical computing schemes [231].

Exciton-polaritons are half-light half-matter quasi-particles formed in semiconductor microcavities and allow high speed propagation from their photonic part while having strong self-interaction from their excitonic fraction. They are extremely promising from both the fundamental and technological point of view given the ease it provides to finely control the parameters of their condensate now routinely produced in different geometries (see e.g. [232]). Indeed, state-of-the-art technology allows to etch any sample shape to sculpt the confining potential seen by the condensate at will. It explains the plethora of recent proposals [233, 35, 36, 37, 38, 39, 40, 41] for polariton devices some of which have been experimentally implemented [229, 230]. The main advantage with respect to standard optical systems in nonlinear media is the very large exciton-mediated nonlinear response of the system reducing the required input power by orders of magnitude. Recently there was a growing interest in demonstrating the formation of (spin polarized) topological defects [234, 235] that are now envisaged as stable information carriers [249, 236, 237] within a young field of research called spin-optronics [238].

In this letter we shall present experimentally trivial schemes for the intended generation and manipulation of stable and fully controllable wave patterns within a quasi-1D microcavity. We will demonstrate the on-demand formation of dark soliton trains within a quasi-1D channel and the optical and electrical dynamical control of their frequency. Finally we shall demonstrate the possibility to control the polarization of the soliton trains.

5.1.2 The model

We shall consider the system modeled in Fig.5.1, namely a wire-shaped microcavity similar to the one implemented in Ref.[240] that bounds the polaritons to a quasi-1D channel. A metallic contact is embed over half of the sample to form a potential step seen by the polaritons and whose amplitude can be tuned on-demand applying an electric field [241]. The spinor polariton field $\boldsymbol{\psi} = (\psi_+, \psi_-)^T$ evolves along a set of effectively

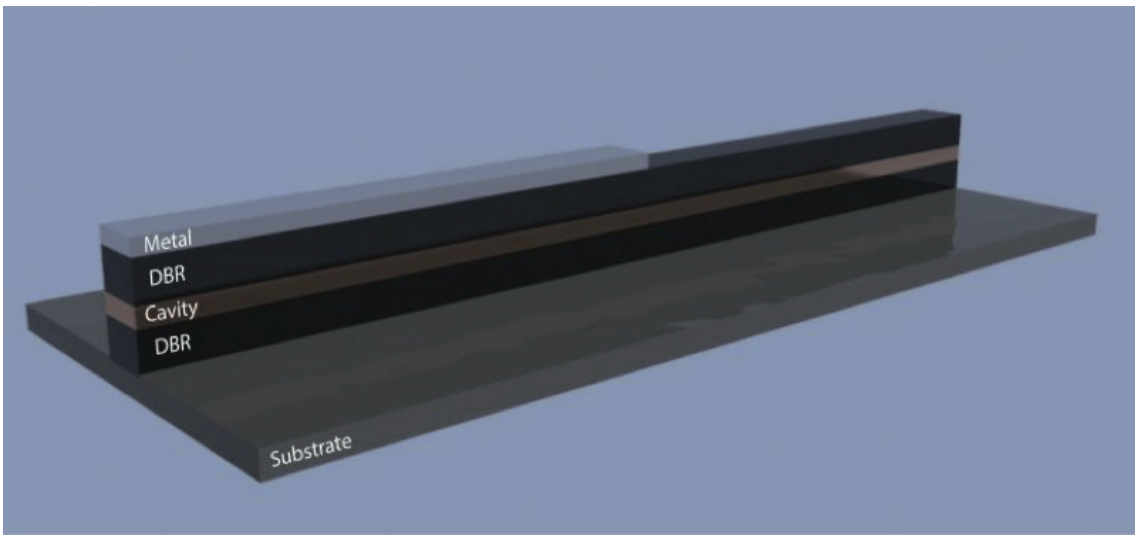

Figure 5.1: (Color online) Model of a potential sample consisting in a quasi-1D microcavity (DBR=distributed Bragg reflectors) embedding a metallic deposition over half of its length to form a potential step. A gate voltage can be applied to the metal to tune dynamically the step amplitude.

1D cGLEs coupled to a rate equation for the excitonic reservoir [241],

$$\begin{aligned} i\hbar\frac{\partial\psi_+}{\partial t} &= \left[-\frac{\hbar^2\Delta}{2m}+\alpha_1\left(|\psi_+|^2+n_R\right)+\alpha_2|\psi_-|^2\right]\psi_+ \\ &+ \left[U-\frac{i\hbar}{2}\left(\Gamma-\gamma n_R\right)\right]\psi_+-\frac{H_x}{2}\psi_- \qquad (5.1.1) \\ i\hbar\frac{\partial\psi_-}{\partial t} &= \left[-\frac{\hbar^2\Delta}{2m}+\alpha_1\left(|\psi_-|^2+n_R\right)+\alpha_2|\psi_+|^2\right]\psi_- \\ &+ \left[U-\frac{i\hbar}{2}\left(\Gamma-\gamma n_R\right)\right]\psi_--\frac{H_x}{2}\psi_+ \qquad (5.1.2) \\ \frac{\partial n_R}{\partial t} &= P-\Gamma_R n_R-\gamma\left(|\psi_+|^2+|\psi_-|^2\right)n_R. \qquad (5.1.3) \end{aligned}$$

This model describes in a simple way the phenomenology of the condensate formation under non-resonant pumping. We assume a parabolic dispersion of polaritons associated with an effective mass $m = 5\times10^{-5}m_0$ where m_0 is that of the free electron and a decay rate $\Gamma = 1/100$ ps^{-1}. $U(x,t) = [U(t)+U_0]\,H(x)$, where $H(x)$ is the Heaviside function $U_0 = -0.5$ meV is the step height induced by the presence of the metal solely and $U(t)$ is the potential landscape imposed by the external electric field. $\alpha_1 = 6xE_b a_B^2/S = 1.2\times10^{-3}$ meV$\cdot\mu$m and $\alpha_2 = -0.1\alpha_1$ are respectively the parallel and antiparallel spin interaction strength given x, E_b and a_B the excitonic fraction, binding energy and Bohr radius respectively and S the pump spot area. $H_x = 0.01$ meV is the amplitude of the effective magnetic field induced by the energy splitting between TE and TM eigenmodes that couples the spin components. The excitonic reservoir characterized by the decay

rate $\Gamma_R = 1/400$ ps^{-1} is driven by the pump term $P = A_P \exp(-x^2/\sigma^2)$ where $\sigma = 20$ μm and A_P is taken in the range of hundreds of Γ_R. It exchanges particles with the polariton condensate at a rate $\gamma = 2 \times 10^{-2}\Gamma_R$.

We note that while the stimulated scattering is taken into account by Eqs.(5.1.1-5.1.3), energy relaxation processes dominant under the pump spot, apart from the lifetime induced decay of the interactions energy, are neglected in this framework and could be treated e.g. within the formalisms of Refs.[242]. Energy relaxation would not impact our results qualitatively especially for the finite pump spot size we consider here.

5.1.3 Soliton train generation

As shown in Ref.[113] a local abrupt change of self-interaction strength of the condensate leads to the formation of a stable and regular dark soliton train. It happens when the flow in the direction of decreasing interaction due to particle repulsions is locally crossing the speed of sound $c_s(x) = \sqrt{\mu(x)/m}$ where $\mu(x) = \alpha_1 n(x)$ (for a scalar condensate) at the point of abrupt change in self-interactions, solitons are formed from dispersive shock waves [243] that dissipate the local excess of energy. In polariton condensates the interaction strength α_1 is varied tuning the exciton/photon detuning and therefore the excitonic fraction, but it can hardly be made inhomogeneous within a given sample nor tuned dynamically. A valuable alternative we follow here is to introduce the tunable potential step $U(x,t)$ in Eqs.(5.1.1,5.1.2). The mechanism for soliton generation is the following (see supplemental material for a more details). Let us suppose we a homogeneous density n_0 at $t = 0$ and neglect the finite lifetime and pumping of quasi particles and the geometry of our pump spot. Then taking the potential U stepwise for all following $t > 0$, we get close to the breaking point at $x = 0$ the density n_1 for $x = 0^-$ and n_2 as $x = 0^+$ and we say $n_1 = k \cdot n_2$ with $1 > k > 0$. Using momentum and mass conservation at $x = 0$ we find the simple criterion $0.6404 > k$ to break the speed of sound in the region $x < 0$, which is in good agreement with our numerical results. In the regime of soliton-train generation, the frequency ν increases with the magnitude of the potential step [**?**] as the corresponding increase of mass passing the step at $x = 0$ allows a more frequent breaking of the local speed of sound. This is analogous to the situation of a superfluid passing an obstacle above criticality for which greater mass transport is equivalent to a higher number of generated vortices in 2D [245].

For a given metal type and deposition thickness on top of the microcavity, Tamm plasmon-polariton modes [246] were predicted to form at the interface inducing a local redshift of the polariton resonances of amplitude U_0 and the required potential step. We note that in the absence of plasmon the interface would form a Schottky junction known to blue detune the polariton modes [247]. The application of a voltage to the metal produces the additional gate redshift $U(t)$ through the excitonic Stark effect up to a few meVs for voltages lying in the range of tens of kV/cm [248] and standing for the input modulation of the polariton condensate. The non-resonant excitation of the system is crucial since in this context the condensate phase is free to evolve under the pump spot by contrast to a resonant injection scheme that would imprint the phase preventing the onset of solitons.

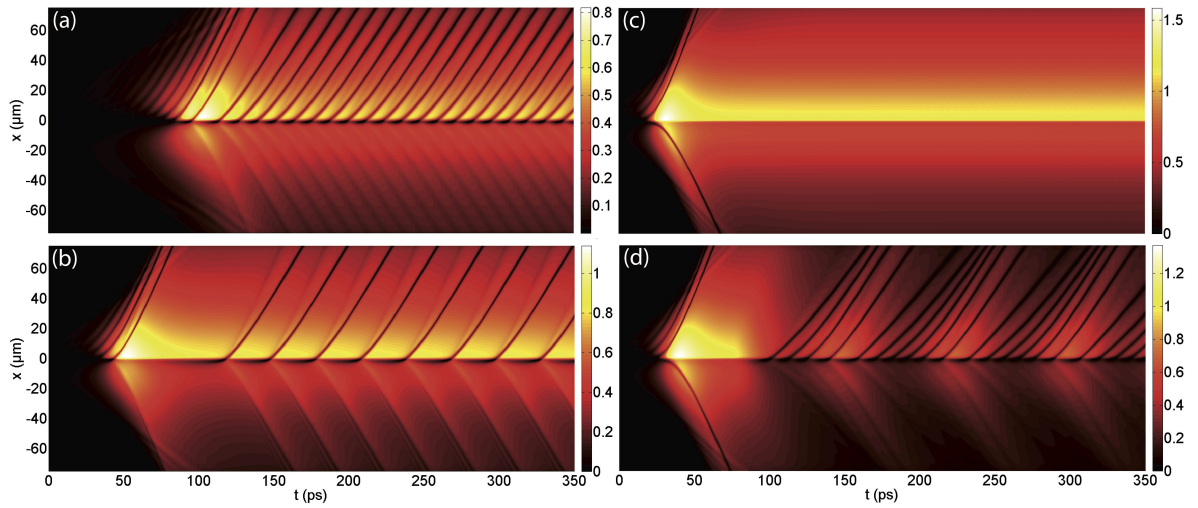

Figure 5.2: (Color online) Optical control. (a), (b) (c) Shows results obtained by pumping over the potential step with increasing pump amplitude of $200\Gamma_R$, $375\Gamma_R$ and $600\Gamma_R$ respectively, we monitor here $\mu(x,t)$ (meV) in the colormap. (d) Sinusoidal modulation of the pump amplitude between 0 and $500\Gamma_R$ and with a period $T = 100ps$ resulting in signal frequency modulation.

5.1.4 Optical control

Let us start with the simplest passive configuration where no voltage is applied and therefore the potential step is *fixed*. We switch on the pump laser focussed on the step at $t = 0$ and wait for the steady state to be reached. The reservoir is filled by the incoherent pump and the stimulation towards the lowest polariton energy state occurs forming the condensate with a chemical potential $\mu = (\alpha_1 + \alpha_2)n/2 - H_x/2$ (corresponding to the measurable blueshift of the polariton emission) where $n = |\psi_+|^2 + |\psi_-|^2 = n_+ + n_-$ is the total polariton density. Given the interrelation $\alpha_1 > \alpha_2$ the condensate interaction energy is minimized for a linear polarization meaning that $n_+ = n_-$ and the condensate is said to be antiferromagnetic [249]. The linear polarization orientation is homogeneous at zero temperature and fixed by the H_x contribution namely along the axis of the wire. In our model we trigger the condensation on the x-polarized ground state with initial populations $n_\pm^0$. Fig. 5.2 shows numerical solutions to Eqs.(5.1.1,5.1.2,5.1.3). We depict the chemical potential $\mu(x,t)$ for crescent pump amplitudes A_P. We clearly see the decrease in the train frequency ν with increasing pump power [panels (a) and (b)] until the train vanishes [panel(c)].

The condensate heals from the step forming an asymmetric gray soliton resulting from the local velocity gradient, as it happens e.g. at the boundaries of condensate trapped in a square potential. The depth of the soliton is imposed by the local background density and velocity. For a high enough background density, the flow is superfluid ($v < c_s$) both around the step and within the soliton that remains pined to the step preventing the

train onset [panel(c)]. For lower densities, the speed of sound can be surpassed at the soliton core which allows the condensate to dissipate the local excess of energy via a dispersive shock wave [243] (see supplemental movies [**?**]) that releases the soliton to the side where the background flow is the highest. Then it takes some time for the condensate to form a new soliton. The higher the density the stiffer is the condensate and therefore the more time it takes to form a new density depletion. This response determines the quasi-linear train frequency ν dependence over the chemical potential shown in the supplemental material [**?**].

Our results demonstrate the possibility to modulate passively an optical signal via the formation of stable dark solitons varying the pump amplitude. The dark soliton signals shall then be detected experimentally at the output via one of the schemes proposed in the context of nonlinear optics [250] to encode information. Indeed, as proposed in [25] soliton trains can be used to store numbers determined uniquely by an adjustable ν. So far, most of the device proposals involving microcavity polaritons have focussed on signal transmission but never on its modulation. Nonetheless, as one can see, the train frequencies lie in the range of THz allowing to perform very high speed processing due to the polariton photonic part combined with a large exciton-mediated nonlinear response.

In Fig.5.2(d), we show an example of sinusoidal input power modulation that leads to a dynamical variation of ν or a modulation of the output on-demand to produce useful wavepackets. The main advantage of this all-optical input modulation scheme is that it allows us to reach high speed variation of ν while the drawback is that the background density of the condensate is obviously affected as well. Finally we note that this setup involving a fixed potential step doesn't require specifically a metallic deposition. A sample split in two parts with slightly different lateral width might be sufficient to reproduce the effects discussed above.

5.1.5 Electric control

Now let us consider the case where the pump power is fixed and in addition an electric field is applied to the metallic contact to modulate the potential step height. Under such assumptions, the chemical potential μ is globally fixed. The higher the step (the electric field), the larger the density gradient and hence one encounters a greater mass transport towards lower energy regions. So similarly to [245] we obtain an increase in dark solitons train frequency as shown in [**?**]. To demonstrate this behavior, we show in the Fig.5.3(a) the results obtained by ramping down linearly the potential step from 0 meV to -1.5 meV which corresponds to an increase in the electric field amplitude. We clearly see the linear increase in ν versus time.

Similarly to the results of Fig.5.2(d) we show in Fig.5.3(b) results obtained from a sinusoidal modulation of the potential step amplitude producing an efficient dynamical modulation of the output signal in the form of wavepackets. Such an electric control of the polariton flow has the advantage of impacting weakly on the background density but there might be some technological limitation on the switching speed.

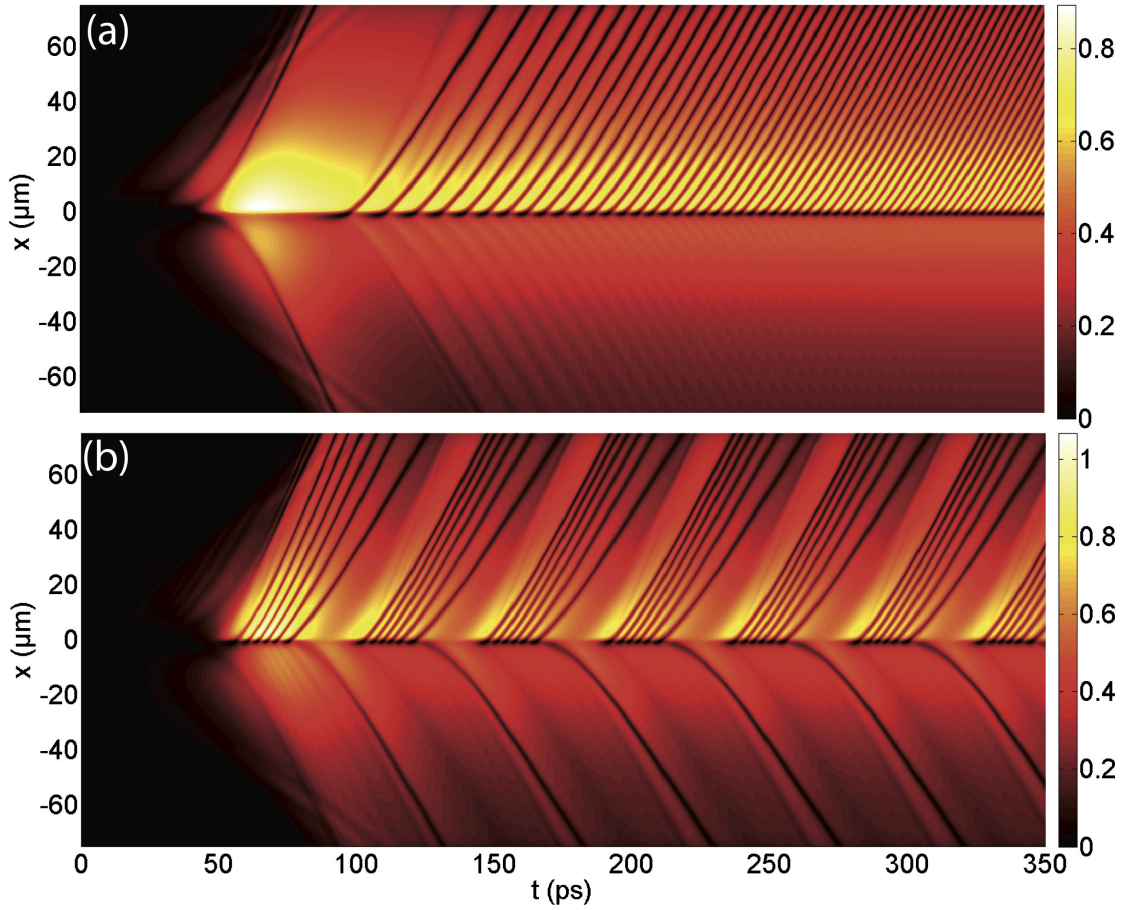

Figure 5.3: (Color online) Electric control of the dark soliton trains. (a) The potential step amplitude $U(t)$ is linearly ramped down versus time from 0 meV to -1.5 meV. (b) Sinusoidal modulation of the step between 0 and -1.5 meV with a period of 50 ps.

5.1.6 Polarization control

So far we have discussed a phenomenology that could be reproduced using a scalar condensate without any need for its spinor character. Indeed we have considered the ideal case of a perfectly linearly polarized condensate with no polarization symmetry breaking namely $n_+(x) = n_-(x)$ for any x position. The consequence is that the dark solitons formed in one spin component are perfectly overlapping with the ones in the other component and are behaving as scalar ones. However in real experimental situations the fluctuations brought by the structural disorder or the background noise can affect the linear polarization of the condensate leading to local inhomogeneities slightly breaking the polarization symmetry or the equivalence between the two spin components. As discussed in [236] these fluctuations can lead to the separation of dark solitons in each component to form pairs of half-solitons [234, 235]. As soon as they are split they will

repel each other under the condition $\alpha_2 < 0$ and start to feel an effective magnetic force imposed by H_x and be accelerated or slowed down depending on their linear polarization texture [236]. This effect produced by local inhomogeneities or random processes would obviously be harmful to the formation of a deterministic spin signal. However as it was observed experimentally in Ref.[251], using a polarized excitation laser can lead to the formation of a circularly/elliptically polarized condensate due to the long characteristic spin relaxation times of excitons. In Fig.5.4, we show results capitalizing on this effect to produce a useful spin signal.

We have modeled a slightly elliptically polarized nonresonant pump introducing two different reservoir/condensate transfer rates γ_1 and γ_2 in Eqs.(5.1.1,5.1.2). We have adjusted the ratio γ_2/γ_1 to 0.90, 1.11 and 0.99 in panels (a), (b) and (c) respectively. The colormap shows the degree of circular polarization $\rho_c(x,t) = (n_+ - n_-)/(n_+ + n_-)$ of the polariton emission. We see that the weak ensuing density imbalance between the two spin components of the condensate leads to a well defined polarization symmetry breaking inducing either the formation of trains of pairs of half-solitons [panel (c)] or trains of half-solitons with a well defined polarization for larger imbalances [panels (a) and (b)]. It means that not only the frequency of the trains can be finely tuned but also their polarization by variation of the input polarization. It provides another degree of freedom to code information.

5.1.7 Conclusions

We have shown the strong potential of microcavities for high speed optical signal modulation for information coding. Our proposal involves the all-optical or electric control of dark soliton trains within a realistic and experimentally trivial scheme. We have demonstrated the possibility to tune both the train frequency and its polarization. The present concept could not only play a central role at the heart of future high speed polariton circuits within the rapidly expanding field of spin-optronics but also allow the very first observation of dark soliton trains in a quantum fluid.

5.2 Supplemental material

5.2.1 Velocities

To clarify the mechanism underlying the dark soliton train formation in our setting, we have computed the speed of sound c_s and the superfluid velocity $v = \hbar/m\nabla\phi$ dynamics (ϕ is the phase of the wave function). Fig. 5.5 shows results obtained for two different pump powers: In the panel (a) the condensate is superfluid ($|v| < c_s$) all over the step and no local energy dissipation can occur to regularize the density and phase modulation (asymmetric grey soliton) imposed by the step. On the contrary in the panel (b) the core of the soliton at the step crosses the speed of sound ($|v| > c_s$) allowing a shock wave to develop releasing the soliton to the right of the step. The frequency of the train is increasing with the stiffness $\rho_s = n\hbar^2/m$ (density) of the condensate since it takes more time to heal (produce a new modulation at the step) for a higher density leading to a lower train frequency [see Fig. 5.2]. The full dynamics is shown in the supplemental movies provided with the manuscript.

5.2.2 Dependencies of the train frequency

We have numerically determined the dependence of the train period T and frequency $\nu = 1/T$ on the chemical potential μ and the potential step amplitude U. The results are presented in Fig. 5.6 and Fig. 5.7 respectively.

5.2.3 Critical density modulation

Our analytical consideration starts with neglecting the spin degree of freedom (antiferromagnetic condensate regime), so we get the governing equation for the condensate wave function ψ given by

$$i\hbar\frac{\partial\psi}{\partial t} = \left(-\frac{\hbar^2\Delta}{2m} + U + \alpha_1''\left(|\psi|^2 + n_R\right) - \frac{i\hbar}{2}\left(\Gamma - \gamma n_R\right)\right)\psi - \frac{H_x}{2}\psi_+. \tag{5.2.1}$$

First, we note that at the breaking point at $x = 0$ the complex pumping and decaying term is positive (for the parameters considered), corresponding to an increase in particles there. We simplify this equation by neglecting the effect of pumping to the condensate, which increases the superfluid's velocity there and by additionally approximating the reservoir population as $n_R \simeq c_1 + c_2|\psi|^2$. The latter expression is due to an assumed quasi-stationary reservoir population $n_R = P/(k_1 + k_2|\psi|^2)$ and further simplified via a Taylor expansion to $n_R = P(k_3 + k_4|\psi|^2)$ and considered for $P = k_5$. Here $c_1, c_2, k_1, k_2, k_3, k_4, k_5$ are constants. Also note that the nonlinearity is small. Although a constant pump is far from the geometry of the exponential distribution used in our simulations, it is the first order approximation to hold at $x = 0$ and as we will see it allows us to make a simple statement about the relevant physics in our soliton generator. Now, by absorbing constant terms into the phase of the wave function via $\psi \to \psi\exp(i\theta t)$ we get the

Gross-Pitaevskii like equation

$$\left(-i\hbar\frac{\partial}{\partial t}-\frac{\hbar^2\Delta}{2m}+U'+\alpha_1'|\psi|^2\right)\psi=0, \tag{5.2.2}$$

where α_1' is the effective self-interaction strength for our simplified exciton-polariton equation. Recall that the potential U' which shall be applied is of stepwise form, i.e. $U_1'>0$ for $x<0$ and $U_2'=0$ for $x>0$ as soon as $t>0$. Using the Madelung ansatz $\psi=n^{1/2}e^{i\phi}$ we get the generalized and rescaled quantum hydrodynamical system [244]

$$\partial_t\rho+\partial_x\cdot(nv)=0 \tag{5.2.3}$$

$$\rho\left(\partial_t v+v\partial_x v\right)=-\partial_x\mathcal{P}+\partial_x\Sigma \tag{5.2.4}$$

with $\mathcal{P}=\alpha_1'/(2m^2)n^2$ and $\Sigma=\left(\hbar/(2m)\right)^2 n\cdot\partial_x^2\ln n$, where the superfluid velocity is given by $v=\partial_x\phi$. The integrated form of mass conservation corresponding to the continuity equation (5.2.3) is

$$\partial_t\int_{x_1}^{x_2}ndx+\int_{x_1}^{x_2}\partial_x\cdot(nv)dx=0. \tag{5.2.5}$$

Considering the limits $x_1\to 0$ and $x_2\to 0$ one gets mass conservation at $x=0$ in elementary form, $n_1v_1=n_2v_2$, where we have introduced the abbreviation $v_1=v(x_1)$ etc.. From (5.2.4) and by dropping the anisotropic quantum stress tensor we get elementary momentum conservation $n_1v_1^2+\alpha_1'n_1^2/4=n_2v_2^2+\alpha_1'n_2^2/4$ [244]. Now, combining both elementary equations (momentum and mass conservation) we get

$$v_1^2=\alpha_1'\frac{n_2}{4n_1}(n_1+n_2) \tag{5.2.6}$$

and

$$v_2^2=\alpha_1'\frac{n_1}{4n_2}(n_1+n_2). \tag{5.2.7}$$

We write $n_1=kn_2$ and suppose $n_2=const.>0$ and $k>0$ as both densities are both positive quantities. In those terms we find criteria for the local velocity to be greater than the local speed of sound $c_s^2=\alpha_1'n_i$ ($i\in\{1,2\}$) depending on the size of density modulation. At $x<0$ we have

$$1>4k^2/(k+1), \tag{5.2.8}$$

where the positive part of the solution is $0<k<0.6404$. For $x>0$ we get

$$\frac{k}{4}(k+1)>1 \tag{5.2.9}$$

with $k>1.562$ being the reciprocal value of the corresponding estimate for $x<0$ and it reflects the symmetry of our argument. Note however, that $k<1$, since the applied potential at $x<0$ will reduce the density n_1 there compared to n_2, hence excluding the second criterium.

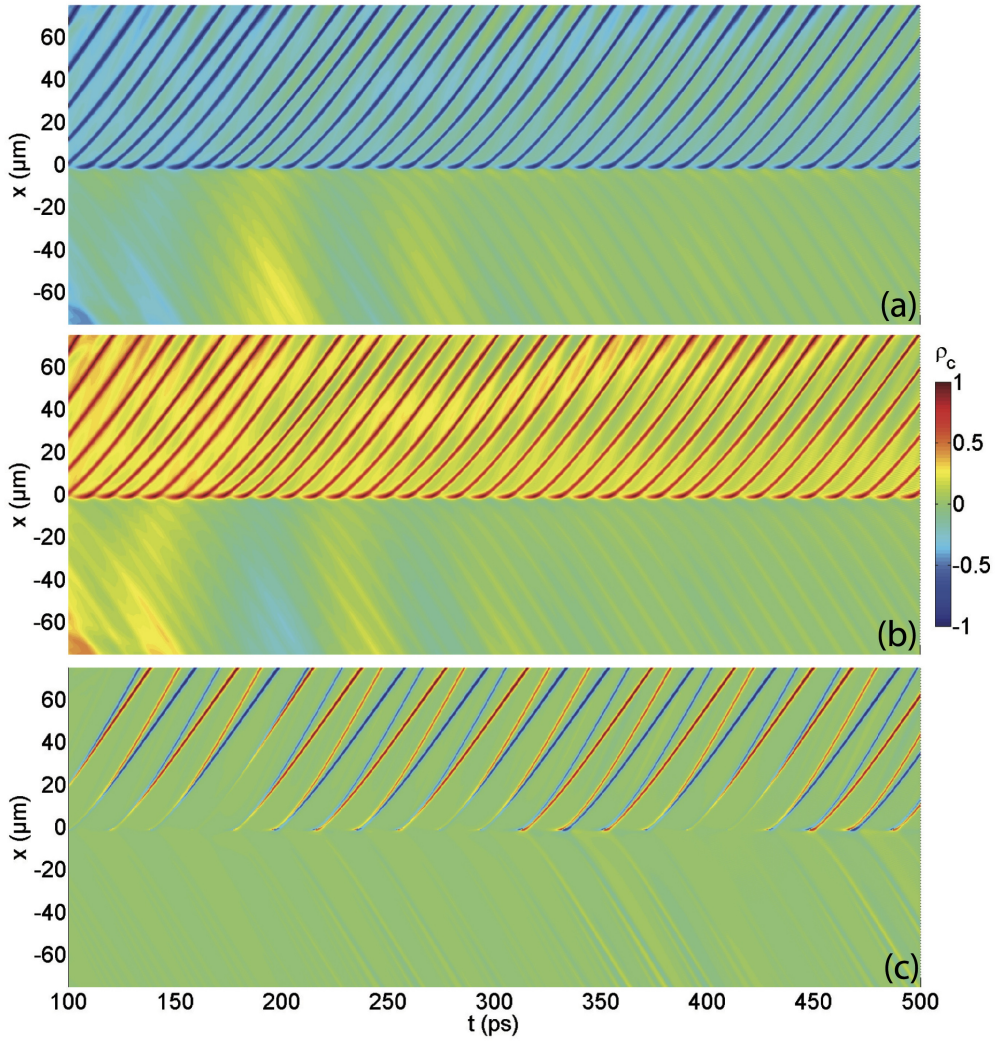

Figure 5.4: (Color online) Control over the polarization of the trains. The colormap shows the degree of circular polarization ρ_c. (a) $\gamma_2/\gamma_1 = 0.90$, (b) $\gamma_2/\gamma_1 = 1.11$ and (c) $\gamma_2/\gamma_1 = 0.99$.

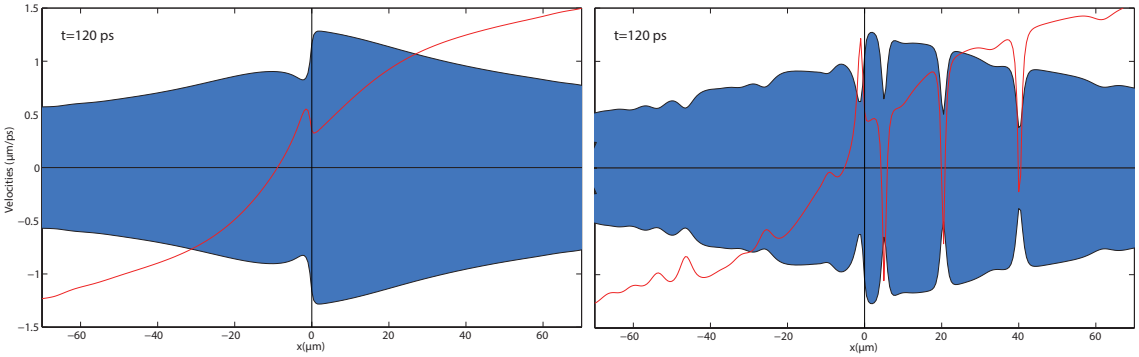

Fig.S 5.5: Snapshots of velocity related quantities taken at $t_s = 120$ ps. The blue envelope displays $\pm c_s(x, t_s)$ (speed of sound) and the red line shows the condensate velocity $v(x, t_s)$. The panel (a) shows results from a pump amplitude $600\Gamma_R$ where no soliton develop [see Fig.1(c)]. The panel (b) shows the development of the train for a lower amplitude of $375\Gamma_R$ [see Fig. 5.1 (b)] due to the local supersonic regions at the step.

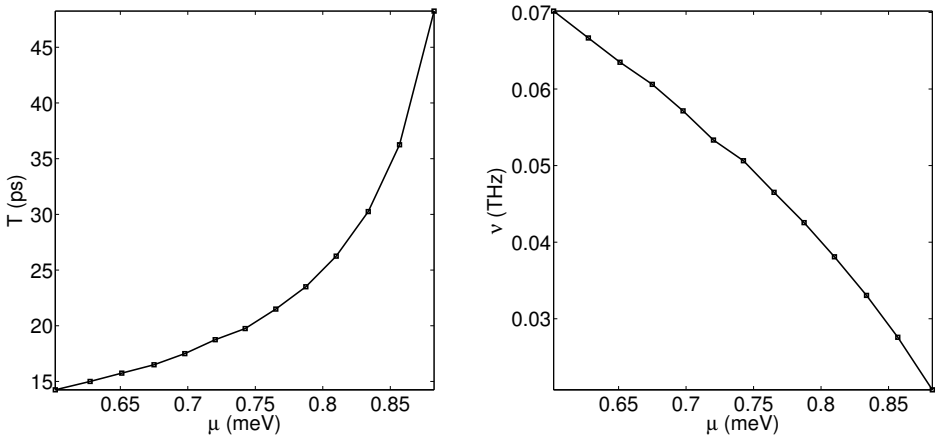

Fig.S 5.6: Train (a) period and (b) frequency versus the local chemical potential obtained from increasing linearly the pump power. Here the step amplitude is fixed to $U_0 = 0.5$ meV. The data points are linearly interpolated.

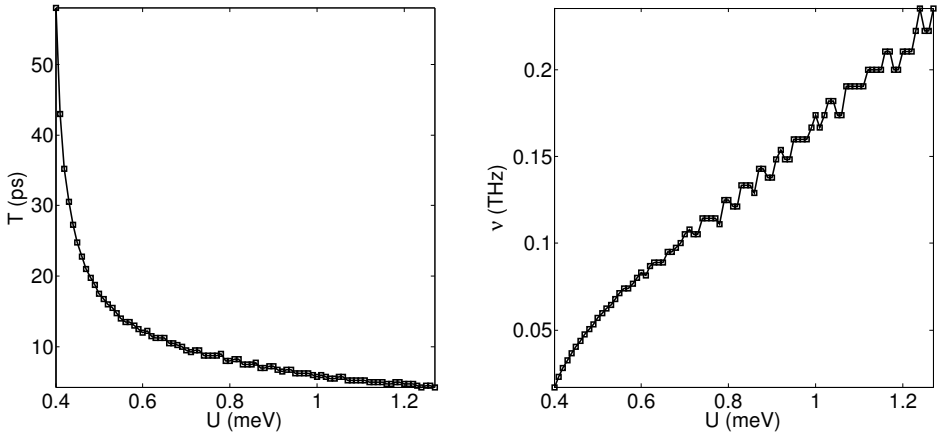

Fig.S 5.7: Train (a) period and (b) frequency versus the potential step heights at fixed pump power $300\Gamma_R$ corresponding to μ=0.7 meV.

6 Coupled counterrotating polariton condensates in optically defined annular potentials

F. Pinsker and N. G. Berloff in collaboration with the experimenters A. Dreismann, P. Cristofolini, R. Balili, G. Christmann, Z. Hatzopoulos, P.G. Savvidis and J. J. Baumberg, doi: 10.1073/pnas.1401988111 (2014).

Polariton condensates are macroscopic quantum states formed by half-matter half-light quasiparticles, thus connecting the phenomena of atomic Bose-Einstein condensation, superfluidity and photon lasing. Here we report the spontaneous formation of such condensates in programmable potential landscapes generated by two concentric circles of light. The imposed geometry supports the emergence of annular states that extend up to, yet are fully coherent and exhibit a spatial structure that remains stable for minutes at a time. These states exhibit a petal-like intensity distribution arising due to the interaction of two superfluids counter-propagating in the circular waveguide defined by the optical potential. In stark contrast to annular modes in conventional lasing systems, the resulting standing wave patterns exhibit only minimal overlap with the pump laser itself. We theoretically describe the system using a complex Ginzburg-Landau equation, which indicates why the condensate wants to rotate. Experimentally, we demonstrate the ability to precisely control the structure of the petal-condensates both by carefully modifying the excitation geometry as well as perturbing the system on ultrafast timescales to reveal unexpected superfluid dynamics.

6.1 Main Work

6.1.1 Author contributions

The contribution by each author are as follows: A.D., P.C., G.C., Z.H., P.G.S., and J.J.B. designed research; A.D., P.C., R.B., and G.C. performed experiments; F.P. and N.G.B. performed theoretical analysis and numerical simulations; F.P. and N.G.B. contributed new analytic tools; Z.H. and P.G.S. managed design and growth of samples; A.D., P.C., R.B., G.C., F.P., N.G.B., and J.J.B. analyzed data; and A.D., P.C., R.B., G.C., F.P., N.G.B., and J.J.B. wrote the paper.

6.1.2 Significance

Collections of bosons can condense into superfluids, but only at extremely low temperatures and in complicated experimental setups. By creating new types of bosons which are coupled mixtures of optical and electronic states, condensates can be created on a semiconductor chip and potentially up to 300 K. One of the most useful implementations of macroscopic condensates involves forming rings, which exhibit new phenomena since the quantum wavefunctions must join up in phase. These are used for some of the most sensitive magnetometer and accelerometer devices known. We show experimentally how patterns of light shone on semiconductor chips can directly produce ring condensates of unusual stability, which can be precisely controlled by optical means.

6.1.3 Introduction

Circular loops are a key geometry for superfluid and superconducting devices, because rotation around a closed ring is coupled to the phase of a quantum wavefunction. So far however they have not been optical accessible, although this would enable a whole new class of quantum devices, particular if room temperature condensate operation is achieved. In lasing systems with an imposed circular symmetry an annulus of lasing spots can sometimes form along the perimeter of the structure [252, 253, 254, 255, 256, 257]. Such transverse modes are often referred to as petal-states [252] or daisy modes [253] and are interpreted as annular standing waves [254], whispering gallery modes [255] or coherent superpositions of Laguerre-Gauss (LG) modes with zero radial index [256, 257]. Their circular symmetry makes them interesting for numerous applications such as free space communication or fibre coupling [258], while their LG-type structure suggests implementations using the orbital angular momentum of light [259], such as optical trapping [260] or quantum information processing [261]. Petal-states have been reported for various conventional lasing systems, including electrically and optically pumped VCSELs [253, 255], as well as microchip [257] and rod lasers[252]. A fundamentally different type of lasing system is the polariton laser [262, 263]. Polaritons are bosonic quasi-particles, resulting from the strong coupling between microcavity photons and semiconductor excitons [262, 263, 264, 16, 265, 266, 267, 268, 270]. Their small effective mass (bestowed by their photonic component) and strong interactions (arising from their excitonic component) favour Bose-stimulated condensation into a single quantum state, called a polariton condensate [16, 265]. These fully coherent light-matter waves spread over tens of microns [266] and exhibit a number of phenomena associated with superfluid He and atomic Bose-Einstein condensation, such as the formation of quantized vortices[267, 268] and superfluid propagation [249]. Their main decay path is the escape of photons out of the cavity, resulting in the emission of coherent light. Note that unlike their weakly-coupled counterparts, polariton lasers require no population inversion since their coherence stems from the stimulated scattering of quasi-particles into the condensate, not the stimulated emission of photons into the resonator mode [262].

In this work we study the spontaneous formation and characteristics of petal-shaped polariton condensates (Fig. 6.1) the strong-coupling analogue to the annular modes

observed in conventional lasers. We show how the fragile ring-states observed previously [270] can be stabilized using carefully-prepared optical confinement, resulting in fully coherent (SI Appendix, SI Text1) and truly macroscopic quantum objects. We dynamically manipulate the latter both by changes of the pump-geometry and ultrafast perturbations, revealing rich many-body physics which is numerically modeled using a complex Ginzburg-Landau equation. We demonstrate an exceptional degree of control over the system suggesting the relevance of our findings for future applications such as all-optical polaritonic circuits [271, 272] and interferometers [273]. We furthermore emphasize differences to the weakly-coupled case, arising as a consequence of the strong nonlinearities that govern the behaviour of polaritons[274, 275] and the fundamentally distinct mechanism responsible for the buildup of coherence.

6.1.4 Petal-condensates

Our experimental setup utilizes a high-resolution spatial light modulator (SLM), which allows phase-shaping of the pump laser into the desired intensity-patterns on the sample (Fig.6.1 (f)). Results here were obtained from a high-quality, low-disorder microcavity, incorporating four sets of three quantum wells. We nonresonantly excite our sample with a single-mode continuous-wave laser, at energies approximately above the bottom of the lower polariton branch. The resulting polariton emission is detected with a CCD for imaging, a monochromator plus CCD for spectral analysis and a streak camera for monitoring its temporal evolution. A Fourier lens and Mach-Zehnder interferometer are used to probe k-space distribution and first-order coherence. All measurements were performed at cryogenic temperatures and on sample locations where the exciton mode is tuned ~ 7 meV below that of the cavity mode.

The excitation-pattern used to stably generate petal-type condensates consists of two concentric circles of laser light (Fig. 6.1 (c), white rings), with a local intensity ratio for inner to outer circle of $1:8$. The nonresonant excitation results in the formation of a cloud of hot excitons at the position of the pump, which subsequently relax in energy, couple to the cavity mode and accumulate at the bottom of the lower-polariton branch. Due to their repulsive interactions, polaritons experience a local blue-shift at positions of high exciton density [266, 276]. For the given pump geometry, this induces a potential landscape resembling an annular waveguide. Strikingly, the resulting polariton condensate forms in the region between the outer and the inner pump ring, thus unlike conventional lasing systems [257, 277] and contrary to Manni et. al. [270] exhibiting only minimal overlap with the pump laser itself (Fig.6.1 (c)). This effect is a direct consequence of the specific properties of polaritons, namely their strong nonlinear interactions with the hot exciton cloud and their ability to propagate over tens of micrometer distances before they decay [266, 276]. The resulting petal-condensates possess a well-defined energy and exhibit a characteristic annular intensity distribution (Fig. 6.1 (a)-(d)), which remains stable for $> 1.000s$ timescales. The real space image of a ring with n intensity lobes translates into a reciprocal space image with an identical number of lobes, where the emission coming from a specific lobe in real space stems from polaritons with equal and opposite wavevectors around the annulus (Fig.6.1 (h)-(k)).

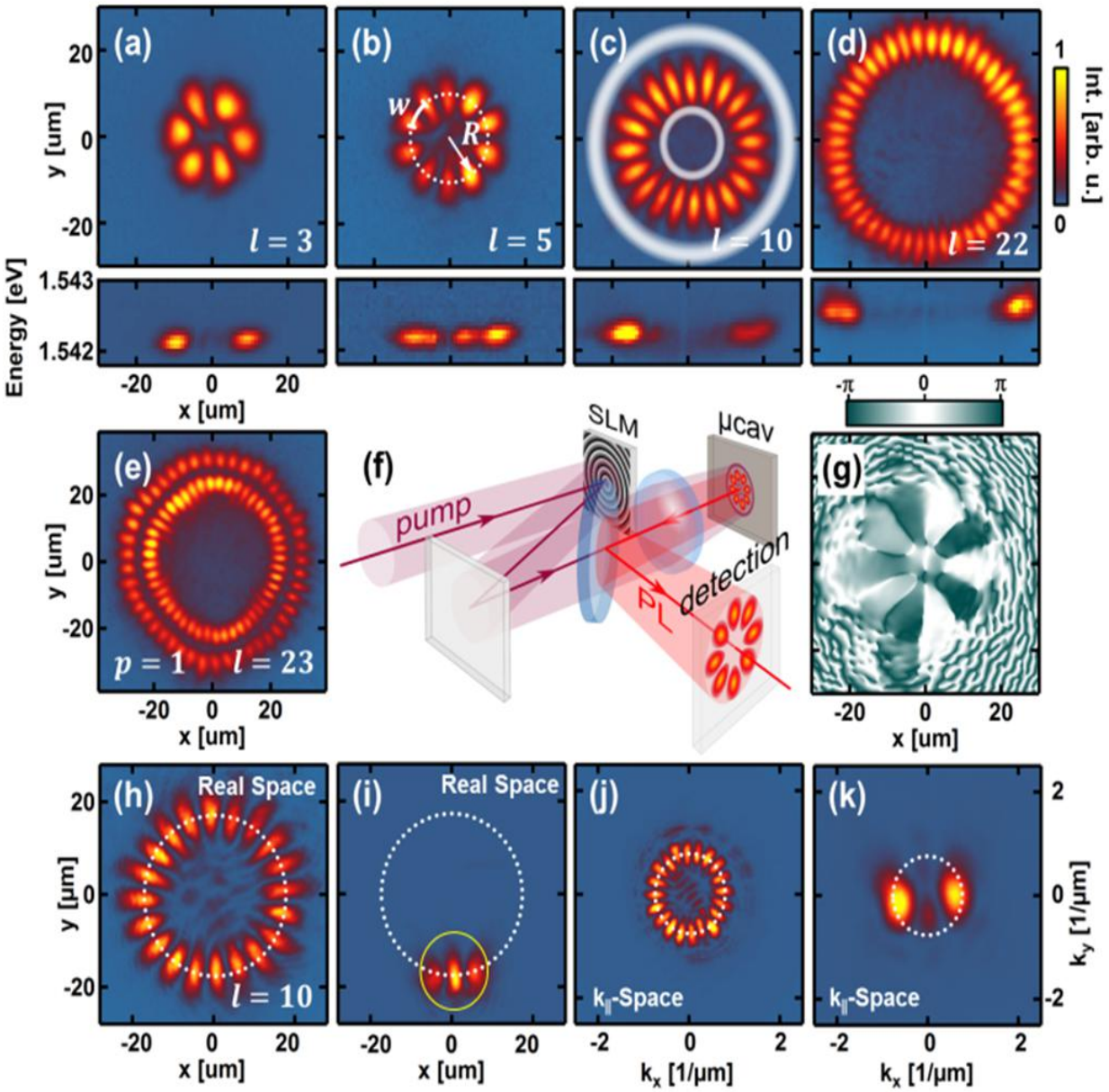

Figure 6.1: Petal-shaped polariton condensates. (a)-(d) Spatial images and spectra (horizontal cut at $y = 0$) of annular states with increasing azimuthal index l. The shaded rings in (c) indicate the position of the pump laser. (e) Double-ring with radial index $p = 1$. (f) Schematic of the experimental setup, showing the phase-shaped pump laser and the resulting polariton emission. (g) phase of the condensate wave function in (b), extracted following the method discussed in [270]. As constant reference, one of the lobes was magnified and superimposed over the whole image. (h)(k) real- and k-space images of the petal state with $l = 10$ The k-space image in (k) is obtained by spatially filtering the polariton emission as shown in (i).

This observation yields the picture of two counter-propagating superfluids, analogous to superconducting loops and qubits [278, 279]. Because both waves are subject to periodic boundary conditions, their superpositions always possess an even number of lobes with a well-defined phase and a phase-jump of π in between lobes (Fig. 6.1 (g)). Mathematically, these properties are consonant with a description as superpositions of two $\mathrm{LG}_{p,\pm l}$ modes with radial index $p = 0$ and azimuthal indices $\pm l$, where the number of lobes n is given by $n = 21$ (SI Appendix, SI Text 2). Adjusting the diameter of the excitation pattern allows the selection of petal-states with an arbitrary even number of lobes, up to a (power-limited) maximum of $n \simeq 120$. However, increasing the separation between inner and outer pumprings results in the formation of higher-order ring-states with radial nodes ($p > 0$) and identical$n$ (Fig.6.1 (e)). The orientation of the nodal lines depends on the relative phase of the two counter-propagating waves; for a uniform pump, it is pinned by local disorder, as can be seen from the rotation of the condensate as we move across the sample (SI Video 1), matching similar observations for the case of VCSELs(2). However, azimuthally modulating the pump intensity allows us to freely select the orientation of the petals, further demonstrating the high degree of control possible over the system (SI Text 3). These ring-states are highly resilient to irregularities of the sample surface, maintaining their shape even in the presence of cracks and other defects (SI Text 4).

6.1.5 Power dependence

To explore the formation process of the reported ring-shaped condensates, we study the evolution of the system as the excitation power increases (Fig. 6.2). The latter causes a growth of the density-induced blue-shift potential at the position of the pump, accelerating polaritons away from the region of their creation and up to a final velocity $v_{max} \simeq \sqrt{2V_0/m^*}$, where m^* is the polariton effective mass. For low pump powers the excited polaritons gain only little momentum and hence cover only short distances before they decay; consequently pump and polariton luminescence coincide (Fig.6.2 (a),(e)). However, as pump intensity and blue-shift increase, so does the momentum of the polaritons. Those travelling towards the centre of the pump-geometry are eventually slowed down by the potential associated with the inner ring and accumulate in the region between both rings (Fig.6.2 (b),(e)). This accumulation is further enhanced by stimulated scattering of polaritons directly from the pump, as can be seen from the non-linear increase of polariton emission from the region between the laser rings even below threshold (green line in Fig. 6.2 (d)). At sufficiently high powers, the corresponding polariton population reaches the critical density for condensation and a petal-state forms (Fig.2c), with the polariton wavevector k_c pointing around the annulus. The formation of the condensate is accompanied by a strong nonlinear increase of emission intensity, while the number of polaritons outside the pump-ring decreases (Fig.6.2 (d),(e)). The latter effect suggests that the condensate now efficiently harvests almost all polaritons created at the pump due to stimulated scattering, as reported for optically confined condensates previously [280]. Increasing the excitation power beyond the condensation threshold P_{thr} quickly leads to the breakdown of the single ring-state,

which unlike in the work of Manni et. al. [270] is only observed within a narrow power range up to $1.3P_{thr}$. We attribute this observation to the repulsive nature of polariton-polariton interactions, which blue-shift the condensate energy with increasing density and eventually screen the influence of the inner pump ring, allowing a superposition of higher-order states to fill up the whole excitation geometry (SI Appendix, SI Text5).

6.2 Mode selection

We next use the flexibility of our setup to systematically vary the pump-geometry and study the mode-selection mechanism linking a specific excitation pattern to the resulting petal-state. As the diameter of the pump ring is gradually increased, the number of lobes n is found to grow as $n \sim r_c^2$, where r_c denotes the radius of the condensate ring (Fig.6.3 (a), green points). Note that in all cases the condensate forms in the region between the two pump rings.

A qualitative explanation for this observation can be found by considering that condensation will initially occur at the point of highest polariton density. Just below threshold, this corresponds to the doughnut-shaped region between the two pump rings, as can be seen from the distribution of polariton emission in Fig.6.2 (b). The optimum overlap between this low-energy polariton reservoir with radius r_{res} and the condensate-pattern is achieved for $\mathrm{LG}_{0,\pm l}$-states of identical radius, i.e. $r_c = r_{res}$ [256, 257]. Consequently, these states possess the lowest condensation threshold and first start oscillating as the pumping increases. Because this argument holds equally for the energetically degenerate left- and right-handed $\mathrm{LG}_{0,\pm l}$ modes, both are excited simultaneously, resulting in the observed standing wave patterns. The radius of maximum intensity for a superposition of $\mathrm{LG}_{0,\pm l}$ modes lies at $r_c = w\sqrt{l/2}$, where w denotes the width of the cavitys fundamental mode (SI Appendix, SI Text2). Taking into account that the number of lobes$n$ is given by $n = 2l$, we arrive at the relation $n = [2/w]^2 r_c^2$, which reproduces the experimental data for $w \simeq 9.3\mu$ m (green line in Fig.6.3 (a)).

6.2.1 Theoretical description

To theoretically approach the observed phenomena we use a complex Ginzburg-Landau (cGL)-type equation [91] incorporating energy relaxation [281] and a stationary reservoir:

$$i\partial_t \psi = (1 - i\eta)\frac{H}{\hbar}\psi \tag{6.2.1}$$

$$\frac{H}{\hbar} = \left[-\frac{\hbar\nabla^2}{2m} + V(\vec{x},t) + \frac{i}{2}\left(\delta_R N(\vec{x},t) - \gamma_C\right)\right] \tag{6.2.2}$$

Here, $\psi(\vec{x},t)$ represents the order parameter of the condensate, η the rate of energy relaxation and m the effective mass of polaritons on the lower branch of the dispersion curve. $\delta_R N/2$ and γ_C are the condensate gain and loss rates, respectively; and $V(\vec{x},t) = g_R N + g_C|\psi|^2 + V_{dis}$ denotes the potential landscape experienced by the condensate, which arises due to interactions with the reservoir ($g_R N$), polariton-polariton

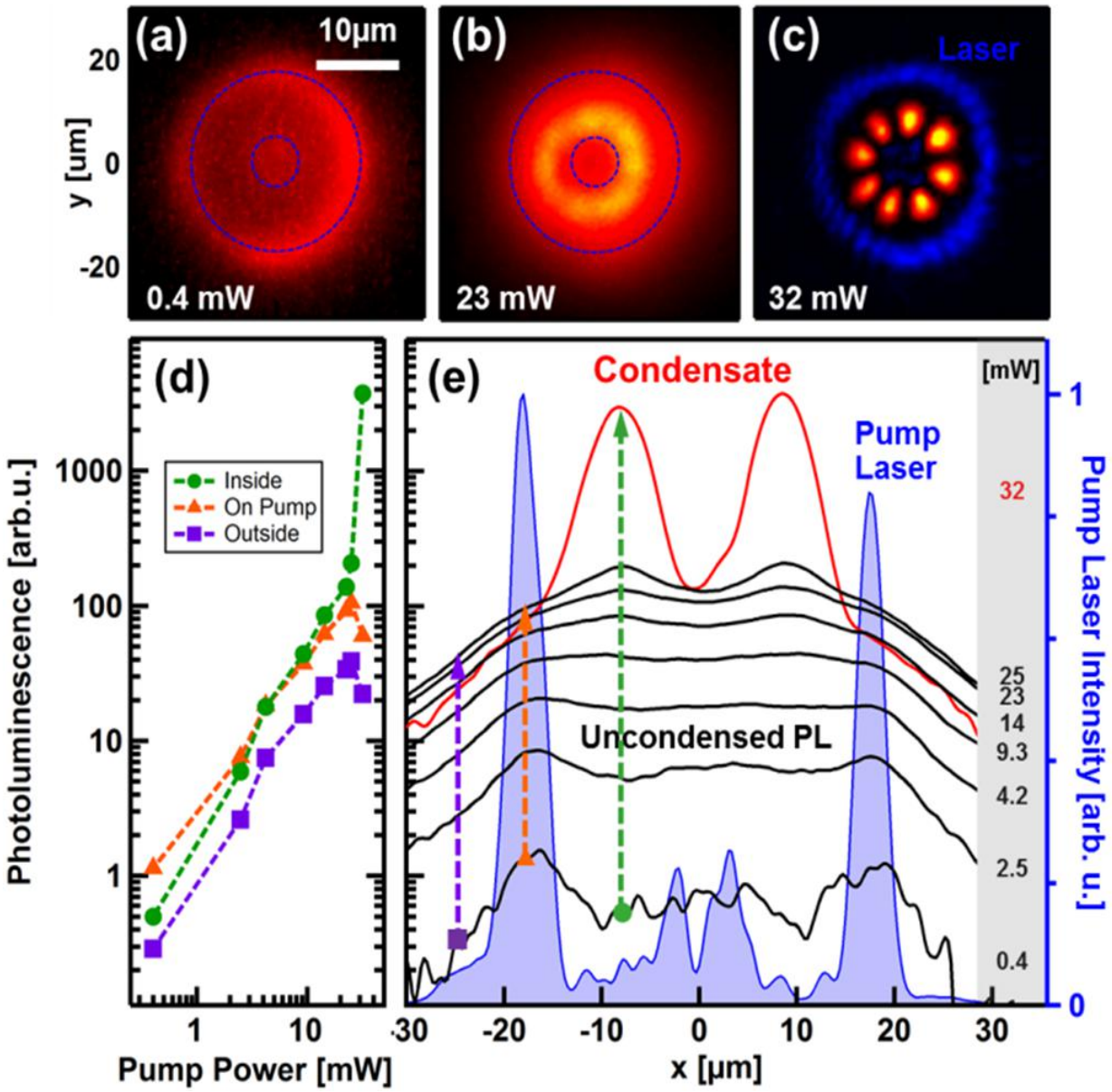

Figure 6.2: Sample luminescence with increasing excitation power. (a,b,c) Spatial image of the polariton emission with increasing pumping power. Dashed blue line indicates the position of the laser as shown in (c). (d,e) Power dependence of the intensity distribution along a central horizontal cut.

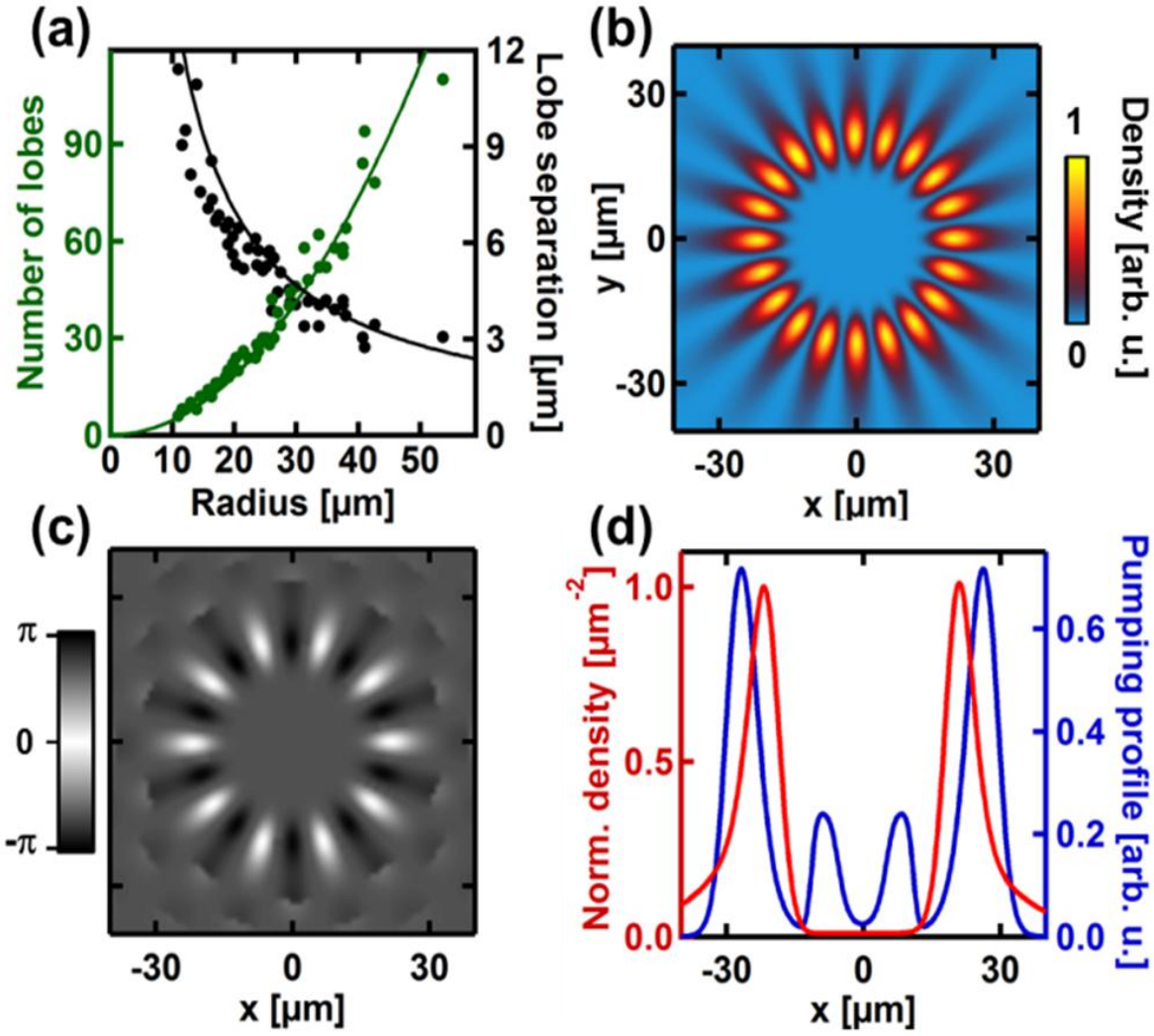

Figure 6.3: (a) Measured number of lobes n (green points) and spatial separation between lobes (black points) as a function of condensate radius r_c. Fits are obtained from simulations of the cGL equation for different pump radii (SI Appendix, SI Text 6) or the analytic expression for the density-maximum of LG-modes (SI Appendix, SI Eq. S4). (b) Simulated spatial density of a petal-condensate with $n = 20$ lobes and (c) corresponding phase. (d) Horizontal cut of (b), indicating the relative position of the condensate and the pumping profile.

interactions ($g_C|\psi|^2$) and energy fluctuations due to sample disorder (V_{dis}). The radially symmetric pumping profile $P(\vec{x})$ is chosen to reproduce the experimental double-ring excitation-geometry (SI Appendix, SI Text 6), giving rise to a reservoir density distribution following $\partial_t N = -(\gamma_R + \beta|\psi|^2)N + P$, where γ_R represents the reservoir decay and β the condensate-reservoir scattering rate. Because the relaxation of the reservoir is much faster than the decay of the condensate ($\gamma_R \gg \gamma_C$) [281], the reservoir dynamics can be approximated by the stationary value $N \simeq P(\vec{x},t)/(\gamma_R + \beta|\psi|^2) \simeq P/\gamma_R + (P\beta/\gamma_R^2)|\psi|^2$, where in the second step $|\psi|$ was assumed to be small. Numerical solutions of equation (6.2.1) for the parameters given in the Materials and Methods section are presented in Fig.6.3. The simulated condensate density and corresponding phase (Fig. 6.3 (b),(c)) are obtained for a pumping profile matching that of Fig.6.1 (c). The simulation clearly reproduces the observed petal-structure with $n = 20$ lobes. Note that energy relaxation and disorder prove critical to stabilize the angular orientation of the calculated petal-modes (SI Appendix, SI Text 6). The maxima of condensate and reservoir are spatially separated (Fig. 6.3 (d)) in accordance with the experiment (Fig.6.2 (e)), although their separation is less pronounced in the simulation (Fig.6.2 (e)). We attribute this deviation to the simplicity of our model which does not incorporate the propagation of uncondensed polaritons. Gradually increasing the radius of the simulated pumping profile results in the formation of states with a higher (even) number of lobes. The relation between condensate radius and lobe number agrees precisely with the experimental data (green and black lines in Fig.6.3 (a), SI Appendix, SIText6). An analytic estimation for the observed relation is provided in the Supporting Information (SI Appendix, SI Text 7). Note that the formation of lobes corresponds to excitations of the systems ground state. In the linear picture the latter are associated with the larger in-plane wave vectors of higher-order -modes, whereas from the viewpoint of a (nonlinear) complex Ginzburg-Landau equation the phase-jumps observed between adjacent lobes and the vanishing condensate density can be interpreted as a signature of dark solitons or solitary waves. However, the standing wave pattern appears in simulations even if the real nonlinearity is set to zero ($g_C = 0$). The weak nonlinearity slightly modifies the density profile, but does not change the number or position of the lobes. While this implies that the formation mechanism of the petal-structure can be understood in terms of linear physics, the condensate itself and each of its lobes still represent a highly non-linear system due to polariton-polariton interactions. Arrays of the lobes represent excitations of the condensate ground state and can arise due to the interaction of counter-propagating superfluids in an effective setting [282, 26]. We assume that the reported ring-condensates occupy excited states instead of their ground states to maintain energy conservation: Polaritons generated in the blue-shifted pumping regions which scatter into the condensate lack an efficient mechanism for energy relaxation [276], as evidenced by the fact that both possess the same energy (SI Text 8). Since the blue-shift at the position of the condensate is much smaller than that at the pump, the condensate must form in an excited state, translating into a transverse wave vector $k_c > 0$ (linear picture) or the formation of an array of dark solitary waves (non-linear picture). Increasing the radius of the pump rings results in the formation of states with a higher number of lobes, corresponding to higher condensate energies (SI Appendix, SI Text 9). Qualitatively, one can associate

this with an accelerated rotation of the two counter-propagating condensates. A related phenomenon was studied in [48], where the authors show that inhomogeneous pumping of large-area trapped condensates can spontaneously induce condensate rotation and the formation of vortex lattices. Assuming the annular waveguide forms a harmonic trap with level spacing $\hbar\omega$, the stable rotation speed is $\Omega = n_V/\tilde{r}^2 = 1$, where $\tilde{r} = r/\sqrt{\hbar/m\omega}$. n_V represents the number of vortices in the lattice and was shown to grow quadratically with the radius of the pump. However we note that this intuitive explanation does not include the presence of 2 counter-propagating condensates, and that given the one dimensional geometry here, vortex pairs are not seen [24] but instead a standing wave with the full condensate density depletions.

6.2.2 Condensate dynamics

To explore the time dynamics of the system, we non-resonantly perturb the *cw*-pumped petal condensate with a 150−fs pulsed laser, which is focussed on the side of the ring (Fig.4a, inset). Fig.6.4 (a) shows a cylinder projection of the polariton emission around the condensate ring at different times t, as reconstructed from a full set of tomographic streak camera measurements. Before it is perturbed ($t < 0ps$), the condensate forms a stable petal-state with $n = 22$ lobes. The initial effect of the perturbing pulse P at $t = 0$ps is a strong reduction of the overall polariton emission after ~ 2ps (Fig.4a,b). We attribute this behaviour to photons that are rapidly generated by the laser pulse and subsequently propagate ballistically across the cavity, where they extract gain from the exciton reservoir due to stimulated emission into the wave-guided mode. The additional exciton population locally introduced by the laser pulse creates a localized blue-shift potential barrier, analogous to the weak links forming Josephson junctions in superconducting loops and SQUIDs. The potential barrier breaks up the ring state by pushing apart its lobes while transiently reducing their number, corresponding to a reduction of the respective vorticity of each counter-propagating wave. Note that the modified potential landscape at this point no longer imposes periodic boundary conditions on the system, thus allowing the formation of states with an odd number of lobes as well. The additional gain provided by the laser pulse creates an imbalance of the polariton density around the ring (green and pink lines, Fig.4b). The high density of polaritons formed on either side of the disturbance propagate along the annulus at a velocity $v \simeq 1.3\mu m/ps$ (dashed line in Fig.6.4 (a)), matching that expected for polariton wave packets oscillating in a harmonic potential [280]. As a consequence, density oscillations with a period of $T \simeq 14ps$ are observed when the lobes are perturbed sideways by the impulse (Fig.6.4 (b) and (c)). As the exciton reservoir generated by the laser pulse decays and further feeds the condensate, the overall polariton emission increases above its initial value due to the additional gain provided (Fig.6.4 (a) and (b)). The reduction of the corresponding potential barrier at the same time allows the convergence of the separated lobes and finally the re-formation of the petal-state after $t > 400ps$. Simulations confirm that this behaviour is characteristic of the cGL nonlinear quantum dynamics (SI Video 2).

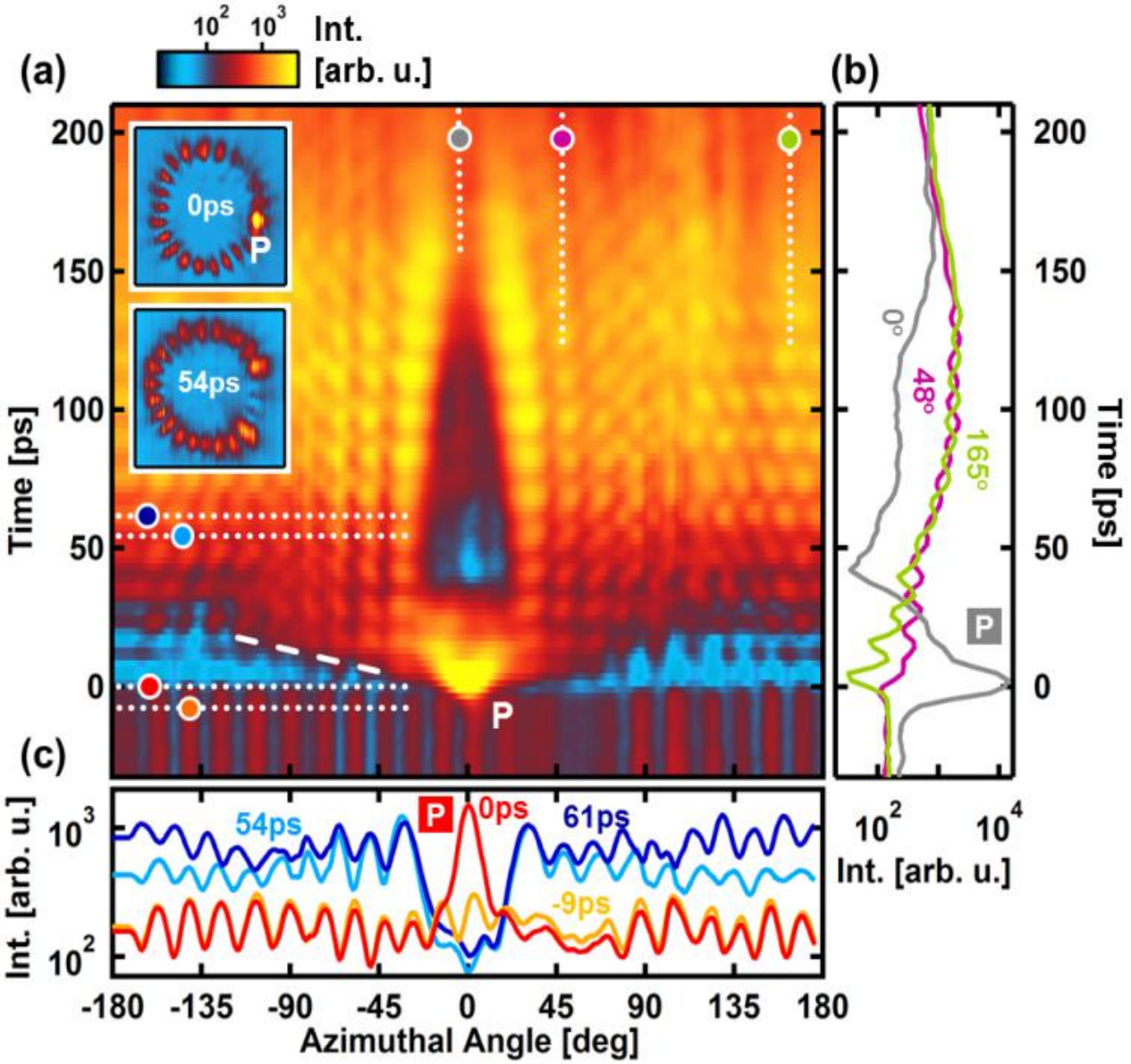

Figure 6.4: Time dynamics of a perturbed petal-condensate. (a) Cylinder projection of the polariton emission around the condensate annulus at different times . The perturbing pulse P arrives at $t = 0ps$. The insets show spatial images of the condensate ring at $t = 10ps$ and $t = 54ps$. Dotted lines indicate the position of space cuts depicted in (b) and time cuts depicted in (c). Dashed line is a guide to the eye. (Insets) Spatial images at different times.

6.2.3 Summary and conclusion

We have studied the properties of exciton-polariton condensates in optically-imposed annular potentials. The pumping-geometry supports the formation of quantum states that extend up to $100\mu m$, are highly resilient to defects and sample disorder and remain stable for minutes at a time. The observed phenomena are reproduced by simulations of a complex Ginzburg-Landau type equation. The spatial separation of pump reservoir and condensate minimizes dephasing and other perturbations due to interactions with hot excitons [283], thus making this excitation geometry highly-advantageous for stable macroscopic quantum devices operating at ultra-low thresholds. Exploitation of such states on semiconductor chips is analogous to those of superconducting weak-link devices. Since the pure $LG_{0,\pm l}$ modes carry a net orbital angular momentum associated with a helically propagating phase and exhibit a vortex in their centre, lifting the degeneracy between the counter-propagating modes (e.g. with magnetic fields) can result in a pure rotating condensate with giant stable vortex core. The ability to sculpt the polariton potentials into arbitrary shapes (SI Appendix, SI Text 10) opens up new explorations of condensate superfluid flow in a wide variety of topologies.

6.2.4 Materials and Methods

The sample consists of a $5\lambda/2$ AlGaAs/AlAs microcavity, with a quality factor exceeding $Q > 16,000$, corresponding to cavity-photon lifetimes $\tau > 7ps$. Four sets of three quantum wells are placed at the antinodes of the cavity optical field, with an exciton-photon Rabi splitting of $9meV$. All reported experiments were performed at sample positions where the cavity mode is detuned $7meV$ below the exciton energy. The system is pumped with a $\lambda = 755 - nm$ single-mode continuous wave Ti:Sapphire laser, which is projected through a $4x$ telescope and a $50x$ high-NA microscope objective acting as a Fourier lens. The resulting polariton emission of $\sim 800nm$ is collected with the same microscope objective and separated from the laser radiation by means of a tuneable Bragg filter; it is detected by a Si CCD for imaging, a $.055m$ monochromator with a nitrogen-cooled CCD for spectral analysis and a streak camera (time resolution $2.5ps$) for monitoring the temporal evolution. A Fourier lens and a Mach-Zehnder interferometer were used to probe its k-space distribution and first-order coherence. The parameters used in the simulation were chosen in agreement with Refs. [270, 281, 284], where energy relaxation rate $\eta = 0.02$, reservoir decay rate $\gamma_R = 10ps^{-1}$, condensate decay rate $\gamma_C = 0.556ps^{-1}$, reservoir interaction constant $g_R = 0.072\mu m^2 \cdot ps^{-1}$, self-interaction constant $g_c = 0.002\mu m^2 \cdot ps^{-1}$, factor of condensate gain rate $\delta_C = 0.06\mu m^2 \cdot ps^{-1}$, condensate-reservoir scattering rate $\beta = 0.05\mu m^2 \cdot ps^{-1}$. The effective mass of the lower polariton branch was measured as $m = 4.7 \cdot 10^{-35} kg$.

6.3 Supporting information

6.3.1 Macroscopic coherence

The petal-type condensates discussed in this work extend over tens of microns while being fully coherent, thus beautifully depicting truly macroscopic quantum-states. Fig.6.5 illustrates this by probing the coherence of a ring with $n = 80$ lobes and a diameter of approximately $90\mu m$. The condensate emission is analysed with a Mach-Zehnder interferometer, resulting in two spatially separated images (Fig.6.5 (a)). The coherence between opposite sides of the ring is probed by overlapping the corresponding parts of the emission, clearly resulting in the appearance of interference fringes (Fig.6.5 (b)).

6.3.2 Laguerre-Gauss modes

The electric field of a Laguerre-Gauss mode with radial index p and azimuthal index l is given by (6.5):

$$LG_{p,l} = \sqrt{\frac{2p!}{\pi(p+|l|)!}} \cdot \frac{1}{w(z)} \left(\frac{r\sqrt{2}}{w(z)}\right)^{|l|} L_p^{|l|}\left(\frac{2r^2}{w^2(z)}\right) \cdot \exp\left(r^2\left(-\frac{1}{w^2(z)} - ik\frac{1}{2R(z)}\right) + i(2p+|l|+1)\zeta(z) - il\phi\right) \quad (6.3.1)$$

with

$$\zeta(z) = \arctan\left(\frac{z}{z_R}\right) \quad (6.3.2)$$

and where r and ϕ are the radial and azimuthal coordinates respectively. z denotes the propagation distance, with $w(z)$, $R(z)$ and z_R as the width, the radius of curvature and the Rayleigh range of a Gaussian beam defined in the usual way. $L_p^{|l|}(z)$ represents a generalized Laguerre-polynomial. The observed petal-states with a single ring closely resemble coherent superpositions of two LG modes with zero radial and opposite azimuthal indices, which are given by:

$$LG_{0,\pm l} = LG_{0,+l} + LG_{0,-l} \quad (6.3.3)$$

The angular dependence of this expression is carried by the last factor, which can be written as $\cos(l\phi)$. Collapsing all other factors for the explicitly given function into the function $A(r, z, l)$, Eq.(4.2.9) takes the form:

$$LG_{0,\pm l} = A(r, z, l)\cos(l\phi), \quad (6.3.4)$$

giving the characteristic relation between number of lobes and azimuthal index: $n = 2l$.

Finally, the radius of maximum intensity of the $\mathrm{LG}_{0,\pm l}$ mode is found for $\partial_r|A|^2 = 0$, yielding:

$$r_{max} = \sqrt{l/2}w(z). \quad (6.3.5)$$

Three examples for superpositions of $\mathrm{LG}_{p,l}$ modes are shown in Fig.6.6.

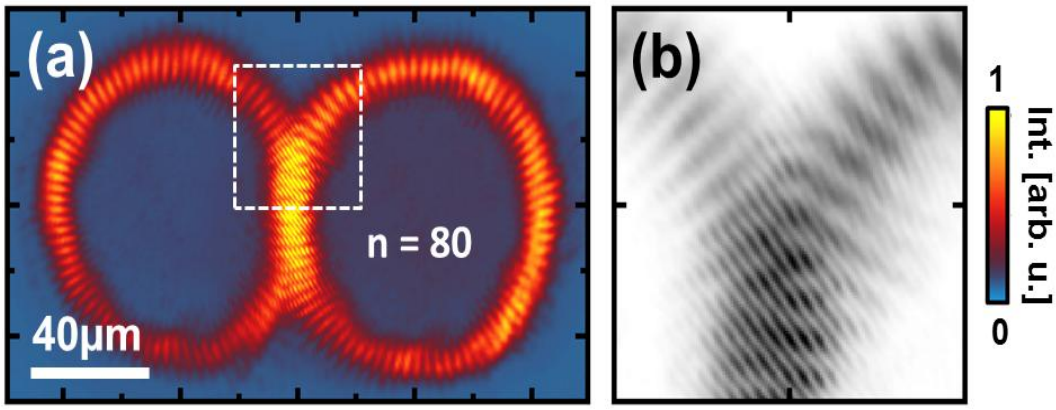

Figure 6.5: Coherence of petal-states. (a)Superposition of two spatial images of one petal-state with $n = 80$ lobes, as recorded with a Mach-Zehnder interferometer. The two images are offset to probe the coherence between the opposite sides of the ring. (b)Magnified view of the area marked by the dashed square in (a), showing the interference between the two images .

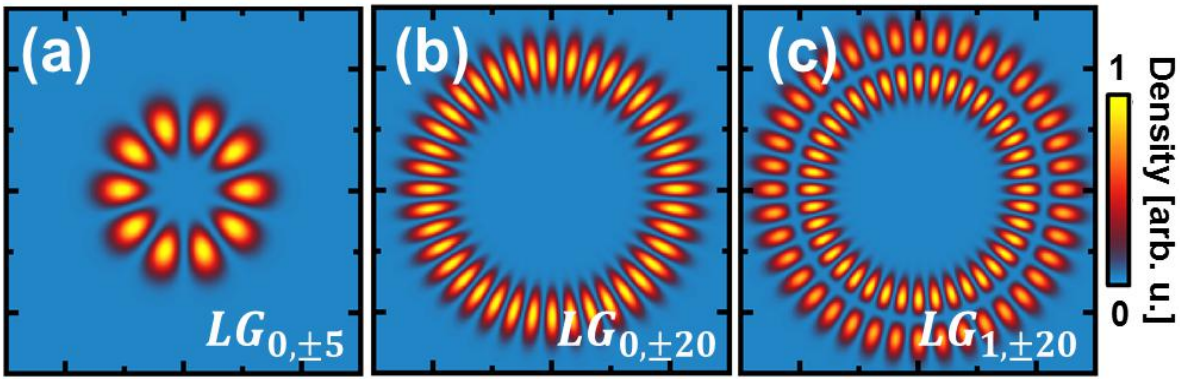

Figure 6.6: Superpositions of Laguerre-Gauss modes. (a,b) Modes with zero radial index $l = 5$ and azimuthal indices $l = 20$ and , respectively. (c)Double-ring with $p = 1$ and $l = 20$.

6.3.3 Optical pinning

Spatially modulating the pump laser allows us to overcome the influence of the local disorder-potential and determine the orientation of a petal-state. Fig. 6.7 (a) shows an azimuthally modulated laser circle with 8 intensity maxima. This pump configuration results in the formation of a petal-state with $n = 10$ lobes (Fig. 6.7 (b)), the orientation of which can be changed by rotating the pump (Fig. 6.7 (c) and (d)).

6.3.4 Stability with respect to defects and disorder

The observed petal-condensates are highly resilient to defects on the sample surface, as demonstrated in Fig. 6.8. The location of a crack is revealed by illuminating it with a single excitation spot (Fig. 6.8 (a)). In this case some of the resulting polariton emission is scattered along the edge of the crack, as indicated by the dashed white line. In Fig. 6.8 (b) an annular pump is used to generate a petal-state with $n = 18$ lobes at the same position, which remains stable despite the fact that the crack intersects it at two points.

Fig. 6.8.(c),(d),(e) illustrates the stability of the ring-condensate with respect to movement across the sample, i.e. sample disorder. Despite the fact that the pump is shifted by $80\mu m$ between Fig. 6.8 (c) and Fig. 6.8 (e), the observed petal-state remains unaltered, except for a slight rotation of the orientation of the pattern. Fig. 6.9 demonstrates the influence of a point-defect on a double-ring state with $n = 32$ lobes (azimuthal index $l = 16$) and one radial node ($p = 1$). The undisturbed state is shown in Fig. 6.17 (a). As the pump (Fig. 6.9 (i)) is moved across the sample surface, a point defect perforates the outer ring from the top, suppressing one of its lobes (Fig. 6.9 (b)). Note that at this point the outer ring possesses an odd number of lobes, suggesting that here the system is no longer object to periodic boundary conditions. As the pump is moved further and the defect blocks the inner ring as well (Fig. 6.9 (c)), the petal-state collapses and a complicated polariton distribution fills out the whole ring, with maximum intensity at the centre of the geometry. Fig. 6.9 (h) shows that a local disturbance of the condensate can sometimes lead to rearrangement of the full pattern, in this case resulting in a somewhat rectangular wavefunction.

6.3.5 Power dependence

This section provides additional details for the discussion of the condensate power dependence of the main text. Fig. 6.10 shows spectra corresponding to the spatial images presented in Fig. 6.2 (a)-(c) (main text), measured along a central horizontal cut. The spectra demonstrate the increasing blue-shift of the lowest energy polariton states with increasing pumping power as well as their spatial shift towards the position of the petal-structure. The weaker intensity luminescence observed at higher energies stems from the decay of polaritons that have not yet relaxed to the lowest energy state.

The ring-states reported in this work are only stable within a narrow power range of approximately $1 - 1.3P_{thr}$. Fig. 6.11 (a) shows a petal state with 34 lobes, as observed directly at condensation threshold ($P_{thr} = 47.0mW$). The bottom panel shows the

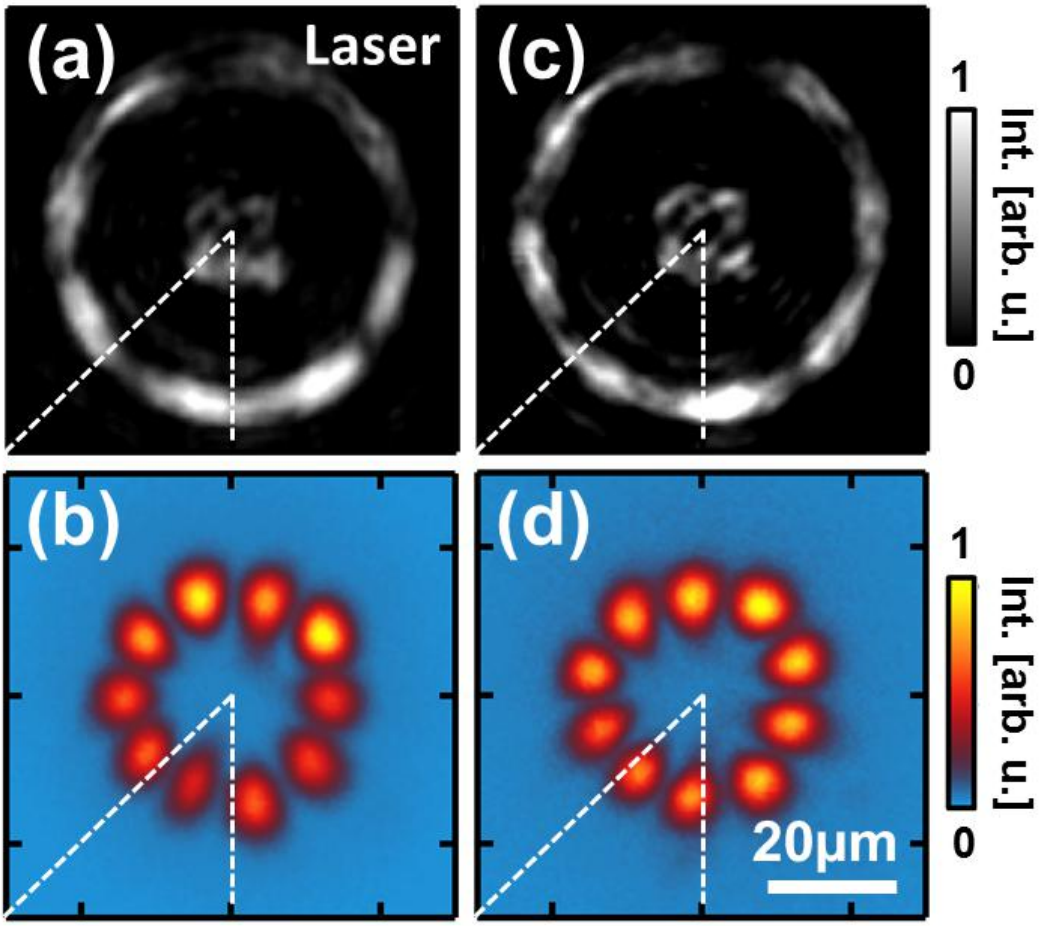

Figure 6.7: Determining the orientation of a petal-state by modulating the pump. (a),(c)Spatial images of the pump laser, azimuthally modulated with 8 intensity maxima. The geometry in (c) is rotated by 28 with respect to(a). (b),(c)Corresponding $n = 10$ petal states, with lobe-orientations determined by the orientation of the pump. .

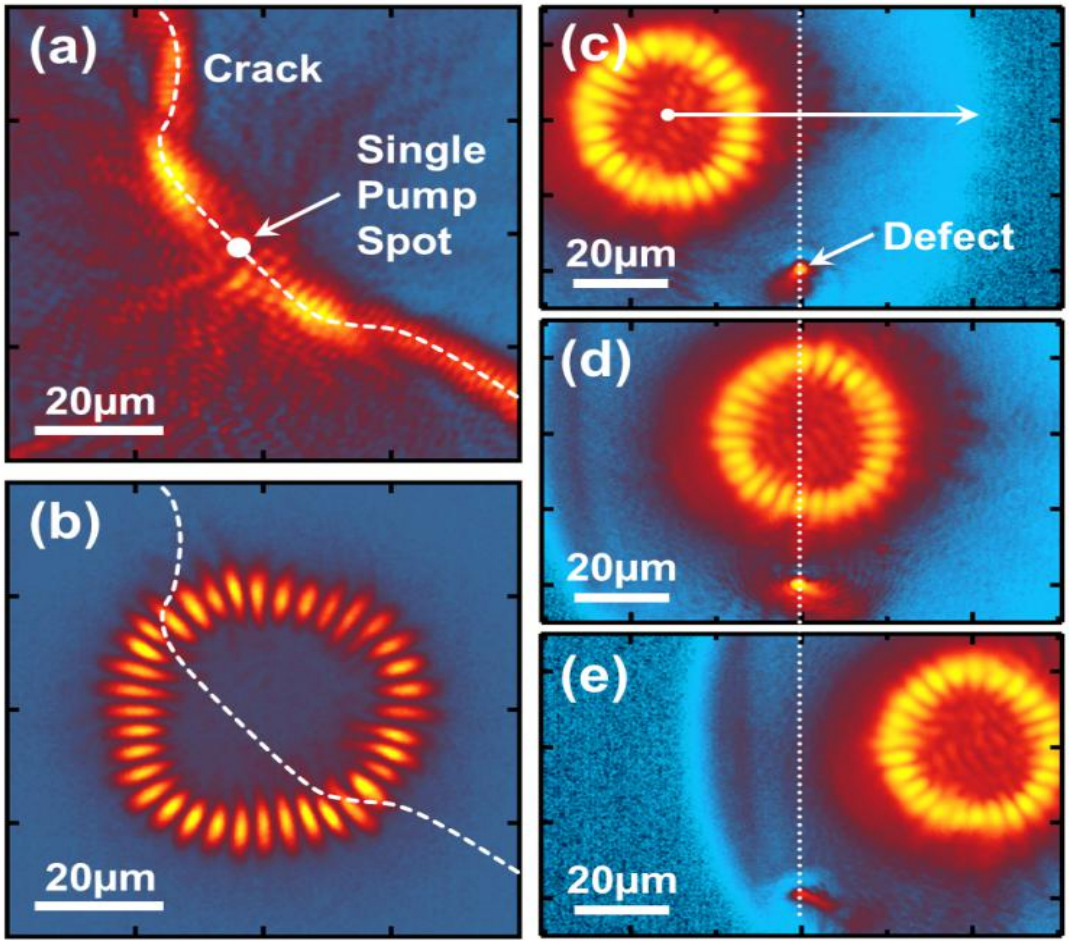

Figure 6.8: Stability of petal-states with respect to defects and disorder. (a) Single excitation spot revealing a crack on the sample. Dashed white line illustrates the location of the crack. (b) Petal-state at the same position. (c-e) Petal-state as the pump is moved across the sample. Point-defect at the bottom provides a reference for the movement. .

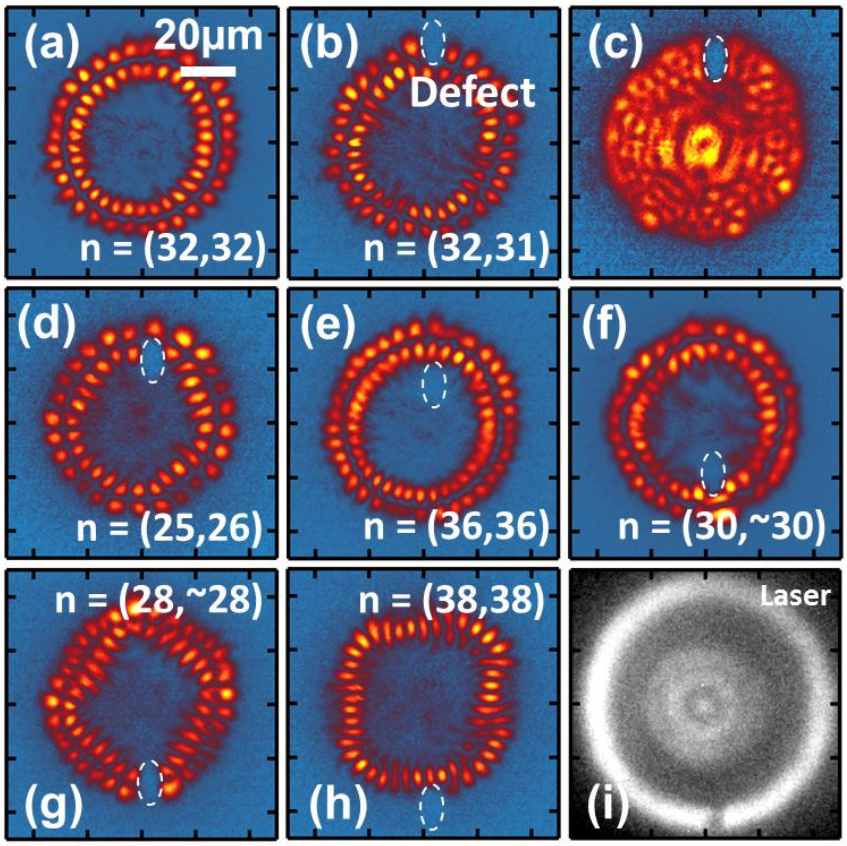

Figure 6.9: Double-ring state with $n = 32$ lobes and one radial node (a) moving across a point-defect. Depending on the relative position of the defect, the number of lobes in the outer or inner ring is reduced (b,d,f,g), the ring-state is destroyed (c) or changes its shape(h). (i) shows the position of the pump laser.

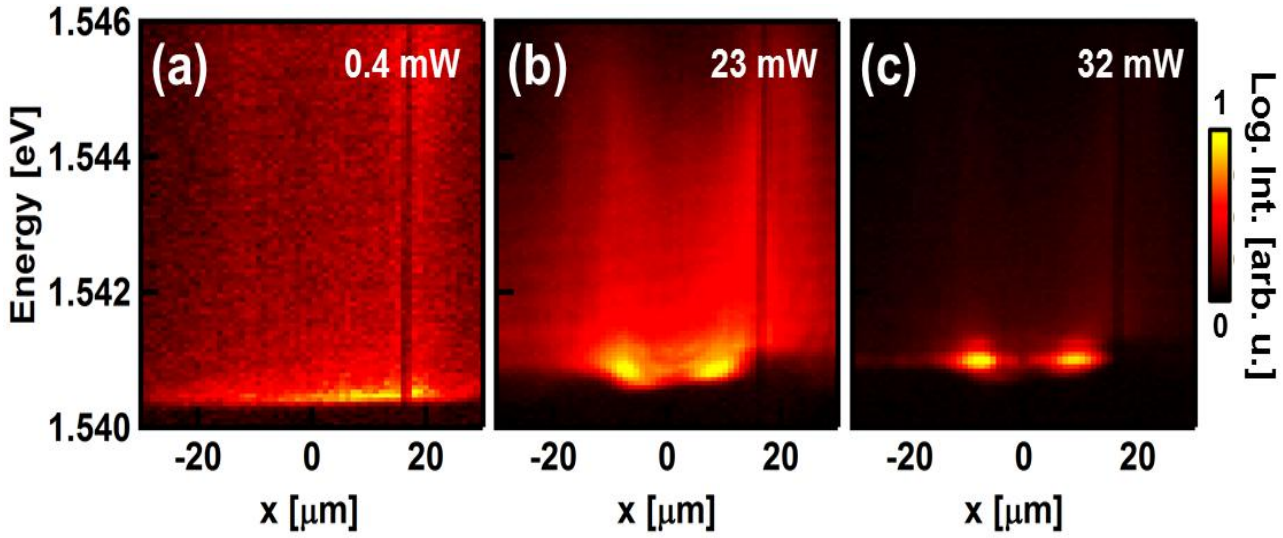

Figure 6.10: Spectra obtained along a central horizontal cut of the near-field images shown in Fig. 6.2 a-c (main text). Colour scale normalized on each.

corresponding spectrum, exhibiting a well-defined single energy. As the excitation power is increased above threshold $P = 60mW$, multiple petal-states of different energies and lobe number form in the optical potential (Fig. 6.11 (b)). This effect is accompanied by an overall increase of the polariton emission. For even higher excitation powers ($P = 70.7mW$), the ring-regime eventually collapses and superpositions of various states fill up the whole pump geometry, with a maximum polariton density at the centre of the ring (Fig. 6.11 (c)). The observed power dependence is well reproduced in simulations of the complex Ginzburg-Landau (cGL) equation for conditions similar to those of the experiment (Fig. 6.12).

6.3.6 Simulations of the complex Ginzburg-Landau equation

Fig. 6.13 (a) shows the spatial distribution of the blue-shift potential associated with the repulsive interaction between polaritons and the exciton reservoir, as used in our simulations of the cGL equation (c.f. paragraph 3 of the main text). Fig. 6.13 (b) depicts a number of randomly distributed potential spikes accounting for sample disorder. The latter are necessary to radially stabilize the simulated petal-states, i.e. prevent fluctuations of the lobe orientation which would result in a washed-out intensity distribution in a time-averaged measurement. To additionally stabilize the simulation, we introduce the energy relaxation constant η (c.f.Eq.1, main text).

Fig. 6.14 reports the simulated number of lobes n and separation between adjacent lobes Δ obtained for a stepwise increase of the radius of the pumping profile. Fitting of both datasets results in the relations $n \simeq r_C^2$ and $\Delta \simeq 1/r_c$, in agreement with the experimental data presented in Fig. 6.3 (a) (main text).

6.3.7 Analytic estimate of the relation between number of lobes and condensate radius

After having demonstrated good agreement between numerical simulations and experimental data (Fig. 6.3, main text), here we provide an analytic estimate for the relation between number of lobes and condensate radius. In the steady state, the order parameter of the condensate satisfies $\partial_t \psi(t) = -i\mu\psi$, where μ denotes the chemical potential and we set $\hbar = 1$ so that:

$$\mu_1 \psi = (1 - i\eta)\left(-\nabla^2 + a_0(r) + a_1(r)|\psi|^2\right)\psi \tag{6.3.6}$$

with $a_0(r) = 2m(g_R P(r)/\gamma_R + i\delta_c P(r)/(2\gamma_R) - i\gamma_c/2)$, $a_1 = 2m(g_c - g_R\beta P(r)/\gamma_R^2 - i\delta_c\beta P(r)/(2\gamma_R^2))$ and $\mu_1 = 2m\mu$. Including the energy relaxation constant η is essential for the numerical stability of the lobes, but can be neglected for an analytic approximation. In Ref. [253] the appearance of lobes as solutions of a linear problem at the lowest linear threshold has been demonstrated by solving the linear eigenvalue problem for asymmetric pumping profiles. Identifying the lobes in our set-up with the linear problem as well we are looking for the standing wave solutions of the form $\psi = A\exp(iS)\cos(n\theta)$. The term $Re[a_1(r)]A^2$ is small for the experimental parameters and does not affect the

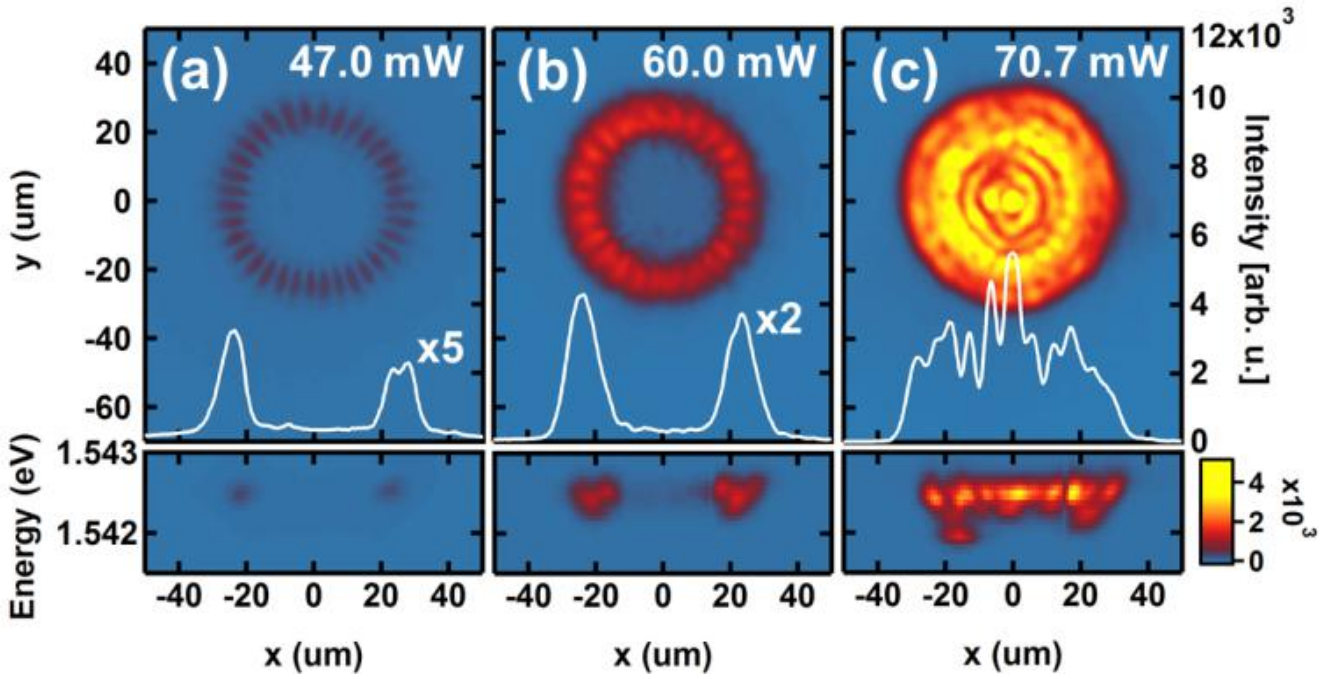

Figure 6.11: Effects of increasing the pump above condensation threshold. (a)Petal-state with $n = 34$ lobes, as observed at condensation threshold. The white line depicts the intensity distribution along a horizontal cut through the centre of the ring. The bottom panel shows the spectrum for the same cut. (b) As the power increases, multiple petal-states start to overlap, (c) until the ring-condensate eventually breaks-down and superpositions of different states fill the whole pump geometry, with the maximum intensity in the centre.

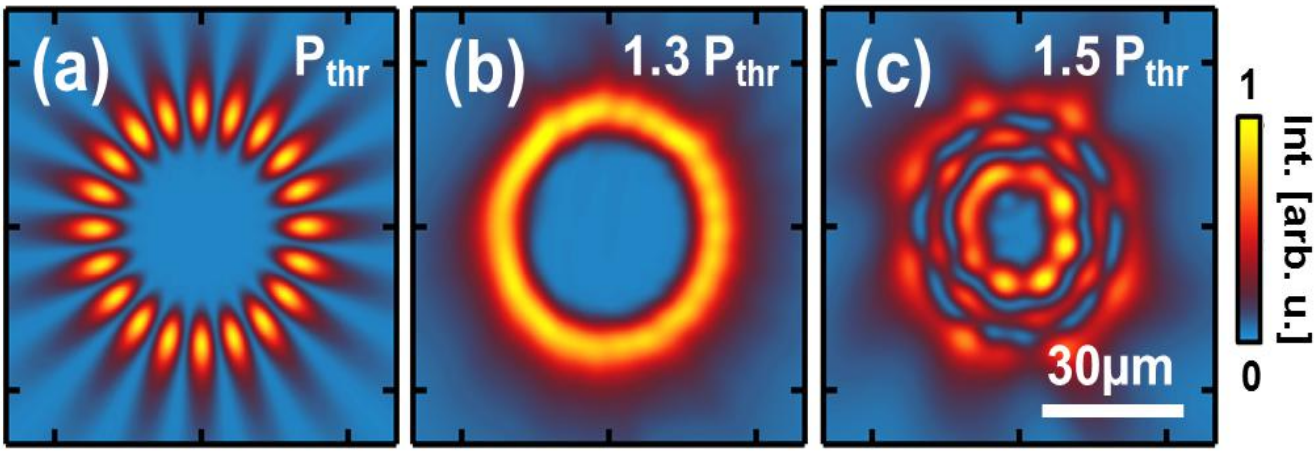

Figure 6.12: Simulated power dependence for a petal-condensate with $n = 22$ lobes. The behaviour of the system matches that shown in Fig.6.11 as the excitation power increases.

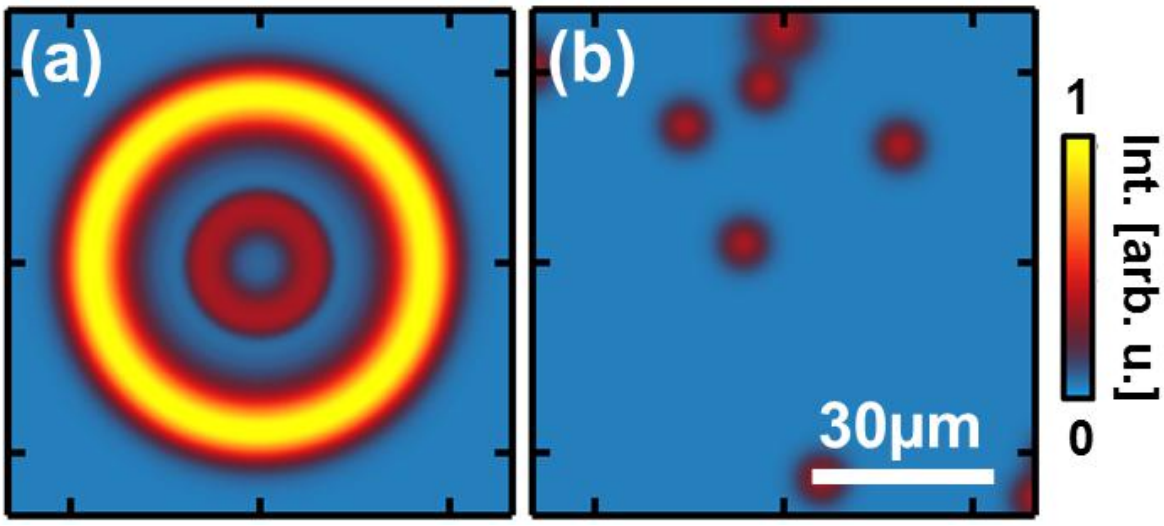

Figure 6.13: Conditions for simulations of the cGL equation. (a) Blueshift-potential corresponding to the pumping profile and (b) random disorder potential.

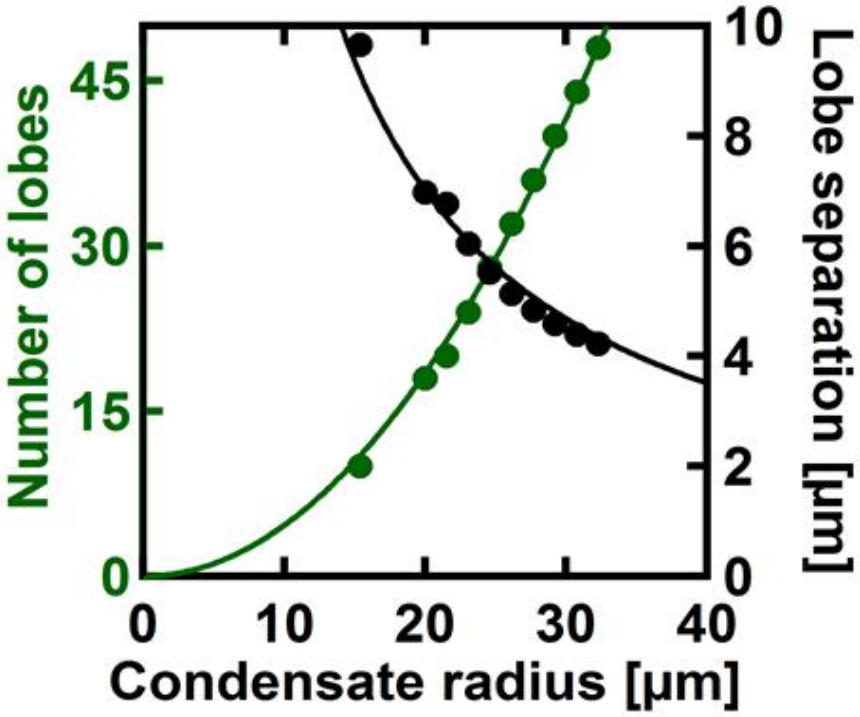

Figure 6.14: Simulation of the condensate distribution for varying pump radii. Shown are the number of lobes (green points) and separation between adjacent lobes Δ (black points) as the condensate radius increases. Solid lines are fits. The special scaling was chosen so that the simulated relation matches the experimental data, with $n = 0.046[\mu m^{-2}]r_c^2$ and $\Delta = 140.3[\mu m^2]/r_c$.

formation of the lobes, so it will be neglected in what follows. The term $Im[a_1(r)]A^2$ does not affect the formation and number of lobes as well, but leads to density saturation. The real and imaginary parts of Eq. 6.3.6 then become:

$$\mu_1 = \frac{n^2}{r^2} - \frac{A'' + A'/r}{A} + Re[a_0(r)] + S'^2 \tag{6.3.7}$$

$$0 = 2\frac{A'}{A}S' + S'' + \frac{S'}{r} - Im[a_0(r)]. \tag{6.3.8}$$

At large distances $Im[a_0(r)]$ converges to the constant value $-m\gamma_c$, while $Re[a_0(r)]$ decays exponentially, implying $S' \to const. \equiv v_{max}$. From Eqs. (6.3.7), (6.3.8) we have to the leading order $(\log A)' = -m\gamma_c/(2v_{max}) - 1/(2r)$ or $A \simeq \sqrt{r}\exp(-m\gamma_c r/(2v_{max}))$. Inserting this in Eqs. 6.3.7 gives:

$$\mu_1 = v_{max}^2 - \left(\frac{m\gamma_c}{2v_{max}}\right)^2. \tag{6.3.9}$$

Next, we take the linearized Eq.(6.3.6) and its complex conjugate, subtract and integrate within a circle of radius $r_1 \gg r_c$, where r_c is the radius of the condensate, to get:

$$A(r_1)^2 S'\Big|_{r=r_1} \simeq \int_{r\le r_1} Im(a_0)A^2 r dr = A(\overline{r})^2 \int_{r\le r_1} Im(a_0) r dr. \tag{6.3.10}$$

Here $\overline{r}$ denotes some point inside the circle $r \le r_1$. Taking a sufficiently large radius r_1 we get $v_{max} \simeq r_c$, so the velocity of the outflow is proportional to the pumping radius. (As an alternative way to arrive at this conclusion, one might also observe that due to mass continuity, the flux of the outflow at a fixed radius is proportional to the number of particles created. The number of particles is in turn proportional to the area of the condensate, i.e. the segment between the outer and the inner laser rings, which is proportional to the radius r_c). Together with Eqs. 6.3.7 and Eq. 6.3.9 this finally gives the number of lobes as $n^2 \simeq r_c^2\mu_1 \simeq r_c^4$, in agreement with the experimental and numerical findings. Eq. 6.3.10 also gives the linear dependence of the pumping power on the velocity outflow at a large radius. For a fixed pumping radius, Eq. 6.3.9 gives the criterion for the condensation: the condensate emerges when μ_1 becomes positive.

6.3.8 Polariton energies at different positions

Fig. 6.15 demonstrates that the energy of the condensed polaritons remains constant as they move across the sample. Fig. 6.15 (a),(b) show a petal-condensate with $n = 18$ lobes and the corresponding dispersion curve (spectrometer slit horizontally aligned at $y = 0$). In images Fig. 6.15 (b) - (d), an iris is employed to spatially select the polariton emission from different positions on top of and outside of the condensate pattern. Fig. 6.15 (c) corresponds approximately to the position of the pump ring where polaritons are created with $k = 0$. Fig. 6.15 (f) to (h) depict the corresponding dispersion curves, showing that the energy of the condensed polaritons (intensity maximum) remains approximately

constant at different spatial positions. This observation implies that polaritons do not relax in energy as they move from the pump ring (Fig.6.15 (c)) to the petal-condensate (Fig. 6.15 (b)). Similar results have been obtained for freely-flowing condensates in previous works [253, 254].

6.3.9 Condensate energy and condensation threshold vs radius

Fig. 6.16 (a) depicts the measured condensate blueshift energy for a number of petal-states with different radii, demonstrating that higher order states are energetically excited. The solid line is derived from the fitted relation between number of lobes and condensate radius $n = 0.046\mu m^{-2} r_c^2$, (see main text), and the measured polariton effective mass $m \simeq 4.5 \cdot 10^{-35} kg$. Due to the periodic boundary conditions of the annular states condensate radius and wavevector are related as $2\pi r_c = n\lambda_c/2 = n\pi/k_c$, where λ_c and k_c denote the condensate wavelength and wavevector, respectively. Together with the polariton dispersion $E(k_c) = E_0 + \hbar^2 k_c^2/(2m)$ (quadratic approximation), we arrive at a relation between condensate energy and radius:

$$E(r_c) = E_0 + \frac{\hbar^2 n^2}{8m r_c^2} = E_0 + \frac{\hbar^2 0.046^2 r_c^2}{8m} \tag{6.3.11}$$

6.3.10 Flexibility of excitation method and variations of the double-ring geometry

Although we focus on annular pump geometries and the resulting petal-states in this work, our experimental setup in practise allows the generation of polariton condensates with arbitrary pump distributions and corresponding blue-shift potentials, as demonstrated in Fig. 6.17.

An alternative approach to generate petal-shaped condensates is explored in Fig. 6.18. Instead of a pump distribution consisting of two concentric laser rings (with the maximum of the laser intensity at the outer ring), a single spot above condensation threshold is placed in the centre of a lower power circular pump. If only a single laser spot is present (Fig. 6.18 (a)) the local blue-shift at the pump leads to the formation of a radially expanding condensate (Fig. 6.18 (b)) [254, 255]. An additional ring of laser light around the excitation spot is employed in Fig. 6.18 (c). The ring-shaped pump is driven below condensation threshold, thus serving as a potential barrier for the polaritons expanding from the central spot. The latter are slowed down and accumulate in the doughnut-shaped region between the inner spot and the ring. However, no distinct intensity distributions like in the case of petal-type states are observed.

Finally, in Fig. 6.19 we utilize the flexibility of our excitation method to study how the shape of the annular condensates changes depending on the relative intensity of the inner and the outer pump rings. Fig. 6.19 (b) shows a petal-state with lobes with an intensity ratio between inner and outer pump of $1:8$, which is the ratio used for the examples discussed in the main text. In this configuration, the inner ring creates a weak

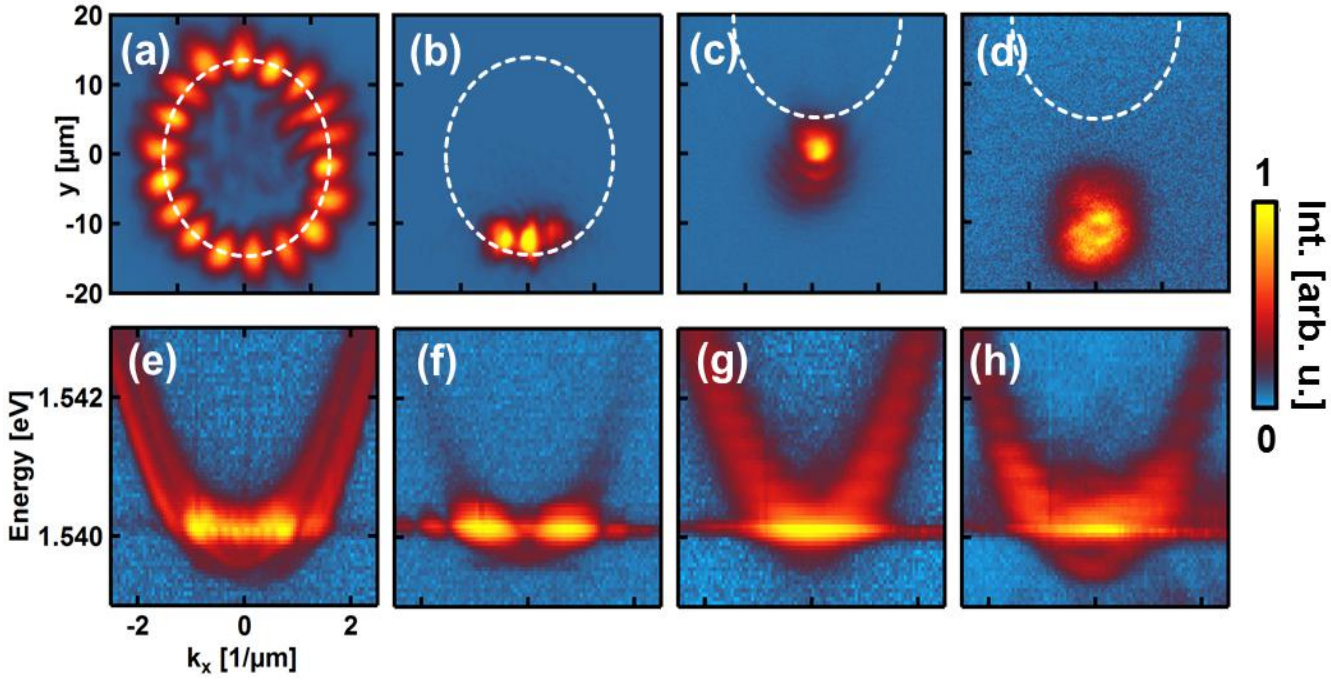

Figure 6.15: Polariton energy at varying spatial positions. Top row shows spatial images of a condensate ring with lobes. (a) Full spatial image, (b-d) polariton emission from different spatial positions as selected with an iris. Dashed white line indicates the position of the ring-state. The bottom row depicts the corresponding dispersion curves, indicating the polariton energy (logarithmic colour scale).

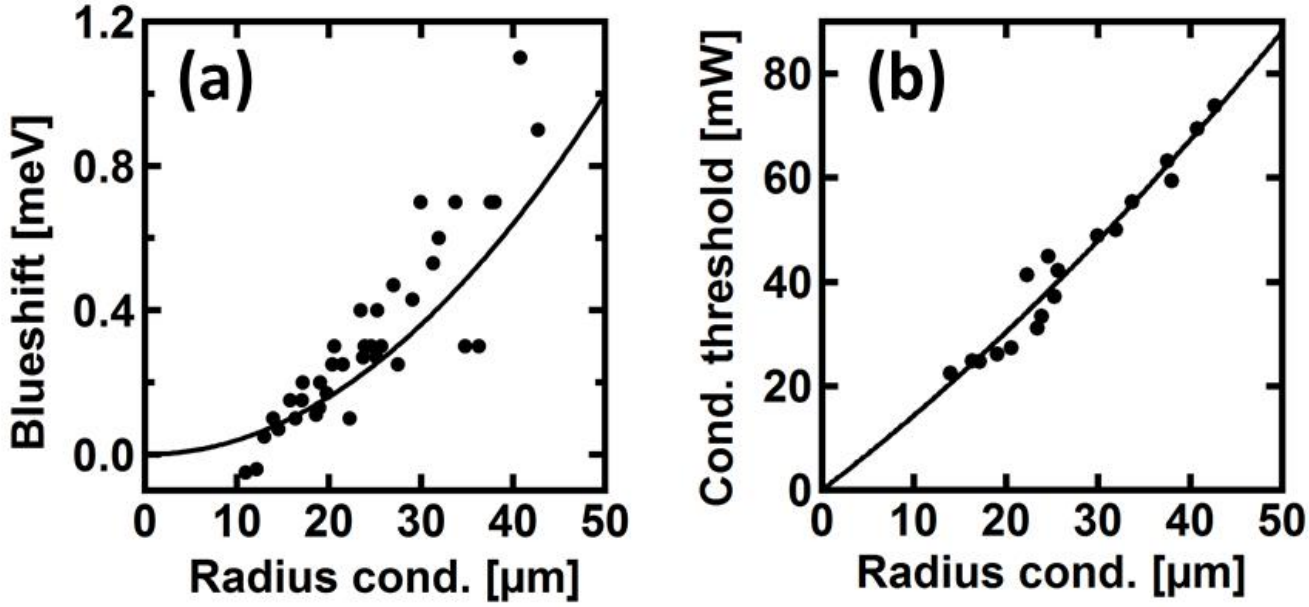

Figure 6.16: (a) Measured condensate blueshift ΔE as a function of the condensate radius. The solid line depicts their relation as expected from Eq.6.13, namely: $\Delta E(r_c) = E(r_c) - E_0 \simeq 4 \cdot 10^{-7} meV \mu m^{-2} r_c^2$. (b) Condensation threshold as a function of condensate radius. Solid line corresponds to the fit $P_{thr} \simeq 1.350 mW + 8 \cdot 10^{-3} mW \mu m^{-2} r_c^2$.

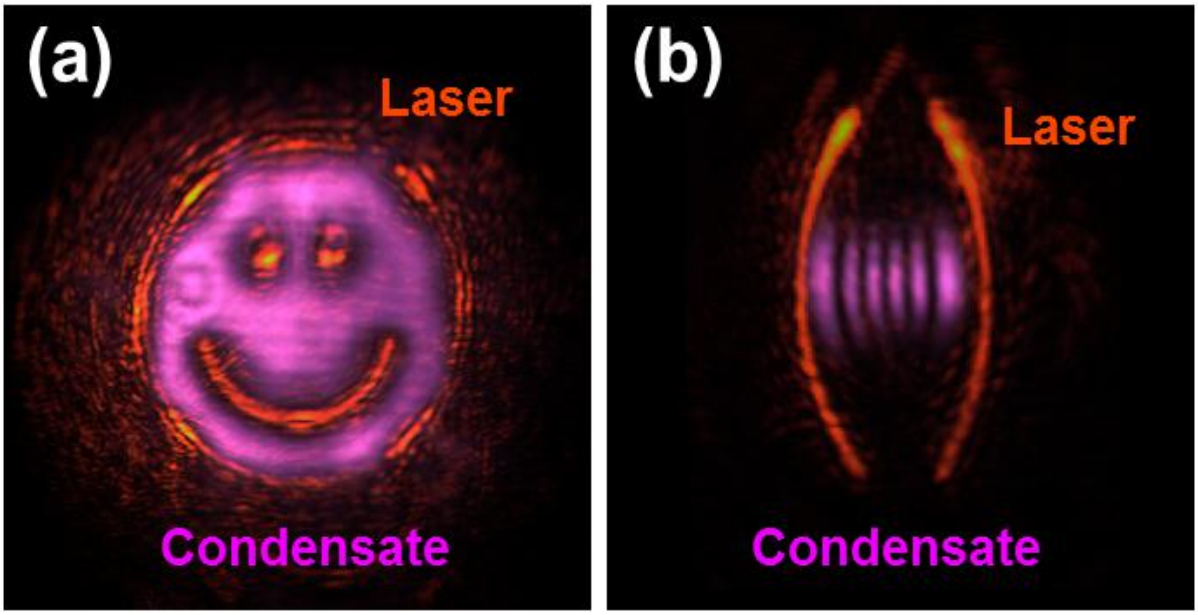

Figure 6.17: Different pump geometries and resulting polariton condensates. (a) Spatial image of a 'happy condensate', generated with a pump shaped like a smiley face. The laser luminescence appears orange, the polariton luminescence violet. (b) Resonator-style pump, resulting in a localized standing wave.

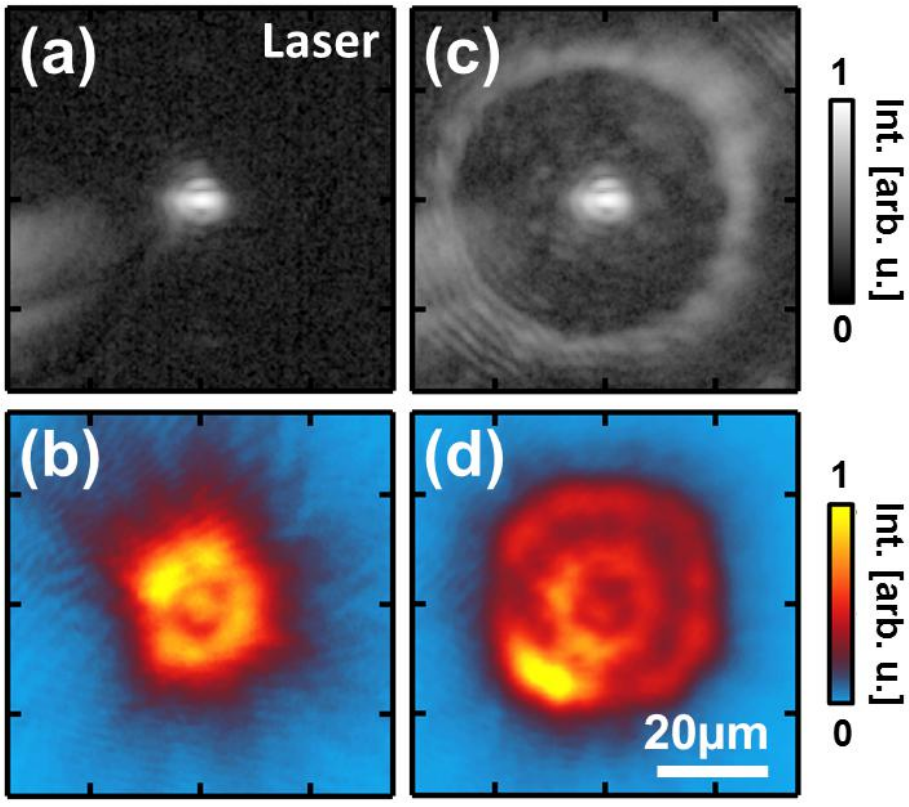

Figure 6.18: Condensate generated by a single excitation spot inside a circular optical potential. (a)Spatial image of the excitation spot and (b) resulting emission, corresponding to a radially expanding condensate. (c)Same excitation spot now surrounded by a circle of laser light below threshold. (d)The formerly free-flowing condensate created at the spot is confined by the potential and accumulates in the ring.

annular waveguide potential resulting in a clear petal state. If the inner pump ring is omitted (Fig. 6.19 (a)) polaritons created at the outer ring are no longer prevented from travelling towards the centre of the excitation-geometry, the whole ring-trap is filled with polaritons and a superposition of various states is observed. If, on the other hand, the intensity of the inner ring is increased, the additional gain and corresponding blue-shift in the central region distort the previously clear petal-state and eventually result in unwanted filling of the area inside the inner pump with condensate, thus drastically changing the mode shape (Fig. 6.19 (c)). Thus the inner pump ring blue-shift has to be high enough to confine the condensate in the multi-lobe configuration but weak enough to contribute only marginally to the overall gain of the condensate.

6.3.11 Video 1: Sample disorder and lobe orientation

We have developed simulations showing the behaviour of a petal state with $n = 8$ lobes as the pump is moved across the sample. The video is available in the published version. The movement of the pump can be tracked from the relative motion of the two point-defects at the left side of the image. The orientation of the lobe-pattern remains stable for a stationary pump (first $5s$ of the video). Moving the pump, however, triggers fluctuations of the lobe orientation, demonstrating that in the case of a uniform pump the latter is set by local variations of the potential landscape, i.e. sample disorder.

6.3.12 Video 2: Simulation of the dynamics of a locally disturbed condensate

The video shows a simulation of the time evolution of a petal-condensate with $n = 20$ lobes, as it is disturbed by an additional laser pulse on top of the ring. The parameters for the simulation are the same as the ones listed in the Materials and Methods section of the main text. The disturbing laser pulse is modeled as additional Gaussian peak in the pump distribution of the form

$$P_{pulse} = (4 \pm \tau/\tau_0) \cdot \exp\left(-0.8 \cdot (x - x_0)^2 - 0.8 \cdot (y)^2\right), \tag{6.3.12}$$

where the maximum amplitude of the disturbing pulse is 100 times that of the maximum of the annular pump. Here τ denotes the time steps of the simulation with $\tau = \{0, \ldots, 2225000\}$ and $\tau_0 = 110000$. At $\tau = \tau_0$ the sign of the second term is changed from plus to minus, simulating first growth and then decay of the disturbing pulse. The position of the pulse x_0 is at the radius of the maximum of the lobes. The simulated condensate behaviour is similar to that observed in the experiment. The initial petal-state observed at $\tau = 0$ is destroyed upon the arrival of the disturbance. The additional gain provided by the perturbing pulse creates out-of-equilibrium polariton populations on its sides, which subsequently counter-propagate along the annulus, resulting in the observed oscillatory behaviour. As the additional blueshift potential of the pulse decays, the initial petal-state recovers.

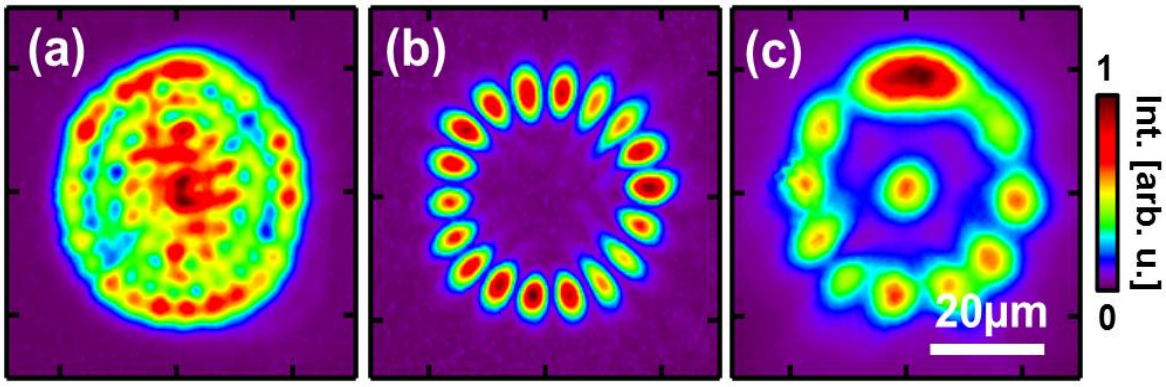

Figure 6.19: Influence of the inner pump ring. All images were observed for the same overall pumping power of , but with varying ratios between the intensities of the inner and the outer pump-rings. The ratios between the inner and the outer ring for the different measurements were (a) 0:8, (b) 1:8 and (c) 5:8.

Bibliography

[1] L. Wittgenstein, "Logisch-philosophische Abhandlung - Tractatus logico-philosophicus", Suhrkamp, Frankfurt am Main, Germany (1998).

[2] J. A. Evans, "Future Science", Science **342**, 44 (2013); DOI: 10.1126/science.1245218

[3] T. Tao, "Universelle Gesetze", Spekt. d. Wiss., 60 (2014).

[4] M. H. Anderson, J. R. Ensher, M. R. Matthews, C. E. Wieman and E. A. Cornell, "Observation of Bose-Einstein Condensation in a Dilute Atomic Vapor", Science **269**, 198 (1995).

[5] K. B. Davis, M. O. Mewes, M. R. Andrews, N. J. van Druten, D. S. Durfee, D. M. Kurn, and W. Ketterle, "Bose-Einstein Condensation in a Gas of Sodium Atoms", Phys. Rev. Lett. **75**, 3969 (1995).

[6] C. C. Bradley, C. A. Sackett, J. J. Tollett, and R. G. Hulet, "Evidence of Bose-Einstein Condensation in an Atomic Gas with Attractive Interactions", Phys. Rev. Lett. **75**, 1687 (1995).

[7] L. P. Pitaevskii, "Vortex Lines in an Imperfect Bose Gas", Zh. Eksp. Teor. Fiz. **40**, 646 (1961); Sov. Phys. JETP **13**, 451 (1961).

[8] E. P. Gross, "Structure of a quantized vortex in boson systems", Nuovo Cimento **20** 451 (1961); J. Math. Phys. **4** 195 (1963).

[9] N. N. Greenwood and A. Earnshaw, "Chemie der Elemente", Wiley-VCH, ISBN 3-527-26169-9, Weinheim, Germany (1988).

[10] A. J. Leggett, "Bose-Einstein condensation in the alkali gases: Some fundamental concepts", Rev. Mod. Phys. **73**, 307 (2001).

[11] L.P. Pitaevskii and S. Stringari, "Bose-Einstein Condensation", Clarendon, Oxford, United Kingdom (2003).

[12] A. Einstein, "Quantentheorie des einatomigen idealen Gases II", Sitzungsber. Preuss. Akad. Wiss., 3 (1925).

[13] L. Onsager and O. Penrose, "Bose-Einstein condensation and liquid helium", Phys. Rev. **104**, 576 (1956).

[14] J. Klaers, J. Schmitt, F. Vewinger and M. Weitz, "BoseEinstein condensation of photons in an optical microcavity", Nature **468**, 545 (2010).

[15] I. Carusotto and C. Ciuti, "Quantum fluids of light", Rev. Mod. Phys. **85**, 299 (2013).

[16] J. Kasprzak, M. Richard, S. Kundermann, A. Baas, P. Jeambrun, J. M. J. Keeling, F. M. Marchetti, M. H. Szymanska, R. Andé, J. L. Staehli, V. Savona, P. B. Littlewood, B. Deveaud and Le Si Dang, "Bose-Einstein condensation of exciton polaritons", Nature **443**, 409 (2006).

[17] C. Sun, S. Jia, C. Barsi, S. Rica, A. Picozzi and J. W. Fleischer, "Observation of the kinetic condensation of classical waves", Nature Physics **8**, 437 (2012).

[18] F. London, "The λ-Phenomenon of Liquid Helium and the Bose-Einstein Degeneracy", Nature **141**, 643 (1938).

[19] C. Raman, R. Onofrio, J. M. Vogels, J. R. Abo-Shaeer and W. Ketterle,"Dissipationless Flow and Superfluidity in Gaseous Bose-Einstein Condensates", Journal of Low Temperature Physics, **122**, 99-116 (2001).

[20] K. G. Lagoudakis, M. Wouters, M. Richard, A. Baas, I. Carusotto, R. André, Le Si Dang and B. Deveaud-Plédran, "Quantized vortices in an exciton-polariton condensate", Nature Physics **4**, 706-710 (2008).

[21] M. Correggi, F. Pinsker, N. Rougerie and J. Yngvason, "Rotating superfluids in anharmonic traps: From vortex lattices to giant vortices", Phys. Rev. A **84**, 053614 (2011).

[22] M. Correggi, F. Pinsker, N. Rougerie and J. Yngvason, "Critical rotational speeds in the Gross-Pitaevskii theory on a disc with Dirichlet boundary conditions", J. Stat. Phys. **143**, 261- 305 (2011).

[23] M. Correggi, F. Pinsker, N. Rougerie and J. Yngvason, "Critical rotational speeds for superfluids in homogeneous traps", J. Math. Phys. **53**, 095203 (2012).

[24] F. Pinsker, N. G. Berloff and V. M. Pérez-García,"Nonlinear quantum piston for the controlled generation of vortex rings and soliton trains", Phys. Rev. A **87**, 053624 (2013).

[25] F. Pinsker, "Computing with soliton trains in Bose-Einstein condensates", arXiv:1305.4088 (2013).

[26] F. Pinsker and H. Flayac, "On-Demand Dark Soliton Train Manipulation in a Spinor Polariton Condensate", Phys. Rev. Lett. **112**, 140405 (2014).

[27] S. Inouye, M. R. Andrews, J. Stenger, H.-J. Miesner, D. M. Stamper-Kurn and W. Ketterle, "Observation of Feshbach resonances in a BoseEinstein condensate", Nature **392**, 151-154 (1998).

[28] H. Deng, H. Haug and Y. Yamamoto, "Exciton-polariton Bose-Einstein condensation", Rev. Mod. Phys. **82**, 1489 (2010).

[29] J. J. Hopfield, "Theory of the Contribution of Excitons to the Complex Dielectric Constant of Crystals", Phys. Rev., **112**, 15551567 (1958).

[30] C. Weisbuch, M. Nishioka, A. Ishikawa and Y. Arakawa, "Observation of the coupled exciton-photon mode splitting in a semiconductor quantum microcavity", Phys. Rev. Lett. **69**, 33143317 (1992).

[31] J. D. Plumhof, T. Stöferle, L. Mai, U. Scherf and R. F. Mahrt, "Room-temperature BoseEinstein condensation of cavity exciton-polaritons in a polymer", Nature Materials **13**, 247-252 (2014).

[32] A. Dreismann, P. Cristofolini, R. Balili, G. Christmann, F. Pinsker, N. G. Berloff, Z. Hatzopoulosd, P. G. Savvidis and J. J. Baumberg,"Coupled counterrotating polariton condensates in optically defined annular potentials", Proceedings of the National Academy of Sciences, 201401988; doi: 10.1073/pnas.1401988111 (2014).

[33] B. Nelsen, G. Liu, M. Steger, D. W. Snoke, R. Balili, K. West, L. Pfeiffer, "Coherent Flow and Trapping of Polariton Condensates with Long Lifetime", arXiv:1209.4573

[34] T. Gao, P. S. Eldridge, T. C. H. Liew, S. I. Tsintzos, G. Stavrinidis, G. Deligeorgis, Z. Hatzopoulos, and P. G. Savvidis, "Polariton condensate transistor switch", Phys. Rev. B **85**, 235102 (2012).

[35] T. C. H. Liew, M. M. Glazov, K. V. Kavokin, I. A. Shelykh, M. A. Kaliteevski, and A. V. Kavokin,"Proposal for a Bosonic Cascade Laser", Phys. Rev. Lett. **110**, 047402 (2011).

[36] T. C. H. Liew, A.V. Kavokin, T. Ostatnicky, M. Kaliteevski, I.A. Shelykh and R.A. Abram,"Optical Circuits Based on Polariton Neurons in Semiconductor Microcavities", Phys. Rev. Lett. **101**, 016402 (2008).

[37] I. A. Shelykh, G. Pavlovic, D. D. Solnyshkov, and G. Malpuech, "Proposal for a Mesoscopic Optical Berry-Phase Interferometer", Phys. Rev. Lett. **102**, 046407 (2009).

[38] I. A. Shelykh, R. Johne, D. D. Solnyshkov, and G. Malpuech, "Optically and electrically controlled polariton spin transistor", Phys. Rev. B **82**, 153303 (2010).

[39] T. Espinosa-Ortega and T. C. H. Liew,"Complete architecture of integrated photonic circuits based on and and not logic gates of exciton polaritons in semiconductor microcavities", Phys. Rev. B **87**, 195305 (2013).

[40] H. Flayac, and I. G. Savenko, "An exciton-polariton mediated all-optical router", Appl. Phys. Lett. **103**, 201105 (2013).

[41] T. C. H. Liew, I.A. Shelykh and G. Malpuech, "Polaritonic devices", Physica E **43** (9), 1543-1568 (2011).

[42] D. Ballarini, M. De Giorgi, E. Cancellieri, R. Houdré, E. Giacobino, R. Cingolani, A. Bramati, G. Gigli and D. Sanvitto, "All-optical polariton transistor", Nature Communications **4** 1778 (2013).

[43] C. Antón, T.C.H. Liew, J. Cuadra, M.D. Martín, P.S. Eldridge, Z. Hatzopoulos, G. Stavrinidis, P.G. Savvidis, L. Vina, "Quantum reflections and the shunting of polariton condensate wave trains: implementation of a logic AND gate", arXiv:1305.5678 (2013).

[44] C. Sturm, D. Tanese, H.S. Nguyen, H. Flayac, E. Gallopin, A. Lemaitre, I. Sagnes, D. Solnyshkov, A. Amo, G. Malpuech, J. Bloch, "Giant phase modulation in a Mach-Zehnder exciton-polariton interferometer", arXiv:1303.1649 (2013), to appear in Nature Communications.

[45] G. Malpuech, A. Di Carlo, A. Kavokin, J. J. Baumberg, M. Zamfirescu and P. Lugli, "Room-temperature polariton lasers based on GaN microcavities", Appl. Phys. Lett. **81**, 412 (2002).

[46] A. Kavokin,"Exciton-polaritons in microcavities: Recent discoveries and perspectives", physica status solidi **247**, 1898-1906, (2010).

[47] N.G. Berloff and J. Keeling, Chapter to appear in Springer and Verlag book on "Quantum Fluids: hot-topics and new trends" eds. A. Bramati and M. Modugno

[48] J. Keeling and N. G. Berloff, "Spontaneous rotating vortex lattices in a pumped decaying condensate", Phys. Rev. Lett. **100**, 250401 (2008).

[49] F. Manni, K. G. Lagoudakis, T. C. H. Liew, R. André, and B. Deveaud-Plédran, "Spontaneous pattern formation in a polariton condensate", Phys. Rev. Lett. **107**, 106401 (2011).

[50] M.O. Borgh, G. Franchetti, J. Keeling and N. G. Berloff "Robustness and observability of rotating vortex lattices in an exciton-polariton condensate", Phys. Rev. B **86**, 035307 (2012).

[51] S. Bose, "Plancks Gesetz und Lichtquantenhypothese", Zeitschrift fr Physik **26**, 178 (1924).

[52] F. Pinsker, "A Fast Rotating Bose-Einstein Condensate on a Disc", Diploma thesis, University of Vienna (2010).

[53] C.J. Pethick, H. Smith, "Bose-Einstein Condensation in Dilute Gases", Cambridge University Press, Cambridge, UK (2002).

[54] W. Ketterle, "Nobel lecture: When atoms behave as waves: Bose-Einstein condensation and the atom laser", Rev. Mod. Phys., **74**, (2002).

[55] B. Schlein, "Contribution to the Proceedings of the Conference 'Days on PDEs'", Biarritz (2011).

[56] S. Jochim, M. Bartenstein, A. Altmeyer, G. Hendl, S. Riedl, C. Chin, J. Hecker Denschlag and R. Grimm, "Bose-Einstein condensation of molecules", Science **302**, 2101 (2003); DOI: 10.1126/science.1093280

[57] F. Dalfovo, S. Giorgini, L. P. Pitaevskii and S. Stringari, "Theory of Bose-Einstein condensation in trapped gases", Rev. Mod. Phys. **71**, 463, (1999).

[58] E.H. Lieb and R. Seiringer, "Proof of Bose-Einstein condensation for dilute trapped gases", Phys. Rev. Lett. **88**, 170409 (2002).

[59] C.N. Yang, "Concept of Off-Diagonal Long-Range Order and the Quantum Phases of Liquid He and of Superconductors ", Rev. Mod. Phys. **34**, 694 (1962).

[60] V. I. Yukalov, "Basics of Bose-Einstein condensation", Physics of Particles and Nuclei **42**, 460-513 (2011).

[61] L.D. Landau and E.M. Lifshitz, "Quantum mechanics, Non-relativistic Theory", Pergamon Press (1965).

[62] E.H. Lieb, J. P. Solovej, R. Seiringer, J. Yngvason, "The Mathematics of the Bose Gas and its Condensation." Oberwolfach Seminars, **34**, Birkhäuser, Basel, 184pp. (2001).

[63] J. Dalibard, "Bose - Einstein condensation in gases", Proceedings of the International School of Physics Enrico Fermi, Course CXL, Varenna (1998).

[64] M.L. Harris, "Realisation of a Cold Mixture of Rubidium and Caesium", PhD thesis, Durham University (2008).

[65] M. Theis, "Optical Feshbach Resonances in a Bose-Einstein Condensate", PhD thesis, Innsbruck University (2005).

[66] W. Bao, "Numerical methods for the nonlinear Schrödinger equation with nonzero far-field conditions" International Press **11**, (3), 001022, (2004).

[67] B. Svistunov, E. Babaev, and N. Prokofev, "Superfluid States of Matter", Taylor & Francis, (2014).

[68] J. Bladel, "On Helmholtz's Theorem in Finite Regions", Midwestern Universities Research Association, (1958).

[69] A. L. Fetter, "Rotating trapped Bose-Einstein condensates", Rev. Mod. Phy., **81**, 1-45 (2009).

[70] E. Madelung, "Eine anschauliche Deutung der Gleichung von Schrödinger", Die Naturwissenschaften, **13** (45) 1004 (1926).

[71] E. Madelung, "Quantentheorie in hydrodynamischer Form", Zeitschrift für Physik, **40**, Issue 3-4, pp 322-326 (1927).

[72] L. Ambrosio, G. Crippa, A. Figalli and L. V. Spinolo, "Existence and Uniqueness Results for the Continuity Equation and Applications to the Chromatography System", IMA Vol. Math. Appl. **153** (2010).

[73] N.G. Berloff, "Padé approximations of solitary wave solutions of the Gross-Pitaevskii equation", Journal of Physics A: Mathematical and General, **37**, 1617 (2004).

[74] I. Gasser and P. A. Markowich, "Quantum Hydrodynamics, Wigner Transforms and the Classical Limit", Asymptotic Analysis, **14** pp. 97-116 (1997).

[75] T. C. Wallstrom, "Inequivalence between the Schrdinger equation and the Madelung hydrodynamic equations", Phys. Rev. A **49** Number 3, 1613 (1993).

[76] E. Schrödinger, "Die Mehrdeutigkeit der Wellenfunktion", Ann. Physik **32**, 49 (1938).

[77] D.S. Petrov, D.M. Gangardt and G.V. Shlyapnikov, "Low-dimensional trapped gases", J. Phys. IV France, **1**, (2008).

[78] N. Parker, "Numerical Studies of Vortices and Dark Solitons in Atomic Bose-Einstein Condensates", PhD thesis, Durham University (2004).

[79] A. Görlitz, J. M. Vogels, A. E. Leanhardt, C. Raman, T. L. Gustavson, J. R. Abo-Shaeer, A. P. Chikkatur, S. Gupta, S. Inouye, T. Rosenband, and W. Ketterle, "Realization of Bose-Einstein Condensates in Lower Dimensions", Phys. Rev. Lett. **87**, 130402 (2001).

[80] R. Kollar, "Existence and Stability of Vortex Solutions of Certain Nonlinear Schrödinger Equations", PhD thesis, University of Maryland (2004).

[81] F. Kh. Abdullaev and J. Garnier, "Emergent nonlinear Phenomena in Bose-Einstein condensates: Theory end experiment", Springer series on atomic, optical and plasma physics (2008).

[82] J.S. Russell, "Report on waves". Fourteenth meeting of the British Association for the Advancement of Science (1844).

[83] Y.S. Kivshar and G.P. Agrawal, "Optical Solitons", Elsevier Science, USA (2003).

[84] N. Parker, "Numerical Studies of Vortices and Dark Solitons in Atomic Bose-Einstein Condensates", Thesis, University of Durham (2004).

[85] R. Balakrishnan and I. I. Satija, Pramana, "Solitons in BoseEinstein condensates", J. Phys., **77**, pp. 929-947, (2011).

[86] A.A. Abrikosov, "On the magnetic properties of superconductors of the second group", Zh. Exp. Teor. Phz. **32**, 1442 (1957).

[87] H. Flayac, "New Trends in the Physics of spinor exciton-polariton condensates", PhD thesis, Universite Blaise Pascal (2013).

[88] F. Pinsker and N. G. Berloff, Phys. Rev. A **89** (5), 11 (2014).

[89] S. Pau, J. Jacobson, and Y. Yamamoto, "Microcavity exciton-polariton splitting in the linear regime", Phys. Rev. B, **51**, no. 20, pp. 14 43714 447, (1995).

[90] A. Dreismann, first year report, Cambridge University (2012).

[91] M. Wouters and I. Carusotto, "Excitations in a nonequilibrium Bose-Einstein condensate of exciton polaritons", Phys. Rev. Lett. **99**, 140402 (2007).

[92] Y. Xue, M. Matuszewski, "Creation and abrupt decay of a quasi-stationary dark soliton in a polariton condensate", arXiv:1401.2412 (2014).

[93] S. B. Papp, J. M. Pino and C. E. Wieman, "Tunable Miscibility in a Dual-Species Bose-Einstein Condensate", Phys. Rev. Lett. **101**, 040402 (2008).

[94] H. Flayac, I. A. Shelykh, D. D. Solnyshkov, and G. Malpuech, "Topological stability of the half-vortices in spinor exciton-polariton condensates", Phys. Rev. B **81**, 045318 (2008).

[95] A. Aftalion, "Vortices in Bose-Einstein Condensates", Progress in Nonlinear Differential Equations and their Applications **67**, Birkhäuser, Basel, 2006.

[96] A.L. Fetter, "Rotating Trapped Bose-Einstein Condensates", Rev. Mod. Phys. **81**, 647-691, (2009).

[97] E.H. Lieb, R. Seiringer, J.P. Solovej, J. Yngvason, "The Mathematics of the Bose Gas and its Condensation", Oberwolfach Seminar Series **34**, Birkhäuser, Basel (2005).

[98] E.H. Lieb, R. Seiringer, J. Yngvason, "Bosons in a Trap: A Rigorous Derivation of the Gross-Pitaevskii Energy Functional", Phys. Rev. A. **61**, 043602, (2000).

[99] E.H. Lieb and R. Seiringer, "Derivation of the Gross-Pitaevskii Equation for Rotating Bose Gases", Comm. Math. Phys. **264**, 505-537 (2006).

[100] J.-B. Bru, M. Correggi, P. Pickl and J. Yngvason, "The TF Limit for Rapidly Rotating Bose Gases in Anharmonic Traps", Comm. Math. Phys. **280**, 517-544 (2008).

[101] L. Erdős, B. Schlein, H.T. Yau, "Rigorous Derivation of the Gross-Pitaevskii Equation", Phys. Rev. Lett. **98**, 040404 (2007).

[102] L. Erdős, B. Schlein, H.T. Yau, "Derivation of the Gross-Pitaevskii Equation for the Dynamics of Bose-Einstein Condensate", Ann. Math. **172**, 291-370 (2010).

[103] P. Pickl, "Derivation of the Time Dependent Gross Pitaevskii Equation with External Fields", preprint arXiv:1001.4894v2 [math-ph] (2010).

[104] E.H. Lieb, R. Seiringer and J. Yngvason, "The Yrast Line of a Rapidly Rotating Bose Gas: The Gross-Pitaevskii Regime", Phys. Rev. A **79**, 063626 (2009).

[105] M. Lewin, R. Seiringer, "Strongly Correlated Phases in Rapidly Rotating Bose Gases", J. Stat. Phys. **137**, 1040-1062 (2009).

[106] M. Correggi, T. Rindler-Daller and J. Yngvason, "Rapidly Rotating Bose-Einstein condensates in Homogeneous Traps", J. Math. Phys. **48**, 102103 (2007).

[107] L. C. Evans, "Partial Differential Equations", reprinted edition, Amer. Math. Soc., RI. (2008).

[108] A. N. and I. Shafrir, "Minimization of a Ginzburg-Landau Type Functional with Nonvanishing Dirichlet Boundary Condition" Calc. Var. Partial Differential Equations **7**, 191-217. (1998).

[109] H. Brezis, L. Oswald, "Remarks on Sublinear Elliptic Equations", Nonlinear Analysis, **10**, 55-64 (1986).

[110] S. Serfaty, "On a Model of Rotating Superfluids", ESAIM: Control Optim. Calc. Var. **6**, 201-238 (2001).

[111] M. Correggi and J. Yngvason, "Energy and Vorticity in fast Rotating Bose-Einstein Condensates" J. Phys. A.: Theor. **41**, 445002, 19pp. (2008).

[112] E. Sandier, S. Serfaty, "On the Energy of Type-II Superconductors in the Mixed Phase", Rev. Math. Phys. **12**, 1219-1257 (2000).

[113] S. Burger, K. Bongs, S. Dettmer, W. Ertmer, K. Sengstock, A. Sanpera, G. V. Shlyapnikov, and M. Lewenstein, "Dark solitons in Bose-Einstein condensates", Phys. Rev. Lett. **83**, 5198 (1999); S. Stellmer, C. Becker, P. Soltan-Panahi, E.-M. Richter, S. Dörscher, M. Baumert, J. Kronjäger, K. Bongs, and K. Sengstock, "Collisions of dark solitons in elongated Bose-Einstein condensates", Phys. Rev. Lett. **101**, 120406 (2008); A. Weller, J. P. Ronzheimer, C. Gross, J. Esteve, M. K. Oberthaler, D. J. Frantzeskakis, G. Theocharis and P. G. Kevrekidis, "Experimental observation of oscillating and interacting matter wave dark solitons", Phys. Rev. Lett., **101**, 130401 (2008).

[114] K.E. Strecker, G.B. Partridge, A.G. Truscott, G.B. Hulet, "Formation and propagation of matter-wave soliton trains", Nature **417**, 150 (2002); L. Khaykovich, F. Schreck, G. Ferrari, T. Bourdel, J. Cubizoller, L.D. Carr, Y. Castin, C. Salomon, "Formation of a matter-wave bright soliton", Science **296**, 1290 (2002); S. L. Cornish, S. T. Thompson, and C. E. Wieman, "Formation of bright matter-wave solitons during the collapse of attractive Bose-Einstein condensates", Phys. Rev. Lett. **96**, 170401 (2006).

[115] B. Eiermann, Th. Anker, M. Albiez M. Taglieber, P. Treutlein, K.-P. Marzlin, and M. K. Oberthaler, "Bright Bose-Einstein gap solitons of atoms with repulsive interaction", Phys. Rev. Lett. **92**, 230401(2004).

[116] C. Becker, S. Stellmer, P. Soltan-Panahi, S. Dörscher, M. Baumert, E.-M. Richter, J. Kronjäger, K. Bongs, and K. Sengstock, "Oscillations and interactions of dark and darkbright solitons in BoseEinstein condensates", Nature Phys. **4**, 496 (2008).

[117] M. R. Matthews, B. P. Anderson, P. C. Haljan, D. S. Hall, C. E. Wieman, and E. A. Cornell, "Vortex formation in a stirred Bose-Einstein condensate", Phys. Rev. Lett. **83**, 2498 (1999).

[118] K. W. Madison, F. Chevy, W. Wohlleben and J. Dalibard, "Vortex formation in a stirred Bose-Einstein condensate", Phys. Rev. Lett., **84**, 806 (1999).

[119] S. Inouye, S. Gupta, T. Rosenband, A. P. Chikkatur, A. Görlitz, T. L. Gustavson, A. E. Leanhardt, D. E. Pritchard, and W. Ketterle, "Observation of Vortex Phase Singularities in Bose-Einstein Condensates ", Phys. Rev. Lett. **87**, 080402 (2001).

[120] B. P. Anderson, P. C. Haljan, C. A. Regal, D. L. Feder, L. A. Collins, C. W. Clark, and E. A. Cornell, "Watching dark solitons decay into vortex rings in a Bose-Einstein condensate", Phys. Rev. Lett. **86**, 2926 (2001).

[121] Z. Dutton, M. Budde, C. Slowe and L. V. Hau, "Observation of quantum shock waves created with ultra-compressed slow light pulses in a Bose-Einstein condensate", Science **293**, 663 (2001).

[122] N. S. Ginsberg, J. Brand and L. V. Hau, "Observation of Hybrid Soliton Vortex-Ring Structures in Bose-Einstein Condensates", Phys. Rev. Lett. **94**, 040403 (2005); I. Shomroni, I. Shomroni, E. Lahoud, S. Levy and J. Steinhauer, "Evidence for an oscillating soliton/vortex ring by density engineering of a BoseEinstein condensate", Nature Phys. **5**, 193 (2009).

[123] K. M. Mertes, J. W. Merrill, R. Carretero-González, D. J. Frantzeskakis, P. G. Kevrekidis, and D. S. Hall, "Nonequilibrium dynamics and superfluid ring excitations in binary Bose-Einstein condensates", Phys. Rev. Lett. **99**, 190402 (2007).

[124] P. Engels, C. Atherton, and M. A. Hoefer "Observation of Faraday waves in a Bose-Einstein condensate", Phys. Rev. Lett. **98**, 095301 (2007); J. J. Chang, P.

Engels, and M. A. Hoefer,"Formation of dispersive shock waves by merging and splitting Bose-Einstein condensates", *ibid.* **101**, 170404 (2008).

[125] C. C. Bradley, C. A. Sackett, and R. G. Hulet, "Bose-Einstein condensation of lithium: Observation of limited condensate number", Phys. Rev. Lett. **78**, 985 (1997); J. L. Roberts, N. R. Claussen, S. L. Cornish, E. A. Donley, E. A. Cornell, and C. E. Wieman, "Controlled collapse of a Bose-Einstein condensate", Phys. Rev. Lett. **86**, 4211 (2001).

[126] R. Carretero-González, D. J. Frantzeskakis and P. G. Kevrekidis, "Nonlinear waves in BoseEinstein condensates: physical relevance and mathematical techniques", Nonlinearity **21**, R139 (2008).

[127] V. M. Pérez-García, N. G. Berloff, P. G. Kevrekidis, V.V. Konotop, and B. A. Malomed, "Nonlinear phenomena in degenerate quantum gases", Physica D **238**, 1289 (2009).

[128] C. Yin, N. G. Berloff, V. M. Pérez-García, D. Novoa, A. V. Carpentier, and H. Michinel, "Coherent atomic soliton molecules for matter-wave switching", Phys. Rev. A **83**, 051605(R) (2011).

[129] G. K. Batchelor, "An Introduction to Fluid Dynamics", Cambridge University Press, Cambridge, England (1967).

[130] R. J. Donnelly, "Quantized Vortices in Helium II", Cambridge University Press, Cambridge, England (1991).

[131] S. Komineas and N. Papanicolaou, "Nonlinear waves in a cylindrical Bose-Einstein condensate", Phys. Rev. A **67**, 023615 (2003); *ibid.* **68** 043617 (2003).

[132] C. A. Jones and P. H. Roberts, "Motions in a Bose condensate. IV. Axisymmetric solitary waves", J. Phys. A: Math. Gen. **15** 599 (1982); C. A. Jones, S. J. Putterman and P. H. Roberts, "Motions in a Bose condensate. V. Stability of solitary wave solutions of non-linear Schrödinger equations in two and three dimensions", J. Phys. A, Math. Gen. **19** 2991 (1986).

[133] N. G. Berloff and C. F. Barenghi, "Vortex nucleation by collapsing bubbles in Bose-Einstein condensates", Phys. Rev. Lett., **93** , 090401, (2004).

[134] E. A. Kuznetsov and J. J. Rasmussen, "Instability of two-dimensional solitons and vortices in defocusing media", Phys. Rev. E **51** (5), 4479-4484 (1995).

[135] D. R. Scherer, C. N. Weiler, T. W. Neely, and B. P. Anderson, "Vortex formation by merging of multiple trapped Bose-Einstein condensates", Phys. Rev. Lett. **98**, 110402 (2007); R. Carretero-González, B. P. Anderson, P. G. Kevrekidis, D. J. Frantzeskakis and C. N. Weiler, "Dynamics of vortex formation in merging Bose-Einstein condensate fragments", Phys. Rev. A **77**, 033625 (2008).

[136] A. Glezer, "The formation of vortex rings", Phys. Fluids **31** 3532 (1988).

[137] S. E. Pollack, D. Dries, M. Junker, Y. P. Chen, T. A. Corcovilos, and R. G. Hulet, "Extreme Tunability of Interactions in a ^{7}Li Bose-Einstein Condensate", Phys. Rev. Lett. **102**, 090402 (2009).

[138] F. K. Abdullaev, J. G. Caputo, R. A. Kraenkel, B. A. Malomed, "Controlling collapse in Bose-Einstein condensates by temporal modulation of the scattering length", Physical Review A **67**, 013605 (2003); H. Saito, and M. Ueda, "Dynamically stabilized bright solitons in a two-dimensional Bose-Einstein condensate", Phys. Rev. Lett. **90**, 040403 (2003).

[139] V. M. Pérez-García, V. V. Konotop and V. A. Brazhnyi, "Feshbach resonance induced shock waves in Bose-Einstein condensates", Phys. Rev. Lett. **92**, 220403 (2004).

[140] J. Belmonte-Beitia, V. M. Pérez-García, V. Vekslerchik, V. V. Konotop, "Localized nonlinear waves in systems with time-and space-modulated nonlinearities" Phys. Rev. Lett. **100**, 164102 (2008); V. V. Konotop and P. Pacciani, "Collapse of solutions of the nonlinear Schrdinger equation with a time-dependent nonlinearity: Application to Bose-Einstein condensates", *ibid.*, **94**, 240405 (2005); Y. Sivan, G. Fibich, and M. I. Weinstein, "Waves in nonlinear lattices: ultrashort optical pulses and Bose-Einstein condensates", *ibid.* **97**, 193902 (2006); G. Theocharis, P. Schmelcher, P. G. Kevrekidis, and D. J. Frantzeskakis, "Matter-wave solitons of collisionally inhomogeneous condensates", Phys. Rev. A **72**, 033614 (2005).

[141] A. M. Kamchatnov, A. Gammal and R. A. Kraenkel, "Dissipationless shock waves in repulsive Bose-Einstein condensates", Phys. Rev. A **69**, 063605 (2004).

[142] A. V. Gurevich and A. L. Krylov, "Nondissipative shock waves in media with positive dispersion", Zhurnal Eksperimental Noi I Teoreticheskoi Fiziki, **92**, 1684-1699 (1987).

[143] G. A. El and A. L. Krylov, "General solution of the Cauchy problem for the defocusing NLS equation in the Whitham limit", Phys. Lett. A **203**, 77-82 (1995).

[144] M. A. Hoefer, M. J. Ablowitz, I. Coddington, E. A. Cornell, P. Engels, and V.Schweikhard, "Dispersive and Classical Shock Waves in Bose-Einstein Condensates and Gas Dynamics", Phys. Rev. A **74**, 023626 (2006).

[145] I. Kulikov and M. Zak, "Shock waves in a Bose-Einstein condensate", Phys. Rev. A **67**, 063605 (2003)

[146] C. Wang, P. G. Kevrekidis, T. P. Horikis, D. J. Frantzeskakis, "Collisional-inhomogeneity-induced generation of matter-wave dark solitons", Phys. Lett. A **37**, 3863 (2010).

[147] T. F. Scott, R. J. Ballagh and K Burnett, "Formation of fundamental structures in Bose- Einstein condensates", J. Phys. B: At. Mol. Opt. Phys. **31** 329-335 (1998).

[148] M. R. Matthews, B. P. Anderson, P. C. Haljan, D. S. Hall, C. E. Wieman and E. A. Cornell,"Vortices in a Bose-Einstein condensate", Phys. Rev. Lett., **83**, 2498 (1999).

[149] M. I. Rodas-Verde, H. Michinel, V. M. Pérez-García, "Controllable soliton emission from a Bose-Einstein condensate", Phys. Rev. Lett. **95**, 153903 (2005).

[150] A. V. Carpentier, H. Michinel, M. I. Rodas-Verde, V. M. Pérez-García, "Analysis of an atom laser based on the spatial control of the scattering length", Phys. Rev. A **74** 013619 (2006).

[151] K. E. Strecker, G. B. Partridge, A. G. Truscott and R. G. Hulet, "Formation and propagation of matter-wave soliton trains", Nature **417**, 150-153 (1999).

[152] W. Bao, S. Jin and P.A. Markowich, "Numerical solution of the GrossPitaevskii equation for BoseEinstein condensation", J. Comput. Phys. **187**, 318-342 (2003).

[153] In simulations, we used $\Delta x = 1/6$, $\Delta t = 0.0015$, $z \in (-500, 500)$, $\mu = 0.1$ and reflective boundary conditions.

[154] F. Béthuel, P. Gravejat and J.-C. Saut, "Existence and properties of travelling waves for the Gross-Pitaevskii equation", arXiv:0902.3804v1 (2009).

[155] T. Tsuzuki, "Nonlinear waves in the Pitaevskii-Gross equation", J. Low Temp. Phys. **4**, 441(1971).

[156] E. A. Kuznetsov and M. D. Spector, "Modulation instability of soliton trains in fiber communication systems", Theor. and Math. Phys. **120**, 997-1008 (1999).

[157] P. F. Byrd and M.D. Friedman, "Handbook of Elliptic Integrals for Engineers and Scientists", Springer-Verlag, Berlin, Germany (1954).

[158] L. D. Carr, W. C. Clark and W.P. Reinhardt, "Stationary solutions of the one-dimensional nonlinear Schrdinger equation. I. Case of repulsive nonlinearity", Phys. Rev. A **62**, 063610 (2000).

[159] L. D. Carr, W. C Clark and W.P. Reinhardt, "Stationary solutions of the one-dimensional nonlinear Schrdinger equation. II. Case of attractive nonlinearity", Phys. Rev. A **62**, 063611 (2000).

[160] W-P. Zhong, M. R. Belic, Y. Lu and T. Huang, "Traveling and solitary wave solutions to the one-dimensional Gross-Pitaevskii equation", Phys. Rev. E, **81**, 016605 (2010).

[161] V. V. Konotop and L. Pitaevskii, "Landau dynamics of a grey soliton in a trapped condensate", Phys. Rev. Lett. **93**, 240403 (2004).

[162] J. Brand and W.P. Reinhardt, "Solitonic vortices and the fundamental modes of the snake instability: Possibility of observation in the gaseous Bose-Einstein condensate", Phys. Rev. A, **65**, 043612 (2002).

[163] N.G. Berloff, "Evolution of rarefaction pulses into vortex rings", Phys. Rev. B, **65**, 0236031 (2002).

[164] We used a computational window of 240 space units in z and 10 units along the transverse directions x, y. Typical space steps are about $\Delta x = 0.25$ and the time steps $\Delta t \simeq 1.5 \times 10^{-4}$.

[165] N.G. Berloff, "Pade approximations of solitary wave solutions of the Gross-Pitaevskii equation", J. Phys. A: Math. Gen., **37** (5), 1617-1632 (2004).

[166] Kapitza, P., "Viscosity of liquid helium below the λ-point", Nature **141**, 74, (1938).

[167] Allen, J. F., Misener, A. D., "Flow of liquid helium II", Nature **141**, 75, (1938).

[168] L. Tisza, "Transport phenomena in helium II", Nature **141**, 913 (1938).

[169] C. Raman, M. Kohl, R. Onofrio, D.S. Durfee, C.E. Kuklewicz, Z. Hadzibabic and W. Ketterle, "Evidence for a critical velocity in a Bose-Einstein condensed gas", Phys. Rev. Lett. **83** (13), pp. 2502-2505 (1999).

[170] R. Onofrio, C. Raman, J. M. Vogels, J. Abo-Shaeer, A. P. Chikkatur and W. Ketterle, "Observation of Superfluid Flow in a Bose-Einstein Condensed Gas", Phys. Rev. Lett. **85**, 2228-2231 (2000).

[171] P. Engels and C. Atherton, "Stationary and Nonstationary Fluid Flow of a Bose-Einstein Condensate Through a Penetrable Barrier", Phys. Rev. Lett. **99**, 160405 (2007).

[172] T. Frisch, Y. Pomeau and S. Rica, "Transition to dissipation in a model of superflow", Phys. Rev. Lett. **69**, 1644-1647 (1992).

[173] C. Josserand, Y. Pomeau and S. Rica, "Vortex shedding in a model of superflow", Physica D **134**, 111-125 (1999).

[174] V. Hakim, "Nonlinear Schrödinger flow past an obstacle in one dimension", Phys. Rev. E **55**, 28352845 (1997).

[175] T. Winiecki, J. F. McCann, and C. S. Adams, "Pressure drag in linear and nonlinear quantum fluids", Phys. Rev. Lett. **82**, 5186-5189 (1999).

[176] J. S. Stießberger and W. Zwerger, "Critcal velocity of superfluid flow past large obstacles in Bose-Einstein condensates", Phys. Rev. A **62**, 061601(R) (2000).

[177] N.G. Berloff and P.H.Roberts,"Motions in a Bose condensate: VII. Boundary-layer separation", J. Phys. A: Math. Gen. **33**, 4025-4038 (2000).

[178] N. Pavloff, "Breakdown of superfluidity of an atom laser past an obstacle", Phys. Rev. A **66**, 013610 (2002).

[179] G. Watanabe, F. Dalfovo, F. Piazza, L. P. Pitaevskii and S. Stringari, "Critical velocity of superfluid flow through single-barrier and periodic potentials", Phys. Rev. A **80**, 053602 (2009).

[180] G.E. Astrakharchikab and L.P. Pitaevskii, "Motion of a heavy impurity through a Bose-Einstein condensate", Phys. Rev. A **70**, 013608 (2004).

[181] Y.G. Gladush, L.A. Smirnov and A.M. Kamchatnov, "Generation of Cherenkov waves in the flow of a BoseEinstein condensate past an obstacle", J. Phys. B: At. Mol. Opt. Phys. **41** 165301 (6pp) (2008).

[182] A.L. Fetter, "Rotating trapped Bose-Einstein condensates", Rev. Mod. Phys. **81**, 647–691 (2009).

[183] A.L. Fetter, "Rotating vortex lattice in a Bose-Einstein condensate trapped in combined quadratic and quartic radial potentials", Phy. Rev. A **64**, 063608 (2001).

[184] A.L. Fetter, N. Jackson and S. Stringari, "Rapid rotation of a Bose-Einstein condensate in a harmonic plus quartic trap", Phys. Rev. A **71**, 013605 (2005).

[185] D. E. Miller, J. K. Chin, C. A. Stan, Y. Liu, W. Setiawan, C. Sanner and W. Ketterle, "Critical velocity for superfluid flow across the BEC-BCS crossover", Phys. Rev. Lett. **99**, 070402 (2007).

[186] S. Giorgini, L. P. Pitaevskii and S. Stringari, "Theory of ultracold atomic fermi gases", Rev. Mod. Phys. **80**, 1215-1274 (2008).

[187] A. S. Rodrigues, P. G. Kevrekidis, R. Carretero-Gonzlez, D. J. Frantzeskakis, P. Schmelcher, T. J. Alexander and Yu. S. Kivshar, "Spinor Bose-Einstein condensate flow past an obstacle", Phys. Rev. A **79**, 043603 (2009).

[188] D.M. Stamper-Kurn, M. R. Andrews, A. P. Chikkatur, S. Inouye, H.-J. Miesner, J. Stenger and W. Ketterle, "Optical Confinement of a Bose-Einstein Condensate", Phys. Rev. Lett. **80**, 2027 (1998).

[189] M.-S. Chang, C. D. Hamley, M. D. Barrett, J. A. Sauer, K. M. Fortier, W. Zhang, L. You and M. S. Chapman, "Observation of Spinor Dynamics in Optically Trapped Rb87 Bose-Einstein Condensates", Phys. Rev. Lett. **92**, 140403 (2004).

[190] A. Amo, J. Lefrére, S. Pigeon, C. Adrados, C. Ciuti, I. Carusotto, R. Houdré, E. Giacobino and A. Bramati, "Superfluidity of polaritons in semiconductor microcavities", Nat. Phys. **5**, 805. (2009).

[191] A. Amo, D. Sanvitto, F. P. Laussy, D. Ballarini, E. del Valle, M. D. Martin, A. Lemaítre, J. Bloch, D. N. Krizhanovskii, M. S. Skolnick, C. Tejedor and L. Vina, "Collective fluid dynamics of a polariton condensate in a semiconductor microcavity", Nature **457**, 291-295 (2009).

[192] S. Pigeon, I. Carusotto and C. Ciuti, "Hydrodynamic nucleation of vortices and solitons in a resonantly excited polariton superfluid", Phys. Rev. B **83**, 144513 (2011).

[193] J. Keeling and N. G. Berloff, "Spontaneous Rotating Vortex Lattices in a Pumped Decaying Condensate", Phys. Rev. Lett. **100**, 250401 (2008).

[194] C. Connaughton, Christophe Josserand, Antonio Picozzi, Yves Pomeau and Sergio Rica, "Condensation of classical nonlinear waves", Phys. Rev. Lett. **95**, 263901 (2005).

[195] H. Salman and N. G. Berloff, "Condensation of classical nonlinear waves in a two-component system," Special issue on quantum gasses, Physica D, **238**, 1482, (2009).

[196] J. Keeling and N. G. Berloff, "Condensed-matter physics: Going with the flow", Nature **457**, 273-274 (2009).

[197] G. Grimberg, W. Pauls and U. Frisch, "Genesis of dAlemberts paradox and analytical elaboration of the drag problem", Phys. D, Nonl. Phen. **237**, 1878 - 1886 (2008).

[198] J.O. Hirschfelder, C. J. Goebel and L. W. Bruch, "Quantized vortices around wavefunction nodes. II", J. Chem. Phys. **61**, 5456 (1974).

[199] C. Huepe and M.-E. Brachet, "Scaling laws for vortical nucleation solutions in a model of superflow", Physica D **140** 126-140 (2000).

[200] N. G. Berloff and B. V. Svistunov, "Scenario of strongly nonequilibrated Bose-Einstein condensation", Phys. Rev. A **66**, 013603 (2002).

[201] N. G. Berloff and A. J. Youd, "Dissipative dynamics of superfluid vortices at nonzero temperatures", Phys. Rev. Lett. **99**, 145301 (2007).

[202] N.G. Berloff, "Interactions of vortices with rarefaction solitary waves in a Bose-Einstein condensate and their role in the decay of superfluid turbulence", Phys. Rev. A **69**, 053601 (2004).

[203] T. W. Neely, E. C. Samson, A. S. Bradley, M. J. Davis and B. P. Anderson, "Observation of Vortex Dipoles in an Oblate Bose-Einstein Condensate", Phys. Rev. Lett. **104**, 160401 (2010).

[204] J. Catani, G. Lamporesi, D. Naik, M. Gring, M. Inguscio, F. Minardi, A. Kantian and T. Giamarchi, "Quantum dynamics of impurities in a one-dimensional Bose gas", Phys. Rev. A **85**, 023623 (2012).

[205] S. Rica, "A remark on the critical speed for vortex nucleation in the nonlinear Schrödinger equation", Physica D **148**, 221-226 (2001).

[206] C. A. Jones and P. H. Roberts, "Motions in a Bose condensate. IV. Axisymmetric solitary waves", J. Phys. A: Math. Gen. **15** 2599 (1982).

[207] We numerically generated solutions using fourth order finite differences scheme in space and the fourth order Runge-Kutta time integration on a computational window of 361 space units in x and 121 units along the direction y transverse to the superfluid flow. Typical space steps are about $\Delta x = 0.25$ and time steps $\Delta t = 10^{-3}$. At the boundaries we have implemented an absorption layer of 20 grid points to minimize the reflection of emitted waves.

[208] We have considered a grid of 350 units in the x direction and 200 in the transverse direction. Step sizes in both directions have been 1/5 healing layer and time steps have been $\Delta t = 0.00015$.

[209] We have considered a Dirichlet-type obstacle at a computational grid of 700 units in x direction and 400 in the transverse direction. Step sizes in both directions have been 1/10 healing layer and time steps have been $\Delta t = 0.00005$.

[210] We have considered a computational grid of 500 units in the x direction and 500 in transverse direction. Step sizes in both directions have been 1/5 healing layer and time steps have been $\Delta t = 0.00002$.

[211] The grid was 500 units in x direction and 500 in the transverse direction. Step sizes in both directions have been 1/4 healing layer and time steps have been $\Delta t = 0.0001$.

[212] G. A. El, A. Gammal, and A. M. Kamchatnov, "Oblique Dark Solitons in Supersonic Flow of a Bose-Einstein Condensate", Phys. Rev. Lett. **97**, 180405 (2006).

[213] D.H. Santamore, E. Timmermans, "Multi-impurity polarons in a dilute Bose-Einstein condensate", New J. Phys. **13** 103029 (2011).

[214] The computing grid has been chosen to be 440 points in the x direction and 200 points in the y direction. Time steps were about $\Delta t = 0.004$ and space steps $\Delta x = 1$. At the boundaries of the grid we have implemented an absorption layer of 14 points in width to simulate open boundary conditions.

[215] P. Mason, N. G. Berloff, and A. L. Fetter, "Motion of a vortex line near the boundary of a semi-infinite uniform condensate", Phys. Rev. A **74**, 043611 (2006).

[216] The computing grid has been chosen to be 900 points in the x direction and 500 points in the y direction. Time steps were about $\Delta t = 0.00025$ and space steps $\Delta x = 0.5$. At the boundaries of the grid we have implemented an absorption layer of 14 points in width to simulate open boundary conditions.

[217] Our simulations on randomly distributed atoms relied on the Fortran RANDOM NUMBER routine and we have used the standard seed.

[218] The computing grid has been chosen to be 880 points in x direction and 480 points in transversal direction. Time steps were about $\Delta t = 0.0004$ and space steps $\Delta x = 0.5$. At the boundaries of the grid we have implemented an absorption layer of 14 points in width.

[219] S. O. Demokritov, V. E. Demidov, O. Dzyapko, G. A. Melkov, A. A. Serga, B. Hillebrands and A. N. Slavin, "Bose-Einstein condensation of quasi-equilibrium magnons at room temperature under pumping", Nature **443**, 430 - 433 (2006).

[220] L. V. Butov, "Cold exciton gases in coupled quantum well structures", J. Phys. Condens. Matter **19**, 295202 (2007).

[221] I. S. Aranson and L. Kramer, "The world of the complex GinzburgLandau equation", Rev. Mod. Phys. **74**, pp. 99-143 (2002).

[222] G. P. Agrawal, "Nonlinear Science at the Dawn of the 21st Century", Lecture Notes in Physics **542**, pp. 195-211 (2000).

[223] J. Scheuer, M. Orenstein, and D. Arbel, "Nonlinear switching and modulational instability of wave patterns in ring-shaped vertical-cavity surface-emitting lasers", JOSA B **19**, pp. 2384-2390 (2002).

[224] G. P. Agrawal and H. A. Haus, "Applications of Nonlinear Fiber Optics", Physics Today **55** pp. 58 (2002).

[225] D. Woods, T. J. Naughton, "Optical computing: Photonic neural networks", Nature Physics **8**, 257-259 (2012).

[226] E. M. Dianov, P. V. Mamyshev and A. M. Prokhorov, "Nonlinear fiber optics", Sov. j. quantum electron **18**, 1-15. (1988).

[227] L. Bi, H. Juejun, P. Jiang, H. D. Kim, F. G. Dionne, L.C. Kimerling, C. A. Ross, "On-chip optical isolation in monolithically integrated non-reciprocal optical resonators", Nature Photonics **5**, pp. 758-762 (2011).

[228] W. Chen, K. M. Beck, R. Bücker, M. Gullans, M. D. Lukin, H. Tanji-Suzuki and V. Vuletić ,"All-Optical Switch and Transistor Gated by One Stored Photon", Science **341** 768-770 (2013).

[229] D. Ballarini, M. De Giorgi, E. Cancellieri, R. Houdré, E. Giacobino, R. Cingolani, A. Bramati, G. Gigli and D. Sanvitto "All-optical polariton transistor", Nature Communications **4** 1778 (2013).

[230] C. Antón, T.C.H. Liew, J. Cuadra, M.D. Martín, P.S. Eldridge, Z. Hatzopoulos, G. Stavrinidis, P.G. Savvidis and L. Vina, "Implementation of a logic AND gate with polariton condensate bullets", arXiv:1305.5678 (2013).

[231] D. Woods and T. J. Naughton, "Optical computing", Applied Mathematics and Computation **215**, pp. 1417-1430 (2009).

[232] G. Tosi, G. Christmann, N. G. Berloff, P. Tsotsis, T. Gao, Z. Hatzopoulos, P. G. Savvidis and J. J. Baumberg, "Sculpting oscillators with light within a nonlinear quantum fluid", Nature Physics **8**, 190-194 (2012).

[233] T. Gao, P. S. Eldridge, T. C. H. Liew, S. I. Tsintzos, G. Stavrinidis, G. Deligeorgis, Z. Hatzopoulos and P. G. Savvidis, "Polariton condensate transistor switch", Phys. Rev. B **85**, 235102 (2012).

[234] R. Hivet, H. Flayac, D. D. Solnyshkov, D. Tanese, T. Boulier, D. Andreoli, E. Giacobino, J. Bloch, A. Bramati, G. Malpuech and A. Amo, "Half-solitons in a polariton quantum fluid behave like magnetic monopoles", Nature Physics **8**, 724-728 (2012).

[235] D. D. Solnyshkov, H. Flayac and G. Malpuech, "Stable magnetic monopoles in spinor polariton condensates", Phys. Rev. B **85**, 073105 (2012).

[236] H. Flayac, D. D. Solnyshkov and G. Malpuech, "Separation and acceleration of magnetic monopole analogs in semiconductor microcavities", New J. Phys. **14**, 085018 (2012).

[237] H. Terças, H. Flayac, D. Solnyshkov and G. Malpuech, "Non-Abelian Gauge Fields in Photonic Cavities and Photonic Superfluids", arXiv:1310:6588 (2013).

[238] I. A. Shelykh, A. V. Kavokin, Y. G. Rubo, T. C. H. Liew and G. Malpuech, "Polariton polarization-sensitive phenomena in planar semiconductor microcavities", Semicond. Sci. Technol. **25**, 013001 (2010).

[239] F. Manni, "Coherence and Topological Defects in Exciton-Polariton Condensates", PhD thesis, Ècole polytechnique fèdèrale de Lausanne, Lausanne, Switzerland (2013).

[240] E. Wertz, L. Ferrier, D. D. Solnyshkov, R. Johne, D. Sanvitto, A. Lemaítre, I. Sagnes, R. Grousson, A. V. Kavokin, P. Senellart, G. Malpuech and J. Bloch, "Spontaneous formation and optical manipulation of extended polariton condensates", Nature Physics **6**, 860 (2010).

[241] H. Flayac, G. Pavlovic, M. A. Kaliteevski and I. A. Shelykh, "Electric generation of vortices in an exciton-polariton superfluid", Phys. Rev. B **85**, 075312 (2012).

[242] I. G. Savenko, T. C. H. Liew, and I. A. Shelykh, "Stochastic Gross-Pitaevskii Equation for the Dynamical Thermalization of Bose-Einstein Condensates", Phys. Rev. Lett. **110**, 127402 (2013).

[243] Y. V. Kartashov and A. M. Kamchatnov, "Two-dimensional dispersive shock waves in dissipative optical media", Optics Letters, 38, Issue 5, pp. 790-792 (2013).

[244] N. G. Berloff and Victor M. Perez-Garcia, "A nonlinear quantum piston for the controlled generation of vortex rings", (preprint) arXiv:1006.4426 (2010).

[245] N. G. Berloff and P. H. Roberts, "Motions in a Bose condensate: VII. Boundary-layer separation", J. Phys. A: Math. Gen. **33** 4025 (2000).

[246] M. Kaliteevski, I. Iorsh, S. Brand, R. A. Abram, J. M. Chamberlain, A. V. Kavokin and I. A. Shelykh, "Tamm plasmon-polaritons: Possible electromagnetic states at the interface of a metal and a dielectric Bragg mirror", Phys. Rev. B **76**, 165415 (2007).

[247] C. W. Lai, N. Y. Kim, S. Utsunomiya, G. Roumpos, H. Deng, M. D. Fraser, T. Byrnes, P. Recher, N. Kumada, T. Fujisawa and Y. Yamamoto, "Coherent zero-state and pi-state in an excitonpolariton condensate array", Nature, **450**, 529-532 (2007).

[248] T. C. H. Liew, A. V. Kavokin, T. Ostatnicky, M. Kaliteevski, I. A. Shelykh and R. A. Abram, "Exciton-polariton integrated circuits", Phys. Rev. B **82**, 033302 (2010).

[249] H. Flayac, H. Terças, D. D. Solnyshkov, and G. Malpuech, "Superfluidity of spinor Bose-Einstein condensates", Phys. Rev. B **88**, 184503 (2013).

[250] N. Q. Ngo, "Proposal for a high-speed optical dark-soliton detector using a microring resonator", Phot. Technol. Lett. 19, 7 (2007).

[251] E. Kammann, T. C. H. Liew, H. Ohadi, P. Cilibrizzi, P. Tsotsis, Z. Hatzopoulos, P. G. Savvidis, A. V. Kavokin and P. G. Lagoudakis, "Nonlinear Optical Spin Hall Effect and Long-Range Spin Transport in Polariton Lasers", Phys. Rev. Lett. **109**, 036404 (2012).

[252] Y. Senatsky, J.-F. Bisson, J. Li, A. Shirakawa, M. Thirugnanasambandam and K. Ueda "LaguerreGaussian Modes Selection in Diode-Pumped Solid-State Lasers", Opt. Rev. **19**, (4) 201-221 (2012).

[253] S. F. Pereira, M. B. Willemsen, M. P. van Exter and J. P. Woerdman, "Pinning of daisy modes in optically pumped vertical-cavity surface-emitting lasers." Appl. Phys. Lett. **73**, (16), 2239-2241 (1998).

[254] M. Schulz-Ruhtenberg, Y. Tanguy, R. Jger, T. Ackemann, "Length scales and polarization properties of annular standing waves in circular broad-area vertical-cavity surface-emitting lasers", Appl. Phys. B **97**, (2), 397-403 (2009).

[255] Q. Deng, H. Deng and D. G. Deppe, "Lasing on higher-azimuthal-order modes in vertical cavity surface emitting lasers at room temperature", Opt. Lett. **22**, (7) 463-465 (1997).

[256] D. Naidoo, K. Ait-Ameur, M. Brunel and A. Forbes, "Intra-cavity generation of superpositions of Laguerre-Gaussian beams", Appl. Phys. B **106**, (3), 683-690 (2012).

[257] Y.F. Chen, Y.P. Lan and S.C. Wang, "Generation of LaguerreGaussian modes in fiber-coupled laser diode end-pumped lasers", Appl. Phys. B **72** (2) 167-170 (2001).

[258] M. Grabherr, M. Miller, R. Jäger, D. Wiedenmann, R. King, "Commercial VCSELs reach 0.1 W cw output power", Proc. SPIE 5364: 174-182 (2004).

[259] L. Allen, M. W. Beijersbergen, R.J.C Spreeuw, J.P. Woerdman, "Orbital angular momentum of light and the transformation of Laguerre-Gaussian laser modes", Phys. Rev. A **45**, (11), 8185-8189 (1992).

[260] J.A. Rodrigo, A.M. Caravaca-Aguirre, T. Alieva, G. Cristóbal, M.L. Calvo, "Microparticle movements in optical funnels and pods", Opt. Express **19** (6) 5232-5243 (2011).

[261] G. Molina-Terriza, J.P. Torres and L. Torner, "Twisted photons", Nat. Phys. **3** (5), 305-310 (2007).

[262] A. Imamoglu, R.J. Ram, S. Pau and Y. Yamamoto, "Nonequilibrium condensates and lasers without inversion: Exciton-polariton lasers", Phys. Rev. A **54**, (6), 4250-4253 (2006).

[263] H. Deng, G. Weihs, D. Snoke, J. Bloch and Y. Yamamoto, "Polariton vs. photon lasing in a semiconductor microcavity", P. Natl. Acad. Sci. **100**, (26), 15318-15323 (2003).

[264] C. Weisbuch, M. Nishioka, A. Ishikawa and Y. Arakawa, "Observation of the coupled exciton-photon mode splitting in a semiconductor quantum microcavity", Phys. Rev. Lett. **69**, (23), 3314-3317 (1992).

[265] R. Balili, V. Hartwell, D. Snoke, L. Pfeiffer and K. West, "Bose-Einstein Condensation of Microcavity Polaritons in a Trap", Science **316** (5827) 1007-1010 (2007).

[266] E. Wertz, L. Ferrier, D. D. Solnyshkov, R. Johne, D. Sanvitto, A. Lemaítre, I. Sagnes, R. Grousson, A. V. Kavokin, P. Senellart, G. Malpuech and J. Bloch, "Spontaneous formation and optical manipulation of extended polariton condensates", Nat. Phys. **6**, (11), 860-864 (2010).

[267] K. G. Lagoudakis, M. Wouters, M. Richard, A. Baas, I. Carusotto, R. André, Le Si Dang and B. Deveaud-Plédran, "Quantized vortices in an exciton-polariton condensate", Nat. Phys. **4**, (9), 706-710 (2008).

[268] D. Sanvitto, F. M. Marchetti, M. H. Szymańska, G. Tosi, M. Baudisch, F. P. Laussy, D. N. Krizhanovskii, M. S. Skolnick, L. Marrucci, A. Lemaítre, J. Bloch, C. Tejedor and L. Vina, "Persistent currents and quantized vortices in a polariton superfluid", Nat. Phys. **6**, (7), 527-533 (2010).

[269] Amo A, et. al. (2009) Collective fluid dynamics of a polariton condensate in a semiconductor microcavity. Nature 457(7227):291-296l.

[270] F. Manni, K. G. Lagoudakis, T. C. H. Liew, R. André, B. Deveaud-Plédran, "Spontaneous pattern formation in a polariton condensate", Phys. Rev. Lett. **107**, (10), 106401 (2011).

[271] T. C. H. Liew, A. V. Kavokin, I. A. Shelykh, "Optical Circuits Based on Polariton Neurons in Semiconductor Microcavities", Phys. Rev. Lett. **101**, (1), 016402 (2008).

[272] A. Amo, T. C. H. Liew, C. Adrados, R. Houdré, E. Giacobino, A. V. Kavokin and A. Bramati, "Exciton-polariton spin switches", Nat. Photonics **4**, (6), 361-366 (2010).

[273] G. Franchetti, N. G. Berloff and J. J. Baumberg, "Exploiting quantum coherence of polaritons for ultra sensitive detectors", arXiv:1210.1187 (2012).

[274] G. Nardin, K. G. Lagoudakis, M. Wouters, M. Richard, A. Baas, R. André, Le Si Dang, B. Pietka and B. Deveaud-Plédran, "Dynamics of Long Range Ordering in an Exciton Polariton Condensate", Phys. Rev. Lett. **103**, (25), 256402 (2009).

[275] R. Spano, J. Cuadra, G. Tosi, C Antón, C. A. Lingg, D. Sanvitto, M. D. Martín, L. Vina, P. R. Eastham, M. van der Poel and J. M. Hvam, "Coherence properties of exciton polariton OPO condensates in one and two dimensions", New J. Phys. **14**, 075018, (2012).

[276] G. Christmann, G. Tosi, N. G. Berloff, P. Tsotsis, P. S. Eldridge, Z. Hatzopoulos, P. G. Savvidis and J. J. Baumberg, "Polariton ring condensates and sunflower ripples in an expanding quantum liquid. Phys. Rev. B **85**, (23), 235303 (2012).

[277] D. Naidoo, T. Godin, M. Fromager, E. Cagniot, N. Passilly, A. Forbes and Kamel Ait-Ameurc, "Transverse mode selection in a monolithic microchip laser", Opt. Commun. **284**, (23), 5475-5479 (2011).

[278] R. Kleiner, D. Koelle, F. Ludwig, J. Clarke, "Superconducting quantum interference devices: State of the art and applications", Proc. IEEE, **92** (10), 1534 (2004).

[279] T. P. Orlando, J. E. Mooij, L. Tian, C. H. van der Wal, L. S. Levitov, S. Lloyd, J. J. Mazo, "Superconducting persistent-current qubit", Phys. Rev. B **60**, (22), 15398-15413 (1999).

[280] P. Cristofolini, A. Dreismann, G. Christmann, G. Franchetti, N. G. Berloff, P. Tsotsis, Z. Hatzopoulos, P. G. Savvidis and J. J. Baumberg, "Optical Superfluid Phase Transitions and Trapping of Polariton Condensates", Phys. Rev. Lett. **110**, (18), 186403 (2013).

[281] M. Wouters, T. Liew, V. Savona, "Energy-relaxation in one-dimensional polariton condensates", Phys Rev B **82**, (24), 245315 (2010).

[282] T. F. Scott, R. J. Ballagh and K. Burnett, "Formation of fundamental structures in Bose-Einstein condensates", J. Phys. B: At. Mol. Opt. Phys. **31**, (8), 329 (1998).

[283] Askitopoulos A, H. Ohadi, A. V. Kavokin, Z. Hatzopoulos, P. G. Savvidis, and P. G. Lagoudakis, "Polariton condensation in an optically induced two-dimensional potential", Phys. Rev. B **88**, (4), 041308(R) (2013).

[284] L. Ge, A. Nersisyan, B. Oztop and H.E. Treci, "Pattern Formation and Strong Nonlinear Interactions in Exciton-Polariton Condensates", arXiv:1311.4847 (2013).

[285] D. Naidoo, K. Ait-Ameur, M. Brunel and A. Forbes, "Intra-cavity generation of superpositions of LaguerreGaussian beams", Appl. Phys. B **106**, (3), 683-690 (2012).